NOVEL COBALT- AND IRON-BASED HALF METALLIC AND SPIN GAPLESS HEUSLER COMPOUNDS WITH POTENTIAL FOR SPINTRONICS DEVICE APPLICATIONS

by

RABIN MAHAT

PATRICK R. LECLAIR, COMMITTEE CHAIR
ARUNAVA GUPTA, COMMITTEE CO-CHAIR
ADAM HAUSER
GEORG SCHWIETE
MARCOS SANTANDER

A DISSERTATION

Submitted in partial fulfillment of the requirements
for the degree of Doctor of Philosophy
in the Department of Physics and Astronomy
in the Graduate School of
The University of Alabama

TUSCALOOSA, ALABAMA

2022

ABSTRACT

Heusler alloys are at the center of scientific research for their potential use in spintronics device applications, since several among them have been predicted to show half-metallicity at room temperature due to their observed high Curie temperature and large interinsic magnetic moments. However, the experimentally observed spin polarization of most of the ternary Heusler alloys are always much smaller than the predicted theoretical values. The discrepancy between theory and experiment is expected due to the structural disorder in the crystal lattices. In this work, we have introduced a new approach of designing novel materials to precisely control the relationship between structure and various physical properties. Here, promising alloys were first screened and investigated utilizing theoretical approach, followed by experimental analysis on the bulk properties of Heusler alloys. Our findings shed light on tuning the electronic and magnetic properties to get robust half-metallicity.

Full Heulser alloys (X_2YZ) exhibit exceptional tunability in the electronic and magnetic phenomenon depending upon the nature of elements occupying X and/or Y site. This work utilizes the substitution of low valence transition metal atoms Sc, Ti, V, Cr, Mn, or Fe as a quaternary element in X site. Various Co- and Fe-based ternary Heusler alloys Co_2FeZ (Z = Ge, Si, Ga, Al) are selected and the substitutional effect of all low valence transition metal atoms Y = Sc, Ti, V, Cr, Mn, or Fe for Co atom in the parent system on structural, electronic, magnetic, electron transport and mechanical properties of quaternary Heusler compounds $Co_{2-x}Y_xFeZ$ ($0 \leq x \leq 1$) are examined, both experimentally and theoretically.

The first Heusler system that we studied is the substitution of Cr and V for Co in disordered Co_2FeGe. Our investigations revealed that Cr and V substitutions for Co not only stabilized the disordered Co_2FeGe, but also tuned the electronic and magnetic properties, making Cr and V ideal dopant for achieving robust half-metallic behavior. The next system studied was $Co_{2-x}Y_xFeSi$ (Y = Sc, Ti, V, Cr, Mn, or Fe, $0 \leq x \leq 1$), which eventually leads to a global overview of the electronic, magnetic, electron transport and mechanical properties of promising candidates for spintronics applications. Next, our investigations for finding half-metallic Heuslers led to synthesizing $Co_{2-x}Y_xFeGa$/Al (Y = Ti, V, Cr, Mn, or Fe, $x = 0.50$) where we found $Co_{1.50}Mn_{0.50}FeGa$ to show spin-gapless semiconducting behavior in the complete temperature regime (5K-400K). Other alloys in the series are also observed to show interesting tunable half-metallic behavior.

Further, inspired from the fact that identifying a hexagonal Heusler analogue that retains half-metallic and exhibits a high magneto-crystalline anisotropy may be very attractive for applications such as perpendicular media, current perpendicular to plane giant magnetoresistance (CPP-GMR), and spin-torque-transfer RAM (STT-RAM), we synthesized and investigated the Fe-based Heusler alloys $Fe_{3-x}Y_xGe$ (Y = V, or Cr, $0 \leq x \leq 1$) with the hexagonal DO_{19} structure. These materials possess high magnetic moment and high magneto-crystalline anisotropy, which adds a step toward finding the half-metallic Heusler compounds in hexagonal crystal structure for their potential use in perpendicular media and CPP-GMR.

DEDICATION

To my late father Laxman Bahadur Mahat, who unfortunately didn't stay in this world long enough to see his son become a doctor.

LIST OF ABBREVIATIONS AND SYMBOLS

AFM	Antiferromagnetic
a.u.	Arbitrary Units
BSE	Backscattered Electrons
CE	Cluster Expansion
CFA	Co_2FeAl
CFG	Co_2FeGe
CFCG	CoFeCrGe
CFS	Co_2FeSi
CFVG	CoFeVGe
χ	Chi factor
CPP-GMR	Current Perpendicular to Plane Giant Magnetoresistance
d	Interplanar Spacing
Δ	Energy gap for the minority spins at E_F
DFT	Density Functional Theory
DOS	Density of States
DSC	Differential Scanning Callorimetry
EBSD	Electron Back Scatter Diffraction
EDS	Energy Dispersive Spectroscopy

E_f	Fermi Energy Level
fcc	Face-Centered Cubic
FE	Field Emission
FESEM	Field Emission Scanning Electron Microscope
FHA	Full Heusler Alloys
FIB	Focused Ion Beam
FM	Ferromagnetic
FWHM	Full Width at Half Maximum
GGA	Generalized Gradient Approximation
GMR	Giant Magnetoresistance
GTMR	Giant Tunneling Magnetoresistance
HMF	Half-Metallic Ferromagnet
IPF	Inverse Pole Figure
λ	Wavelength
MCSQS	Monte Carlo Special Quasirandom Structure
MR	Magnetoresistance
MRAM	Magnetic Random Access Memory
MTJ	Magnetic Tunnel Junction
MOKE	Magneto Optic Kerr Effect
M_s	Saturation Moment
μ_B	Bohr Magnetron
n	Integer

n	Number of Electrons in the Minority Channel
N	Number of Experimental Data Points
NM	Non-Magnetic
N_V	Number of Valence Electrons
Ω	Ohm
ω	Angular Frequency
PAW	Projector Augmented-Wave
PBE	Perdew-Burke-Enzerhof
PCAR	Point Contact Andreev Reflection
PDOS	Partial Density of States
Φ	Magnetic Flux
PPMS	Physical Property Measurement System
RAM	Random Access Memory
R_{exp}	Expected R factor
R_{wp}	Weight-Profile R factor
SD	Standard Deviation
SE	Secondary Electron
SEM	Scanning Electron Microscopy
SFET	Spin Polarized Field Effect Transistor
SGS	Spin Gapless Semiconductor
S-P	Slater-Pauling
SQS	Special Quasirandom Structure

STT	Spin Torque Transfer
T_c	Curie Temperature
TDOS	Total Density of States
TEM	Transmission Electron Microscopy
θ	Bragg Angle
TMR	Tunneling Magnetoresistance
UA	University of Alabama
UAHPC	UA High Performance Computing Facility
VASP	Vienna *ab initio* Simulation Package
VSM	Vibrating Sample Magnetometry
w	Weighting factor
WDS	Wavelength-Dispersive X-ray Spectroscopy
XRD	X-Ray Diffraction

ACKNOWLEDGMENTS

My deepest gratitude goes to my advisor and the chairman of my dissertation committee Dr. Patrick R. LeClair who supported me to the fullest throughout the course of my graduate study at The University of Alabama. Without his expert-level, guidance and continuous encouragements, this dissertation could not be completed. I also appreciate the support from NSF DMREF Grant number 1235396, and NSF DMR Grant number 1508680.

My gratitude also goes to my co-advisor Dr. Arunava Gupta for his continuous advice, support and outstanding technical management and organizational leadership from very beginning of my Ph.D. journey. I would like to express my gratitude to my other Masters' and Ph.D. graduate advisory committee members, Dr. Adam Hauser, Dr. Georg Schwiete, and Dr. Marcos Santander for their valuable inputs during the past years. My sincere gratitude also goes to Dr. Iosif Galanakis from University of Patras, Greece who as a world renowned expert of the field, agreed to mentor me in computational simulations. I am highly indebted to Dr. Iosif. I would also like to thank Dr. William Butler for sharing his knowledge and expertise in theoretical calculations. I am grateful for his help in granting VASP access from UAHPC. My sincere gratitude extends to all great instructors including Dr. Tim Mewes, Dr. Claudia Mewes, Dr. Takao Suzuki, and Dr. Gary Mankey for having introduced me to the frontier research areas of advanced magnetism and magnetic materials.

Also, I would like to acknowledge our great colloborators whose collaboration was indispensable in culmination of many projects; Dr. Can Ataca and his group from the University of Maryland Baltimore County for collaboration in theoretical calculations, Dr. Victorino Franco and his group

from Universidad de Sevilla and Dr. Prahallad Padhan from Indian Institute of Technology Madras for collaboration in high temperature magnetometry, Dr. Shane Street and his group from UA for collaboration in magnetic nanoparticales, Dr. Rachael White for her help in differential scanning calorimetry measurement and Dr. Mark Weaver for helpful discussions on measurements of mechanical properties.

I am especially thankful to Dr. Nariman Naghibolashrafi for introducing me research methods and analysis. I would like to thank to my friends, colleagues, and seniors Dr. Josh Jones, Dr. Amit Singh, Dr. Behrouz Khodadadi, Dr. Zhong Li, Sudhir Regmi, Dr. Abhishek Srivastava, Dr. William Sides for their help and collaborations. My thanks also go to technical staffs from physics department machine shop, electronic technicians, and members of Alabama Analytical Research Center (AARC) in The University of Alabama whose help was essential in my progress toward finishing this dissertation. I am also grateful to UA High Performance Computing Facility (UAHPC) for providing the resource for theoretical calculations.

Most importantly, none of this could have happened without unwavering support from my dear family in Nepal. I am deeply indebted to my mother, Tika Devi Mahat, my brother, Rajan Mahat and my sisters, Sophiya and Sonia for always having an open door to me. My beloved wife Upama, thank you for believing in me at every step and sticking with me to the end, your love and kindness has kept me sane in every aspect of my life. My beautiful daughter Alaiyah, you inspire me everyday to grow and be better, I love you and I can't express the joy I have in soon being near each other again. Last but not the least, I am eternally grateful to Matthew Abbott, Beverly Abbott, and Nesha Smelley for their constant support and encouragement. None of this would be possible without having these many wonderful people around me.

CONTENTS

LIST OF TABLES

LIST OF FIGURES

CHAPTER 1

INTRODUCTION

1.1 Spintronic devices: recent development and future perspectives

Spintronics, spin-based electronics, is one of the most promising and rapidly developing paradigm of electronics based on spin degree of freedom in addition to the charge of electrons. Spintronics devices have a potential to revolutionize the world of electronics. The discovery of giant magnetoresistance (GMR) by Fert *et al.* [23] and Grünberg *et al.* [24] independently was the first major breakthrough in the field of spintronics. In GMR effect, the electrical resistance can be switched from high to low and vice-versa significantly just by switching the magnetization of adjacent ferromagnetic layers separated by thin non-magnetic spacer from antiparallel alignment to parallel and vice-versa, respectively by applying an external magnetic field. This phenomenon is utilized in the development of data storage devices, such as magnetic field sensors, hard disk drives, magnetic random access memory (MRAM) and biosensors [25–28]. The improvement in MR junctions are magnetic tunnel junctions (MTJ) where ferromagnetic layers are separated by an oxide tunnelling barrier. MTJ are promising in spin transfer torque-magnetic random access memory (STT-MRAM) as shown in Fig. 1.1(a). The performance of MTJ is determined in terms of tunnelling magnetoresistance (TMR) ratio as;

$$\text{TMR ratio} = \frac{2P_1P_2}{(1-P_1P_2)} \tag{1.1}$$

where P_1 and P_2 are effective spin polarisation of ferromagnetic layers. Ferromagnetic layers with 100% spin polarization are expected for the coherent tunnelling which ideally results the TMR ratio

of infinity. STT is reported to provide an ultra-low-power switching (writing) solution and make a down-scaling of the individual bit cell below 10 nm possible [1]. Another promising spintronics device is spin-polarized field effect transistor (SFET) whose performance depends on the injected spin current through source (ferromagnetic electrode) as shown in Fig. 1.1(b). In order to detect all the current without any loss through transistor gate, injection of 100% spin polarized current is expected.

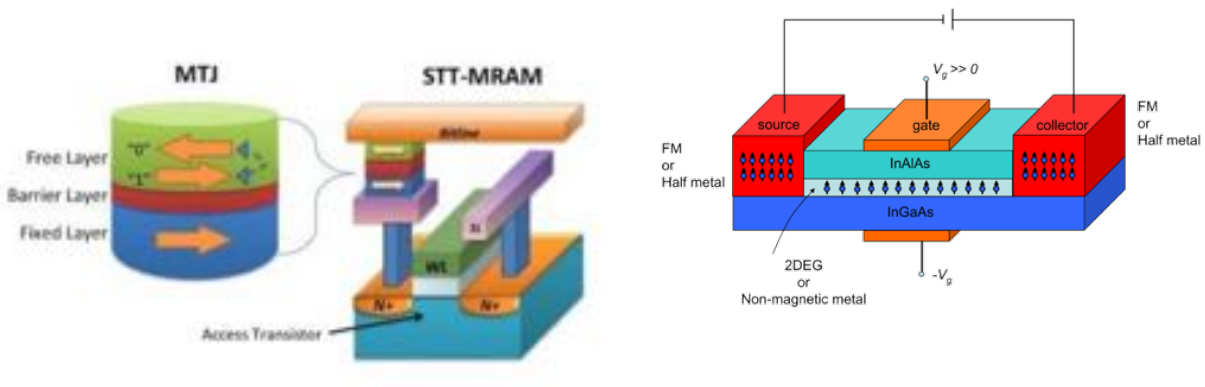

(a) (b)

Figure 1.1: Schematic of (a) STT-MRAM and (b) SFET showing the possible use of half-metallic ferromagnets. Reproduced after [3, 4]

To improve the performance of spintronics devices which use MR junctions including MTJ, half-metallic ferromagnets (HMFs) are promising to achieve 100% spin polarisation at the Fermi energy level (E_F) at room temperature, leading to an infinite MR ratio. The half-metallicity is to due the exceptional electronic structure with a energy band gap at E_F in one of the spin sub-band in density of states (DOS) as schematically shown in Fig. 1.10 [20, 29–34]. There are mainly four types of HMFs predicted theoretically and demonstrated experimentally; (1) oxide compounds (*e.g.,* rutile CrO_2 [35] and spinel Fe_3O_4 [36]), (2) perovskites (*e.g.,* (La,Sr)MnO_3) [37], (3) magnetic semiconductors, including Zinc-blende compounds (*e.g.,* EuO and EuS [38], (Ga,Mn)As and CrAs) [39], and (4) Heusler alloys (*e.g.,* NiMnSb) [29]. Among these HMFs, 100% spin polarization has been reported in the magnetic semiconductors due to their Zeeman

splitting in two spin bands. However, their Curie temperatures (T_c) are below room temperature [40]. There are no experimental reports with half-metallicity at room temperature to date. The Heusler alloys are observed to exhibit the half-metallicity at room temperature [41–43] and a 100% spin polarization for bulk MnNiSb was confirmed by polarized positron-annihilation experiments and inverse photo-emission [44–46] and about 93% spin polarization has been reported in an in-situ Heusler films [47]. Therefore, the Heusler alloys can be the most promising candidate for the room temperature half-metallicity due to their lattice matching with major substrates, high T_c and large band gap at E_F and hence ideal spin injectors into a semiconductor.

1.2 Heusler Compounds

Heusler compounds, first discovered by and named after Fritz Heusler in 1903 [48], are very unique and versatile because one can get ferromagnets from the mixture of non-magnetic constituents, such as the first Heusler prototype Cu_2MnAl. Heusler compounds have attracted the interest of scientific community due to their immense technological potential exhibiting a series of diverse magnetic phenomena such as itinerant magnetism, localized magnetism, antiferromagnetism [49], ferrimagnetism [50], Pauli paramagnetism [51], heavy-fermionic behaviour [52], half-metallicity [29], spin-glass semiconducting behaviour [53], magneto-caloric behavior [54], magneto-optic behavior [55], superconductivity [56], and thermo-electricity [57]. Because of the fact that Heusler alloys exhibit these above mentioned diverse magnetic phenomena, they are promising in spintronics technology, yet to be realized, which would also help in advancing high-density memory storage. The Nobel Prize in physics in 2007 for the discovery of GMR clearly demonstrates the paramount interest in this field [23, 24]. Additionally, some of the Heuslers are recently predicted to be topological insulators [58] and Weyl Semi-metals [59], making this family appealing to explore new physics creating multifunctional topological heterostructures. In addition, the thermoelectric properties of Heusler alloys are promising in the energy harvesting technologies in industries [57, 60]. Considerable amount of dissipated heat in industries can be converted back into electricity using thermoelectric Heuslers which are environment friendly and

mechanically robust. Various aspects of Heusler compounds are displayed in Fig. 1.2

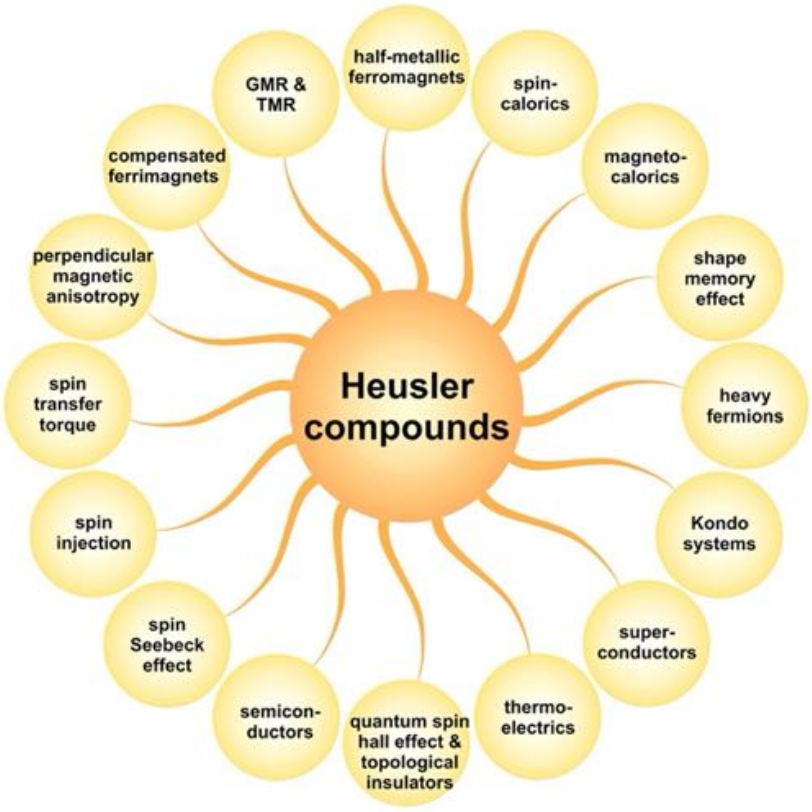

Figure 1.2: Different aspects of Heusler compounds, Reproduced after [1].

1.2.1 Types, crystal structure and atomic ordering

Mainly, there are four types of Heusler compounds, based on their crystal structure and the number of constituents elements: Full Heusler, Half-Heusler, Inverse-Heusler, and Quaternary-Heusler compounds. Properties of these compounds depend on the crystal structure, atomic and chemical ordering of the elements in the structure.

Full Heusler compounds have the stoichiometry 2:1:1 with chemical formula X_2YZ, where X and Y are transition metal atoms and Z is main group element. The elements normally associated with X, Y and Z are indicated in Fig. 1.3. At the stoichiometric composition, full Heusler alloys crystallize in the $L2_1$ structure with space group $Fm\bar{3}m$ (#225) which consists of four interpenetrating face-centred cubic (*fcc*) sublattices (with two magnetic sublattice) with the Wyckoff positions

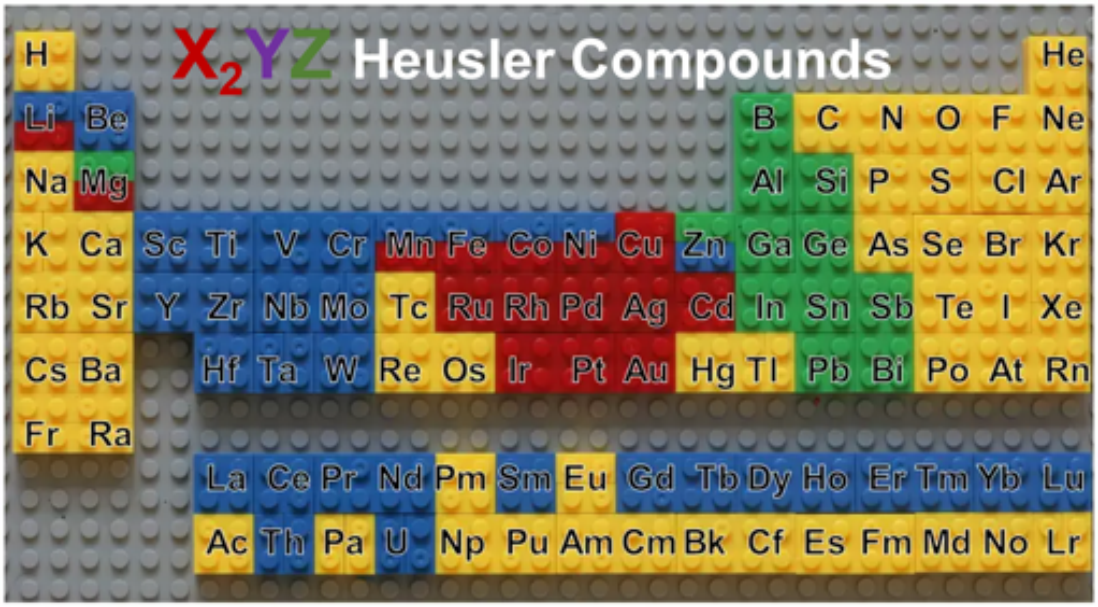

Figure 1.3: The periodic table of the elements showing the candidates for Heusler compounds according to the color scheme. Reproduced after [5].

8c($\frac{1}{4},\frac{1}{4},\frac{1}{4}$) (or 4c($\frac{1}{4},\frac{1}{4},\frac{1}{4}$), and 4d($\frac{3}{4},\frac{3}{4},\frac{3}{4}$)) for X, 4b($\frac{1}{2},\frac{1}{2},\frac{1}{2}$) for Y, and 4a(0,0,0) for Z [1, 61], as shown in Fig. 1.4(a). In the chemical formula X_2YZ, the low valence transition metal atom Y with least electronegativity, and the most electronegative main group element Z form NaCl-type ionic bonding and occupy the octahedral positions while transition metal atoms X are of the intermediate electronegativity values and fill the tetrahedral positions in the crystal structure forming zinc blende-type covalent bonding with Z atoms.

Half Heusler compounds have the stoichiometry 1:1:1 with chemical formula XYZ. They crystallize in the $C1_b$ structure with space group $F\bar{4}3m$ (#216) which consists of three interpenetrating fcc sublattices (with one magnetic sublattice) with the Wyckoff positions 4c($\frac{1}{4},\frac{1}{4},\frac{1}{4}$) for X, 4b($\frac{1}{2},\frac{1}{2},\frac{1}{2}$) for Y, and 4a(0,0,0) for Z [1, 61], as shown in Fig. 1.4(b). The two structures $L2_1$ and $C1_b$ are closely related with vacant cite 4d, $C1_b$ structure can be obtained from $L2_1$ just by replacing half of the X site elements in an ordered fashion so that the structure is no longer centro-symmetric. In the chemical formula XYZ, the low valence transition metal atom Y with least electronegativity, and the most electronegative main group element Z form NaCl-type ionic

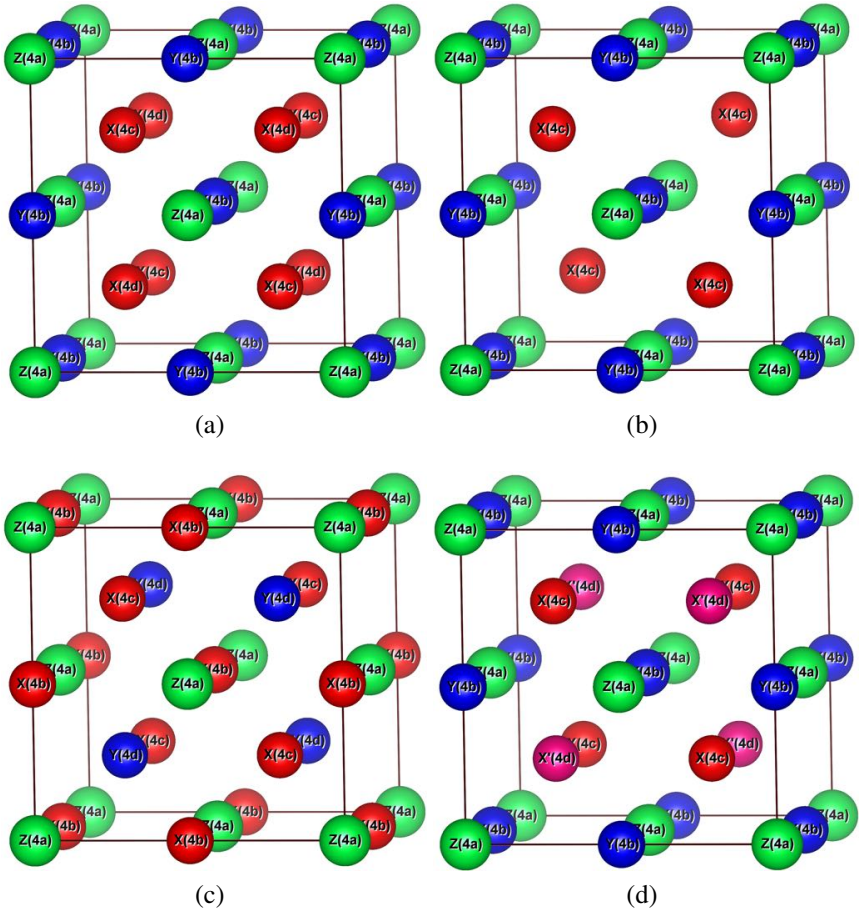

Figure 1.4: Crystalline structures of the (a) full-Heusler alloys ($L2_1$), (b) half-Heusler alloys ($C1_b$), (c) inverse-Heusler alloys (XA), and (d) quaternary-Heusler alloys (Y). The VESTA program was used to visualize the crystalline structures [274].

bonding and occupy the octahedral positions while transition metal atom X is of the intermediate electronegativity value and fill the tetrahedral positions in the crystal structure forming strong zinc blende-type covalent bonding with Z atoms.

Inverse Heusler compounds have chemical formula YX_2Z, where the valence of the Y element is the largest. These compounds crystallize in the so-called XA structure with space group $F\bar{4}3m$ (#216) which consists of four interpenetrating fcc sublattices similar to the case of full Heuslers, with the Wyckoff positions 4c($\frac{1}{4},\frac{1}{4},\frac{1}{4}$), and 4b($\frac{1}{2},\frac{1}{2},\frac{1}{2}$) for X, 4d($\frac{3}{4},\frac{3}{4},\frac{3}{4}$)) for Y, and 4a(0,0,0) for Z, as shown in Fig. 1.4(c).

For quaternary Heusler compounds, one of the higher valence transition metal atom X is re-

Table 1.1: Sites occupancy of atoms in various Heusler types in their ordered form.

Types	4a (0,0,0)	4b $(\frac{1}{2},\frac{1}{2},\frac{1}{2})$	4c $(\frac{1}{4},\frac{1}{4},\frac{1}{4})$	4d $(\frac{3}{4},\frac{3}{4},\frac{3}{4})$
Full Heuslers ($L2_1$)	Z	Y	X	X
Half Heuslers ($C1_b$)	Z	Y	X	-
Quaternary Heuslers (Y)	Z	Y	X	X'
Inverse Heuslers (XA)	Z	X	X	Y

placed by different higher valence transition metal atom X', with chemical formula XX'YZ. The crystal structure of these compounds is Y with space group $F\bar{4}3m$ (#216) which consists of four interpenetrating fcc sublattices (with two magnetic sublattice) with the Wyckoff positions 4c($\frac{1}{4},\frac{1}{4},\frac{1}{4}$) for X, 4d($\frac{3}{4},\frac{3}{4},\frac{3}{4}$)) for X', 4b($\frac{1}{2},\frac{1}{2},\frac{1}{2}$) for Y, and 4a(0,0,0) for Z, as shown in Fig. 1.4(d).

The sites occupancy of atoms in various Heusler types in their ordered form are summarized in Table 1.1.

1.2.2 Atomic order-disorder

Electronic and magnetic properties of Heusler compounds, including their half-metallicity and spin polarization, are known to be fragile against atomic disorders in their crystal structure. Any kind of disorder induce states at the edges of the minority-spin band gap leading eventually to the loss of half-metallicity for a critical value of disorder, the later being specific and depending on the kind of disorder [1, 62]. In such cases, the magnetic moments may still follow a Slater-Pauling rule (described in the forthcoming section). Thus, understanding the possible types of atomic disorders, their experimental realizations and the effects on the properties of materials is vital to control the desired properties.

At the stoichiometric composition as well, disorder can occur in various forms due to partial interchange of atoms in different sublattices. The random partial distribution of Y and Z atoms in 4a and 4b positions leads to the CsCl-like structure also known as a B2-type disorder, as shown in Fig. 1.5(a). This kind of disorder reduces the symmetry, and the resulting space group is $Pm\bar{3}m$ (#221). The ratio of the $L2_1$/B2 strongly depends on the annealing conditions. The smaller inter-

Table 1.2: Site occupancy, general formula and crystal structure of atomically ordered/disordered full Heusler compounds. Crystal structures are reported according to notations from Crystal Structure Database (ICSD), the Strukturberichte (SB), alongside the space groups, after [1].

Site occupancy	Formula	Strukturberichte	Prototype	Space group	No.
X, X', Y, Z	XX'YZ	Y	LiMgPdSn	$F\bar{4}3m$	216
X = X', Y, Z	X_2YZ	$L2_1$	Cu_2MnAl	$Fm\bar{3}m$	225
X, X'= Y, Z	YX_2Z	XA	$CuHg_2Ti$	$F\bar{4}3m$	216
X = X'= Y, Z	X_3Z	DO_3	BiF_3	$Fm\bar{3}m$	225
X = X', Y = Z	X_2Y_2	B2	CsCl	$Pm\bar{3}m$	221
X = Y, X'= Z	X_2X_2'	B32a	NaTl	$Fd\bar{3}m$m	227
X = X' = Y = Z	X_4	A2	W	$Im\bar{3}m$	229

atomic distance in B2 disorder is known to result antiferromagnetic ordering [63]. The random partial distribution of X (or/and X') and Y atoms in 8c(4c and 4d) and 4b positions leads to BiF_3-like structure known as a DO_3-type disorder (space group $Fm\bar{3}m$, #225), as shown in Fig. 1.5(b). Further, the random partial distribution of X (or/and X') and Y atoms; and X and Z atoms leads to NaTl-like structure known as a B32a-type disorder (space group $Fd\bar{3}m$, #227), as shown in Fig. 1.5(c). While complete intermixing of X (and/or X'), Y and Z elements in the crystal structure results to W (tungsten)-type (bcc) structure, known as A2-type disorder (space group $Im\bar{3}m$, #229), as shown in Fig. 1.5(d). Table 1.2 summarizes various ordering/disordering variants of Full Heusler compounds [1].

Due to strong covalent bonding between atoms in half-Heusler compounds, the disordered structures are rarely happen. Table 1.3 summarizes various possible ordering/disordering for half-Heusler compounds [1].

Table 1.3: Site occupancy, general formula and crystal structure of atomically ordered/disordered half Heusler compounds. Crystal structures are reported according to notations from Crystal Structure Database (ICSD), the Strukturberichte (SB), alongside the space groups, after [1].

Site occupancy	Formula	Strukturberichte	Prototype	Space group	No.
X, Y, Z	XYZ	$C1_b$	LiAlSi	$F\bar{4}3m$	216
X , Y = Z	XZ_2	C1	CaF_2	$Fm\bar{3}m$	225
X, Y = Z	XY_2	B2	CsCl	$Pm\bar{3}m$	221
X = Y, Z	Y_2Z	B32a	NaTl	$Fd\bar{3}m$m	227
X = Y = Z	X_3	A2	W	$Im\bar{3}m$	229

In addition to the above atomic disorders in the general cubic structure of Heusler compounds,

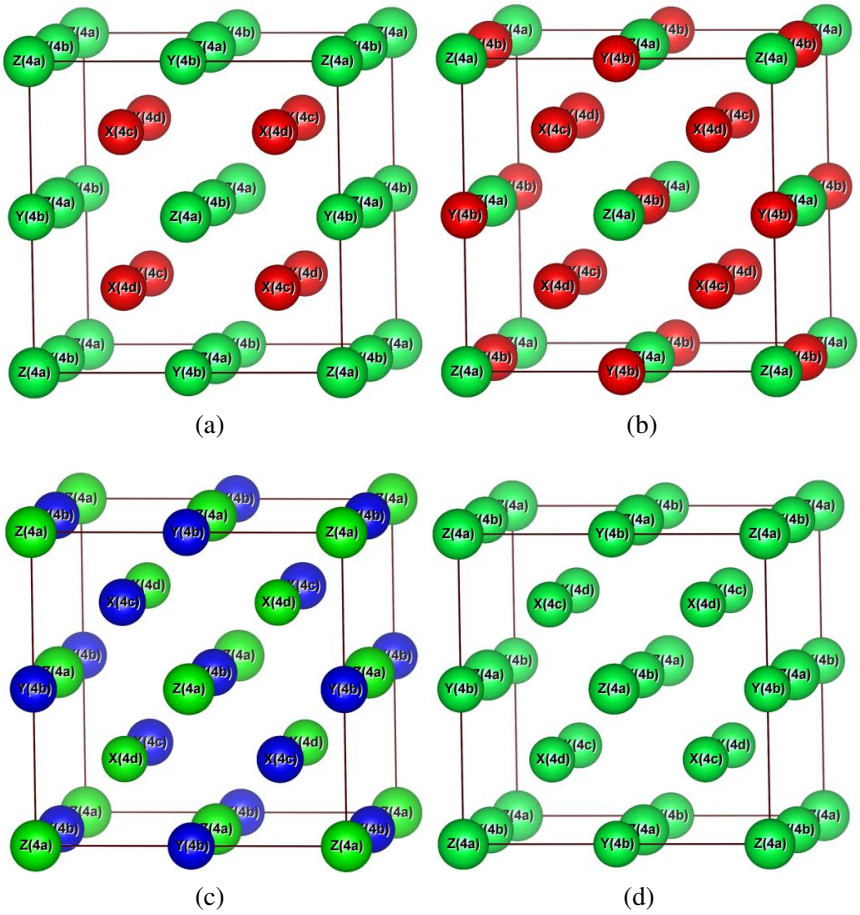

Figure 1.5: Atomically disordered structures in full Heusler alloys (a) CsCl-type disorder (B2, Y=Z), (b) BiF3-type disorder (DO_3, X=Y), (c) NaTl-type disorder (B32a, X=Y, X=Z), and (d) W-type disorder (A2=*bcc*, X=Y=Z).

there also occurs structural deformation. The deformation via compression or elongation along one of the cubic axes (say; [100]) generates a tetragonal ($D0_{22}$) lattice with space group $I4/mmm$ (139) and a similar deformation along the body diagonal [111] direction results in a hexagonal ($D0_{19}$) structure with space group $P6_3/mmc$ (194) [64, 65]), as shown in Fig. 1.6. For applications in magnetics and spintronics [66], the inherently low magnetocrystalline anisotropy in cubic Heusler compounds can be a limiting factor [67]. Identifying a tetragonal or a hexagonal Heusler analogue that exhibits a high magneto-crystalline anisotropy may be very attractive for applications such as perpendicular media, current perpendicular to plane giant magnetoresistance (CPP-GMR), and spin-torque-transfer RAM (STT-RAM) [68–71]. In tetragonal Heuslers, the preferred magnetiza-

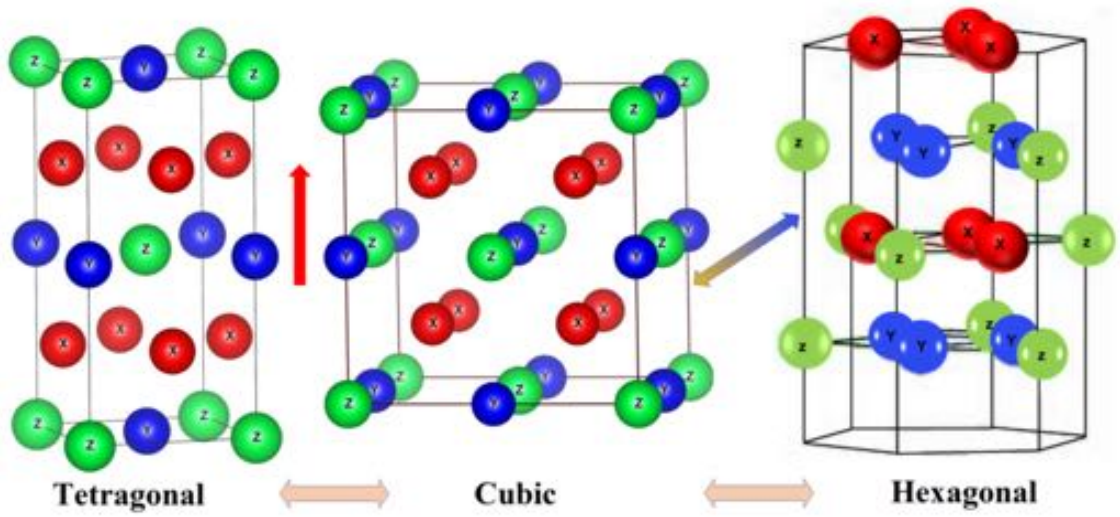

Figure 1.6: Tetragonal and Hexagonal distortion in cubic Heusler compounds. Reproduced after [6]

Table 1.4: Structure factors for completely ordered $L2_1$ structure and disordered B2-, DO_3, and A2-structures.

Crystal Structure	4a	4b	4c	4d	F_{111}	F_{200}	F_{220}
$L2_1$	Z	Y	X	X	$4\lvert f_Y - f_Z\rvert$	$4\lvert 2f_X - (f_Y + f_Z)\rvert$	$4\lvert 2f_X + (f_Y + f_Z)\rvert$
B2	B	B	X	X	0	$4\lvert 2f_X - 2f_B\rvert$	$4\lvert 2f_X + 2f_B\rvert$
DO_3	Z	D	D	D	$4\lvert f_D - f_Z\rvert$	$4\lvert f_D - f_Z\rvert$	$4\lvert 3f_D + f_Z\rvert$
B32a	Z	Y	Z	Y	$4\lvert f_Y - f_Z\rvert$	0	$8\lvert f_Y + f_Z\rvert$
A2	A	A	A	A	0	0	$4\lvert 4f_A\rvert$

tion orientation can be tuned from in-plane to out-of-plane directions and sometimes stabilize in a complex non-collinear order due to large magneto-crystalline anisotropy [6].

1.2.3 Experimental determination of atomic ordering in the crystal structures

As mentioned earlier, the study of the crystal structure and degree of chemical ordering in Heusler compounds are vital to understand and control electronic and magnetic properties, including their half-metallicity and spin polarization. The most common and accessible method to analyze the crystal structure and chemical ordering of materials is the standard X-ray powder diffraction (XRD) technique. Although, XRD suffers from some limitations for compounds with the constituent elements having very similar atomic scattering factors, an important struc-

tural information concerning atomic disorder can be obtained from the analysis of the relative intensities of the superstructure reflection peaks (111) and (200). Simple structural information of a cubic single phase can be gained by indexing all XRD peaks. For all Heusler cubic phases, only three distinct reflection peaks (h, k, l all odd or even) are observed; fundamental peaks with $h+k+l=4n$, even superlattice peaks with $h+k+l=4n+2$ and odd superlattice peaks with $h+k+l=2n+1$. Heusler alloys in the ordered $L2_1$ structure are characterized by the presence of superlattice diffraction peaks; the presence of (111) peak indicates the chemical ordering of atoms in octahedral positions, and (200) peak indicates the order for atoms in tetrahedral positions, while (220) peak is a principal reflection which is independent of the state of the order [72]. The intensities of superstructure peaks are sensitive to different kinds of atomic disorders, *e.g.*, (i) A2-type disordered structure with vanishing superstructure peaks when all the atoms are randomly distributed over lattice sites 4a, 4b, 4c, and 4d, (ii) disordered $L2_1$ structure (like B2-type in FHA) with only the (200) superstructure peak and vanishing (111) peak when there is a disorder between atoms in 4a and 4b sites, and (iii) B32a type when disorder is between atoms in 4a and 4c sites, and 4b, and 4d sites [1, 73]. This disordered structure DO_3 results (111) superstructure peak with much higher intensity than the (200) peak. Table 1.4 lists the structure factors for ordered and disordered full Heusler compounds with corresponding XRD patterns of Co_2FeSi using a Co K_α radiation source, simulated by CaRine software shown in Fig. 1.7. The simulated powder diffraction pattern of Co_2FeSi (fig. 1.7) shows the (111) and (200) superstructure peaks for the defect free structure.

Besides XRD, other important and more efficient techniques in determining the crystal structure and the degree of chemical disordering in Heusler compounds are: Extended X-ray absorption fine structure (EXAFS) [74], spin echo nuclear magnetic resonance [75], Mössbauer spectroscopy [76], and anomalous X-ray studies with synchrotron source [77]. During our investigations of Heusler compounds in this dissertation, structural characterization has been performed with XRD as the standard method. The CaRIne crystallography 4.0 software [78], Vesta, as well as in-house PYTHON code [79] including the dispersive corrections to the atomic scattering factors, Crystal impact Match! software were used to simulate the expected XRD pattern for different Heusler

compounds. In order to confirm the predicted crystal structure of the materials, Rietveld refinement was done using a MATCH! software based on the FullProf algorithm [80] which is described in the forthcoming experimental section in detail.

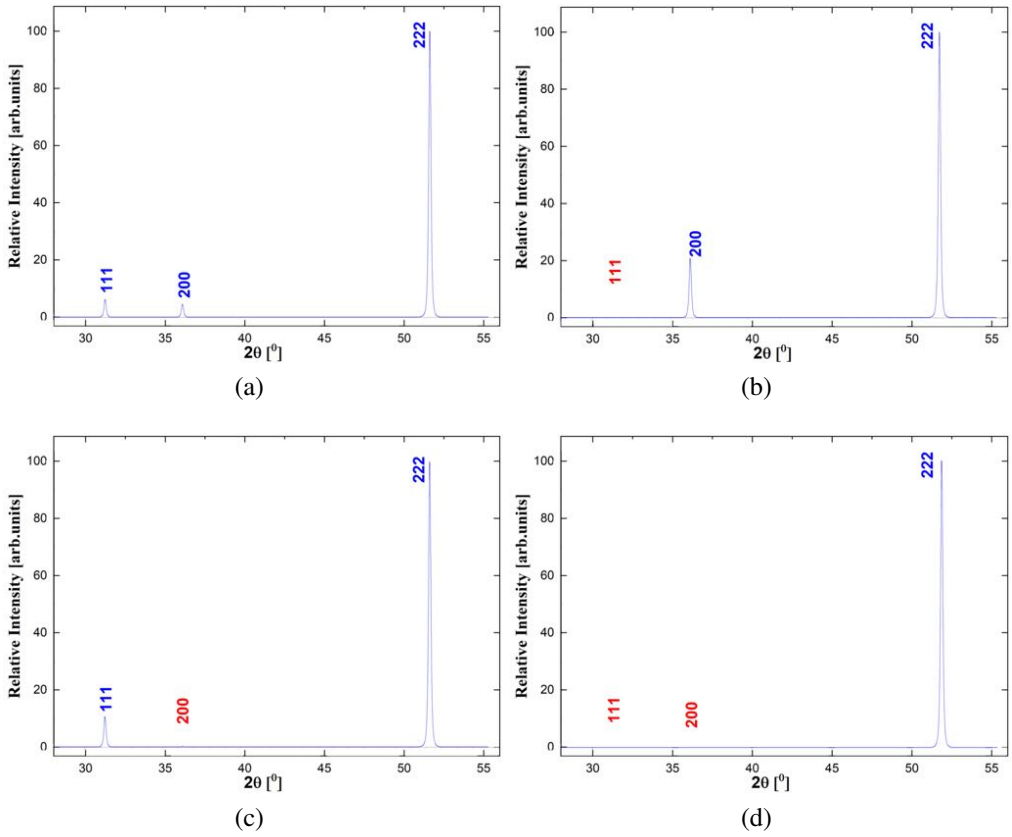

Figure 1.7: X-ray diffraction pattern of ordered and disordered full-Heusler Co_2FeSi using a Co K_α radiation source, (a) $L2_1$, (b) B2, (c) B32a, and (d) A2.

1.2.4 Magnetic properties and Slater-Pauling behaviour in Heusler compounds

The saturation magnetization values of the 3d transition metals and their alloys are observed to depend on total number of valence electron concentration (N_V), calculated by Slater and Pauling using both collective-electron and rigid-band models [81, 82] as shown in Fig. 1.8(a). The graph shown in Fig. 1.8(a) known as Slater-Pauling curve shows two distinct locus of lines for the saturation magnetization value of 3d metals and their alloys. The first line is a linear increase of saturation magnetization from Cr to Fe for $N_V \leq 8$ and bcc structure with localized magnetism

and another is a linear decrease, dropping to zero magnetization between Ni and Cu for $N_V \geq 8$ and *fcc* or *hcp* structures with itinerant magnetism. Heusler compounds exhibit various magnetic phases (ferromagnetic, antiferromagnetic, fully compensated ferrimagnetism) that the constituent atoms cannot. In 1984, Kübler introduced the concept to predict the net magnetic moment of Heusler compounds by counting the total number of valence electrons in the compound, also know as Generalized Slater-Pauling rule [83].

The total number of valenece electrons (N_V) and magnetic moment (m; in unit of Bohr magneton, μ_B) for an atom with number of majority spin-up ($n\uparrow$) and minority spin-down ($n\downarrow$) electrons are given by;

$$N_V = n\uparrow + n\downarrow \tag{1.2}$$

$$m = n\uparrow - n\downarrow = N_V - 2n\downarrow \tag{1.3}$$

The minority spin channel of half-metallic alloys including Heusler compounds has exactly $n\downarrow$ = 3 electrons per atom. So, the magnetic moment per atom is given by;

$$m = N_V - 6 \tag{1.4}$$

The magnetic moment per atom of Heusler compounds with *bcc*-driven crystal structures ($L2_1$ and $C1_b$) should increase with increasing number of valence electrons as shown on the left half of the Slater-Pauling curve (Fig. 1.8(a)). In the full Heusler alloys, the minority electron population is fixed to 12 electrons per unit cell: four occupying the low lying s and p bands of the sp element and 8 in the d-bands ($2-e_g, 3-t_{2g}$, and $3-t_{1u}$), so that the screening is achieved by filling the majority band [7]. Thus, the Slater-Pauling rule for full Heusler alloys, as shown Fig. 1.8(b), is given by;

$$m = N_V - 24 \tag{1.5}$$

While there are nine minority bands below the Fermi level; four with s, p character and five with d character in half Heusler compounds. So, the Slater-Pauling rule for half Heusler alloys, as

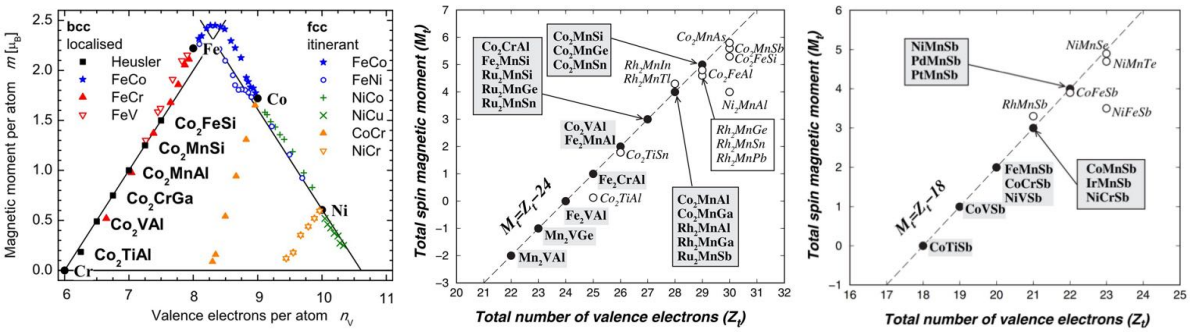

(a) (b) (c)

Figure 1.8: (a) Slater-Pauling curve for 3d transition metals, their binary and ternary alloys, including Heusler compounds, after [1], Slater-Pauling behaviour of the total magnetic moment for (b) full Heusler alloys, after [7], and (c) half Heusler alloys, after [8].

shown Fig. 1.8(c), is given by;

$$m = N_V - 18 \tag{1.6}$$

As shown in Fig. 1.9(a), Co_2-based full Heusler compounds which exhibit half metallic ferromagnetism follow the linear trend of the Slater-Pauling rule while a considerable deviation has been observed in Fe_2-and Ni_2-based Heusler compounds [1]. Co_2FeSi is reported to have the highest magnetic moment of 5.97 $\mu_B/f.u.$ at T=5 K and Curie temperature of T_c 1100 K among the known Heusler compounds [20]. Further, Co_2-based full Heusler compounds are observed to exhibit a linear dependence of the Curie temperature on the magnetic moment as shown in Fig. 1.9(b) [1].

1.2.5 Half-metallicity, spin-gapless behavior and spin-polarization

Fig. 1.10 displays a schematic illustration of the spin resolved density of states (DOS) of normal metals, ferromagnets, half-metallic ferromagnets, spin-gapless semiconductors, and compensated half-metallic ferrimagnets, respectively. As shown in Fig. 1.10(a), normal metals contain finite density of states at the Fermi level on both the spin channels and are identical and equally occupied which results zero net magnetization. Fig. 1.10(b) shows the DOS of ferromagnets, in which the majority and minority states are shifted against each other, leading to a finite net mag-

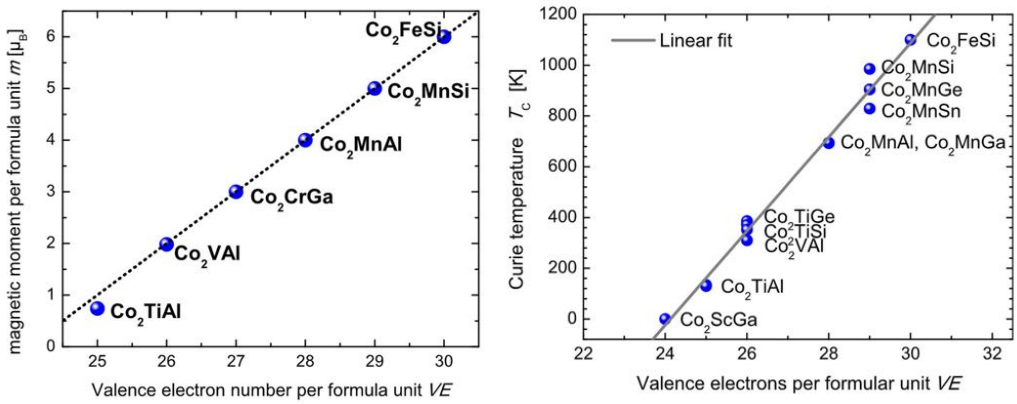

(a) (b)

Figure 1.9: (a) Magnetic moment, and (b) Curie temperature of Co_2-based full-Heusler compounds as function of total number of valence electrons in their formula unit, after [1].

netization. In such materials, there exists limited spin polarization at the Fermi level. The spin polarization P at E_F is defined as;

$$P = \frac{\rho_{\uparrow}(E_f) - \rho_{\downarrow}(E_f)}{\rho_{\uparrow}(E_f) + \rho_{\downarrow}(E_f)} \tag{1.7}$$

where $\rho_{\uparrow}(E_f)$ and $\rho_{\downarrow}(E_f)$ are the DOS of majority spin channel and minority spin channel, respectively.

Half-metallic ferromagnets (HMFs) behave like a metal for one spin channel (*e.g.* majority/up) and like an insulator or semiconductor for another spin channel (*e.g.* minority/down), as shown in Fig. 1.10(c). So, half metallic ferromagnets can exhibit, ideally, a 100% spin polarization at the Fermi level, and hence generate a fully spin-polarized current which makes them ideal spin injectors into a semiconductor, maximizing the efficiency of spintronic devices. Heusler compounds, especially Co_2-based full Heusler compounds with stoichiometric composition Co_2YZ, (Co,Y) being two transition metals, and Z being main group element, crystallizing in the $L2_1$ structure (space group $Fm\bar{3}m$, # 225 [64, 65]) belong to the most promising candidates of this family scientifically and technologically [1, 30, 66, 84–91]. These materials exhibit high Curie temperature (T_c), varying magnetic moments ranging from 0.3 μ_B to 1.0 μ_B at the Co site (depending on the constituents Y and Z), compatible lattice mismatch with conventional semiconductors, and 100% spin polariza-

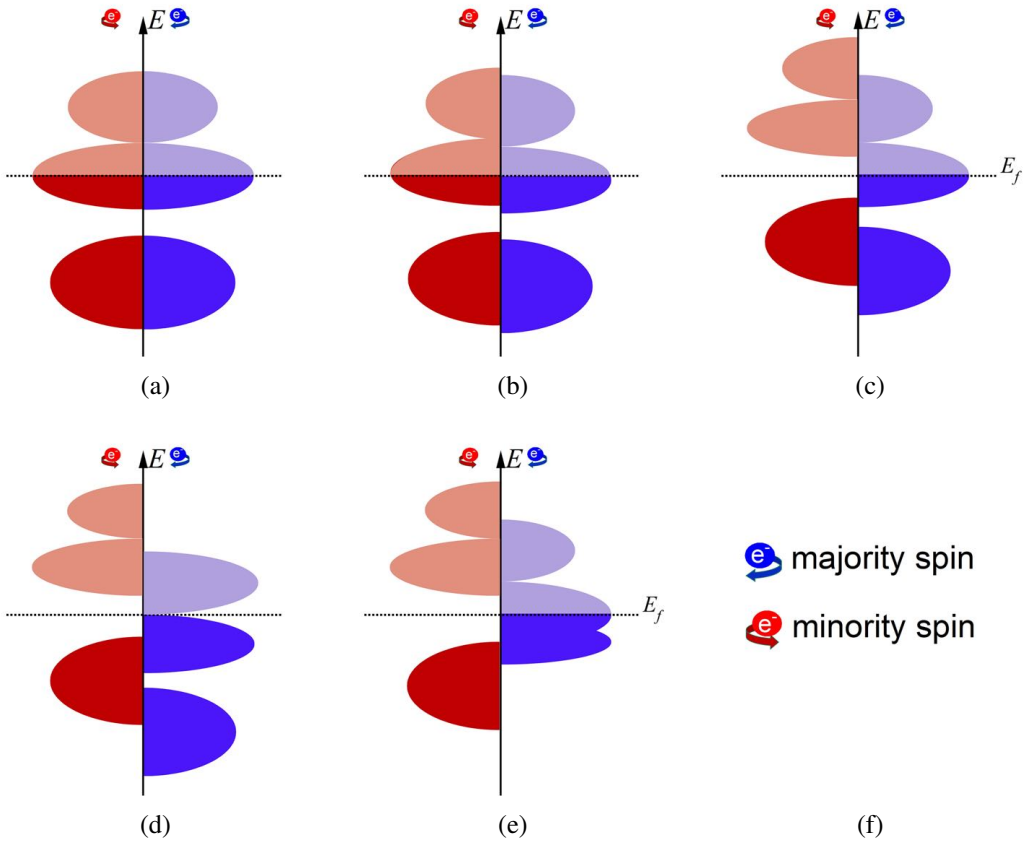

Figure 1.10: Schematic diagrams of the spin resolved density states (DOS) of (a) nonmagnetic metals, (b) ferromagnets, (c) half-metallic ferromagnets, (d) spin-gapless semiconductors, (e) compensated half-metallic ferrimagnets, and (f) labelling of electron spins.

tion at room temperature, arising from the exceptional electronic structure with a energy band gap at E_F for minority spin sub-band [20, 29–34]. However, the complete spin polarization of charge carriers in a HMF is expected for vanishing spin–orbit interactions. Since most of the Heusler compounds containing only 3d elements do not show any spin–orbit coupling, they are ideal candidates to exhibit robust half-metallic ferromagnetism [1].

Some of the Heusler compounds characterized by a unique spin-polarized band structure known as Spin-gapless semiconductors (SGSs), shown in Fig. 1.10(d). Unlike conventional semiconductors or half-metallic ferromagnets, SGSs carry a finite band gap for one spin channel and a close (zero) gap for the other [1]. These are the latest classes of materials considered for spintronics device applications because of their high Curie temperature, almost no threshold energy required to

excite electrons from the valence to conduction band, and the availability of both charge carriers, *i.e.,* electrons as well as holes, where excited electrons have spin polarisation of 100% [92–96].

Another important class of Heusler materials for spintronic applications are half-metallic ferrimagnets as shown in Fig. 1.10(e). These materials offer distinct advantages over their ferromagnetic counterparts because of their small magnetic moment resulting from the compensation of the moments carried by the different sublattices. The total magnetic moment of an ideal compensated half-metallic ferrimagnet is zero. Because of zero or small magnetic moment, they do not give rise to strong stray fields and are less affected by external magnetic fields which makes them ideal to consider as a perfectly stable spin-polarized electrode in MTJs [1].

Best way to predict above mentioned properties in Heusler compounds is by first-principles studies based on the density functional theory (DFT) calculations, which will be explained in the forth-coming section. Experimental realization of half-metallicity is possible through techniques, such as point contact Andreev reflection (PCAR) [97], positron-annihilation studies [45], Infrared absorption [46], spin polarized tunneling [98].

1.2.6 Electron transport properties

Electrical resistivity, commonly measured as a function of temperature $\rho(T)$ is one of the useful physical properties of metals that provide information about the electronic structure of materials. In concentrated metallic alloys, it is difficult to study the physical origin of electrical resistivity as it involves contributions from various scattering mechanisms. According to Matthiessen's rule [99], the total contribution from different and independent scattering mechanisms to the electrical resistivity is additive, however this rule fails if there exists any correlation between the scattering mechanisms. In order to understand the temperature dependence of electrical resistivity in metals and alloys, various theoretical models have been proposed. The total resistivity of magnetic alloys is reported to follow the following Matthiessen's rule [99];

$$\rho(T) = \rho_0 + \rho_{e-ph}(T) + \rho_{e-m}(T) \tag{1.8}$$

where ρ_0 is the temperature independent residual resistivity due to lattice imperfections, impurities *etc.*, ρ_{e-ph} and ρ_{e-m} are temperature dependent terms due to the scattering by phonons and magnons respectively.

According to Bloch model, the periodicity in solids allows treating the electron wave functions as Bloch waves. So, as the temperature of the material raises, the thermal vibrations of atoms/ions about their equilibrium position increases which enhance the probability of conduction electron scattering by phonons. At high temperatures ($T >> \theta_D$), the electron-phonon (ρ_{e-ph}) interaction is the dominant mechanism contributing linear temperature dependence to the total electrical resistivity. For other temperatures ($T \leq \theta_D$), ρ_{e-ph} is given by Bloch-Grüneisen formula;

$$\rho_{e-ph}(T) = A\left(\frac{T}{\theta_D}\right)^n \left[\int_0^{\frac{T}{\theta_D}} \frac{x^n}{(e^x-1)(1-e^x)} dx\right] \tag{1.9}$$

Where A is a constant for different metals (depends on the velocity of electrons at Fermi surface and density of states), θ_D is Debye temperature, the integral within brackets is the Bloch-Grüneisen function and n is an index that depends on nature of the scattering mechanism.

$n = 5 \rightarrow$ electron-phonon scattering in case of non-magnetic metals,

$n = 3 \rightarrow s-d$ electrons scattering by phonons (transition metals),

$n = 2 \rightarrow$ electron-electron interaction.

In the case of magnetic materials, electron-magnon interaction to the total electrical resistivity in addition to the usual electron-phonon interaction needs to be considered. In strong ferromagnets, the resistivity is reported to arise from intraband ($s-s$; $d-d$) and interband ($s-d$) spin-flip transitions caused by electron-magnon scattering [100] which exits at low temperatures and has T^2 dependence.

However, temperature dependence of the resistivity considering the conventional electron-magnon scattering of ferromagnets has been reported to be not sufficient in half-metallic systems. In half-metallic ferromagnets, due to the presence of a gap at the Fermi level in one of the spin

channels (say, the minority spin channel), a minimum excitation energy $k_B\Delta$ of majority charge carriers is required to occupy empty minority states involving a spin flip. As a consequence, the usual quadratic magnonic term (ρ_{e-m}) is expected to be exponentially suppressed at low temperatures [101, 102]. Thus, the usual electron-magnon scattering term can be modified by adding a Boltzmann factor as [102–105],

$$\rho_{e-m}(T) = \beta T^2 e^{-\Delta/T} \tag{1.10}$$

where Δ is a measure of the energy gap between the Fermi level and the band edge of the unoccupied band. The exponential suppression of one magnon scattering implies the possibility of HMF behavior.

The possibility of half-metallic ferromagnetism in Heusler alloys has also been studied by looking for the signature of two-magnon scattering in the low temperature resistivity, which should present a power law dependence as [106–109];

$$\rho_{e-m}(T) = \beta T^m \tag{1.11}$$

where m is an exponent factor. In conventional ferromagnets, since one-magnon scattering (or electron-electron scattering) dominates the resistivity at low temperature, m becomes 2 theoretically [108]. For half-metallic ferromagnets, due to the 100% spin polarisation, the one-magnon scattering is suppressed by the factor of $e^{-\Delta/T}$ (Δ is energy gap for the minority spins at E_F), so typically m lies between $3.5 \leq m \leq 4.5$ at low temperature [107–109]. At a finite temperature, spin fluctuation activates the minority band and unconventional one-magnon scattering starts to happen [106].

Due to the unique electronic structure in spin gapless Heusler compounds, the free carriers are not only fully spin polarized but are also easily excited. Further, free carriers have high mobility compared to conventional semiconductors. Relatively lower electrical conductivity compared to that of HMFs in spin gapless Heusler compounds makes them suitable to inject spin current in semiconductors (because of better conductivity match). In general, the main experimental signa-

tures of a spin-gapless semiconductors (SGS) include [110];

- nearly temperature-independent low conductivity (but resistivity decreases linearly with temperature),
- relatively low and almost temperature independent charge carrier concentration,
- a vanishingly small Seebeck coefficient,
- quantum linear magneto-resistance (MR) at low temperatures, and
- low anomalous Hall conductivity.

1.3 MOTIVATION, OBJECTIVES AND SCOPE OF THE PRESENT WORK

Ternary Co_2-based Heusler compounds with stoichiometric composition Co_2YZ, (Co,Y) being two transition metals, and Z being main group element, crystallizing in the $L2_1$ structure (space group $Fm\bar{3}m$, # 225 [64, 65]) belong to the most promising candidates of Heusler family scientifically and technologically for their potential use in spin-electronic device applications [1, 20, 30, 66, 85, 89, 111]. These materials are predicted to exhibit highly stable half-metallic ferromagnetism (100% spin polarization at the Fermi level E_F) arising from the exceptional electronic structure with an energy band gap at the Fermi level (E_F) for minority spin sub-band over wide range of temperature due to their high Curie temperature (T_c), highest among the known half-metallic ferromagnets, varying magnetic moments ranging from 0.3 μ_B to 1.0 μ_B at the Co site (depending on the constituents Y and Z), and compatible lattice mismatch with conventional semiconductors [20, 29, 30, 32, 34]. However, the experimentally observed highest spin polarizations of most of the Co_2-based ternary Heusler alloys amount to 60-70% at low temperatures, with much smaller value at room temperature [112–114]. Thus, the search of Heusler alloys with robust half-metallicity is still the focus of interest. The discrepancy in spin polarization between theory and experiment is expected to be due to the structural and chemical disorder in the crystal lattices [1, 41]. In the past, improvements in various properties such as structure, magnetization, transport,

critical temperature T_c, magnetoresistance as well as high spin polarization are realised in slightly disordered Heusler alloys by the substitution of a quaternary element, as quaternary element additions are observed to reduce the structural disorder and change the degree of hybridization between the 3*d* orbitals of different elements with consequent changes in the position of the Fermi level with respect to the spin sub-band [115–120]. In particular, low valence transition metal atom substitution in ternary Heusler alloys has been observed theoretically to tailor the Fermi level to fall exactly in the middle of the energy gap, giving rise to 100% spin polarization and half-metallic character [107, 121, 122]. So, doping is considered as one of the promising ways to stabilize Co_2-based new robust half-metals [122].

In ternary Heusler alloys X_2YZ where X is higher valence transition metal atom, Y is lower valence transition metal atom, and Z is main group element (see Fig. 1.3), the band gap at the Fermi level can be tuned by substituting a fourth element in various ways [41, 62, 123–127];

- substitution at Z site, *i.e.,* $X_2YZ_{1-x}Z^*_x$, where Z, and Z^* both are main group elements,
- substitution at Y site, *i.e.,* $X_2Y_{1-x}Y^*_xZ$, where Y, and Y^* both are low valence transition metal atoms,
- substitution at X site, *i.e.,* $X_{2-x}X^*_xYZ$, where X, and X^* both are higher valence transition metal atoms, and
- substitution at X site, *i.e.,* $X_{2-x}Y^*_xYZ$, where X is higher valence and Y^* is least valence transition metal atoms

The substitution at X/Y site is reported to be more convincing as X/Y site element plays main role in tailoring the half-metallicity and magnetic properties compared to Z site [128]. Substitution on the X site is rather less explored. First three types of substitutions are direct substitution of atoms in the crystal lattice but the forth type of substitution that we introduced for the first time is bit tricky and indirect substitution of atoms in the crystal lattice, as substituted Y^* atom being the least electronegative among others prefers to make an ionic-type sublattice with most electronegative main

group element Z. In this course, substituted Y^* atoms are assumed to replace Y atoms partially towards vacated X site, as X and Y both have intermediate electronegativity. This phenomenon is discussed in more detail in the result section later.

Among the various Heuslers, ternary Co_2FeZ (Z = Ge, Si, Ga, Al) are always the promising candidates to be used in spintronic devices. The Co_2FeGe (CFG) system is of interest in spintronic applications because of its high Curie temperature of 981 K [17]. CFG is predicted theoretically to be stable crystallizing in the $L2_1$ structure, with Fermi level falling on the conduction band edge of the minority spin channel, but it is observed experimentally to be unstable in bulk form [17, 129]. In the past, quaternary element substitution has been adopted to stabilize and study the electronic and magnetic properties of the disorderd CFG system. Most of the previous studies on CFG system are based on the quaternary element substitution on Y or Z sites only [105, 130, 131]. If one of the Co atom in CFG is substituted by another low valence transition metal atom Y = Fe, Mn, Cr, V, Ti, or Sc, alloys with rich and useful properties can be tailored. The quaternary Heusler alloy CoFeCrGe is observed theoretically and experimentally to be half metallic with Fermi level falling on the edge of the minority valence band, leading to an unstable half-metallicity [18, 132–134]. Similarly, high spin polarization of 70% is reported in half-metallic CoFeMnGe [135, 136].

The Co_2FeSi (CFS) is another most studied Heusler system because of its large magnetic moment of 6 μ_B and highest Curie temperature of 1100 K among known Heusler systems so far [20]. However, both half-metallic [137] and non-half-metallic [7] properties have been reported theoretically in CFS. But again, the Fermi level falls on the edge of the minority conduction band, leading to an unstable half-metallicity. If one of the Co atom in CFS is substituted by Fe, *i.e.,* inverse Heusler alloy Fe_2CoSi has been reported to be zero-gap half-metal with very low Gilbert damping parameter [138, 139]. The quaternary Heulser alloy CoFeMnSi has been observed theoretically and experimentally to be spin-gapless semiconductor [93, 140, 141], CoFeCrSi has been reported to be half-metallic with some structural disorder [133], while CoFeVSi and CoFeTiSi are reported theoretically to be nearly half-metallic and half-metallic respectively, but both have been observed experimentally to show multi-phase behavior in bulk form [142, 143]. In all these quaternary

Heusler alloys, the Fermi level again lies on the edge of the minority valence band.

Further, Co_2FeGa (CFGa) is reported to be stable with excellent transport properties [144]. The quaternary Heulser alloy CoFeMnGa has been observed theoretically and experimentally to be nearly half-metallic [136] with possibility to tune spin gapless semiconducting behavior with chemical substitution. CoFeCrGa has been reported to be spin gapless semiconductor [92], while CoFeVGa and CoFeTiGa are reported theoretically to be nearly half-metallic and semiconductor respectively [142].

Again, Co_2FeAl (CFA) is one of the most studied full-Heusler compounds because of it's reported giant tunneling magnetoresistance (GTMR) of up to 330% at room temperature in magnetic tunnel junctions [145, 146] and low Gilbert damping parameter of ~ 0.001 [147], as low damping is essential for spin switching with low currents and spin torque oscillators. The well known B2-type disorder in the crystal structure of CFA is observed to be effective in enhancing the TMR effect and Gilbert damping parameter due to the the fact that the density of states calculated from first principles decreases with increasing the degree of B2 ordering [145–147]. CoFeMnAl has been reported to be stable with half-metallic properties both experimentally and theoretically [136] while CoFeCrAl is reported to be spin-gapless semiconductor both experimentally and theoretically [148, 149]. But, both of them are again B2-disordered. Both CoFeVAl and CoFeTiAl are reported theoretically to be nearly half-metallic and semiconducting with some anti-site disorder [142, 150].

In all ternary Heusler compounds Co_2FeZ (Z = Ge, Si, Ga, Al), it is seen clearly that the Fermi level lies near the conduction band edge of minority spin channel in their reported spin-polarized DOS [7, 17, 129, 137, 144, 151]. If one of the Co atom in Co_2FeZ (Z = Ge, Si, Ga, Al) is replaced by another low valence transition metal atoms like Ti, V, Cr, Mn, and Fe, then the Fermi level in resulting quaternery Heusler compounds is reported to fall near the valence band edge in DOS with interesting half-metallic and spin-gapless behavior [18, 92, 93, 132–136, 140–143, 148–150]. So, as we go from ternary Co_2FeZ (Z = Ge, Si, Ga, Al) to quaternary CoFeYZ (Y = Ti, V, Cr, Mn, Fe; Z = Ge, Si, Ga, Al), Fermi level is observed to shift from lower edge of conduction band to upper edge

of valence band in minority spin channel which is in accordance to the calculations by Galanakis *et al.* [128]. They have suggested that an expansion of the lattice should shift the Fermi level deeper in energy and the contraction should shift it higher in energy. If the Fermi energy is near one of the band edges, the energy gap may easily be smeared out at finite temperatures or destroyed by quasiparticle excitation [107, 152]. Therefore, one can expect robust half metallicity with Fermi level exactly at the middle of the band gap for some intermediate Y content in $Co_{2-x}Y_xFeZ$ (Y = Sc, Ti, V, Cr, Mn, Fe; Z = Ge, Si, Ga, Al; $0 \leq x \leq 1$) due to the expansion of the lattice when Y atom with larger atomic radius substitutes for Co [153]. The substitution of Y atom for Co may be also seen as *d*-electron deficiency.

The half-metallic ferromagnets with a high thermal stability of energy gap in minority spin channel are desired for technical applications [107, 152]. For such robustness, compounds with high Curie temperature and Fermi level located at the middle of the energy gap are highly preferred [107, 152]. For that, our new substitutional approach is more promising where alloys with rich and useful properties can be tailored. Furtehr, in most of the experimentally reported Heusler compounds, especially in their bulk form, the metallography and hence the microstructural analysis has not been performed throughly as expected from a metallurgy or materials science standpoint. This all inspired us to synthesize the promising Heusler compounds $Co_{2-x}Y_xFeZ$ (Y = Sc, Ti, V, Cr, Mn, Fe; Z = Ge, Si, Ga, Al; $0 \leq x \leq 1$) and investigate the structural, electronic, magnetic, transport, and mechanical properties [105, 154–162].

Further, our study also extends to the search of hexagonal analogue of Heusler compounds, as such compounds are expected to exhibit high magneto-crystalline anisotropy promising for perpendicular media, current perpendicular to plane giant magnetoresistance (CPP-GMR), and spin-torque-transfer RAM (STT-RAM) [68–71]. For that, we have synthesized the Fe-based Heusler compounds $Fe_{3-x}Y_xGe$ (Y = V, Cr; $0 \leq x \leq 1$) and investigated the structural, electronic, magnetic, transport, and mechanical properties [163–166].

CHAPTER 2

EXPERIMENTAL AND CHARACTERIZATION TECHNIQUES

2.1 Sample synthesis : Arc-melting

The poly-crystalline ingots of Heusler compounds were synthesized using arc-melting technique under an Argon atmosphere using an Edmund Bühler compact arc melter MAM-1, as shown in Fig. 2.1(a). Arc-melting is a well-established technique for processing different metallic compounds and alloys because of its relatively high speed of sample preparation, high homogeneity and user facility. This technique uses a strong electric discharge between two electrodes of opposite polarity to produce an electric arc. A sharp tip tungsten rod connected to a variable high voltage DC power supply capable of producing ~ 600 amp acts as anode and a dismountable copper crucible plate connected to the ground acts as the cathode and both are water-cooled, as shown in Fig. 2.1(b). This technique can attain temperature close to 3500°C.

The initial step starts with weighting the constituent elements at a 3N minimum purity level in their relative atomic weight ratio according to the stoichiometric proportions using a precise weighting scale with credible calibration. An electronic balance, A&D Weighting^{TM} ER-182A with a precision of 0.1 milligrams is utilized for our work. An extra 5% of the initially calculated mass must be added to compensate the loss of volatile elements such as Manganese, during arc-melting. The mixture of constituent elements was then placed in a shallow hemispherical cavity of the water-cooled copper hearth. A small piece of Titanium was also placed in another cavity as an oxygen getter.

The next step starts with the evacuation of the melting chamber using a roughing pump (rotary pump) to the pressure of $\sim 10^{-2}$ mbar and purging with an ultrahigh 5N purity argon gas.

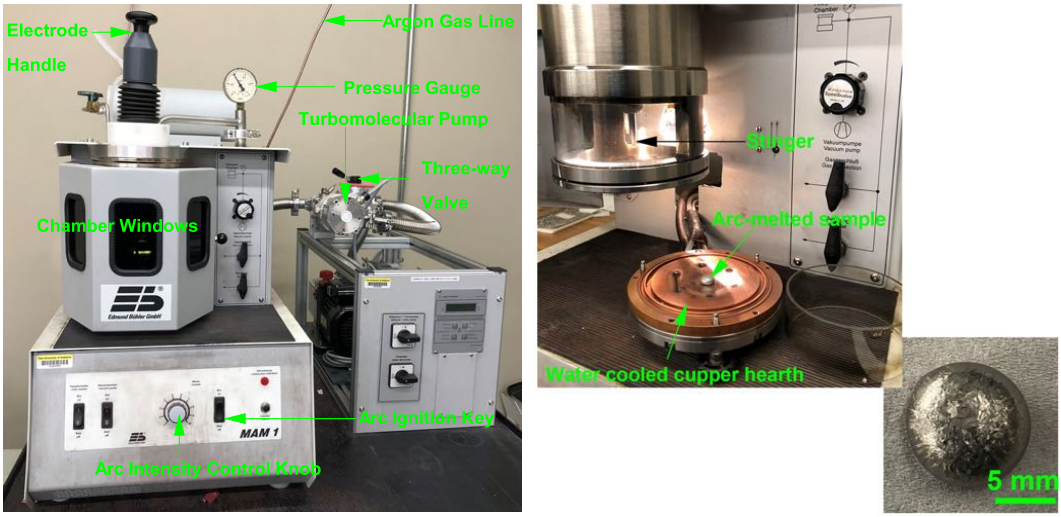

(a) (b)

Figure 2.1: (a) Outside view of arc melting unit with Edmund Bühler GmbH compact arc melter MAM-1 and its main components, and (b) inside view of the arc-melting chamber (top left) and arc-melted $Co_{1.50}Mn_{0.50}FeSi$ as-cast sample (bottom right).

Then, the chamber was evacuated to a pressure of $\sim 10^{-5}$ mbar using a turbo-molecular pump. After reaching a base pressure of less than $5x10^{-5}$ mbar, the chamber was filled with argon gas which ensures the removal of other gases present in the chamber. Then, Ti was melted prior to each arc-melting round, to get rid of the oxygen left in the chamber and to avoid the possible oxidization of the samples. The shiny silver colour of Ti, after melting indicates oxygen-free argon atmosphere whereas the light yellow/dark blue colour of Ti indicates the presence of oxygen remains inside the chamber. After ensuring that the chamber is free from oxygen, the mixture of elements to form the alloys was melted together. During the melting procedure the cupper crucible was constantly water cooled, using a recirculating chiller set at T$\sim$ 15°C. During melting, the electrode was moved over the constituent elements by gradually increasing the arc intensity for about 60 seconds as continuation of the arc might emit hazardous X-rays. After each melting cycle, the sample ingot was turned over and the same procedure was repeated at least 6 times to ensure the chemical homogeneity. A resulting perfect hemispherical shaped (button-shaped) ingot is usually an indication of well mixing while an irregularly-shaped specimen indicates the lack of miscibility. The final mixture of constituents (ignot) was again weighted in order to examine the

(a) (b)

Figure 2.2: (a) Tube, and (b) box furnaces used for thermal treatments of the Heusler samples.

mass loss during the melting procedure. The weight loss during the process was negligible. The resulting ingot was cut into pieces and examined using an energy dispersive X-ray spectroscopy (EDS) detector equipped in JEOL 7000 or Apreo Field Emission Scanning Electron Microscope (FESEM) to ensure the stoichiometry and homogeneity, which is explained in section II. Ater ensuring stoichiometry and homogeneity, as-cast samples undergo thermal treatment (annealing) to get optimum crystallization to promote the formation of the targeted Heusler phase.

2.2 Thermal treatment : Annealing

Annealing is a heat treatment process in which the metal/alloy is warmed to a temperature over its recrystallization temperature, preserved at that temperature for quite a while for homogenization of temperature followed by exceptionally moderate cooling to create an equilibrium structure in the alloys. In this process, the distorted lattice structure is reformed to one which is strain-free through the solicitation of heat. The annealing process is categorized into three phases: recovery, re-crystallization, and grain growth. Recovery is a process by which deformed grains can reduce their stored energy by the removal or rearrangement of defects in their crystal structure. Re-crystallization is a process by which deformed grains are replaced by a new set of defect-free grains that nucleate and grow until the original grains have been entirely consumed. Re-crystallization is usually accompanied by a reduction in the strength and hardness of a material and a simultaneous

increase in ductility. Grain growth is the increase in the size of grains (crystallites) in a material at a high temperature. This occurs when recovery and re-crystallization are complete and a further reduction in the internal energy can only be achieved by reducing the total area of the grain boundary. Large grains enhance ductility.

After confirming the correct stoichiometry and homogeneity, the as-cast ignots were sealed in evacuated quartz tubes prior to heat treatments. The phase purity as well as the crystal structure can be improved by subsequent annealing of the as-cast ignots in a sealed quartz tubes. In general, high annealing temperatures are preferred since the diffusion velocity is increased and impurities vanish more easily [1]. However, some Heusler compounds undergo structural phase transitions at elevated temperatures which needs to be taken into account before starting the annealing process. Thermal treatments were done using tube and box furnaces, under atmospheric pressure, and for various annealing temperatures and dwell times, as shown in Fig. 2.2. At the end of each temperature cycle, samples were cooled slowly in the furnace to get optimum crystallization to promote the formation of targeted Heusler structure. Occasionally, some samples were quenched in ice-water mixture, to check the effect of cooling rates on the properties of the materials. To make the comparison uniform, only the samples annealed under similar heat treatments are reported for each series. The heat treatments were followed by metallography to produce a metallic shiny surface for micro-structural analysis.

2.3 Hot mounting and metallography

A hot mounting technique was used to mount the annealed samples in conductive graphite powder for metallography, using Struers LaboPress-3^{TM} hot mounting press, as shown in Fig. 2.3(a). The graphite powder avoids charge accumulation by providing conductive path during SEM/EDS analysis.

The metallography begins with grinding using silicon carbide abrasive discs (120 through 1200 grit size) followed by diamond suspension polishing to achieve a submicron surface roughness required for SEM/EDS analysis. Colloidal silica suspension of grit size $0.02\,\mu m$ was used at

(a) (b)

Figure 2.3: (a) Struers LaboPress-3^{TM} hot mounting press (reproduced after Ref. [9]), and (b) grinding/polishing machines for metallography.

last for the finest polishing. After obtaining a smooth and reflective surface, the samples were chemically etched using various etchants, including Marble, Kalling No2, Kroll, Nital, Adler, and Walner, depending on the type of their elemental constituents and reactions to these etchants. The purpose of etching is that etchant attacks different phases present in the samples at different rates, and provides high quality surface contrast for microstructure characterization. Choosing proper chemical etchant and etching times are crucial to investigate detailed microstructures. The detail on how to choose the proper chemical etchants and the ingredients of the chemical etchants can be found on ASM handbook, volume 9 [167]. Fig. 2.3(b) shows the grinding/polishing machine used.

2.4 Microscopy Techniques

XRD can not detect additional phases when the impurity phase contents are either below the detection limit of XRD (less than roughly 5% of the overall volume) or amorphous in nature [163, 168, 169]. In such case, optical microscopy and SEM of polished and etched samples are the most direct ways to characterize the microstructure because they give a morphological image which can clearly figure out secondary phases and grain boundary segregation even for minor constituents.

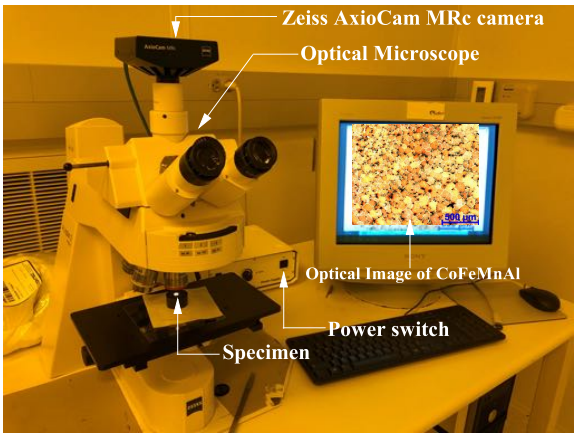

Figure 2.4: An external image of Optical microscope system used to take optical images. The image displaying in PC screen is of CoFeMnAl Heusler alloy annealed at 850°C for 7 days.

2.4.1 Optical Microscopy Technique

Optical microscopy is the first magnification technique to see morphology of alloys under study. It is a direct and simple technique that can be used to visualize amorphous and crystalline materials with homogeneous or heterogeneous micro-structure and grains as well. Fig. 2.4 shows the external image of optical microscope system utilized for optical microscopy. After adjusting optics and observing different contrast in etched specimen seen from optical microscopy, we can speculate the presence of impurity phases, or possible different crystallite orientations.

2.4.2 Electron Microscopy and Compositional Analysis Technique

Scanning electron microscopy technique is one of the important technique to get valuable information about the specimen including external morphology (texture), chemical composition, crystalline structure and orientations. This technique provides higher spatial resolution over optical microscopy ($\sim$ 1 μm spatial resolution). The imaging technique reveals a clear view of the specimen topography and quantitative chemical analysis could be done using energy dispersive spectroscopy (EDS). The back-scattered electrons technique helps us to obtain contrast image for different phases if present in the specimen.

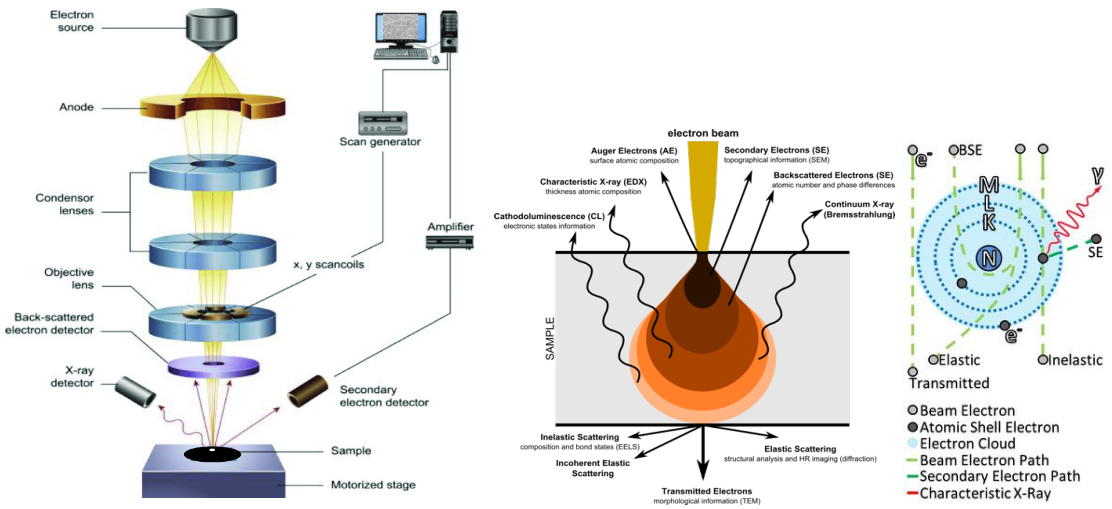

(a) (b) (c)

Figure 2.5: Scanning electron microscope (a) electron scattering mechanism from electronic shells in specimens [10], (b) schematic of scanning electron microscope [11], (c) tear-drop showing the signals emitted from different parts of the interaction volume in the specimen [12].

2.4.2.1 Scanning Electron Microscopy (SEM)

Fig. 2.5(a) shows a schematic diagram of scanning electron microscope (SEM). In SEM, electron source (tungsten filament, cathode) emits electron beam through thermionic or field emission method. The electron beam with energy ranging from 0.2 keV to 40 keV is then focused to pass through the pair of condenser and objective lens. This arrangement helps to control the spot size and the direction of the electron beam over the specimen under the study. The deflector coils (or scanning coils) in the electron columns deflect the electron beam in the x and y direction scanning in a raster fashion over the specimen surface.

When focused primary electron beam interacts with the sample, the electrons lose energy by repeated random scattering and absorption within teardrop-shaped volume, also known as interaction volume. Fig. 2.5(b) shows the interaction volume showing various scattering processes. The depth of various interactions depend on various factors, *i.e.,* the accelerating voltage of the electron source, beam spot size, the type of materials under study. Fig. 2.5(c) shows the interaction of electron beam with a sample having nucleus N, and electronic shells K,L,M etc. Inelastic scattering of primary electron beams results secondary electrons (SE), which can be used for compositional

(a) (b)

Figure 2.6: Scanning electron microscopes (a) JEOL 7000, and (b) Thermo ScientificTH Apreo.

analysis, as well as electron imaging where as elastic scattering of incident electrons by sample nuclei or electrons results back-scattered electrons (BSE) with intensity proportional to the atomic number of the elements in the sample and can be used in compositional contrast and microstructural analysis of the material. In a typical SEM, these informations can be collected by a secondary electron detector, a back-scattered electron detector, a wavelength-dispersive X-ray (WD) detector, an energy-dispersive X-ray detector (EDS), etc, as shown in Fig. 2.5(a).

Both JEOL 7000 and Apreo Field Emission Scanning Electron Microscope (FESEM) with a Schottky type Field Emission (FE) gun, equipped with a secondary electron detector (SED), a back-scattered electron detector (BED), an electron back-scatter diffraction detector (EBSD), an energy-dispersive X-ray spectroscopy detector (EDS), a wavelength-dispersive X-ray spectroscopy detector (WDS), were used for the analysis of specimens, shown in Fig. 2.6. The resolution of this SEM is $\sim$ 1nm with adjustable spot size and accelerating voltage of 0 to 30kV with magnification of 25X to 1,000,000X. Using this SEM, electron images, EDS, and EBSD analysis of our samples were possible. Prior to this analysis, as explained in the previous section, samples need to be mounted in a conducting mount hold, and their surface should be ground and polished to a very smooth surface with submicrometer roughness.

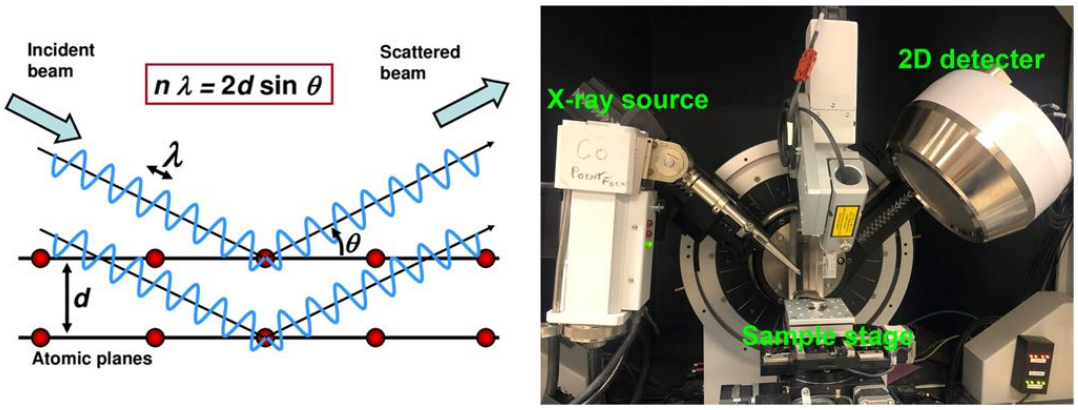

(a) (b)

Figure 2.7: (a) Schematic illustration of Bragg's law. Reprinted after Ref. [13], and (b) Bruker D8 Discover X-ray diffractometer used for our investigations.

2.4.2.2 Energy Dispersive Spectroscopy (EDS)

Observing different contrast in etched sample seen from optical microscopy, we can speculate the presence of impurity phases, and SEM with EDS can be used to directly quantify whether areas of different contrasts represent impurity phases or possible different crystallite orientations.

2.5 Crystal structural analysis Methods

Structural analysis was carried out by using X-ray diffraction (XRD) as the standard method. A brief discussion on the principle of X-ray diffraction and refinement of the crystal structure is given below.

X-ray diffraction technique is one of the most fundamental and versatile non-destructive tool for analyzing the crystal structure of crystalline materials. Fundamentals and physical principles of X-ray diffraction method and how this technique explores the quality of the crystals and relates the information of the reciprocal and real space are thoroughly explained in text books [2, 168–171]. The elastic scattering of incident X-rays from different scattering centers (nuclei) reinforce at certain phase relations which give rise to constructive interference (alternative maximum and minimum intensities). The typical phenomenon is shown in Fig. 2.7(a). The diffraction condition

is given by the Bragg's law;

$$2dSin\theta = n\lambda \tag{2.1}$$

where d is the interplanar spacing, λ is the wavelength of X-ray employed for diffraction and θ is the angle between incident X-rays and crystal planes.

Each crystalline compound possess unique X-ray diffraction pattern. So, for pure crystalline material, it acts as a 'fingerprint'. This uniquesness is due to unique interplanar spacing related to the lattice constant of material and specific planes upon which the Bragg law is allowed. So far, the Heusler alloys are known to crystallize in three crystal structures, namely, cubic (face-centered cubic), tetragonal, and hexagonal. The interplanar spacing d of the planes (hkl) for three different crystal systems is given by [2];

$$\textbf{Cubic}: \frac{1}{d^2} = \frac{h^2+k^2+l^2}{a^2} \tag{2.2}$$

$$\textbf{Tetragonal}: \frac{1}{d^2} = \frac{h^2+k^2}{a^2} + \frac{l^2}{c^2} \tag{2.3}$$

$$\textbf{Hexagonal}: \frac{1}{d^2} = \frac{3}{4}\left(\frac{h^2+hk+k^2}{a^2}\right) + \frac{l^2}{c^2} \tag{2.4}$$

Where a and c are lattice parameters.

Not all the atomic planes in the crystal diffract the incident beam, only the planes meeting the Bragg's conditions with a non-zero consequent structure factor are reflected and observed. The condition for this constructive interference can be calculated for different Bravais lattices as;

Powder X-ray diffraction (XRD) patterns of our Heusler compounds were taken at room temperature using a Bruker D8 Discover X-ray diffractometer equipped with monochromatic Co-Kα (λ = 0.179 nm) radiation, source, a Hi-STAR two dimensional (area) detector, and an Euler cradle with capability to vibrate and rotate the samples during the measurement. This machine can be used to identify crystalline phase, crystal structur, texturing, residual stress of powder, bulk and single crystal samples. The GADDS software was used to collect the data in the 2θ range of $17^\circ < 2\theta < 130^\circ$. In most cases, the bulk ingots were crushed into pieces and ground to obtain

Table 2.1: The planar reflections in specific Bravais lattices. Reprinted with permission form Ref. [2].

Ceystal type	Bravais Lattice type	Reflections possible present	Reflections necessarily absent
Simple	Primitive	Any h, k, l	None
Body-centered	Body-centered	h + k + l even	h + k + l odd
Face-centered	Face-centered	h, k, and l unmixed	h, k, and l mixed
Diamond cubic	Face-centered cubic	As fcc, but if all even and h + k + l $\neq$ 4N; then absent	h, k, and l mixed and if all even and h + k + l $\neq$ 4N
Base-centered	Base-centered	h and k both even or or both odd h + 2k = 3N with l even	h and k mixed
Hexagonal close-packed	Hexagonal	h + 2k = 3N $\pm$ 1 with l odd h + 2k = 3N $\pm$ 1 with l even	h + 2k = 3N with l odd

powders of micron size using hammer. During this process care was taken to avoid possible oxidation and contamination of powder samples. To reduce the surface effects, the polished/powder samples were rotated around the ϕ axis during the XRD measurement. The Bruker D8 Discover X-ray diffractometer used for our investigation is shown in Fig. 2.7(b). The anode current and the excitation voltage were 30 mA and 40 kV respectively for exciting the Co-Kα radiation. Diffractometer is equipped with filters to prevent the detection of parasite wavelengths. These filters act as absorbers with absorption edge close to the spurious wavelengths. The integrated intensity of X-ray diffraction by a diffractometer can be obtained as [171]:

$$I = |F|^2 p \left(\frac{1 + Cos^2 2\theta}{2 Sin^2 \theta Cos\theta} \right) \left(\frac{1}{2\mu} \right) exp^{2B\left(\frac{Sin\theta}{\lambda}\right)^2} \quad (2.5)$$

Where F is the structure factor which depends on the type of crystal structure and atomic ordering, p is multiplicity factor, which represents the number of crystal planes with similar structure factors and spacing, but different orientations. θ is Bragg's angle. The first parentheses in equation 2.5 is known as the Lorentz-polarization (LP) factor, representing the polarization of the X-ray due to the gradient of the electric fields, which results in a difference between the polarizations of X-rays in the plane perpendicular to the propagation direction. The term $\frac{1}{2\mu}$ is the absorption factor,

representing the X-ray absorption by the sample and is constant for thick samples. The last term in equation 2.5 is the temperature factor or Debye-Waller factor, representing the decrease in the X-ray peaks intensity due to the atomic displacement from thermal vibrations of atoms in the crystal, above zero Kelvin. The factor B is the isotropic temperature factor which is proportional to the mean squared displacement of the atoms.

The structure factor for the reflection from (hkl) plane in a unit cell consisting of N atoms at positions (u_n, v_n, w_n) and atomic scattering factors f_n is given by [171];

$$F_{hkl} = \sum_{n=1}^{N} f_n exp^{2\pi i(hu_n+kv_n+lw_n)} \tag{2.6}$$

Considering the fact that Heusler-like compounds can crystallize in a number of structures, particularly the ordered $L2_1$ ($Fm\bar{3}m$, space group no. 225) or Y ($F\bar{4}3m$, space group no. 216) or X$-a$ ($F\bar{4}3m$, space group no. 216 [64, 65]) and possible disordered phases $D0_3$ ($Fm\bar{3}m$, space group no. 225 [64, 65]), $D0_{19}$ ($P6_3$/mmc, space group no. 194 [64, 65]) [172–174], and $D0_{22}$ (I4/mmm, space group no. 139 [64, 65]), structure assignment should be undertaken carefully. The structural deformation through compression or elongation along one of the cubic (100) axes forms a tetragonal lattice while a similar deformation along the (111) direction results in a hexagonal structure [6]. In order to avoid a selection bias, we first determined the crystal class from the XRD data alone, following the procedure in Ref. [171]. From the observed XRD peaks, the values of $\sin^2\theta$ were tabulated. If the structure is in the cubic system, then these values, when properly normalized, will yield a set of integers. Omissions in the list of integers distinguish the type of cubic lattice (*sc, bcc, fcc*). If there is no overall normalization of the values that results in only integral values, the system is not cubic. A similar but slightly more involved procedure [171] can be used to test the XRD data against tetragonal and hexagonal systems. After confirming the crystal system and indexing all XRD peaks, lattice parameters were extracted for all alloys in the series using Cohen's method with a Nelson-Riley extrapolation function [171]. The X-ray patterns were further analyzed by the Rietveld refinement technique.

2.5.1 XRD pattern simulation and structure refinement using the Rietveld method

CaRIne crystallography 4.0 software [78], Vesta, the Crystal impact Match! software [80] as well as in-house PYTHON code [79] including the dispersive corrections to the atomic scattering factors were used to simulate the XRD patterns to compare with the experimental XRD patterns.

Rietveld refinement was done using a MATCH! software based on the FullProf algorithm [80]. Rietveld method is a least-squares approach to fit the experimental XRD intensity profile to the simulated XRD pattern of the possible phases of the materials. In Rietveld refinement, many parameters of crystal structure (s), diffraction optics effects, instrumental factors and other specimen characteristics (*e.g.*, preferred orientation, texture, lattice constants, etc.) are refined iteratively. For the best fit, the difference between the observed and calculated diffraction pattern is minimized in the iteration. The quantity minimized is the residual S_y given by [175];

$$S_y = \sum_{n=i}^{N} \frac{(y_{io} - y_{ic})^2}{y_{io}} \tag{2.7}$$

where, y_{io} and y_{ic} are the observed and calculated intensities of the i^{th} data point respectively.

The intensity of powder X-ray diffraction pattern of a polycrystalline material I_K (where K stands for the Miller indices, h,k,l) is proportional to the square of the absolute value of the structure factor $|F_K|^2$. The calculated intensities y_{ic}, observed at any arbitrarily chosen point are determined from the $|F_K|^2$ values calculated by summing the contributions from neighbouring regions of a particular Bragg's reflection and the background as well is [175];

$$y_{ic} = s\sum_{K} L_K |F_K|^2 \phi(2\theta_i - 2\theta_k) P_K A - y_{ib} \tag{2.8}$$

where s is scale factor, K represents the Miller indices, h,k,l for a Bragg's reflection, L_K is the Lorentzian function, ϕ is the reflection profile function, P_K is the preferred orientation function which is equal to 1 for polycrystalline materials. A is an absorption factor that depends on instrument geometry and is a constant for most instrument geometries used in X-ray diffractometers,

and y_{ib} is the background intensity at the i^{th} step.

For Rietveld refinement, a good starting model is expected because the method is not a structure solution method, it is a structural refinement method. So, the best suitable initial-guesses on various parameters of the unit cell (space group, lattice parameters, fractional coordinates of the atoms/ions present in the unit cell, site occupancy, thermal parameters of atoms/ions, etc.), proper background and profile functions is the key factor. A model which gives the lowest residue among the others upon the completion of the refinements is considered as the best fit. Various figures of merit used to characterize both full pattern decomposition, and Rietveld refinement quality are given below [175];

$$\text{Profile value} : R_p = \frac{\sum |y_{io} - y_{ic}|}{\sum y_{io}} \tag{2.9}$$

$$\text{Weighted value} : R_{wp} = \left[\frac{\sum (y_{io} - y_{ic})}{\sum w_i y_{io}^2}\right]^{1/2} \tag{2.10}$$

$$\text{Bragg's R-factor} : R_B = \frac{\sum |I_{ko} - I_{kc}|}{\sum I_{ko}} \tag{2.11}$$

$$\text{Expected value} : R_{exp} = \left[\frac{N-P}{\sum w_i y_{io}^2}\right]^{1/2} \tag{2.12}$$

$$\text{Goodness of fit} : \chi^2 = \left[\frac{R_{wp}}{R_{exp}}\right]^2 \tag{2.13}$$

Where N = total number of points measured in X-ray diffraction pattern, P = number of free least square parameters, w_i = weight of the i^{th} data point = $\frac{1}{y_{io}}$.

2.5.2 Electron back scattered diffraction

Further, the crystal structures determined from XRD were confirmed using electron backscatter diffraction (EBSD) phase mapping analysis in a JEOL 7000 FESEM system. EBSD is an effective tool where EBSD inverse pole figure (IPF) color map and phase map help us to determine the degree of texturing, crystallographic orientations and purity of phase considered in the microstructure. EBSD is suitable in wide dimensional range of millimeters to nanometers on the sample. The

working principle of EBSD is similar to the XRD method with the exception of diffractive source being the electron beam instead of an X-ray. A very good surface quality of the sample is needed to enhance the signal quality. Usage of final polishing agent with low mesh such as colloidal silica is highly recommended. Also it is essential to minimize the surface charging as much as possible. The sample is tilted at a high angle of 60 to 80 degrees to enhance the received signal during measurement. The patterns formed are called Kikuchi patterns which follow the Bragg's law and their intensity also depends on the structure factors of the diffracted material and is therefore unique. The scanning step size should not be more than a tenth of the average grain or feature size, so that enough data is gathered from the surface.

2.5.3 Phase transformation behaviour and thermal stability

Differential Scanning Calorimetry (DSC) is a simple but an effective tool to identify phase transformation temperatures and melting points of the materials. If the local composition of sample does not change in going from one structure to another, this serves to indicate that the transformation is a diffusionless martensitic transformation. The phase evolution can be clearly identified from the DSC curves by observing the large, sharp endothermic/exothermic peaks during heating and cooling cycles of the samples.

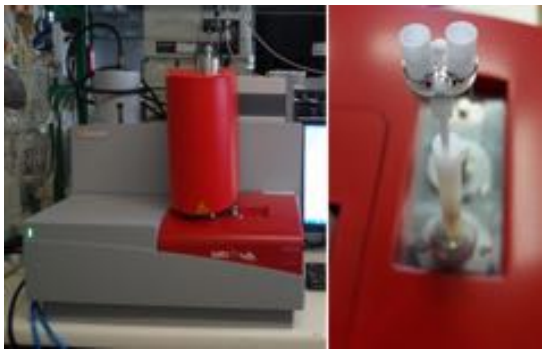

Figure 2.8: Setaram Labsys Evo. which can work in the temperature range between room temperature and 1600°C, the heating and cooling speeds are between 0.01 an 100°C/min. Weighing precision of $\pm$ 0.01%. Reprinted after Ref. [14].

For some of our sample series, DSC measurements were carried out to confirm the diffusionless

martensitic transformation (with a ramp rate 10°C/min during heating and cooling) in the temperature range up to 1200°C in a Setaram Labsys Evo. (see Fig. 2.8) in Ar gas flux at the rate of 20 mL/min to prevent the possible oxidation of the samples. The temperature and the heat reaction were calibrated using high purity indium, aluminum, silver and nickel standards.

2.6 Magnetic Characterization

Vibrating sample magnetometry techniques are widely used to measure the magnetic properties of materials due to high sensitivity and versatility. Here, low temperature magnetic measurements of our polycrystalline samples were performed using VSM option of cryogen-free Quantum design PPMS Dynacol working in the temperature range of T = 1.8 K to 400 K and with maximum possible magnetic field of 9 T. The accuracy level of measuring moments in PPMS is lower than 10^{-6} emu. The high temperature magnetic properties were studied using LakeShore VSM 7407 and 7410 both equipped with a high temperature stage. VSM measures magnetic moment as a function of applied magnetic filed, temperature, and time.

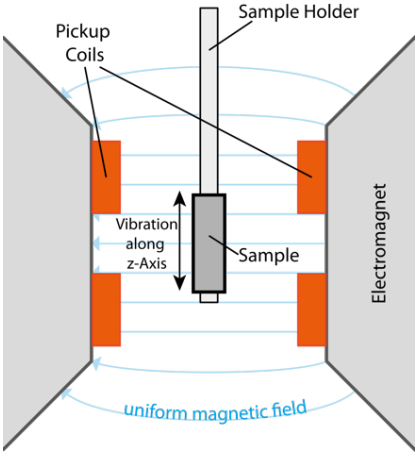

Figure 2.9: Schematic of a Quantum Design VSM system. Reprinted after Ref. [15].

2.6.1 Working principle of VSM

Basic working principle of VSM is based on the Faraday's law of electromagnetic induction, *i.e.,* a changing magnetic flux will induce a voltage in a pickup coil. The voltage induced in a pick-up coil due to change in magnetic flux (Φ) resulting from the oscillation of sample along vertical (z-) direction is given by [176];

$$V_{coil} = \frac{d\Phi}{dt} = \left(\frac{d\Phi}{dz}\right)\left(\frac{dz}{dt}\right) \tag{2.14}$$

$$V_{coil} = 2\pi CmAsin(2\pi ft) \tag{2.15}$$

Where C is a coupling constant, m is the DC magnetic moment of the sample, A is the amplitude of oscillation, and f is the frequency of oscillation.

The VSM option of PPMS contains a motor head module at the top of the sample chamber to produce vertical sinusoidal oscillations of the sample placed at the center of the pick-up coils attaching it to the end of a sample transfer rod and the pick-up coils are placed between two electromagnets at the bottom of the sample chamber, as shown in Fig. 2.9.

For magnetometry such as field dependent magnetization and temperature dependent magnetization, we place a very small sample ($\sim$ less than 5mg) at the center of the gradiometer pick-up coils by a centering technique and the sample is allowed to oscillate sinusoidally with typical frequency $\sim 40\,\mathrm{Hz}$ and amplitude $\sim 2\,\mathrm{mm}$. VSM pick-up coil module records the voltage induced in the coil and the VSM motor module at the top of chamber records the amplitude and position of the sample oscillation. Then, two readings from two different modules are averaged and sent to the CAN bus connected to the PC in order to save the magnetization data.

From the field dependent magnetization data *i.e.,* M(H) curves, we can get the information of the magnetic systems (ferromagnetic, paramagnetic, diamagnetic, etc.), saturation magnetization M_s, coercivity H_c, magnetic remanence M_r, and so on while temperature dependent magnetization data *i.e.,* M(T) curves can be used to examine the Curie temperature of ferromagnets or Neel temperature of antiferromagnets or blocking temperature of superparamagnets etc. M(T) graphs

can detect the existence of multiple phases in the alloys, and also magnetic phase transformations in the materials, and many more.

2.7 Electrical Transport Characterization

Heusler alloys are very promising for their use in potential spintronics device applications, thermopower and thermoelectric applications [1]. Important information about metallic, semiconductiong, insulating, superconductiong behavious of materials can be uncovered by the study of electrical transport measurements. The residual resistivity ρ_0 and residual resistivity ratio (RRR), $\rho(300\,\mathrm{K})/\rho(5\,\mathrm{K})$ in temperature dependence of resistivity and magnetoresistance MR(H) in field dependence of resistance can provide the important bulk properties including half-metallicity, atomic orderings, structural and magnetic transitions etc. The RRR values less than 1 is observed in Heusler alloy Co_2CrAl [177], indicating intrinsic semiconducting behavior. Vary large RRR values of 6.5 and 4.2 are reported in Co_2MnSi [108] bulk single crystal and bulk Co_2TiSn [178] respectively due to the improvement of the crystallinity of the alloy at low temperature.

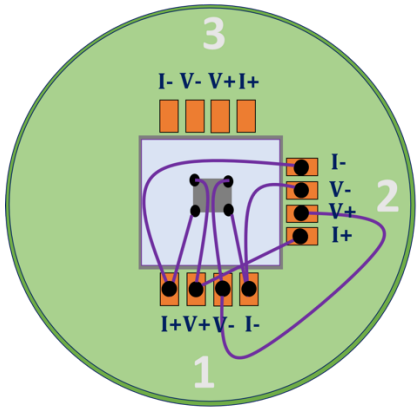

Figure 2.10: PPMS resistivity puck for resistivity measurement in Van der Pauw geometry.

The electrical transport measurements were done using the van der Pauw method [179] in a PPMS Dynacool for samples with approximate dimensions 4 x 4 x 1 mm^3. PPMS can measure the temperature dependent of dc electrical resistance in the range of $10\mu\Omega < R < 4\mathrm{M}\Omega$ with less than

1% error in the temperature ranges from 1.9 K<T<400 K. PPMS Dynacool utilizes a "pulsed tube cooling" technique without the need for liquid Helium and uses cryogenic pumps to reach pressures less than 10^{-4} torr. For magnetic filed dependence of transport measurement such as magnetotransport and Hall measurements, the built-in superconducting magnets can yield the field up to 9 Tesla, which are properly shielded to avoid any interference with nearby instruments. Schematics of the Dynacool cryostat and vacuum system and more details on their operating principles can be found in Dynacool user manual [15]. Heusler bulk samples were placed on the resistivity pucks placing a thin layer of Mica insulating sheet covered with GE varnish underneath which acts as an electrical insulation between the sample and puck, and are ultrasonically wire-bonded on the four corners of the samples to the puck using aluminum wires, shown in Fig. 2.10. The surface of the sample should be clean and free of cracks, any organic and inorganic contaminants for better contact and results. Also, the contacts on the surface of the specimens should be at four corners for more accurate resistivity measurement.

2.8 Mechanical Hardness Characterization

Figure 2.11: Outside view of Buehler model 1600-6100 micro-hardness tester.

Adaptation of materials to industrial applications requires mechanical robustness to undergo

repetitive thermal cycling and resist cracking from vibrations. Most of the previous studies on mechanical properties are theoretical in nature and only few are verified experimentally. The observed disconnect between the few available experimental results and the various theoretical results requires the necessity of more experimental studies in this area. So, the mechanical properties were studied in terms of Vickers hardness by using Buehler model 1600-6100 micro-hardness tester, shown in Fig. 2.11. Hardness values were obtained by taking the average of data taken from at least 12 different regions of each specimen with 0.2 kg load and 10 s loading time.

The whole experimental and characterization techniques are summarized in Fig. 2.12.

Figure 2.12: Flow chart showing experimental and characterization techniquesof Heusler compounds.

CHAPTER 3

THEORETICAL CALCULATIONS

In order to obtain important information about the stability, chemical ordering, ectronic and magnetic properties for potential half-metallic and spin-gapless Heusler compounds, we have performed density-functional theory (DFT) calculations employing the projector augmented wave (PAW) pseudopotentials by Blöchl [180], implemented by Kresse and Furthmüller in the Vienna *ab initio* simulation package (VASP) [181]. We have adopted the generalized-gradient approximation (GGA) in the scheme of PerdewBuekeErnzerhof (PBE) for the electronic exchange-correlation functional [182]. We have used a 16-atom supercell, *i.e.*, 4 formula units of the underlying $L2_1$ structure adopted by the perfect full-Heusler compounds like Co_2MnGe. The integration over the irreducible Brillouin-zone (IBZ) of cubic systems was done with the automatic mesh generation scheme within VASP with the mesh parameter (the number of k points per $^{-1}$ along each reciprocal lattice vector) set to 64 (sometimes 30). Total energies were converged upto 10^{-7}eV/cell with a plane-wave cutoff of 520 eV. Full relaxation of cell (initially cubic) volume, shape and atomic positions were performed until the forces on each atom become less than 10^{-2} meV/cell using the conjugate-gradient method. Our calculations did not include spin-orbit interaction as most of the Heusler compounds containing only 3d elements do not show any spin–orbit coupling, they are ideal candidates to exhibit robust half-metallic ferromagnetism [1, 183].

For theoretical calculations, cubic supercell structures consisting of 16 atoms were constructed using both Special Quasirandom Structure (SQS) and the Monte Carlo Special Quasirandom Structure (MCSQS) method [184] which is a part of the open source ATAT toolkit [185] accessible from [186]. The MCSQS method can handle double-site substitutions as described in experimental section above taking care of nearest neighbor interaction and predicts a special quasirandom structure

by generating a set of clusters with specific correlations relative to a target random structure. The best MCSQS structures were confirmed after waiting for a long enough time until a correlation difference relative to the target random structure approach to zero. The predicted MCSQS structures were then optimized using GGA method.

It is known that standard PBE tends to underestimate the band gap and does not correctly model the electronic properties of materials with strongly correlated electrons [115, 129, 133, 187, 188]. To circumvent this, often times the DFT+U approach is used, which adds an intra-atomic Hubbard like term to the energy functional [189]. The U correction treats the strong on-site Coulomb interaction of localized electrons while the rest of the electrons are treated with normal DFT approximations [189].

The Hubbard U parameter cannot be calculated simultaneously with the minimization of the total energy because total energy remains constant with respect to the U term. Both experimental and computational determination of the U values is very difficult and tedious tasks and in 2013 Sasioglu and collaobrators employed the constrained random-phase approximation (CRPA) scheme to calculate the U values for several half-metals [190]. For the calculations presented in the rest of this work, we have used the semi-empirical values mentioned in Ref. [191], where Kandpal *et al.* have employed the LDA+U scheme to study the electronic structure of several half-metallic Heusler compounds. The considered U values for the d-orbitals of Co, Fe, Mn, Cr, V, Ti, and Sc are 1.92 eV, 1.80 eV, 1.69 eV, 1.59 eV, 1.34 eV, 1.36 eV, and 1.30 eV respectively. Finally, it should be noted that the inclusion of U artificially opens a band-gap in the minority spin channel and only comparison to experimental data guarantees that the used U parameters in the calculations are adequate for a particular material.

Although DFT+U can correct electronic and magnetic properties, the U parameter is usually obtained semi-empirically by fitting to experimental data, making the results not completely ab-initio. As a fully first-principles alternative to DFT+U, we used the hybrid functional HSE-06 [192], which is formed by mixing 75% of the PBE exchange with 25% of the Fock exchange and 100% of the correlation energy from PBE and has been reported to give more accurate re-

sults [16, 193, 194]. In order to account for van der Waals (vdW) effects, the DFT-D2 method of Grimme [195] was implemented for calculations of electronic properties.

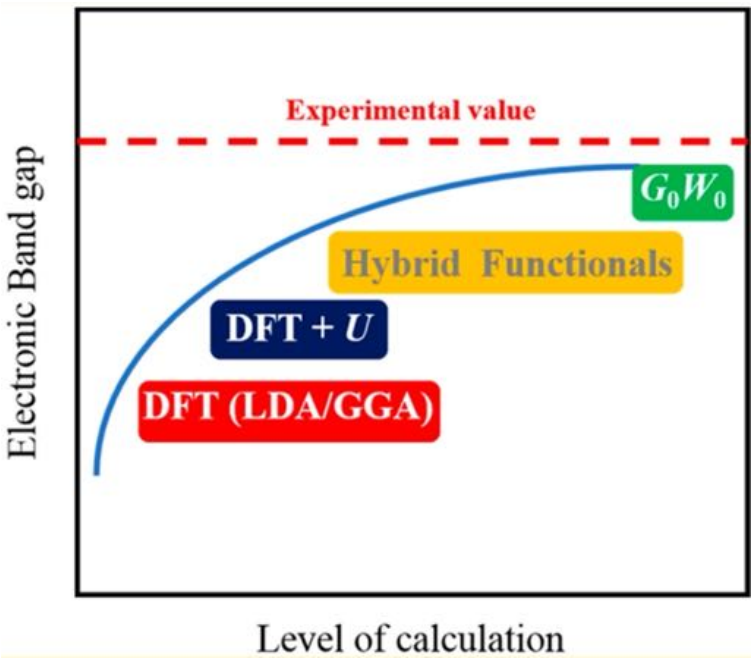

Figure 3.1: Various methods to predict the band gap in solids and their efficacy by using density functional theory calculations, after [16]

Fig. 3.1 shows the validity of various methods to predict the band gap in solids using density functional theory calculations, however the resulting methods appear to be material dependent [16].

Pre- and post-processing modules of the VASPKIT, a command-line program which provides a robust and user-friendly interface to perform high-throughput analysis of various material properties from the raw data produced by the VASP code. The former module was used to prepare input files such as symmetry analysis, and k-path generation for a given crystal structure while the latter module was utilized to extract and analyze the raw data about electronic structure, charge density, and wave function plots in real space. Linux, macOS, and Windows platforms can be used to run VASPKIT. To find the executable versions of VASPKIT and the related examples and tutorials, one can follow its official website vaspkit.com [196]. Further, P4vasp [197] and OriginLab [198] softwere were used for the graphical interpretation of data.

CHAPTER 4

RESULTS

4.1 Possible half-metallic behavior of $Co_{2-x}Cr_xFeGe$ Heusler alloys: Theory and Experiment

4.1.1 Abstract

This work reports a combined experimental and theoretical study of structural, electronic, magnetic, and mechanical properties of quaternary Heusler alloys $Co_{2-x}Cr_xFeGe$ prepared by arc-melting with Cr concentrations $0 \leq x \leq 1$. Single phase microstructures are observed for Cr compositions from $x = 0.25$ to $x = 1$. Lower Cr concentrations are multi-phased. X-ray diffraction patterns at room temperature reveal a face-centered cubic crystal structure in all single phase samples. The low-temperature saturation magnetic moments, as determined from magnetization measurements, agree fairly well with our theoretical results and also obey the Slater-Pauling rule for half-metals, a prerequisite for half metallicity. All alloys are observed to have high Curie temperatures that scale linearly with the saturation magnetic moments. Relatively high mechanical hardness values are also observed. First-principles calculations also predict a finite band gap in the minority spin channel of the alloys, increasing in size with increasing Cr concentration. Cr substitution brings the Fermi level toward the center of this gap while also increasing the majority spin density of states near the Fermi level. As a whole $Co_{2-x}Cr_xFeGe$ shows great promise as a half-metal with 100% spin polarization.

PUBLISHED AS: R. Mahat*, S. KC, U. Karki, J. Law, V. Franco, I. Galanakis, A. Gupta & P. LeClair, *Possible half-metallic behavior of $Co_{2-x}Cr_xFeGe$ Heusler alloys: Theory and Experiment*, Physical Review B, **104**,014430(2021).

4.1.2 Introduction

Heusler alloys consist of a large family of intermetallic compounds exhibiting varieties of magnetic phenomena. Recently, the interest has been focused on those having half metallic character for their potential use in magneto-electronic devices [29]. Co_2-based full Heusler compounds with stoichiometric composition Co_2YZ, (Co,Y) being two transition metals, and Z being main group element, crystallizing in the $L2_1$ structure (space group $Fm\bar{3}m$, # 225 [64, 65]) belong to the most promising candidates of this family scientifically and technologically [1, 30, 66, 84–91]. These materials exhibit high Curie temperature (T_c), varying magnetic moments ranging from 0.3 μ_B to 1.0 μ_B at the Co site (depending on the constituents Y and Z), compatible lattice mismatch with conventional semiconductors, and 100% spin polarization at room temperature, arising from the exceptional electronic structure with a energy band gap at the Fermi level (E_F) for minority spin sub-band [20, 29–34].

However, the experimentally observed spin polarization of most of the Co_2-based ternary Heusler alloys are always much smaller than the theoretical values. The discrepancy between theory and experiment is expected due to the structural disorder in the crystal lattices [1, 41]. In many cases, improvements in various properties such as structure, magnetization, transport, critical temperature T_c, magnetoresistance as well as high spin polarization are realised in slightly disordered Heusler alloys by the substitution of a quaternary element, as quaternary element additions are observed to reduce the structural disorder and change the degree of hybridization between the $3d$ orbitals of different elements with consequent changes in the position of the Fermi level with respect to the spin sub-band [115–120]. Özdoğan *et al.* [121] have done the theoretical study of the doping effect of low-valent transition metal atoms in ternary Heusler alloys. They have observed the change in electronic structure opening the energy gap around Fermi level in minority states by electron doping, which gives 100% spin polarization, stabilizing the half-metallic character. So, doping is considered as one of the promising ways to stabilize Co_2-based new robust half-metals [122].

The Co_2FeGe (CFG) system is of interest in spintronic applications due to its high Curie

temperature and is predicted theoretically to be stable, crystallizing in the $L2_1$ structure with Fermi level falling on the edge of the minority conduction band making the system shy from being half metallic, but it is observed experimentally to show multi-phase behavior in bulk form [17, 105, 129]. High T_c = 981 K and large magnetic moment of 5.74 $\mu_B/f.u.$ for disordered CFG is reported in Ref [17]. Balke *et al.* [199] have observed CFG to crystallize in $L2_1$ structure by analysing the EXAFS data. While, quaternary Heusler alloy CoFeCrGe (CFCG) is observed theoretically and experimentally to be nearly half metallic with Fermi level falling on the edge of the minority valence band, leading to an unstable half-metallicity [18, 132–134]. So, as we go from CFG to CFCG, Fermi level is shifted from lower edge of conduction band to upper edge of valence band in minority spin channel which is in accordance to the calculations by Galanakis *et al.* [128]. They have suggested that an expansion of the lattice should shift the Fermi level deeper in energy and the contraction should shift it higher in energy. Therefore, one can expect robust half metallicity with Fermi level exactly at the middle of the band gap for some intermediate Cr concentrations in CFG due to the expansion of the lattice when Cr with larger atomic radius substitutes for Co [153]. The substitution of Cr to Co may be also seen as d-electron deficiency.

There are some successful reports on CFG system where substitution plays an important role to stabilize the $L2_1$ phase and tune the Fermi level towards the minority band gap. The band gap at the Fermi level can be tuned by substituting a fourth element at X/Y/Z site *i.e.*, $Co_{2-x}Y^*_xYZ$, $Co_2Y_{1-x}Y^*_xZ$ or $Co_2YZ_{1-x}Z^*_x$ where Y, Y* are low valent transition elements and Z, Z* are main group elements [41, 62, 123–127]. The substitution at X/Y site is more convincing as X/Y site element plays main role in tailoring the half-metallicity and magnetic properties compared to Z site [128]. Ti substitution to Co in disordered CFG is reported to stabilize the system and tune the Fermi level towards the middle of the band gap [105]. Venkateswarlu *et al.* [130] were able to obtain the stable $L2_1$ phase in $Co_2Ti_{1-x}Fe_xGe$ substitutional series in bulk form with some antisite disorder. Varaprasad *et al.* [120] were able to measure spin polarization as high as 0.69 in CFG by substituting Ga for Ge *i.e.*, $Co_2Fe(Ga_{1-x}Ge_x)$. All these approaches have inspired us to synthesize CFG, a potential candidate for spintronic applications, and investigate the effect of Cr substitution

for Co in CFG on structural, electronic, magnetic and mechanical properties. In particular, we present results on the extent to which Cr can help to tune the half metallic character stabilizing the $L2_1$ structure in $Co_{2-x}Cr_xFeGe$ Heusler system.

4.1.3 Methods

4.1.3.1 Experimental Methods

The bulk $Co_{2-x}Cr_xFeGe$ $(0 \leq x \leq 1)$ stoichiometric Heusler alloys were prepared by melting Co, Fe, Cr, and Ge pieces of 99.99% purity in an arc furnace on a Cu hearth provided with water cooling under argon flow at a base pressure of 10^{-4} mbar. The mixture was melted at least 6 times to ensure chemical homogeneity. As an oxygen getter, Ti was melted inside the vacuum chamber separately before melting the compound to avoid oxygen contamination. The weight loss during the process was negligible. The resulting ingots were cut into pieces and examined using an energy dispersive X-ray spectroscopy (EDS) detector equipped in a JEOL 7000 field emission scanning electron microscope (FESEM) to ensure the target composition after the arc melting. These pieces were annealed in evacuated quartz tubes for different heat treatments, and cooled slowly in the furnace to get optimum crystallization to promote the formation of $L2_1$ structure. To make the comparison uniform across all compositions, only the samples annealed under similar heat treatments (*i.e.*, 1000°C for 15 days) are reported. The heat treatments were followed by metallography (see details in supplementary information) to produce a metallic shiny surface for microstructure analysis by optical and electron microscopes. After the heat treatment and metallography, the composition and homogeneity of the samples were again confirmed by using EDS.

Structural analysis was carried out by using X-ray diffraction (XRD) using a Bruker D8 Discover X-ray diffractometer equipped with monochromatic Co-Kα (λ = 0.179 nm) radiation. The polished samples were rotated around the ϕ axis during the XRD measurement to minimize surface effects. CaRIne crystallography 4.0 software [78] as well as in-house PYTHON code [79] including the dispersive corrections to the atomic scattering factors were used to simulate the XRD

patterns to compare with the experimental XRD patterns. Rietveld refinement was done using a MATCH! software based on the FullProf algorithm [80]. The low temperature magnetic properties were studied in Quantum Design Physical Properties Measurement System (PPMS), while the high temperature magnetization was measured using LakeShore VSM 7407. The mechanical properties were studied in terms of Vickers hardness by using Buehler model 1600-6100 micro-hardness tester.

4.1.3.2 Computational Methods

We have performed density-functional theory (DFT) calculations employing the projector augmented wave (PAW) pseudopotentials by Blöchl [180], implemented by Kresse and Furthmüller in the Vienna *ab initio* simulation package (VASP) [181]. We have adopted the generalized-gradient approximation (GGA) in the scheme of PerdewBuekeErnzerhof (PBE) for the electronic exchange-correlation functional [182]. We have used a 16-atom supercell, *i.e.*, 4 formula units of the underlying $L2_1$ structure adopted by the perfect full-Heusler compounds like Co_2MnGe. The integration over the irreducible Brillouin-zone (IBZ) of cubic systems was done with the automatic mesh generation scheme within VASP with the mesh parameter (the number of k points per $^{-1}$ along each reciprocal lattice vector) set to 30, which generates a $10 \times 10 \times 10$ Γ-centered Monkhorst-Pack grid in the case of cubic lattices [200]. Total energies were converged upto 10^{-7}eV/cell with a plane-wave cutoff of 520 eV. Full relaxation of cell (initially cubic) volume, shape and atomic positions were performed until the forces on each atom become less than 10^{-2} meV/cell using the conjugate-gradient method. Our calculations did not include spin-orbit interaction but the latter is not crucial for the half-metallic properties of Heusler compounds [183].

4.1.4 Results and Discussions

4.1.4.1 Experimental results and Discussions

4.1.4.1.1 Microstructural and Compositional analysis

XRD can not detect additional phases when the impurity phase contents are either below the detection limit of XRD (less than roughly 5% of the overall volume) or amorphous in nature [105, 168, 169]. In such case, optical microscopy and SEM of polished and etched samples are the most direct ways to characterize the microstructure because they give a morphological image which can clearly figure out secondary phases and grain boundary segregation even for minor constituents. Observing different contrast in etched sample seen from optical microscopy, we can speculate the presence of impurity phases, and SEM with EDS can be used to directly quantify whether areas of different contrasts represent impurity phases or possible different crystallite orientations.

In accordance with previous reports of the full stoichiometric CFG [17, 105, 129, 163], multiphase microstructure was obtained for all the heat treatments performed at 900, 950, or 1000°C for different dwelling times; 3, 7, or 15 days. However, with the substitution of Cr for Co, there is a rapid conversion of this multiphase microstructure toward a single phase microstructure for the samples annealed at 1000°C for 15 days in the composition range $(0.25 \leq x \leq 1)$. Low Cr concentration ($x < 0.25$) produced multiphase behavior. Fig. 4.1 shows the microstructure of all single phase samples observed using optical microscope. The contrast developed in micrograph

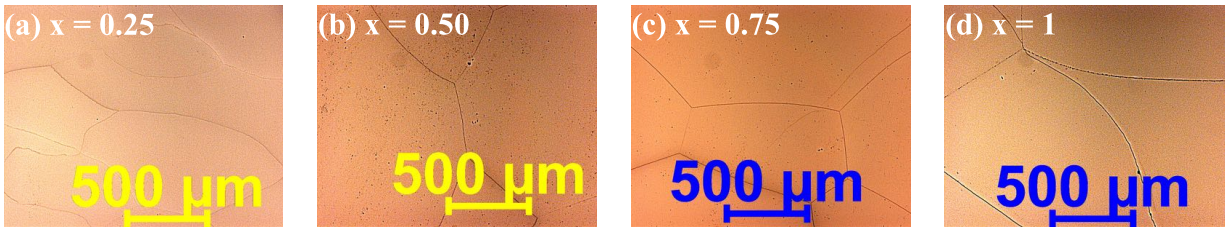

Figure 4.1: Optical micrograph of $Co_{2-x}Cr_xFeGe$ annealed at 1000°C for 15 days followed by slow cooling showing the granular microstructure. The samples were etched for 30 seconds using the Adler etchant.

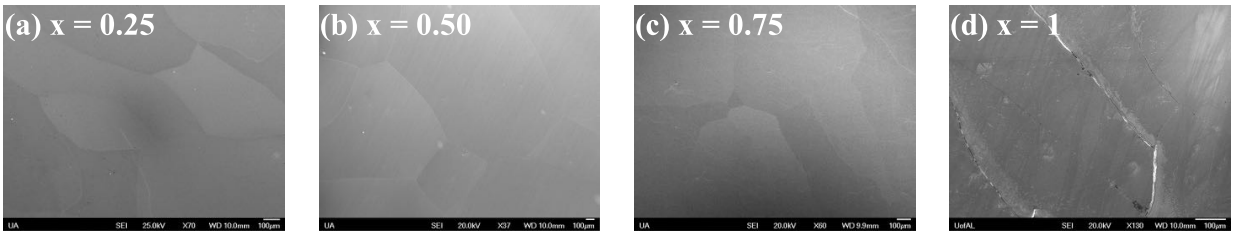

Figure 4.2: SEM micrograph of $Co_{2-x}Cr_xFeGe$ annealed at 1000°C for 15 days followed by slow cooling showing the granular microstructure.

(see details in Supplementary information) suggests significant compositional differences between phases in the case of parent CFG ($x = 0$). The composition was measured to differ from the target composition by more than 5% with the secondary phase mainly located in grain boundaries and same trend is observed with the chromium substitution $x = 0.125$ in place of Co, though the major granular phase was identified to be close to target and nominal secondary phase was observed to segregate in grain boundaries which can also be seen from elemental mapping images of constituent elements in homogenized $Co_{2-x}Cr_xFeGe$ alloys presented in Supplementary information. The stoichiometry within the grains of all the single-phase samples was confirmed as the target composition within an instrumental uncertainty of $\sim 5\%$ using EDS. Typical SEM images displaying the microstructure of single phase samples are shown in Fig. 4.2. Relatively large grains are observed.

4.1.4.1.2 Crystal structure and atomic order analysis

Structural characterization has been performed with XRD as the standard method. Although, XRD suffers from some limitations due to very small differences in the atomic scattering factors between constituent transition elements in $Co_{2-x}Cr_xFeGe$, an important structural information concerning atomic disorder can be obtained from the analysis of the relative intensities of the superstructure reflection peaks (111) and (200). Fig. 4.3 shows the XRD patterns for $Co_{2-x}Cr_xFeGe$ alloys annealed at 1000°C for 15 days, measured at room temperature, using a Co-K_α radiation source. Single phase behavior can be seen only for $0.25 \leq x \leq 1$ while low Cr concentrations are

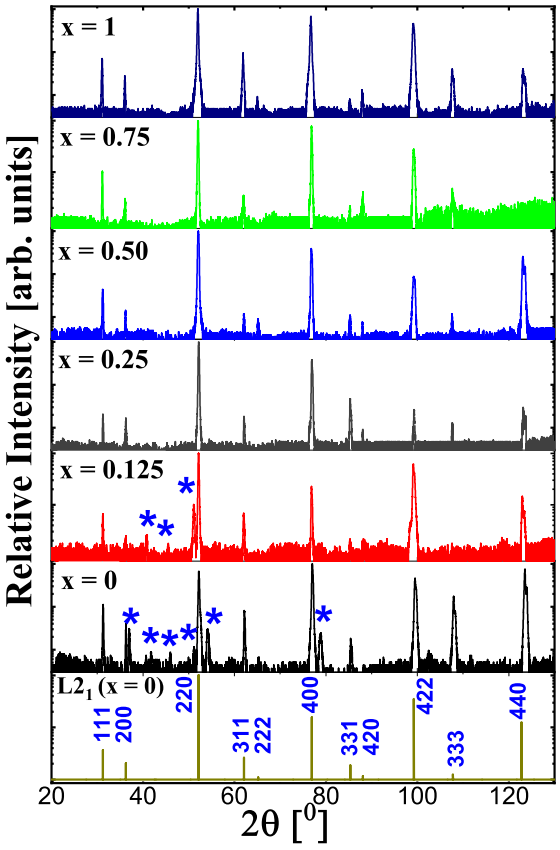

Figure 4.3: Experimental XRD patterns of $Co_{2-x}Cr_xFeGe$ alloy series annealed at 1000°C for 15 days investigated at room temperature, here, $*$ corresponds to the secondary phase/unknown impurity phase. The first from the bottom is the simulated XRD pattern for ordered $L2_1$ structure of CFG. The relative Intensity (y-axis) is plotted in log scale so that all the peaks can be seen clearly.

multi-phase (impurity peaks are represented by asterisks). Simple structural information of a cubic single phase can be gained by indexing all XRD peaks. For all cubic single-phase compositions, only three distinct Heusler-like reflection peaks (h, k, l all odd or even) are observed; fundamental peaks with $h+k+l = 4n$, even superlattice peaks with $h+k+l = 4n+2$ and odd superlattice peaks with $h+k+l = 2n+1$. Heusler alloys in the ordered $L2_1$ structure are characterized by the presence of superlattice diffraction peaks; the presence of (111) peak indicates the chemical ordering of atoms in octahedral positions, and (200) peak indicates the order for atoms in tetrahedral positions, while (220) peak is a principal reflection which is independent of the state of the order [72].

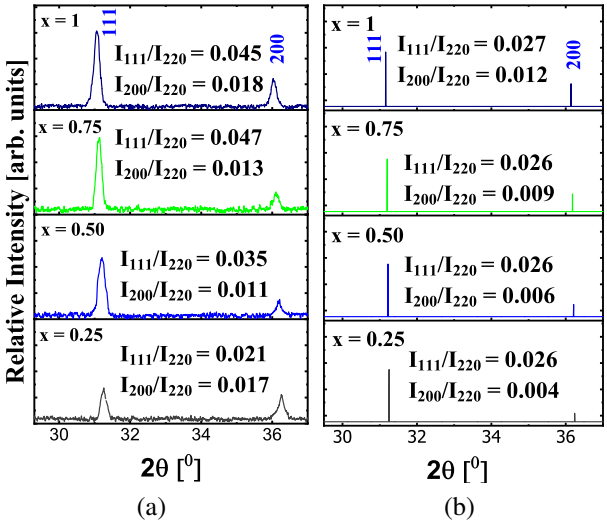

Figure 4.4: (a) Enlargement of (111) and (200) X-ray diffraction peaks of single phase samples and (b) the corresponding simulated patterns for the ideal ordered structure.

In full Heusler alloys (FHA) of the type X_2YZ, transition metal atoms X are of the intermediate electronegativity values and occupy 8c($\frac{1}{4},\frac{1}{4},\frac{1}{4}$) (or 4c($\frac{1}{4},\frac{1}{4},\frac{1}{4}$), and 4d($\frac{3}{4},\frac{3}{4},\frac{3}{4}$)), the low valence transition metal atom Y with least electronegativity occupies 4b($\frac{1}{2},\frac{1}{2},\frac{1}{2}$), and the most electronegative main group element Z occupies 4a(0,0,0) Wyckoff positions of the space group $Fm\bar{3}m$ [1, 61]. Here, we refer 4a and 4b sites as A sublattice and 4c and 4d as B sublattice as shown in Fig. 4.6. If one X is replaced by a different transition metal X', a quaternary Heusler structure (or Y structure) with different symmetry (space group $F\bar{4}3m$ # 216) is obtained and written as XX'YZ. In the present system under study, one can expect a change in structural order from $L2_1$ ($x = 0$) to Y structure ($x = 1$) after Cr substitution, as the parent alloy CFG ($x = 0$) has been reported to crystallize in $L2_1$ structure with some disorder [17, 120, 129]. The intensities of superstructure peaks are sensitive to different kinds of atomic disorders, *e.g.*, (i) A2-type disordered structure with vanishing superstructure peaks when all the atoms are randomly distributed over lattice sites 4a, 4b, 4c, and 4d, (ii) disordered $L2_1$ structure (like B2-type in FHA) with only the (200) superstructure peak and vanishing (111) peak when there is a disorder between atoms in 4a and 4b sites, and (iii) B32a-type when disorder is between atoms in 4a, and 4c sites and 4b, and 4d sites [1, 73].

This disordered structure DO_3 results (111) superstructure peak with much higher intensity than the (200) peak. All these types of disorder induce states at the edges of the minority-spin band gap leading eventually to the loss of half-metallicity for a critical value of disorder, the later being specific and depending on the kind of disorder [62]. In such cases, the magnetic moments may still follow a Slater Pauling rule.

We present the enlargement of the experimental XRD patterns between 29.5° and 37° for single phase samples to clearly show the superlattice reflections (111) and (200) in Fig. 4.4(a) with corresponding simulated patterns of ideal $L2_1$ structure (Y structure for $x = 1$) for comparison in Fig. 4.4(b); the two diffraction peaks are clearly visible as expected for the defect-free ordered Heusler structure, indicating the presence of a long range ordering in these samples. The measured and expected I_{111}/I_{220} and I_{200}/I_{220} are also labeled. These values agree with each other qualitatively.

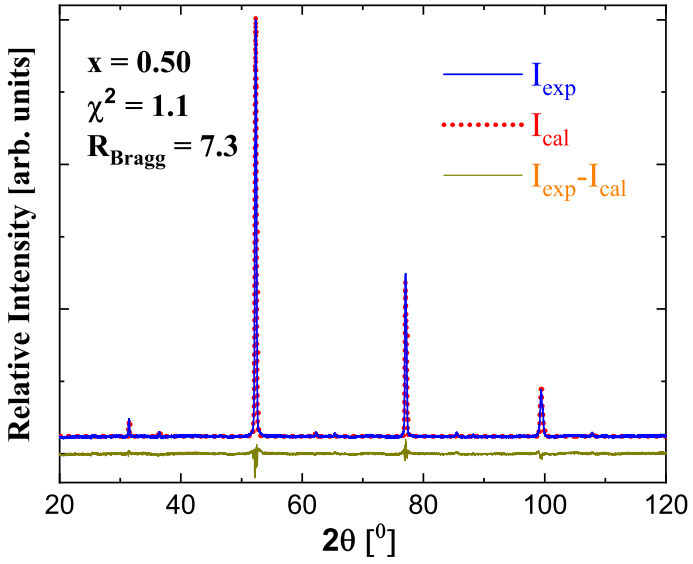

Figure 4.5: Rietveld refinement performed on $Co_{1.50}Cr_{0.50}FeGe$ annealed at 1000°C for 15 days followed by slow cooling considering first atomic configuration given in Table 4.1.

Due to the small differences in the atomic scattering factors between the constituent $3d$-metals in $Co_{2-x}Cr_xFeGe$ and the unknown degree of texturing in the samples which might alter the relative intensity of XRD peaks, it is difficult to identify the exact chemical ordering. Therefore, we performed Rietveld refinement of experimental XRD pattern for $x = 0.50$ *i.e.*, $Co_{1.50}Cr_{0.50}FeGe$

Table 4.1: Possible site assignments for cubic $Co_{2-x}Cr_xFeGe$ with corresponding goodness of fit parameter for $x = 0.50$.

Type	4a (0,0,0)	4b $(\frac{1}{2},\frac{1}{2},\frac{1}{2})$	4c $(\frac{1}{4},\frac{1}{4},\frac{1}{4})$	4d $(\frac{3}{4},\frac{3}{4},\frac{3}{4})$	$\chi^2_{x=0.50}$
I	Ge	$Fe_{1-x}Cr_x$	$Co_{1-x/2}Fe_{x/2}$	$Co_{1-x/2}Fe_{x/2}$	1.1
II	Ge	$Fe_{1-x}Cr_x$	$Co_{1-x}Fe_x$	Co	1.7
III	Ge	$Co_{1-x}Cr_x$	Fe	Co	1.9
IV	Ge	Fe	$Co_{1-x}Cr_x$	Co	2.2

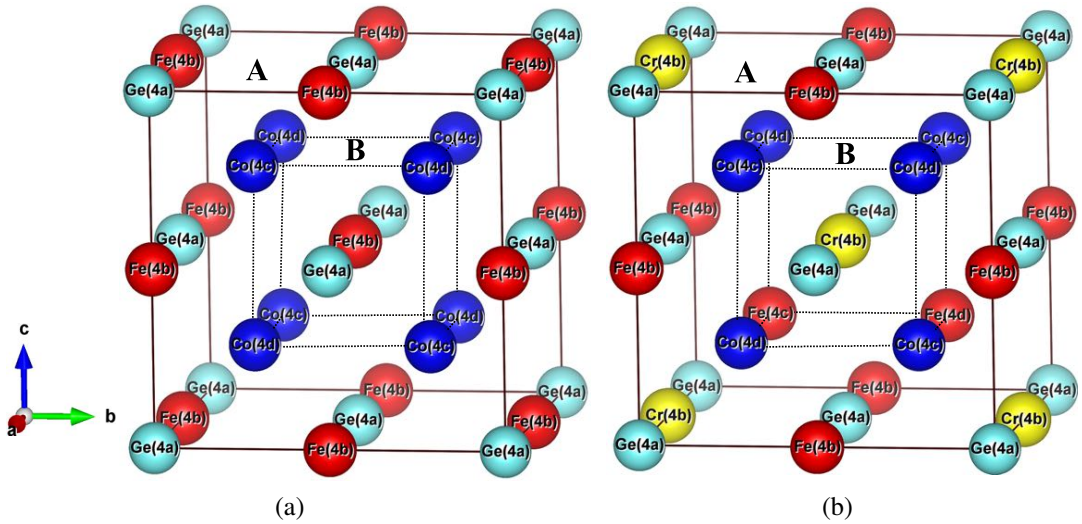

Figure 4.6: Crystal structure in unit cell of (a) CFG and (b) $Co_{1.50}Cr_{0.50}FeGe$ (I) configuration mentioned in Table 4.1 assuming $L2_1$ structure. The structures are shown in their ideal, unrelaxed forms.

considering four non-degenerate configurations. Further detail about other possible chemical orderings will be discussed in the forthcoming theoretical section. These four non-degenerate configurations and corresponding goodness of fit parameters for $x = 0.50$ are shown in Table 4.1. Fig. 4.5 shows the observed, calculated and difference profiles for the best fit configuration (I) after performing the Rietveld refinement. The crystal structure for this configuration is shown in Fig. 4.6(b) (see Supplementary information for crystal structures for other possible configurations). In this configuration, the Ge atoms occupy the 4a position, a statistical distribution of the Fe and the Cr which substitute Co atoms in the chemical formula is expected at 4b, the Fe atoms initially at these site in the perfect $L2_1$ structure migrate to the tetrahedral sublattice B initially occupied

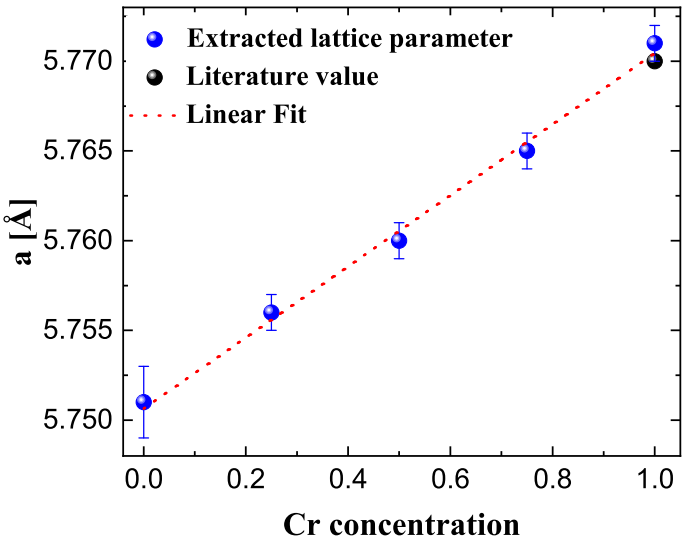

Figure 4.7: Variation of lattice parameter with Cr concentration showing linear behavior. The black data points represent literature values [17, 18].

purely by Co, *i.e.*, Co and Fe are on the tetrahedral sublattice B (4c & 4d) and Fe, Cr, and Ge on the octahedral sublattice A (4a & 4b). In $Co_{2-x}Cr_xFeGe$, Cr is the least electronegative (1.66 Pauli units) [201]. Therefore, we presume that Cr substitution will displace the Fe atoms towards vacated Co sites and it will fill the site previously occupied by Fe forming an ionic-type sublattice with Ge (which has a larger electronegativity of 2.01 Pauli units) rather than with Co and Fe and becomes stable by donating its electrons to other elements in the alloy. Ge tries to accept electrons from other elements. The Co and displaced Fe atoms have intermediate electronegativities and occupy tetrahedral sites [1, 61]. This is also in agreement with the Hume-Rothery condition of phase stability of substitutional solid solution. According to this rule, the atomic size difference between two elements should be no larger than 15% and electron negativity difference no higher than 0.4 in order to form substitutional solid solution [202–204]. In our case, the atomic-size and electronegativity difference between Fe (atomic radius 156 pm & electronegativity 1.83 Pauli units) and Cr (atomic radius 166 pm & electronegativity 1.66 Pauli units) are $\sim 10\%$ and -0.11 respectively and that between Co (atomic radius 152 pm & electronegativity 1.88 Pauli units) and Fe are $\sim 3\%$ and -0.03 respectively [153, 201].

Lattice parameters were calculated using Cohen's method with a Nelson-Riley extrapolation

[171]. Fig. 4.7 displays the dependence of the lattice parameter a on the Cr concentration x for $Co_{2-x}Cr_xFeGe$. It is clearly seen that the lattice parameter increases linearly with increasing chromium content. This behaviour is expected from Vegard's law [205] due to the larger atomic radius of Cr (185 pm) compared with Co (152 pm) [153].

4.1.4.1.3 Magnetic Characterization

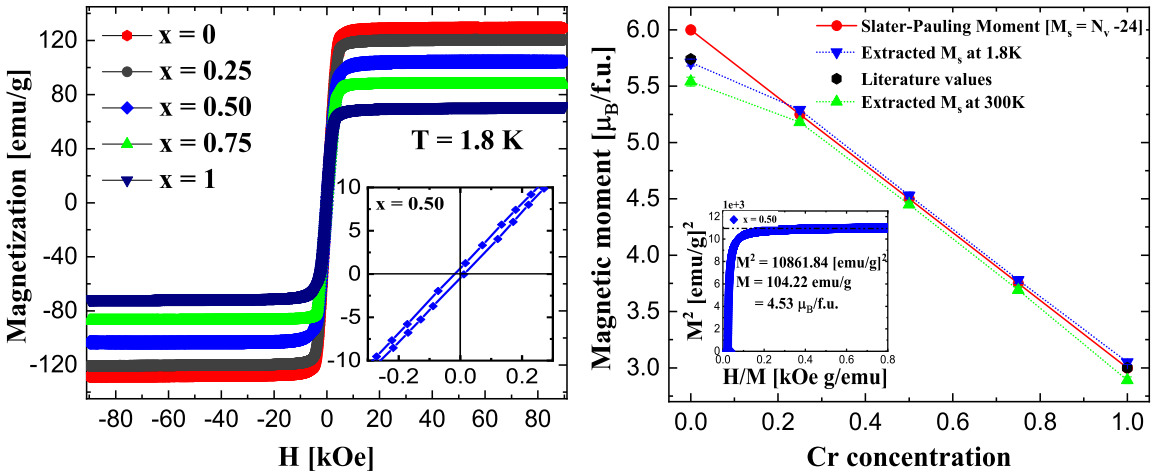

Figure 4.8: (a) The field-dependent magnetization at 1.8 K of $Co_{2-x}Cr_xFeGe$ $(0 \leq x \leq 1)$. The inset shows the enlargement for $x = 0.50$. (b) The saturation magnetic moment versus Cr concentration, both experimental and expected from Slater Pauling rule for half metals.The inset shows the Arrot plot for $x = 0.50$. The black data points represent reported literature values [17, 18].

Most of the Co-based half-metallic Heusler alloys show a Slater-Pauling-like behavior for the magnetization when crystallized in a fully ordered state [206]. The Slater-Pauling (SP) rule relates the dependence of the magnetic moment with the valence electron concentration (Z_t) following a simple electron counting scheme for ordered, half-metallic ferromagnetic Heusler compounds. If the value of the saturation magnetization changes with Cr concentration x according to the Slater-Pauling rule of thumb for half-metals, then we expect the total magnetization to be [1, 7]

$$M_t = [(2-x)Z_{Co} + xZ_{Cr} + Z_{Fe} + Z_{Ge}] - 24 \tag{4.1}$$

where, M_t is the total spin magnetic moment per f.u. in μ_B and Z_i is the number of valence electrons of each individual atom. In $Co_{2-x}Cr_xFeGe$ system, the total number of valence electrons change from 30 in CFG to 27 in CFCG. Therefore, the SP behavior predicts that the saturation magnetic moment should decrease with the partial substitution of Cr for Co. A saturation magnetic moment of

$$M(x) = 6 - 3x \tag{4.2}$$

is expected for $Co_{2-x}Cr_xFeGe$.

The low temperature magnetic measurements for all single-phase alloys were done using the VSM option of a Quantum design PPMS Dynacool working in the temperature range of T = 1.8 K to 400 K and with maximum possible magnetic field of 9 T. Fig. 4.8(a) shows the magnetization curves measured at 1.8 K (see Supplementary information for magnetization curves at 300 K). The magnetization curves shown in Fig. 4.8(a) are characteristic for ferromagnets. All the alloys are saturated in magnetic field of about 5 kOe, indicating small magnetocrystalline anisotropy. All the alloys are observed to be magnetically very soft with low coercivity (H_c) of about 20 Oe (see inset to Fig. 4.8(a) for $x = 0.50$). The spontaneous magnetizations (M_s) were determined from an Arrot plot [207], *i.e.*, by linear extrapolation to H/M=0 of M^2 versus H/M curve (see inset to Fig. 4.8(b)). The saturation magnetic moments deduced from the spontaneous magnetization at 1.8 K are in good agreement with those expected for Slater-Pauling half metals (see red data points) and decrease almost linearly with the increase of Cr content (see Fig. 4.8(b)). The decrease of the total saturation magnetic moment with the increase in Cr content can only be attributed to the decrease in number of Co atoms. The magnetic moment per formula unit for $x = 1$, *i.e.*, CoFeCrGe is measured to be 3.07 μ_B, which is also in agreement with the observation of Enamullah *et al.* [18]. The slight deviation from integer value of magnetic moment could be due to the slight variation in the stoichiometry of the compounds, weighing and measurement errors, partial surface oxidation, and the measurement temperature of 1.8 K. All experimentally extracted saturation magnetic moments are also in good agreement with those obtained from first-principle calculations (see Table 4.4), as described in the forthcoming section.

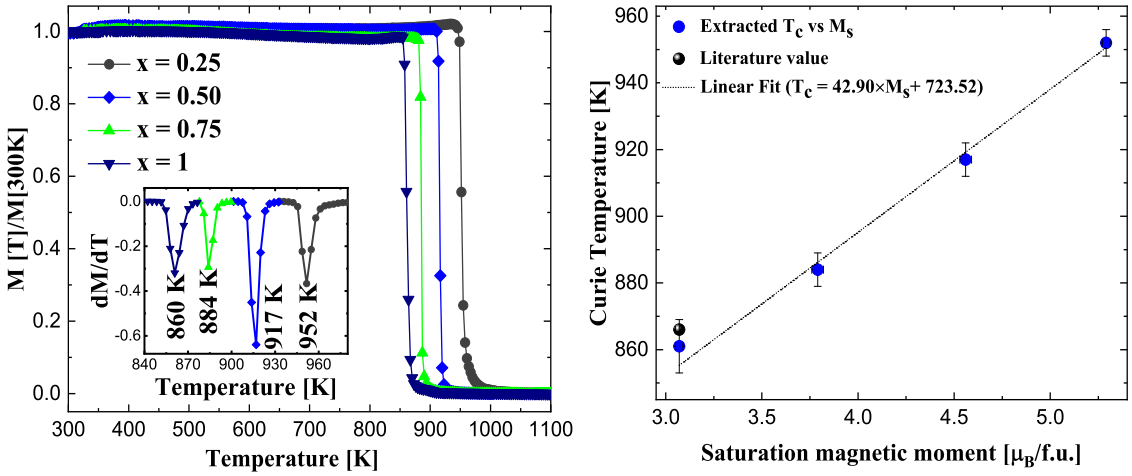

(a) (b)

Figure 4.9: (a) Temperature dependence of magnetization at 100 Oe. The inset shows the first-order derivative of magnetization as a function of temperature, the minima of which is used to extract T_c. (b) Variation of Curie temperature as a function of saturation magnetic moment.The black data points represents reported literature value [18].

Figure 4.9(a) shows the temperature dependent specific magnetization of the investigated specimens, measured by means of a vibrating sample magnetometer (LakeShore VSM 7407) equipped with a high temperature stage. The measurements were performed in a constant magnetic field of 100 Oe. The Curie temperatures of intermetallic alloy series were extracted from the inflection point *i.e.*, by taking the minima of the first-order derivative of M(T) curves (see inset in Fig. 4.9(a)). The Curie temperature is observed to decrease with increasing Cr content due to the weakening of the exchange interaction caused by small magnetic moment of substituted Cr compared to Co. The decrease in T_c can also be attributed to the increase in lattice parameter with the substitution of Cr changing the distance between magnetic ions leading to a weak exchange interaction. Compared to other low valence transition metals V and Ti, the large magnetic moment at the Cr sites due to the exchange splitting between the Cr-*d* states in the spin-up and the spin-down channels is responsible for the small variation of T_c with the increase of Cr content [105, 208]. A linear dependence is obtained when plotting the Curie temperature T_c of all single phase samples as a function of their saturation magnetic moments (see Fig. 4.9(b)), which is expected in half metallic

Table 4.2: Experimental lattice parameters and saturation magnetic moments at T = 1.8 K along with the Slater-Pauling (S-P) values, and the measured Curie temperature (T_c) of $Co_{2-x}Cr_xFeGe$ alloy series. The numbers in parentheses are the uncertainty in the last digit, *e.g.*, $5.29(2) = 5.29 \pm 0.02$.

x	Expt. lattice parameter (Å)	Expt. M_s (μ_B/f.u.)	S-P (μ_B/f.u.)	T_C (K)
0†	a = 5.751(3)	5.71(3)	6.00	981[17]
0.25	a = 5.756(1)	5.29(2)	5.25	952(4)
0.50	a = 5.760(1)	4.53(3)	4.50	917(5)
0.75	a = 5.765(1)	3.78(3)	3.75	864(5)
1	a = 5.771(1)	3.05(2)	3.00	861(8)

† Multiphase specimen

Co-based Heusler alloys [124]. According to this plot, T_c is the highest for those that exhibit a large magnetic moment, or equivalently for those with a high valence electron concentration as derived from the Slater-Pauling rule. The high values of Curie temperatures usually imply stable magnetism and half metallicity over wide temperature range, necessary in practical applications. By extrapolating a linear dependence, T_c is estimated to be 980 K for parent Co_2FeGe ($x = 0$) in good agreement with the reported value 981 K [17].

The experimentally determined lattice parameters, saturation magnetic moments at 1.8 K and corresponding Curie temperature of all single phase samples in $Co_{2-x}Cr_xFeGe$ alloy series are summarized in Table 4.2.

4.1.4.1.4 Vickers micro hardness

Adaptation of materials to industrial applications requires mechanical robustness to undergo repetitive thermal cycling and resist cracking from vibrations. Most of the previous studies on mechanical properties are theoretical in nature and only few are verified experimentally. The observed disconnect between the few available experimental results and the various theoretical results requires the necessity of more experimental studies in this area. Fig. 4.10 shows the variation of Vickers micro hardness of the alloy series with Cr concentration measured at room temperature with corresponding values in Table 4.3. Hardness values reported are the averages of data taken from at least 12 different regions of each sample with 0.2 kg load and 10 s loading time. The

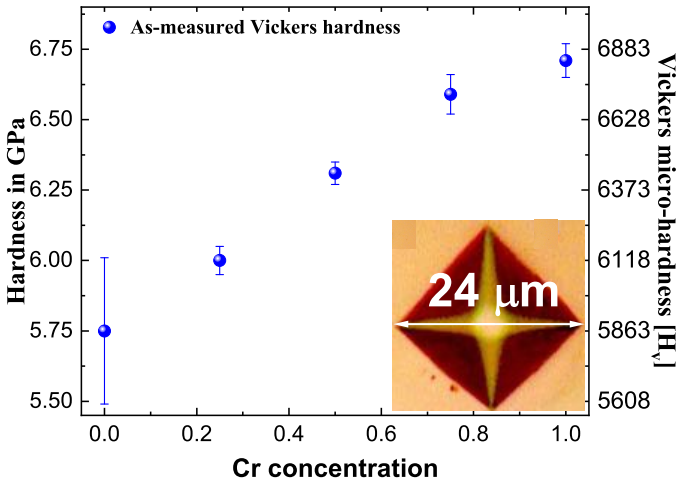

Figure 4.10: Vickers hardness versus Cr concentration in $Co_{2-x}Cr_xFeGe$, all annealed at 1000°C for 15 days, with imprint of the indenter with radial cracks for $x = 0.50$ [bottom right].

Vickers hardness is calculated from

$$HV = 1.8544F/D^2[\mathrm{kg/mm^2}] \tag{4.3}$$

where, D is the diagonal length of the impression of the diamond probe. Relatively high hardness values are measured, approaching 6.71 GPa for $x = 1$, comparable to the values reported for Heuslers in the literature [105, 155, 158, 163, 164, 209, 210]. The hardness is observed to increase almost linearly with the increase of Cr concentration and depends on phases present as reported in the literature [211].

Table 4.3: Vickers micro-hardness of the $Co_{2-x}Cr_xFeGe$ alloy series.

x	Vickers Hardness (GPa)
0†	5.75 ± 0.26
0.25	6.00 ± 0.05
0.50	6.31 ± 0.04
0.75	6.59 ± 0.07
1	6.71 ± 0.06

† Multiphase specimen

4.1.4.2 Theoretical Results and Discussions

From experiment, it is clear that the Cr substitution in Co_2FeGe stabilizes the $Co_{2-x}Cr_xFeGe$ system with XRD patterns consistent with $L2_1$ structure. But, small differences in the atomic scattering factors between the constituent $3d$-metals Co, Fe, and Cr and the unknown degree of texturing in the samples make it difficult to determine the chemical order relying only on XRD data. In order to obtain further information about the stability and chemical ordering in $Co_{2-x}Cr_xFeGe$ system, we have calculated the zero-temperature electronic structure, magnetic structure, and relative site preference energies for various possible atomic configurations, considering the symmetry of $L2_1$, Y and other disordered structures. The site preference energies of different configurations are shown in Fig. 4.11. The magnetic moment value is also depicted in the color axis on the right. The highlighted data points correspond to the most stable configuration (Type I in Table 4.1). These calculations show that the higher Cr content alloys are energetically most stable. Various calculated parameters are summarized in Table 4.4. To describe the atomic configurations, we have used the occupation of the Wyckoff positions of space group 216 (structure Y) referring 4a and 4b sites as A sublattice and 4c and 4d as B sublattice as implemented in Ref. [105]. Before relaxation, both A and B sublattices are simple cubic with every atom on A sublattice at the center of a cube with eight B sublattice atoms at the corners and every atom on the B sublattice at the center of a cube with eight A sublattice atoms at the corners. The distortion from cubic symmetry in most of the considered configurations after relaxation to eliminate the forces on the atom is observed to be of the order of a few percents or less.

From present calculations, the configuration with Ge and Fe atoms occupying A sublattice and Co atoms on B sublattice, which is $L2_1$ structure, appear to be energetically favorable in the case of parent compound CFG ($x = 0$), consistent with the reported results [17, 105, 129, 212]. However, the configuration with Co, Fe, Cr, and Ge atoms occupying 4d, 4c, 4b, and 4a sites, respectively, which is Y structure, is observed to be more stable in the case of other end member CFCG ($x = 1$), which is also consistent with reported results [18, 133]. So, the crystal structure has changed as we go from one end ($x = 0$, $L2_1$) to the other end ($x = 1$, Y). It can also be seen that the Fe atoms

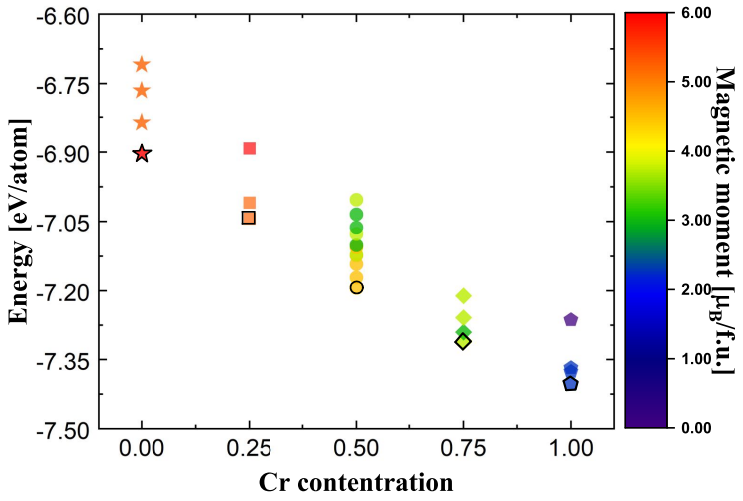

Figure 4.11: Site preference energies (in eV/atom) for different configurations of $Co_{2-x}Cr_xFeGe$ as a function of Cr concentration created manually. Each data point represents a different configuration given in Table 4.4 and the color axis indicates the magnetic moment value for each structure.

can occupy 4b sites sharing the same sublattice A with Ge ($x = 0$) as well as 4c sites sharing the Co sublattice B ($x = 1$).

Out of different possible configurations shown in Table 4.4, only the configurations with Fe, Cr and Ge on A sublattice (4a and 4b sites) and Co and Fe on the B sublattice (4c and 4d sites) appear to be energetically favourable after Cr substitution. This is consistent with the electronegativity rule as Cr is the least electronegative in the series and more likely to form an ionic-type sublattice with the most electronegative Ge rather than Fe or Co as discussed in XRD section above. In the case of $x = 0.50$, the two Cr atoms which substitute Co atoms in the chemical formula occupy actually sites within the A sublattice (4b sites) and the two Fe atoms initially at these sites in the perfect $L2_1$ structure migrate to the B sublattice initially occupied purely by Co atoms. The displaced two Fe atoms occupy 4c and 4d sites one each together with Co atoms in B sublattice. This pattern of atoms distribution among the various sites was found to be the most favorable energetically against any other configuration, that we have considered, as shown in Table 4.4. The effect of Cr substitution seems to be significant on structural parameters. The computationally optimized lattice parameters are found to increase with the increase of Cr content, consistent with experimentally observed values. Due to the fact that experiments were done at a finite temperature,

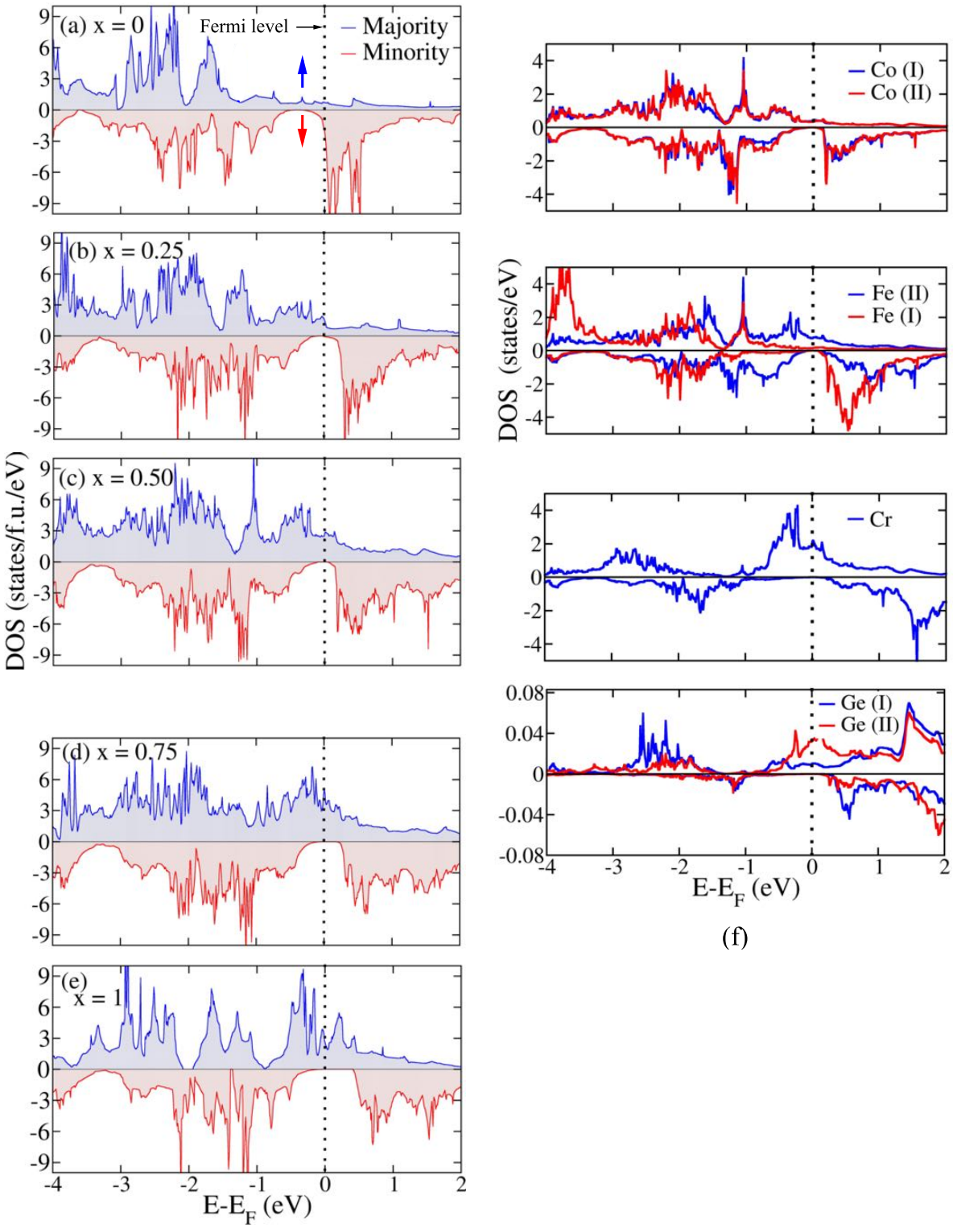

Figure 4.12: (a)-(e) Spin polarized total DOS for $Co_{2-x}Cr_xFeGe$ ($x = 0$, 0.25, 0.50, 0.75 and 1). The blue arrow represents the majority spin channel and red arrow represents minority spin channel. Number of states in each figure is scaled with respect to one formula unit. (f) Atom-resolved DOS for $x = 0.50$. I and II in parenthesis distinguishes the same atom type with different magnetic environment. For simplicity same color is used for minority (lower-half) and majority (upper-half) spin channels in each case.

Table 4.4: Possible atomic configurations and corresponding parameters extraced from DFT calculations. In the table E, E_0, M, M_{SP}, and $\langle a \rangle$ represent calculated energy, energy of most stable configuration, calculated magnetic moment, Slater-Pauling moment, and optimized lattice parameter. The last column shows the tetragonality in the structure.

Configurations	4d	4c	4b	4a	E-E_0 (eV)	M ($\mu_B/f.u.$)	M-M_{SP} ($\mu_B/f.u.$)	$\langle a \rangle$ (Å)	Tet. (a/c-1)
$x = 0$									
Co_8-Fe_4Ge_4	4Co	4Co	4Fe	4Ge	0	5.773	-0.227	5.747	0.000
Co_7Fe-Fe_3CoGe_4	4Co	1Fe,3Co	1Co,3Fe	4Ge	1.060	4.990	-1.010	5.719	0.012
Co_8-Fe_4Ge_4	4Co	4Co	3Fe,1Ge	1Fe,3Ge	2.210	5.031	-0.969	5.731	0.020
Co_7Ge-Fe_4CoGe_3	4Co	1Ge,3Co	4Fe	1Co,3Ge	3.104	4.932	-1.068	5.752	0.020
$x = 0.25$									
Co_7Fe-Fe_3CrGe_4	4Co	1Fe,3Co	1Cr,3Fe	4Ge	0	5.242	-0.008	5.753	0.000
Co_7Cr-Fe_4Ge_4	4Co	1Cr,3Co	4Fe	4Ge	0.546	5.195	-0.055	5.752	0.000
Co_7Ge-Fe_4CrGe_3	4Co	1Ge,3Co	4Fe	1Cr,3Ge	2.421	5.512	0.262	5.798	0.000
x= 0.50									
Co_6Fe_2-$Fe_2Cr_2Ge_4$	1Fe,3Co	1Fe,3Co	2Cr,2Fe	4Ge	0	4.500	0	5.759	0.012
Co_6Fe_2-$Fe_2Cr_2Ge_4$	4Co	2Fe,2Co	2Cr,2Fe	4Ge	0.124	4.495	-0.009	5.755	0.015
Co_4Fe_4-$Co_2Cr_2Ge_4$	4Co	4Fe	2Cr,2Co	4Ge	0.268	4.428	-0.072	5.757	0.024
Co_6Cr_2-Fe_4Ge_4	4Co	2Cr,2Co	4Fe	4Ge	0.571	4.408	-0.092	5.768	0.010
Co_5Fe_3-$CoFeCr_2Ge_4$	1Fe,3Co	2Fe,2Co	1Co,2Cr,1Fe	4Ge	0.600	4.111	-0.389	5.785	0.025
Co_6FeCr-Fe_3CrGe_4	1Fe,3Co	1Cr,3Co	1Cr,3Fe	4Ge	0.860	4.481	-0.019	5.749	0.003
Co_6Cr_2-Fe_4Ge_4	1Cr,3Co	1Cr,3Co	4Fe	4Ge	0.903	4.458	-0.043	5.787	0.020
$Co_4Fe_2Cr_2$-$Co_2Fe_2Ge_4$	4Co	2Fe,2Cr	2Fe,2Co	4Ge	0.930	3.084	-1.416	5.752	0.010
Co_5Cr_2Fe-$CoFe_3Ge_4$	1Cr,3Co	1Cr,1Fe,2Co	1Co,3Fe	4Ge	1.324	3.816	-0.684	5.702	-0.009
$Co_4Fe_2Cr_2$-$Co_2Fe_2Ge_4$	1Fe,1Cr,2Co	1Fe,1Cr,2Co	2Co,2Fe	4Ge	1.544	3.445	-1.055	5.790	0.020
$Co_4Fe_2Cr_2$-Co_4Ge_4	2Fe,1Cr,1Co	2Fe,1Cr,1Co	4Co	4Ge	1.676	3.395	-1.105	5.961	0.089
$Fe_4Co_2Cr_2$-Co_4Ge_4	2Cr,2Co	4Fe	4Co	4Ge	1.756	3.904	-0.596	5.860	0.064
x= 0.75									
Co_5Fe_3-$FeCr_3Ge_4$	1Fe,3Co	2Fe,2Co	3Cr,1Fe	4Ge	0	3.750	0	5.764	0.000
Co_4Fe_4-$CoCr_3Ge_4$	4Co	4Fe	1Co,3Cr	4Ge	0.326	3.124	0.626	5.708	0.001
Co_5Cr_3-Fe_4Ge_4	1Cr,3Co	2Cr,2Co	4Fe	4Ge	0.831	3.746	-0.004	5.729	-0.013
Co_5FeCr_2-$CrFe_3Ge_4$	1Cr,3Co	1Cr,1Fe,2Co	1Cr,3Fe	4Ge	1.593	3.745	0.005	5.759	0.003
x= 1									
Co_4Fe_4-Cr_4Ge_4	4Co	4Fe	4Cr	4Ge	0	3.000	0	5.770	0.000
Co_4Cr_4-Fe_4Ge_4	4Co	4Cr	4Fe	4Ge	0.103	2.963	-0.037	5.759	-0.007
Co_4Cr_4-Fe_4Ge_4	2Cr,2Co	2Cr,2Co	4Fe	4Ge	0.233	2.971	-0.029	5.817	0.021
Co_4Ge_4-Fe_4Cr_4	4Co	4Ge	4Fe	4Cr	2.230	0.611	-2.389	5.767	0.000

the experimental lattice parameters are slightly higher than those calculated from DFT (at 0 K) due to the thermal expansion coefficient of the material.

Co-based Heusler alloys are potential candidates for various spintronic applications. They usually show metallic behavior in the majority spin channel and give significant band gap in the minority spin channel. We have also simulated the spin-polarized electronic structure for most stable configurations of $Co_{2-x}Cr_xFeGe$ (x = 0, 0.25, 0.50, 0.75 and 1). Fig. 4.12 shows the calculated density of states (DOS) plots for majority and minority spin channels where the Fermi level is represented by the zero energy. It can be seen clearly that the system exhibits half-metallic behavior after Cr substitution because there is finite DOS at the Fermi level in the majority spin channel, while a band gap exists in the minority spin channel. In the case of parent compound CFG (Fig.

4.12(a)), there is significant amount of DOS at the Fermi level on both the spin channels. After Cr substitution, the Fermi level is observed to shift deeper in energy-levels and falls at the middle of the energy gap on spin down channel for $x = 0.50$ (Fig. 4.12(c)). Further increase of Cr content shifts the Fermi level towards the lower edge of energy gap due to lattice expansion as reported by Galanakis *et al.* [30]. But, still Fermi level lies within energy gap making the system Half-metallic. The energy gap is observed to increase with the increase of Cr content. Computationally extracted minority spin gaps at Fermi level for x = 0.50, 0.75 and 1 are respectively 0.121 eV, 0.173 eV and 0.471 eV. It can be seen clearly that the equiatomic CFCG system has a significant minority spin gap, agreeing well with the reported results [18, 133]. Although, the calculated minority spin gap is the highest for $x = 1$, the half-metallic gap is greater for $x = 0.50$. Here, the half-metallic gap refers to the spin flip gap and is the minimum between the lower edge of the conduction bands with respect to the Fermi level and the absolute value of the upper edge of the valence bands in the minority spin channel [213, 214]. In $Co_{2-x}Cr_xFeGe$ alloy series, the bottom of the minority conduction bands are located at 0.041 eV, 0.145 eV, and 0.444 eV while the top of the minority valence bands at -0.080 eV, -0.028 eV, -0.027 eV for $x = 0.50$, 0.75 and 1 respectively. So, half-metallic gaps are 0.041 eV, 0.028 eV, and 0.027 eV for $x = 0.50$, 0.75 and 1 respectively.

Fig. 4.12(f) shows the calculated atom-resolved DOS plots for $x = 0.50$. In predicted most stable configuration (I) (Fig. 4.13), it is clear that Fe(I) atoms, which share the same sublattice A with Cr, and Fe(II) atoms sharing the same sublattice B with Co have different nearest neighbor environment. Though all Co atoms occupy A sublattice, there are two different magnetic environments due to Fe atoms which are represented by Co(I) and Co(II) in Fig. 4.13. Likewise, in B sublattice, the nearest neighbour environment of Ge(I) and Ge(II) are different, but that of two substituted Cr atoms is same. The contribution to spin-resolved DOS from same atom types with different nearest neighbor environment is different, which is depicted in Fig. 4.12(f). Further, the atomic spin magnetic moments are calculated to be $1.027\mu_B$, $0.975\mu_B$, $2.795\mu_B$, $1.308\mu_B$ $1.964\mu_B$, $-0.063\mu_B$ and $-0.034\mu_B$ for Co(I), Co(II), Fe(I), Fe(II), Cr, Ge(I) and Ge(II), respectively. We can safely conclude that symmetry and the nearest-neighbors environment play a crucial role in the

properties of the various atoms in half-metallic Heusler compounds. Co(I) and Co(II) atoms at the 4c and 4d sites have the same nearest neighbors (two Fe(I) and two Cr atoms at the 4b sites and four Ge atoms at the 4a sites) but different next-nearest neighbors. Both Co(I) and Co(II) atoms have similar DOS as shown in Fig. 4.12(f) and their atom-resolved spin magnetic moments differ by about only $0.052\mu_B$. In the case of Fe atoms, the situation is more complex. Fe(I) atoms share the same sublattice A with the Cr atoms while Fe(II) atoms share the same sublattice B with the Co atoms. Thus their nearest-neighbors environment is completely different. As a result and as shown in Fig. 4.12(f) their DOS is completely different. The Fe(I) atoms present a d-DOS which shares a lot of features with the one of the Cr atoms. There is a very large exchange splitting between majority-spin occupied and minority-spin unoccupied d-states resulting to a very large minority spin gap and a very large Fe(I) spin magnetic moment of $2.795\mu_B$, which is more than double the spin magnetic moment of the Fe(II) atoms. All 3d atoms in $Co_{2-x}Cr_xFeGe$ series have parallel spin magnetic moments and are ferromagnetically coupled. The details of the calculated atomic spin magnetic moments is provided in Supplementary information section.

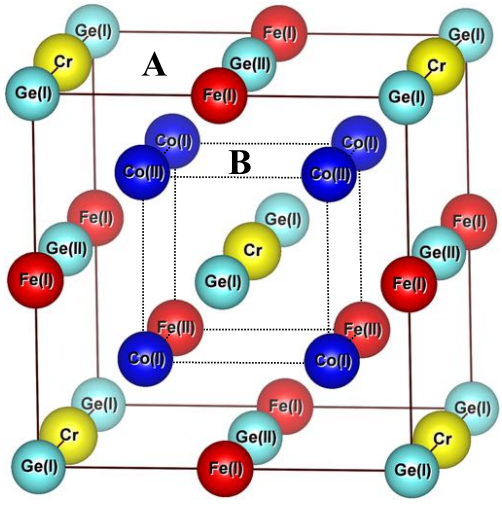

Figure 4.13: Crystal structure showing the different magnetic environments in unit cell of $x = 0.50$ assuming I configuration in Table 4.4.

If one looks at Cr DOS in Fig. 4.12(f), it has some very nice characteristics which make it ideal for using it as an impurity in Heusler alloys. First, there is a large exchange splitting between the

occupied majority-spin and unoccupied minority-spin states. This leads to large band gaps since the conduction minority-spin states are located higher in energy with respect to the Fermi level when compared to Co or Fe atoms. Second and also very important, since Cr has less electrons than Co or Fe, the width of the majority-spin d-bands is smaller in the case of Cr and the Fermi level intersects almost the DOS peak. This leads to considerable higher majority-spin d-DOS at the Fermi level in the Cr-doped CFG compounds which in real world means that these compounds should keep a higher degree of spin-polarization at the Fermi level.

4.1.5 Conclusion

In conclusion, we performed a detailed experimental and theoretical study on the structural, electronic, magnetic and mechanical properties of Cr-substituted Co_2FeGe Heusler alloys. The alloys are found to crystallize in the face-centered cubic structure for $0.25 \leq x \leq 1$. The isothermal magnetization curves showed that the saturation magnetic moment decreases with the increase of Cr content and the values at 1.8 K are found in good agreement with the Slater-Pauling rule of thumb for half-metals. High values of T_c, decreasing with increasing Cr substitution from 952 K for $x = 0.25$ to 861 K for $x = 1$ are measured, allowing for applications at room temperature and above. First-principles calculations predicted finite band gap in the minority spin channel, with half-metallic gaps 0.041 eV, 0.028 eV, and 0.027 eV for $x = 0.50$, 0.75 and 1 respectively. The small finite states at E_F in the minority spin channel of CFG are observed to decrease forming a finite band gap with the increase of Cr content. All these properties, with a confirmation from both theory and experiment, make $Co_{2-x}Cr_xFeGe$ Heusler alloy a promising material for spintronics application. However, experimental study of other properties such as current spin polarization is needed to confirm the above observations.

4.2 Experimental and theoretical study on the possible half-metallic behavior of $Co_{2-x}V_xFeGe$ Heusler alloys

4.2.1 Abstract

We present a combined theoretical and experimental study of quaternary Heusler alloys $Co_{2-x}V_xFeGe$ with $0 \leq x \leq 1$ prepared by arc melting and annealing, arguing they are promising candidates for spintronics applications. Single phase microstructures are observed for V compositions from $x = 0.25$ to $x = 0.625$. Other V concentrations studied are multi-phased. All single phase samples exhibit a face centered cubic crystal structure with a lattice constant increasing linearly with V concentration. The low-temperature saturation magnetic moments agree fairly well with our theoretical results and also obey the Slater-Pauling rule of thumb for half-metals, a prerequisite for half metallicity. All alloys are observed to have high Curie temperatures that scale linearly with the saturation magnetic moment, allowing for applications at room temperature and above. Electrical transport measurements are performed to elucidate the electronic structure of the alloys. The temperature dependence of electrical resistivity is analyzed and discussed in the framework of the two current conduction model taking into account the existence of an energy gap in the electronic spectrum around the Fermi level of the spin down sub-band. Our *ab initio* calculations with the HSE-06 exchange correlation functional also predict half-metallic character in the alloys after V substitution. High mechanical hardness values are also observed.

4.2.2 Introduction

Ternary Co_2-based Heusler compounds with stoichiometric composition Co_2YZ, (Co,Y) being two transition metals, and Z being main group element, crystallizing in the $L2_1$ structure (space group $Fm\bar{3}m$, # 225 [64]) are interesting scientifically and technologically for their potential use in spin electronic device applications [1, 20, 30, 66, 85, 89, 111]. These materials are predicted

PUBLISHED AS: R. Mahat*, D. Wines, S. KC, U. Karki, F. Ersan, J. Law, V. Franco, C. Ataca, A. Gupta & P. LeClair, *Experimental and theoretical study on the possible half-metallic behavior of $Co_{2-x}V_xFeGe$ Heusler alloys*, Manuscript submitted for publication (2022).

to exhibit highly stable half-metallic ferromagnetism (100% spin polarization at the Fermi level E_F) over wide range of temperature due to their high Curie temperature (T_c), highest among the known half-metallic ferromagnets [20, 29, 30, 32, 34]. However, experimentally observed highest spin polarizations of most of the Heusler alloys amount to 60-70% at low temperatures, with much smaller value at room temperature [112–114]. Thus, the search of Heusler alloys with robust half-metallicity is still the focus of interest. The discrepancy in spin polarization between theory and experiment is expected to be due to chemical disorder [1, 41]. In the past, substitution of a fourth element has been used to improve both ordering and spin polarization in ternary Heusler alloys [105, 115, 117–119, 131, 154]. In particular, low valence transition metal atom substitution in ternary Heusler alloys has been observed theoretically to tailor the Fermi level to fall exactly in the middle of the energy gap, giving rise to 100% spin polarization and half-metallic character [107, 121, 122].

The Co_2FeGe system is one of the promising candidates to be used as spin-injector in spintronic devices because of its high Curie temperature of 981 K [17]. Co_2FeGe is predicted theoretically to be stable crystallizing in the $L2_1$ structure, with Fermi level falling on the conduction band edge of the minority spin channel, but it is observed experimentally to be unstable in bulk form [17, 129]. In the past, quaternary element substitution has been adopted to stabilize and study the electronic and magnetic properties of the disorderd Co_2FeGe system. The quaternary element substitution can be done on any of the three (X/Y/Z) sites *i.e.*, $Co_{2-x}Y^*_xYZ$, $Co_2Y_{1-x}Y^*_xZ$ or $Co_2YZ_{1-x}Z^*_x$ where Y, Y* are low valence transition elements and Z, Z* are main group elements [41, 62, 122, 124–127, 215]. Substitution at the X/Y sites is important as X/Y the site elements play a dominant role in tailoring the half-metallicity and magnetic properties compared to Z site element [128]. Most of the previous studies on Co_2FeGe system are based on the quaternary element substitution on Y or Z sites only [105, 130, 131]. Substitution on the X site is rather less explored. We have already reported the tunable properties of Co_2FeGe after Cr and Ti substitution for Co [105, 154]. In this study, we investigate the effect of V substitution for Co on the structural, magnetic, transport, and mechanical properties, even though the end members of the series $Co_{2-x}V_xFeGe$, *i.e.*, both

Co_2FeGe, and CoFeVGe are multi-phase.

The experimental results presented in the following include a structural analysis by powder x-ray diffraction (XRD) and electron backscatter diffraction (EBSD), magnetic and electron transport characterization by a Quantum Design Physical Properties Measurement System (PPMS), and an investigation of the mechanical properties using micro-hardness tester.

4.2.3 Methods

4.2.3.1 Experimental Methods

$Co_{2-x}V_xFeGe$ $(0 \leq x \leq 1)$ bulk samples were prepared by repeated arc melting of mixture of high purity constituents (99.9 % pure, Alfa Aesar) in an argon atmosphere at a base pressure of 10^{-4} mbar. The mixture of constituent elements Co, V, Fe and Ge in a ratios $2-x:x:1:1$ was melted at least 6 times, turning the specimen over before each melting cycle, to ensure chemical homogeneity. Ti, as an oxygen absorber, was melted inside the vacuum chamber separately before melting the mixture to avoid possible oxygen contamination. The as-cast specimens were examined using an energy dispersive X-ray spectroscopy (EDS) detector equipped in a JEOL 7000 field emission scanning electron microscope (FESEM) to ensure the target composition after the arc melting. The specimens were then annealed in an evacuated quartz tube at 950°C for 7 days. The heat treatments were followed by metallography (see details in the supplementary information of our previous publications [164, 216]) which yields a metallic shiny surface for microstructure analysis using optical and electron microscopes. The composition and homogeneity of the specimens were again confirmed by using EDS before other characterizations.

The crystal structure was investigated by means of X-ray diffraction (XRD) using a Bruker D8 Discover X-ray diffractometer equipped with monochromatic Co-Kα (λ = 0.179 nm) radiation. The polished samples were rotated around the ϕ axis during the XRD measurement to minimize surface effects. In-house PYTHON code [79] including the dispersive corrections to the atomic scattering factors were used to simulate the XRD patterns to compare with the experimental XRD

patterns. XRD patterns were analyzed by Rietveld refinement using a MATCH! software based on the FullProf algorithm [80]. Further, the crystal structures determined from XRD were confirmed using electron backscatter diffraction (EBSD) phase mapping analysis in a JEOL 7000 FESEM system. The low temperature magnetic and electrical transport properties were studied in Quantum Design Physical Properties Measurement System (PPMS), while the Lakeshore VSM 7407 was used for the high temperature magnetization measurements. DC electrical resistivity measurements were carried out using van der Pauw method [179]. Al wire bonding was used to make the contacts. Vickers hardness tests were performed on all the polished specimens using Buehler model 1600-6100 micro-hardness tester to study the mechanical properties.

4.2.3.2 Computational Methods

We performed first-principles spin-polarized density functional theory (DFT) calculations using projector augmented-wave (PAW) potentials and the Perdew-Burke-Enzerhof (PBE) functional [180, 182]. Numerical calculations were carried out using the Vienna *ab initio* Simulation Package (VASP) with a plane wave basis set cutoff energy of 400 eV and an 8 x 8 x 8 k-point grid to sample the Brillouin zone within the Monkhorst-Pack scheme [181, 200, 217]. PBE was used to optimize the atomic positions and lattice constants using the conjugate gradient method, where a maximum force of 0.01 eV/Å^{-1} was allowed on each atom and an energy convergence value of 10^{-5} eV between each consecutive step was chosen. For the non-self-consistent calculations of the electronic density of states and projected density of states, a Gaussian-type Fermi-level smearing width of 0.05 eV was used. Due to computational cost, our spin-polarized calculations did not include spin-orbit interactions, which is not necessary to reveal the half-metallic properties of Heusler compounds [183]. Co $3d^8 4s^1$, Fe $3d^7 4s^1$, V $3p^6 3d^5 4s^1$, and Ge $3s^2 3p^2$ are considered as valence electrons.

It is known that standard PBE tends to underestimate the band gap and does not correctly model the electronic properties of materials with strongly correlated electrons [115, 129, 133, 187, 188]. To circumvent this, often times the DFT+U approach is used, which adds an intra-atomic Hub-

bard like term to the energy functional [189]. The U correction treats the strong on-site Coulomb interaction of localized electrons while the rest of the electrons are treated with normal DFT approximations [189]. Although this can correct electronic and magnetic properties (and has been used in similar theoretical studies of Heusler alloys [188, 218]), the U parameter is usually obtained semi-empirically by fitting to experimental data, making the results not completely ab-initio. As a fully first-principles alternative to DFT+U, we used the hybrid functional HSE-06 [192], which is formed by mixing 75% of the PBE exchange with 25% of the Fock exchange and 100% of the correlation energy from PBE and has been reported to give more accurate results [16, 193, 194]. In order to account for van der Waals (vdW) effects, the DFT-D2 method of Grimme [195] was implemented for calculations of electronic properties.

4.2.4 Results and Discussions

4.2.4.1 Experimental results

4.2.4.1.1 Microstructural and Compositional analysis

The detection limit of our XRD under typical conditions is $\sim 5\%$ of the sample volume in our experience, which means XRD is not always sufficient to identify the presence of impurity phases [105, 154, 168, 169]. For this reason, among others, we use optical and electron microscopy of polished and etched specimens to characterize microstructure, revealing grain boundaries, phase boundaries, and inclusion distributions. In this process, SEM with EDS can be used to directly quantify the compositions in different regions of the specimens.

Starting from fully stoichiometric Co_2FeGe, multi-phase microstructures were obtained for all the heat treatments performed: at 900, 950, or 1000°C, for different dwelling times of 3, 7, or 15 days, in accordance with previous reports [105, 129]. However, V substitution for Co in Co_2FeGe is observed to stabilize the system in the composition range $(0.25 \leq x \leq 0.625)$. All other higher V contents measured are observed to produce multiphase behavior, as did the lower V content sample at $x = 0.125$. Fig. 4.14 shows the optical micrographs of all single phase specimens and

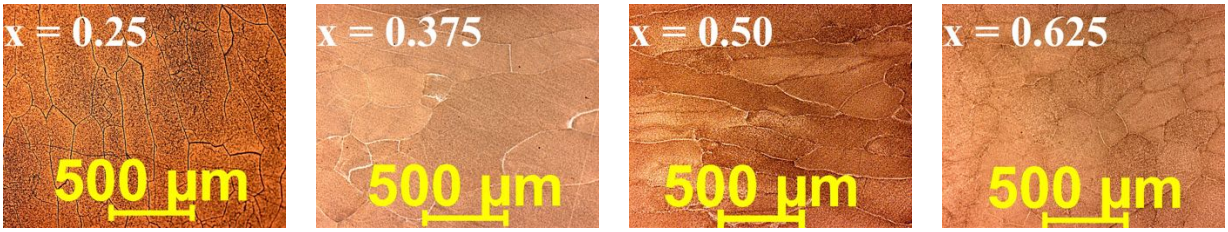

Figure 4.14: Optical micrograph of $Co_{2-x}V_xFeGe$ annealed at 950°C for 7 days followed by slow cooling. The samples were etched for 3 seconds using the Adler etchant.

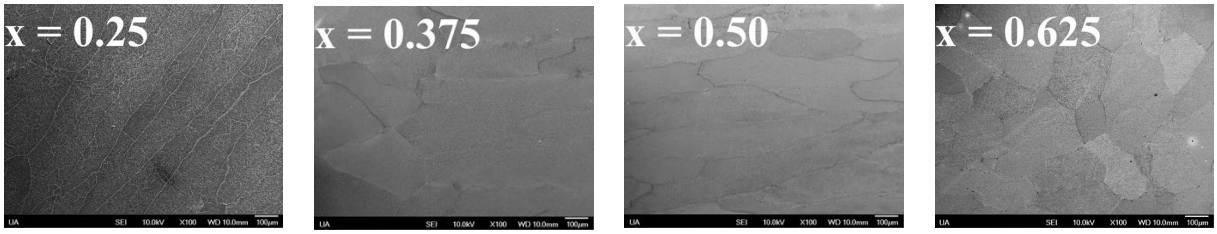

Figure 4.15: SEM micrograph of $Co_{2-x}V_xFeGe$ annealed at 950°C for 7 days followed by slow cooling showing the granular microstructure.

corresponding electron images are shown in Fig. 4.15. The composition within the grains of all the single-phase specimens was measured as the target composition within an instrumental uncertainty of $\sim 5\%$ using EDS (see in Supplementary information). As reported in previous publications, the composition in parent Co_2FeGe ($x = 0$) was measured to differ from the target composition by more than 5 % with the secondary phase mainly located in grain boundaries and only nominal secondary phase was observed to segregate in grain boundaries with the vanadium substitution $x = 0.125$ in place of Co (see in Supplementary for multiphase specimens).

4.2.4.1.2 Crystal structure and atomic order analysis

Fig. 4.16 shows the XRD patterns for $Co_{2-x}V_xFeGe$ alloys annealed at 950°C for 7 days, measured at room temperature, using a Co-K_α radiation source. Consistent with our microstructural analysis, single phase behavior can be seen only for $0.25 \leq x \leq 0.625$ while others are multi-phase (impurity peaks are represented by asterisks). Here, for all single-phase alloys, only three distinct Heusler-like reflection peaks (h, k, l all odd or even) are observed; fundamental peaks with

$h+k+l=4n$, even superlattice peaks with $h+k+l=4n+2$ and odd superlattice peaks with $h+k+l=2n+1$ that are typical for the face centered cubic (fcc) lattice. In general, the presence of (111) peak indicates the chemical ordering of atoms in octahedral positions (4a and 4b), and the presence of (200) peak indicates the order for atoms in tetrahedral positions (4c and 4d), while (220) peak is a principal reflection which is independent of the state of the order [72]. The simulated powder diffraction pattern of Co_2FeGe shown at the bottom of Fig. 4.16 shows the decisive (111) and (200) peaks for the defect-free structure. The presence of both the superlattice diffraction peaks (111) and (200) in our case indicates $L2_1$ type ordering as expected for the defect-free structure.

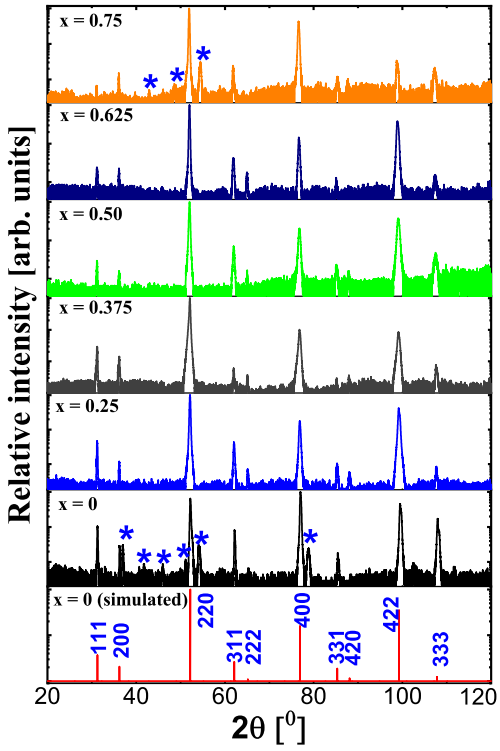

Figure 4.16: Experimental XRD patterns of $Co_{2-x}V_xFeGe$ alloy series annealed at 950°C for 7 days investigated at room temperature, here, * corresponds to the secondary phase/unknown impurity phase. The bottom one is the simulated XRD pattern for CFG ($L2_1$ structure) using CaRIne.

Fig. 4.17(a) shows the enlargement of the experimental XRD patterns between 29.5° and 37° for single phase samples to clearly show the superlattice reflections (111) and (200) with

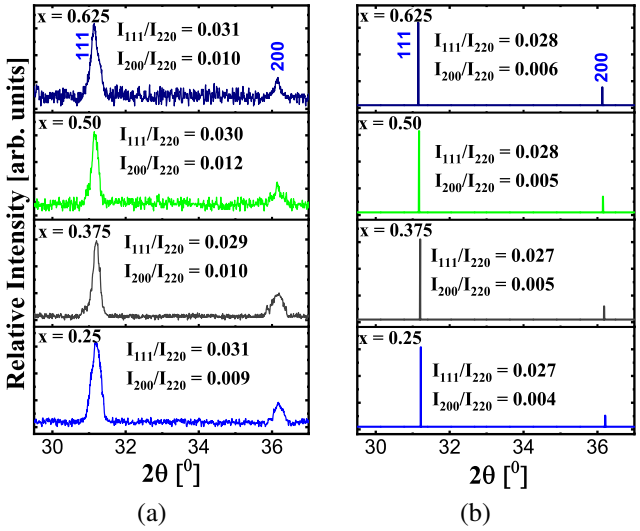

Figure 4.17: (a) Enlargement of (111) and (200) X-ray diffraction peaks of single phase samples and (b) the corresponding simulated patterns for the ideal ordered structure.

corresponding simulated patterns of ideal $L2_1$ structure for comparison in Fig. 4.17(b). The two superlattice diffraction peaks are clearly visible as expected for the defect-free ordered Heusler structure, indicating the presence of a long range ordering in these specimens. The measured and expected I_{111}/I_{220} and I_{200}/I_{220} are also labeled. These values agree with each other qualitatively.

Table 4.5: Possible site assignments for cubic $Co_{2-x}V_xFeGe$ with corresponding goodness of fit parameter for $x = 0.50$.

Type	4a (0,0,0)	4b $(\frac{1}{2},\frac{1}{2},\frac{1}{2})$	4c $(\frac{1}{4},\frac{1}{4},\frac{1}{4})$	4d $(\frac{3}{4},\frac{3}{4},\frac{3}{4})$	$\chi^2_{x=0.50}$
I	Ge	$Fe_{1-x}V_x$	$Co_{1-x/2}Fe_{x/2}$	$Co_{1-x/2}Fe_{x/2}$	0.9
II	Ge	$Fe_{1-x}V_x$	$Co_{1-x}Fe_x$	Co	1.1
III	Ge	$Co_{1-x}V_x$	Fe	Co	1.4
IV	Ge	Fe	$Co_{1-x}V_x$	Co	2.1

In an attempt to determine the possible chemical ordering in the alloys, we further performed Rietveld refinement of experimental XRD pattern for $x = 0.50$ considering four non-degenerate atomic configurations adopted in our previous study [105, 154, 155] (see in Table 4.5, Fig. 4.19(a) & (b) and supplementary information). The corresponding goodness of fit parameters for $x = 0.50$ are also listed in Table 4.5. All structures considered showed a reasonably good fit, but the best fit

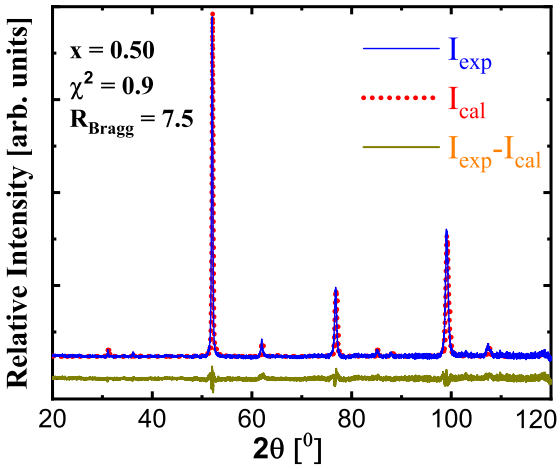

Figure 4.18: Rietveld refinement performed on $Co_{1.50}V_{0.50}FeGe$ annealed at 950°C for 7 days followed by slow cooling considering first atomic configuration given in Table 4.5.

between observed and calculated XRD intensities is observed for the first configuration (reduced $\chi^2 = 0.9$ and weighted average Bragg R-factor = 7.5) as shown in Fig. 4.18. In this configuration, Ge and (Fe+V) occupy the 4b sites on the octahedral A sublattice, while Co and Fe are on the 4c and 4d sites forming the tetrahedral B sublattice. That is: even though V substitutes for Co in the chemical formula as written, V does not actually replace Co directly. If we first consider the removal of Co, Fe atoms initially on octahedral 4b sites in the stoichiometric ideal $L2_1$ compound (at $x = 0$) migrate to the tetrahedral 4c and 4d sites replacing Co. The V atoms introduced occupy the octahedral 4b sites vacated by Fe. This is also what we observed in the $(Co_{2-x}Ti_x)FeGe$ system, where Fe replaced missing Co atoms and Ti occupied the subsequently vacant Fe positions [105]. This scheme also agrees well with electronegativity rule: since V in $Co_{2-x}V_xFeGe$ is the least electronegative (1.63 Pauli units) [201], V atoms therefore displaces Fe atoms towards vacated Co sites and will themselves fill the sites previously occupied by Fe, forming an ionic-type sublattice with most electronegative atom, Ge (2.01 Pauli units). The Co and displaced Fe atoms occupy tetrahedral sites as they have intermediate electronegativities [1].

We have also performed an EBSD inverse pole figure (IPF) color map and phase map of $Co_{1.50}V_{0.50}FeGe$ alloy to determine the degree of texturing and purity of phase considered. The IPF shown in Fig. 4.20(a) shows relatively large grains with some preferred orientation, which

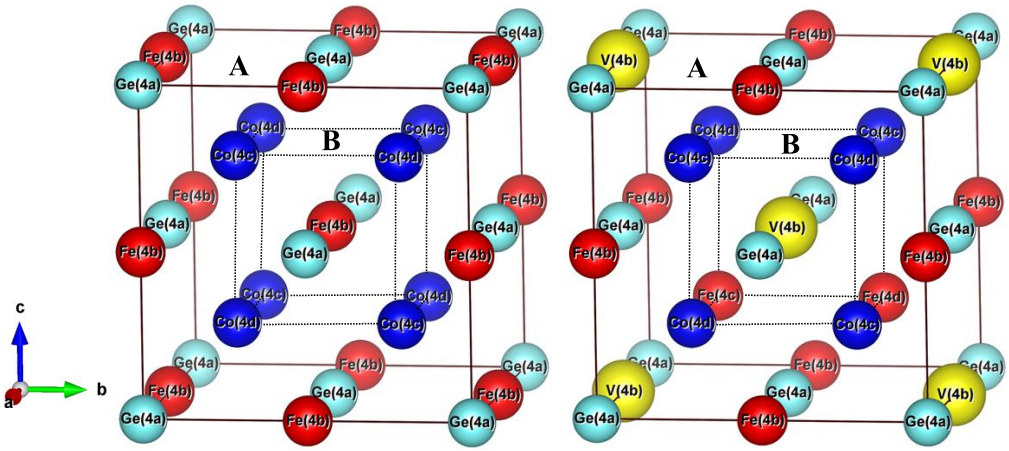

(a) (b)

Figure 4.19: Crystal structure in unit cells of a Heusler alloys (a) Co_2FeGe, and (b) $Co_{1.50}V_{0.50}FeGe$ assuming I configuration in Table 4.5.

can be considered as a possible reason for the observed XRD peak intensities to deviate from the expected values for some peaks. More than 99% of the selected microstructure is observed to match the proposed I configuration (red color in the EBSD phase map (see Fig. 4.20(b)) with some zero solution regions (black spots) mainly due to the artifact of polishing and some nominal composition deviation in grain boundaries.

Fig. 4.21 shows the variation of the lattice parameter a with the V concentration x in $Co_{2-x}V_xFeGe$. Here, Cohen's method with a Nelson-Riley extrapolation is used to extract lattice parameters [171]. It is clearly seen that the lattice parameter increases linearly with increasing V content. This behavior is expected from Vegard's law [205] due to the larger atomic radius of substituted V (171 pm) compared with Co (152 pm) [153].

4.2.4.1.3 Magnetic Characterization

Half-metallic Heusler alloys are expected to follow a Slater-Pauling-like behavior for the magnetization in a fully ordered state [206]. The Slater-Pauling (SP) rule relates the saturation magnetization with the valence electron concentration. Here, we expect the total magnetization to be [1, 7]

$$M_t = (2-x)Z_{Co} + xZ_V + Z_{Fe} + Z_{Ge} - 24. \tag{4.4}$$

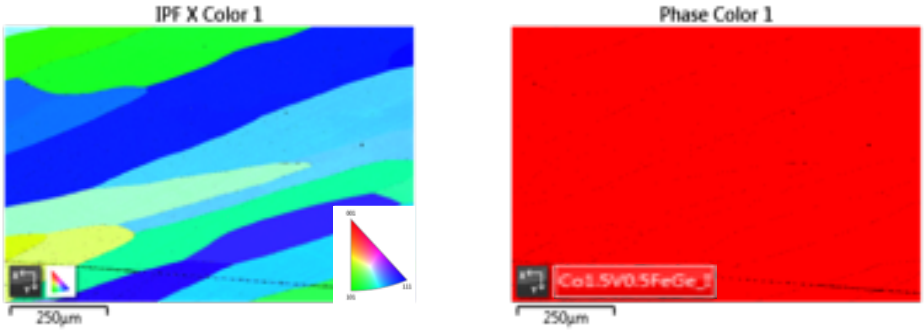

(a) (b)

Figure 4.20: (a) Inverse pole figure (IPF) color map of $Co_{1.50}V_{0.50}FeGe$ taken using EBSD in SEM showing grain orientation with preferred texture. (b) The corresponding EBSD phase map of the same area showing single-phase behavior.

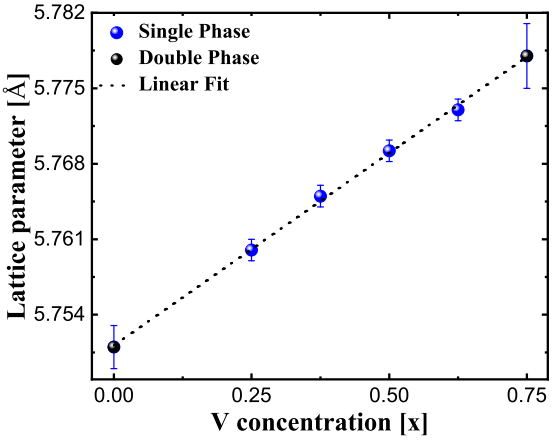

Figure 4.21: Variation of lattice parameter with V concentration showing linear behavior. The black solid end data points represent lattice parameter for multiphase specimens.

where, M_t is the total spin magnetic moment per f.u. in μ_B and Z_i is the number of valence electrons of each individual atom. Further, in $Co_{2-x}V_xFeGe$ system, the total number of valence electrons change from 30 in CFG to 26 in CFVG. Therefore, the SP behavior predicts that the saturation magnetic moment should change with the partial substitution of V for Co, following the equation

$$M(x) = 6 - 4x. \tag{4.5}$$

Fig. 4.22(a) shows the variation of magnetization with applied magnetic field at temperature

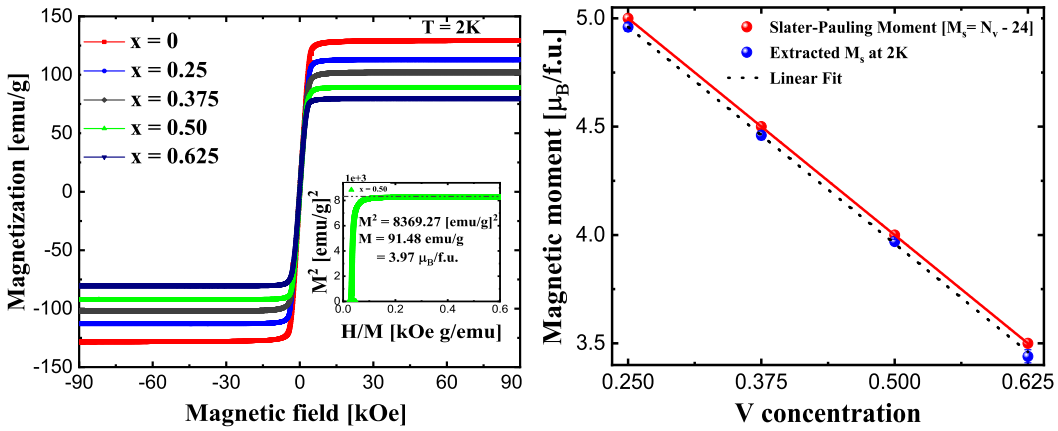

(a) (b)

Figure 4.22: (a) The field-dependent magnetization at 2 K of $Co_{2-x}V_xFeGe$ ($x = 0$, 0.25, 0.375, 0.50, and 0.625) (b) The saturation magnetic moment versus V concentration both experimental and expected from Slater Pauling rule.

2 K. The magnetization curves are typical for the soft ferromagnets. The corresponding magnetic moments at saturation are given in Table 4.6. The saturation magnetic moments (M_s) were extracted from an Arrot plot [207], *i.e.*, by extrapolating the linear part to H/M=0 of M^2 versus H/M curve (see inset to Fig. 4.22(a)). The extracted saturation magnetic moments are observed to follow the SP rule of thumb for half-metals and decrease linearly with the increase of V content (see Fig. 4.22(b)). The decrease of the total saturation magnetic moment with the increase in V content can only be attributed to the decrease in number valence electrons in the system. The slightly smaller values can be attributed to the weighing and measurement errors, sample inhomogeneities, partial surface oxidation, and to the measurement temperature of 2 K. All experimentally extracted saturation magnetic moments are also in good agreement with those obtained from first-principle calculations (see Table 4.6), as described in the forthcoming section.

Fig. 4.23(a) displays the temperature dependent specific magnetization of the investigated samples in a constant magnetic field of 100 Oe. The Curie temperatures T_c were extracted from the inflection point *i.e.*, by taking the minima of the first-order derivative of M(T) curves (see inset in Fig. 4.23(a)). Evidently, all alloys exhibit high T_c, facilitating technological applications at room temperature and above. The T_c is observed to decrease with increasing V content due to the

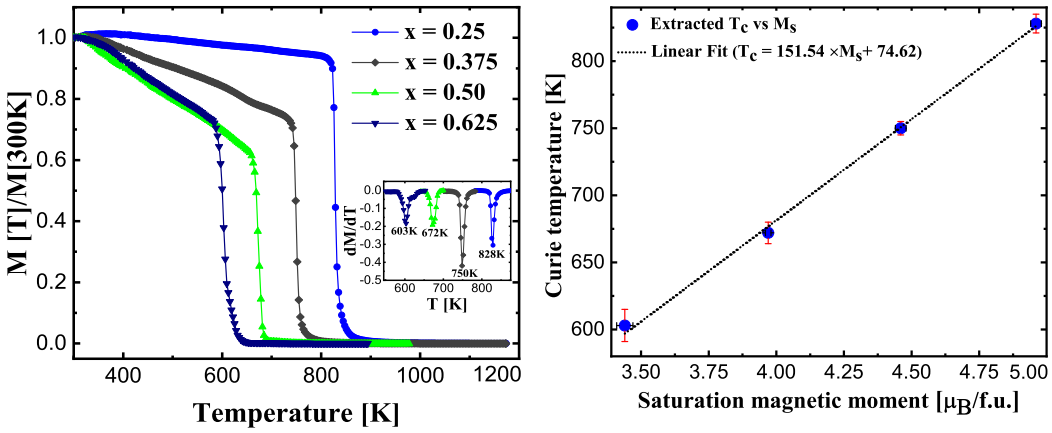

(a) (b)

Figure 4.23: (a) Temperature dependence of magnetization at 100 Oe. The inset shows the first-order derivative of magnetization as a function of temperature, the minima of which is used to extract T_c. (b) Variation of Curie temperature as a function of saturation magnetic moment.

Table 4.6: Experimental and theoretical lattice parameters and saturation magnetic moments at T = 2 K along with the Slater-Pauling (S-P) values in $(\mu_B/f.u.)$, and the measured Curie temperature (T_c) of $Co_{2-x}V_xFeGe$ alloy series. The numbers in parentheses are the uncertainty in the last digit, *e.g.*, $5.751(2) = 5.751 \pm 0.002$.

x	Expt. a (Å)	Theor. a (Å)	Expt. M_s	Theor. M_s	S-P M_s M_s	T_c (K)
0†	5.751(2)	5.735	5.71(3)	6.07	6.00	981[129]
0.25	5.760(1)	5.741	4.96(2)	5.07	5.00	828(7)
0.375	5.765(1)	5.742	4.46(2)	4.56	4.50	750(5)
0.50	5.769(1)	5.742	3.97(1)	4.04	4.00	672(8)
0.625	5.773(1)	5.743	3.44(3)	3.54	3.50	603(12)

† Multiphase specimen

weakening of the exchange interaction caused by small magnetic moment of substituted V compared to Co. Further, T_c is observed to change linearly with the saturation magnetic moment in all single phase alloys, as reported for Co_2-based Heuslers [124] (see Fig. 4.23(b)). By extrapolating a linear dependence, T_c is estimated to be 984 K for parent CFG ($x = 0$), in good agreement with the reported value 981 K [17].

The experimentally determined as well as calculated lattice parameters, saturation magnetic moments at 2 K and corresponding Curie temperature of all single phase samples in $Co_{2-x}V_xFeGe$ alloy series are summarized in Table 4.6.

4.2.4.1.4 Electrical resistivity

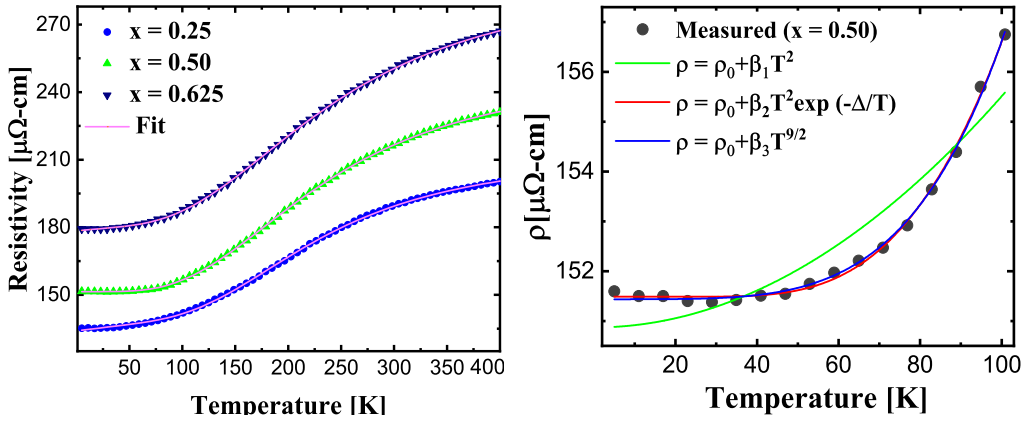

(a) (b)

Figure 4.24: (a) Temperature dependence of electrical resistivity in $Co_{2-x}V_xFeGe$ in zero magnetic field for $x = 0.25$, $x = 0.50$, and $x = 0.625$, and (b) Low temperature (0-100 K) resistivity data fitting for $x = 0.50$.

Temperature dependence of electrical resistivity ρ of the $Co_{2-x}V_xFeGe$ (x = 0.25, 0.50, and 0.625) alloys was measured using the van der Pauw method [179] in a PPMS Dynacool for samples with approximate dimensions 4 x 4 x 1 mm^3. Fig. 4.24(a) shows the variation of resistivity ρ with temperature T for zero magnetic filed measured during cooling process in the temperature range from 5 K to 400 K. The alloys show metallic behavior in the resistivity which decreases with decreasing temperature and remains independent below 50 K. Also, the resistivity is observed to saturate at higher temperatures, indicating weak variation of resistivity resulting from the parallel contribution of the intrinsic resistivity and some limiting resistivity known as shunting with temperature [219, 220]. The total resistivity of magnetic alloys follows Matthiessen's rule [99];

$$\rho(T) = \rho_0 + \rho_{e-ph}(T) + \rho_{e-m}(T) = \rho_0 + \alpha T + \beta T^2 \tag{4.6}$$

where ρ_0 is the temperature independent residual resistivity due to defects in the crystal lattice, ρ_{e-ph} and ρ_{e-m} are temperature dependent terms due to the scattering by phonons and magnons respectively. As reported in the literature [174, 219, 220], a parallel shunting resistivity is also

introduced to the total resistivity to include the contribution from grain boundaries as;

$$1/\rho_{tot}(T) = 1/\rho_i(T) + 1/\rho_{shunt} \tag{4.7}$$

However, the attempt to fit $\rho(T)$ of $Co_{2-x}V_xFeGe$ ($x = 0.25$, 0.50, and 0.625) alloys considering the conventional electron-magnon scattering of ferromagnets using equations 4.6, and 4.7 is observed to be insufficient (see Fig. 4.24(b) for $x = 0.50$ and supplementary information). Thus, we have considered the predicted half-metallic character of the compounds to better understand the transport property. A minimum excitation energy $k_B\Delta$ of majority charge carriers is required to occupy empty minority states involving a spin-flip scattering in half-metallic ferromagnets, due to the presence of a energy gap at the Fermi level in minority spin channel. As a consequence, the usual quadratic magnonic term (ρ_{e-m}) is expected to suppress exponentially at low temperatures [101, 102]. Thus, the usual electron-magnon scattering term can be modied by adding a Boltzmann factor as [102–105],

$$\rho_{e-m}(T) = \beta T^2 e^{-\Delta/T} \tag{4.8}$$

where Δ is a measure of the energy gap between the Fermi level and the nearest band edge of unoccupied minority spin channel. The fitting implies the exponential suppression of T^2 term in all samples. The fitting also yields the energy gap of $k_B\Delta$ = 25.97 meV, 17.78 meV, and 17.17 meV respectively for $x = 0.25$, $x = 0.50$, and $x = 0.625$. The observed exponential suppression of one magnon scattering implies the possibility of HMF behavior in the alloys. Previously, the half-metallic behavior of Heusler alloys has been studied by observing electrical resistivity behavior at low temperature [107–109]. The two-magnon scattering ($T^{9/2}$ dependence) is considered to be the signature of half-metallic ferromagnetism [109, 221]. The observed resistivity data at low temperature is found to fit well for $x = 0.50$ only (see Fig. 4.24(b)) with the relation [107–109]

$$\rho_{e-m}(T) = \rho_0 + \beta T^{9/2} \tag{4.9}$$

This good fitting ($x = 0.50$) with $T^{9/2}$ term over T^2 term suggests a strong contribution from two-magnon scattering process expected in half metallic systems. However, complementary measurements of magnetoresistance, anisotropic magnetoresistance, and Hall resistivity are required to better characterize the transport properties.

Table 4.7: Fitted parameters of resistivity data of $Co_{2-x}V_xFeGe$ ($x = 0.25$, 0.50, and 0.625). The numbers in parentheses are the uncertainty in the last digit, *e.g.*, $151.43(30) = 151.43 \pm 0.30$.

Extracted parameters	$x = 0.25$	$x = 0.50$	$x = 0.625$
ρ_0($\mu\Omega$-cm)	135.92(20)	151.43(30)	179.19(15)
α ($\mu\Omega$-cm/K) $\times 10^{-1}$	4.29(5)	0.17(3)	2.76(3)
β ($\mu\Omega$-cm/K^2) $\times 10^{-2}$	3.53(1)	2.55(1)	2.30(5)
ρ_{shunt}($\mu\Omega$-cm)	213.97(10)	252.08(25)	292.52(20)
Δ (K)	301(14)	206(6)	199(8)
Reduced $\chi^2 \times 10^{-14}$	1.37	4.95	8.98

4.2.4.1.5 Vickers micro hardness

We have also performed Vickers hardness testing, which is an important and widely used test for quickly understanding the mechanical properties of materials. Fig. 4.25 shows the variation of Vickers micro hardness of our alloy series (all annealed at 950°C for 7 days) with V concentration and corresponding values are given in Table 4.8. Hardness values reported are the averages of data taken from at least 12 different regions of each specimen with 0.2 kg load and 10 s loading time. The Vickers hardness is calculated using the equation

$$HV = 1.8544F/D^2[\mathrm{kg/mm^2}] \tag{4.10}$$

where D is the diagonal length of the impression of the diamond probe. Relatively high hardness values are measured, approaching 9 GPa for $x = 0.625$, comparable to the values reported for Heuslers in the literature [105, 154–156, 158, 164, 209, 210, 216]. The hardness is observed to increase with the increase of V concentration and strongly depends on the microstructure and the phases present in the alloys [211].

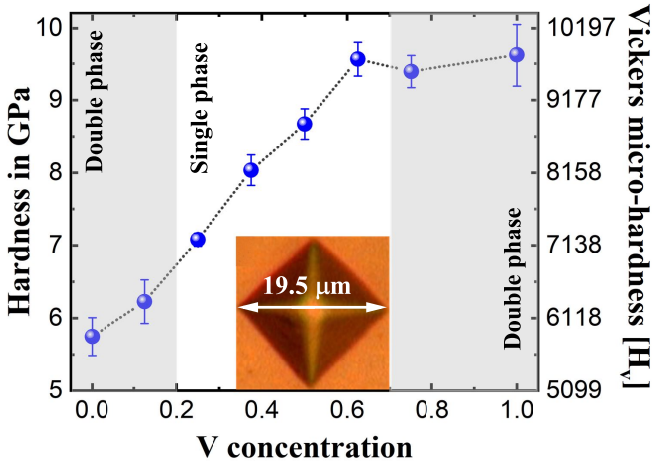

Figure 4.25: Vickers hardness versus V concentration in $Co_{2-x}V_xFeGe$, all annealed at 950°C for 7 days, with imprint of the indenter with radial cracks for $x = 0.625$ [bottom of single phase section]. The data points in shaded regions represent the multi-phase compositions.

Table 4.8: Vickers micro-hardness of the $Co_{2-x}V_xFeGe$ alloy series.

x	Vickers Hardness (GPa)
0	5.75 ± 0.26
0.125	6.23 ± 0.30
0.25	7.08 ± 0.09
0.375	8.04 ± 0.21
0.50	8.67 ± 0.21
0.625	9.56 ± 0.23
0.75	9.39 ± 0.22
1	9.62 ± 0.43

4.2.4.2 Theoretical Results

To investigate the electronic and magnetic properties of the $Co_{2-x}V_xFeGe$ alloy series and compare to experiment, we created alloys using the Monte Carlo Special Quasirandom Structure (MCSQS) [?] method at $x = 0.25$, 0.375, 0.50, and 0.625. It is important to note that this methodology can handle double-site substitutions of the disordered system, making it ideal for predicting the atomic structure of each concentration. After considering double-site substitutions and nearest neighbor interactions, and constraining the supercell to be cubic, we were able to construct MCSQS structures that fit our criteria while matching the maximum amount of correlation functions. Our MCSQS structures are in close agreement with the experimentally predicted configuration of

Fig. 4.19(b) and structure I in Table 4.5 and are composed of a 16 atoms supercell for x = 0.25, 0.50 and 128 atoms for x = 0.375, and 0.625.

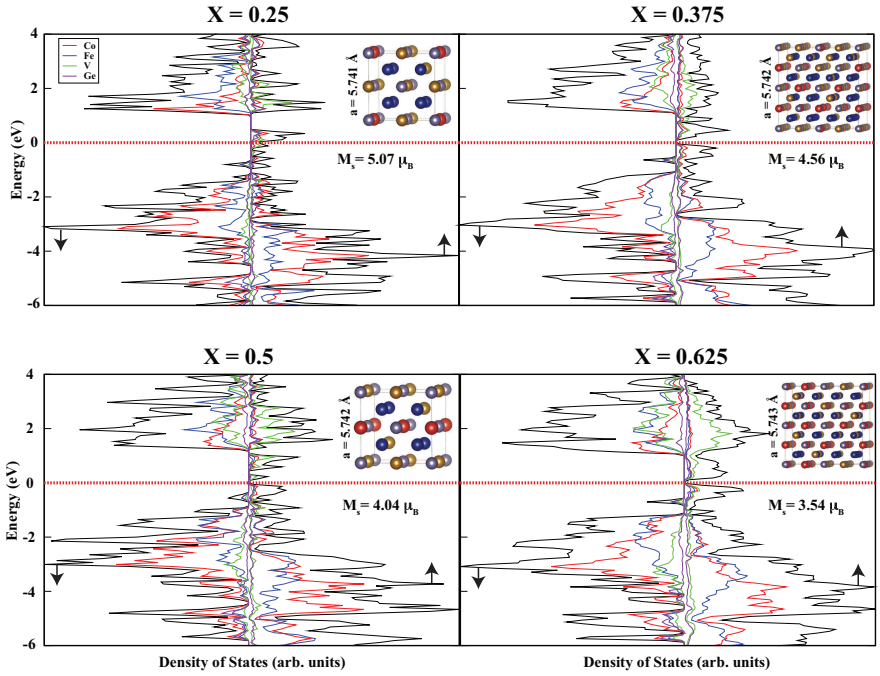

Figure 4.26: The DOS and PDOS of the MCSQS structure for $x = 0.25$, 0.375, 0.50 and 0.625 for the $Co_{2-x}V_xFeGe$ series. The black arrows depict the spin up and spin down contributions and the red dotted line represents the Fermi level. The figure insets include the optimized structures (blue = Co, bronze = Fe, red = V, purple = Ge), magnetic moment values and ground state lattice constants. All results depicted involving electronic and magnetic properties are carried out using the HSE06 functional, while the geometric structure is optimized with PBE.

After obtaining viable MCSQS candidate structures, we optimized lattice constants and atomic positions with PBE. For comparison, we also optimized the structure with PBE-D2 (provided in Supplementary Information), but find that the PBE optimized values are in better agreement with experiment. The PBE calculated lattice parameters of each structure are given in the insets of Fig. 4.26 and Table 4.6 and are in good agreement with measured values (within $\sim$ 0.5%). As expected, the increase of V concentration results in a slight increase in lattice parameter. Due to the fact that experiments were done at a finite temperature, this can cause the lattice parameters of the crystal structure to change from the structures at 0 K due to the thermal expansion coefficient of the material (one might need a longer annealing time to reach the true ground state). This creates

a margin of error such that all the structures generated with MCSQS lie in the range of thermal fluctuation at a given concentration. In addition, the interaction of V with the Co_2FeGe system may be difficult to model with PBE due to the strongly localized $3d$ electrons in the material. This could result in a value of lattice constant that is more off from the experimental value. If these structures were optimized with the HSE06 functional, we could achieve a lattice parameter in closer agreement with experiment, but this is beyond the available computational capabilities.

We employed the HSE06 functional, which has been reported to correct the electronic and magnetic properties for complex materials. To understand the bonding mechanisms of the $Co_{2-x}V_xFeGe$ series, we performed Bader charge transfer analysis. Similar to predictions based on experimental observations outlined in the previous section, we observe that each V atom donates $1.4-1.5e^-$ to other atoms in the crystal for each alloy (due to the electronegativity difference). We observe that the HSE06 magnetic moment values are in excellent agreement with the experimental values and the Slater-Pauling moments (see insets of Fig. 4.26 and Table 4.6). We also observe that as V concentration increases, the magnetic moment decreases, which is in accordance with Hund's rule.

Because the theoretical/measured values for magnetic moment are close to the Slater-Pauling moment, we expect to see half metallic properties for these alloys. This is confirmed from our HSE06 corrected density of states (DOS) depicted in Fig. 4.26 where we see a gap in the spin-down channel for all structures. It is important to note that when the DOS is calculated with solely PBE (as opposed to the HSE06 corrected DOS), we do not observe this gap in the spin-down channel (see Supplementary Information). There is significant contribution in the DOS from Co, Fe and V around the Fermi level in the spin-down channel for all alloys in the series. The gap in the spin-down channel for Co_2FeGe is 2.03 eV, which is significantly higher than previous computational results [188]. This is expected because PBE and PBE+U are expected to underestimate the gap, while HSE06 has been shown to yield gap values in closer agreement with experiment and higher order Green's function methods (GW approximation). As V is introduced into the structure, the spin-down gap is effectively lowered. For $x = 0.25$ we calculate a gap of 1.93 eV, and as V concentration increases we calculate gaps of 1.82 eV, 1.79 eV, and 1.75 eV for $x = 0.375$, $x = 0.50$,

and $x = 0.625$ respectively. We also observe a systematic lowering of the Fermi level as we introduce V into the structure. From these results we can say that V substitution can effectively tune the band gap in the spin-down channel of this alloy series, opening up the possibility to engineer these materials for applications in spintronics and magnetic devices. These results also demonstrate that the use of the fully first-principles HSE06 functional can yield electronic and magnetic properties in closer agreement to experiment than PBE for Heusler systems without any semi-empirical correction (such as DFT+U). For comparison and benchmarking purposes, we provide the PBE calculated DOS and PDOS of the alloy series in addition to the HSE06 calculated band structures (see Supplementary Information). We also provide the PBE and HSE06 calculated data for the Co_2FeGe structure ($x = 0$).

4.2.5 Conclusion

In conclusion, we have synthesized $Co_{2-x}V_xFeGe$ Heusler alloys using arc melting and performed a detailed experimental and theoretical study on the structural, magnetic, transport, electronic and mechanical properties. X-ray diffraction revealed the $L2_1$ structure type for all single phase samples of the series. The experimental saturation magnetic moment values are in good agreement with the theory as well as Slater-Pauling rule. These alloys possess high values of Curie temperature. The resistivity measurements indirectly support the half-metallic behavior. The atomic and magnetic disorders can be considered as the main reasons for high values of the electrical resistivity of the alloys studied in this work. The ab intio calculations based on the hybrid exchange-correlation functional (HSE-06) also predict the half-metallic ferromagnetic state with high spin polarization in all these alloys. Thus, nearly half-metallic character with high T_c makes these mechanically hard alloys promising for spintronic applications at room temperature and above.

4.3 Structural, electronic, magnetic, transport and mechanical properties of the half-metal-type quaternary Heusler alloy $Co_2Fe_{1-x}V_xGe$

4.3.1 Abstract

We report on the bulk properties of the Heusler alloy system $Co_2Fe_{1-x}V_xGe$ with $0 \leq x \leq 1$ in steps of 0.125. We find single-phase alloys only for $x = 0.25$ and $x = 0.375$, both of which exhibit an $L2_1$ crystal structure. The alloys are found to be soft ferromagnets with high Curie temperatures ($\sim 800\,K$). Magnetization measurement shows the saturation magnetization to be 5.21 $\mu_B/f.u.$ and 4.78 $\mu_B/f.u.$ for $Co_2Fe_{0.75}V_{0.25}Ge$ and $Co_2Fe_{0.625}V_{0.375}Ge$ respectively, in good agreement with the values expected from a Slater-Pauling rule for half metals. In zero applied magnetic field, the resistivity versus temperature of these alloys does not display the usual T^2 dependence at low temperatures indicative of electron-magnon scattering, another indirect suggestion of half metallicity. Our *ab initio* calculations also predict half-metallic character in the alloys after V substitution. The large exchange splitting between the occupied majority- and unoccupied minority-spin states leads to the Fermi level almost intersecting a peak in the V majority density of states. This leads to a markedly higher spin polarization upon V doping, making V an ideal dopant for achieving half-metallic behavior in Co_2FeGe. Relatively high mechanical hardness values are also observed.

4.3.2 Introduction

Half-metallic ferromagnets are ideal candidates for spintronic applications because of their high spin polarization (almost 100%) of charge carriers at the Fermi level [29, 128]. A high Curie temperature is an important prerequisite from a practical standpoint [7, 85, 124]. Co_2Fe- based Heusler alloys ($L2_1$ structure, space group $Fm\bar{3}m$, # 225 [64, 65]) have recently attracted great interest because most of these alloys are expected to have both of these properties [20, 32, 69, 146, 222]. However, the experimental values of spin polarization for most ternary Heusler alloys

PUBLISHED AS: R. Mahat*, S. KC, U. Karki, J. Law, V. Franco, I. Galanakis, A. Gupta & P. LeClair, *Structural, electronic, magnetic, transport and mechanical properties of the half-metal-type quaternary Heusler alloy $Co_2Fe_{1-x}V_xGe$*, Journal of Magnetism and Magnetic Materials, **539**,168352(2021).

are substantially smaller than those predicted theoretically, due to anti-site disorder in their crystal lattices among other things [1, 62, 223]. Anti-site disorder destroys the high spin polarization, and as such precise control of atomic structure is necessary. One of the approaches to control structural disorder is to substitute a fourth element to the ternary Heusler alloys [41, 62, 105, 123–127].

The Co_2FeGe system is one of the candidates with a high Curie temperature which is predicted theoretically to be stable in the $L2_1$ structure, with the Fermi level falling on the edge of the minority conduction band leading to high spin polarization. However, it is observed experimentally to show multi-phase behavior in bulk form [17, 129]. Kumar *et al.* have reported high T_c 980 K and large magnetic moment 5.6 $\mu_B/f.u.$ for disordered Co_2FeGe. A reduction in the total number of valence electrons by partial replacement of the element Fe by low valence transition elements is found to be an effective way to stabilize the $L2_1$ phase, and achieve a virtual shift of E_F within the half-metallic band gap in Co_2FeGe [121]. The decrease in the total number of valence electrons to tune the position of E_F in the band gap can be performed by substituting a fourth element at Y/Z site *i.e.*, $Co_2Y_{1-x}Y^*_xZ$ or $Co_2YZ_{1-x}Z^*_x$ where Y, Y* are low valence transition elements and Z, Z* are main group elements [41, 62, 123–127]. Özdoğan and collaborators[224] have shown in quinary half-metallic heusler alloys Co_2 $[Cr_{1-x}Mn_x][Al_{1-y}Si_y]$ that the properties scale in the same way with the number of valence electrons irrespective of whether the change in the valence charge comes from the transition metal or the metalloids atoms. Substitution at the Y site is perhaps more convincing, as the Y site element plays a main role in tailoring the half-metallicity and magnetic properties compared to the Z site [128]. Varaprasad *et al.* [120] were able to obtain spin polarization as high as 0.69 in Co_2FeGe by substituting Ga for Ge, *i.e.*, $Co_2Fe(Ga_{1-x}Ge_x)$. Venkateswarlu *et al.* [130] were able to obtain a stable $L2_1$ phase in $Co_2Ti_{1-x}Fe_xGe$ substitutional series in bulk form with some anti-site disorder.

All these approaches inspired us to synthesize Co_2FeGe, a potential candidate for spintronic applications, and investigating the effect of V substitution for Fe on the structural, electronic, magnetic, transport, and mechanical properties, even though both end members of the series $Co_2Fe_{1-x}V_xGe$, *viz.* Co_2FeGe and Co_2VGe, are not stable.

4.3.3 Methods

4.3.3.1 Experimental Methods

The polycrystalline bulk samples $Co_2Fe_{1-x}V_xGe$ with x varying in steps of 0.125 from $x = 0$ to $x = 1$, were prepared by arc melting the appropriate quantities of the constituents in an argon atmosphere at 10^{-4} mbar (see details in Supplementary Information). The ingots were flipped and melted at least 6 times for homogeneity. To further increase the homogeneity, the ingots were then annealed in an evacuated quartz tube for 9 days at different temperatures 900, 950 and 1000°C, and at the end of each annealing cycle, the samples were cooled slowly in the furnace or quenched in ice/water mixture to get optimum crystallization to promote the formation of $L2_1$ structure. To make the comparison uniform, only the samples annealed under similar heat treatments (*i.e.*, 1000°C for 9 days quenched in ice/water mixture) are reported in main manuscript. Metallography techniques were utilized to investigate the microstructure of alloys under study. The details on Metallography techniques are described in the supplementary information of our previous publications [163, 164].

The crystal-structural studies were carried at room temperature by means of X-ray diffraction (XRD) using a Bruker D8 Discover X-ray diffractometer equipped with monochromatic Co-Kα (λ = 0.179 nm) radiation. To reduce the surface effects, the polished samples were rotated around the ϕ axis during the XRD measurement. The obtained XRD patterns were analyzed using least square fitting program in CRYSTAL IMPACT MATCH! software based on the FULLPROF algorithm [80]. The low temperature magnetic and electrical transport measurements were performed using Quantum Design Physical Properties Measurement System (PPMS), while the high temperature magnetization was measured using the Lakeshore VSM 7407. Temperature dependent of dc electrical resistivity measurements were performed using van der Pauw method [179]. Al wire bonding was used to make the contacts. Vicker's hardness values were measured using a Buehler model 1600-6100 micro-hardness tester.

4.3.3.2 Computational Methods

The present paper additionally reports density-functional theory (DFT) calculations employing the projector augmented wave (PAW) pseudopotentials by Blöchl [180], implemented by Kresse and Furthmüller in the Vienna *ab initio* simulation package (VASP) [181]. We have adopted the generalized-gradient approximation (GGA) in the scheme of Perdew-Bueke-Ernzerhof (PBE) for the electronic exchange-correlation functional [182]. We have used a 16-atom supercell, *i.e.*, 4 formula units of the underlying $L2_1$ structure. A $2 \times 2 \times 2$ supercell involving 128 atoms/cell with 64 Co, 20 Fe, 12 V, and 32 Ge atoms is used specifically to study the $x = 0.375$ alloy. The integration over the irreducible Brillouin-zone (IBZ) of cubic systems was done with the automatic mesh generation scheme within VASP with the mesh parameter (the number of k points per Å^{-1} along each reciprocal lattice vector) set to 64. The integration employed the linear tetrahedron method with Blöchl corrections. Total energies were converged up to 10^{-7}eV/cell with a plane-wave cutoff of 520 eV. Full relaxation of cell (initially cubic) volume, shape and atomic positions were performed until the forces on each atom become less than 0.01 meV/cell using the conjugate-gradient method. Our calculations did not include the spin-orbit interaction.

Kandpal and collaborators in 2006 have argued employing *ab-initio* electronic structure calculations that in the case of Heusler compounds with 30 valence electrons per formula unit it is essential to account for the on-site electronic correlations [225]. They have used as prototypes for their study Co_2MnSi and Co_2FeSi, which have 29 and 30 valence electrons per formula unit and employed the LDA+U method to account for the on site electronic correlations. The so called Hubbard U is described by Anisimov *et al.* to add an orbital-dependent electron-electron correlation, which is absent in the plain LDA or GGA schemes [226]. Kandpal *et al.* have shown that the inclusion of U alters considerably the energy position of the minority-spin bands in the case of the Co_2FeSi compounds making it a real half-metal while its effect on Co_2MnSi was much more mild [225]. Thus we expect on-site electronic correlations to play an important role also in the case of Co_2FeGe compound which has also 30 valence electrons per formula unit as suggested also by other authors [115, 129, 187, 212]. The total energy is not variational with respect to the U term

and thus cannot be calculated simultaneously with the minimization of the total energy. Experimental determination of the U term is very difficult and data are scarce. Even the computational determination of the U values is a tedious task and in 2013 Sasioglu and collaborators employed the constrained random-phase approximation (CRPA) scheme to calculate the U values for several half-metals [190]. In our study, we have used the semi-empirical values mentioned in Ref. [191], where Kandpal *et al.* have employed the LDA+U scheme to study the electronic structure of several half-metallic Heusler compounds. We have included in our study the U values for the d-orbitals of the three transition metal atoms: Co, Fe and V and the considered values were 1.92 eV, 1.80 eV, and 1.34 eV for Co, Fe, and V respectively. Finally, we should note that actually the inclusion of U artificially pushes apart the bands below and above the Fermi level and only comparison to experimental data guarantees that the used U values in the calculations are adequate for a particular material.

4.3.4 Results and Discussions

4.3.4.1 Experimental Results and Discussions

Starting from the full stoichiometric Co_2FeGe, substitution was made with x in steps of 0.125. Out of all, only the alloy with $x = 0.25$ in $Co_2Fe_{1-x}V_xGe$ series is observed to be stable phase in slow cooling method, while $x = 0.375$ in addition to $x = 0.25$ is found to be stable using the rapid ice/water mixture quenching method. Multi-phase microstructures were obtained for all other alloys in the series (see details in Supplementary Information). Fig. 4.27 shows the optical microscopy of ice/water mixture quenched single phase alloys from the series $Co_2Fe_{1-x}V_xGe$. The composition of all the stable single phase specimens in the series are confirmed to be close to the target composition, within $\sim 5\%$ instrumental uncertainty range using EDS. The nominal composition of all including multiphase samples is presented Supplementary Information. SEM images displaying the microstructure for single phase specimens are shown in Fig. 4.28.

Structural characterization has been performed with X-ray diffraction using a Co-K_α radiation

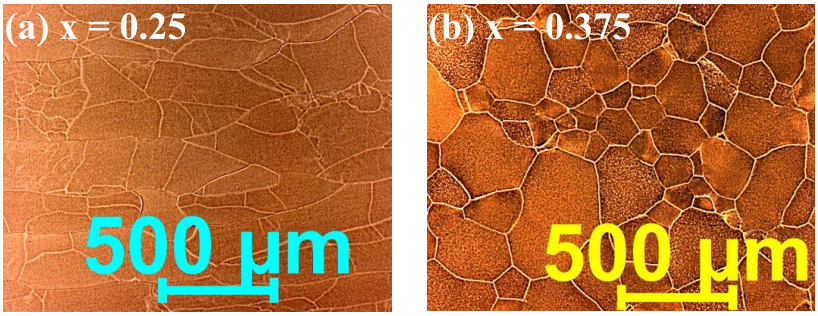

Figure 4.27: Optical micrograph of (a) $Co_2Fe_{0.75}V_{0.25}Ge$, and (b) $Co_2Fe_{0.625}V_{0.375}Ge$ heat treated at 1000°C for 9 days followed by ice/water mixture quenching. The samples were etched for 5 seconds using the Adler etchant.

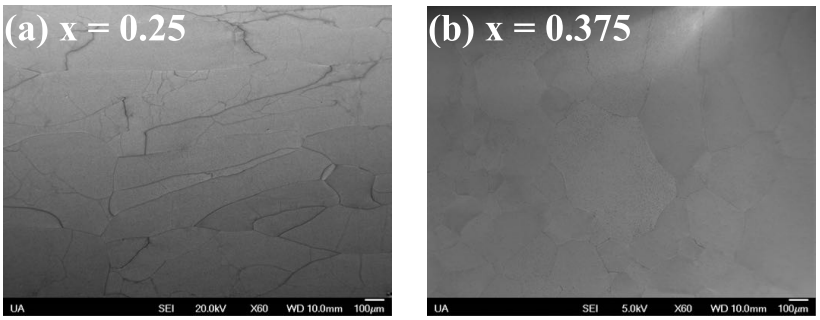

Figure 4.28: SEM micrograph of (a) $Co_2Fe_{0.75}V_{0.25}Ge$, and (b) $Co_2Fe_{0.625}V_{0.375}Ge$ heat treated at 1000°C for 9 days followed by ice/water mixture quenching showing the granular microstructure.

source at room temperature as the standard method. Simple structural information of a single cubic phase can be gained by indexing all XRD peaks as shown in Fig. 4.29. Comparatively small (5% of the (220) peak) (111) and (200) superstructure peaks are observed for the face centered cubic (*fcc*) structure. The simulated powder diffraction pattern of Co_2FeGe (Fig. 4.29, bottom pattern) shows the (111) and (200) superstructure peaks for the defect free structure. The random occupation of all lattice sites 4a(0,0,0), 4b($\frac{1}{2},\frac{1}{2},\frac{1}{2}$), and 8c ($\frac{1}{4},\frac{1}{4},\frac{1}{4}$) results in a A2-type disordered structure with vanishing superstructure peaks while random occupation of 4a and 4b sites by V, Fe, and Ge gives a B2 structure with only the (200) superstructure peak and a vanishing (111) peak. If one of the Co sites atoms is replaced by Fe or V, and another by Ge, the disordered structure is called B32a structure [1, 73]. This disordered structure results in a (111) superstructure peak with much higher intensity than the (200) peak. All these types of disorder would destroy the half-metallicity of the

material by closing the band gap at Fermi level in the minority spin channel of density of states (DOS) [62]. In such cases, the magnetization values may still follow a Slater-Pauling rule. Our experimental data for single phase samples shows both the (111) and (200) peaks with nearly equal intensity for $x = 0.25$ as expected for the defect free structure, but the (111) peak is clearly more intense than (200) peak for $x = 0.375$, as shown in Fig. 4.29.

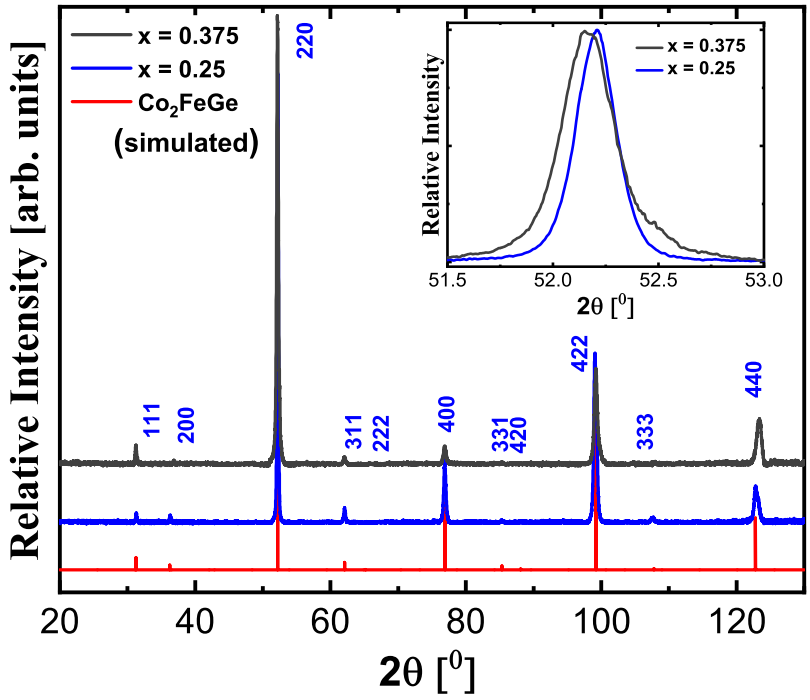

Figure 4.29: Experimental XRD patterns of $Co_2Fe_{1-x}V_xGe$ ($x = 0.25$ and $x = 0.375$) annealed at 1000°C for 9 days followed by ice/water mixture quenching). The simulated XRD pattern is for ordered $L2_1$ structure of Co_2FeGe. The inset shows the systematic shifting of fundamental peak with the increase of V concentration.

The Rietveld refinement of a room temperature XRD pattern was performed using the FullProf suite considering three non-degenerate atomic arrangements (see Table 4.9). The goodness of fit parameters are listed in Table 4.9 for both $x = 0.25$ and 0.375 alloys. Slightly higher values than those expected for a perfect fit are due to the sample texture altering the relative intensities of experimental XRD peaks compared to the calculated pattern. The corresponding crystal structures along with parent Co_2FeGe are shown in Fig. 4.31 (see also Supplementary information). The refinement reveals that both $x = 0.25$ and 0.375 crystallize in the $L2_1$(I) (see Fig. 4.30) structure with

Table 4.9: Possible site assignments for cubic $Co_2Fe_{1-x}V_xGe$ ($x = 0.25$, and 0.375) assuming space groups $L2_1$ ($Fm\bar{3}m$).

Type	4a (0,0,0)	4b($\frac{1}{2},\frac{1}{2},\frac{1}{2}$)	8c ($\frac{1}{4},\frac{1}{4},\frac{1}{4}$)	$\chi^2_{x=0.25}$	$\chi^2_{x=0.375}$
I	Ge	$Fe_{1-x}V_x$	Co_2	1.1	1.9
II	Ge	$Co_{1-x}V_x$	$Fe_{1-x}Co_{1+x}$	1.6	2.1
III	Ge	Co	$Fe_{1-x}V_x$ Co	2.3	2.8

lattice constants (5.755 ± 0.001)Å and (5.760 ± 0.002)Å, respectively. The refinement yielded a reasonably good fit for all of the structures, but the best fit is obtained for a structure where the Ge atoms occupy the 4a position, the 8c position is occupied by Co atoms, and a statistical distribution of the Fe and V atoms at 4b is expected, *i.e.*, Co atoms occupy the tetrahedral sublattice and Fe, V, and Ge on the octahedral sublattice. This is also in accordance with the Pauling electronegativity rule [1] as V and Ge prefer to form a ionic type lattice and coordinate octahedrally due to their higher electronegativity difference.

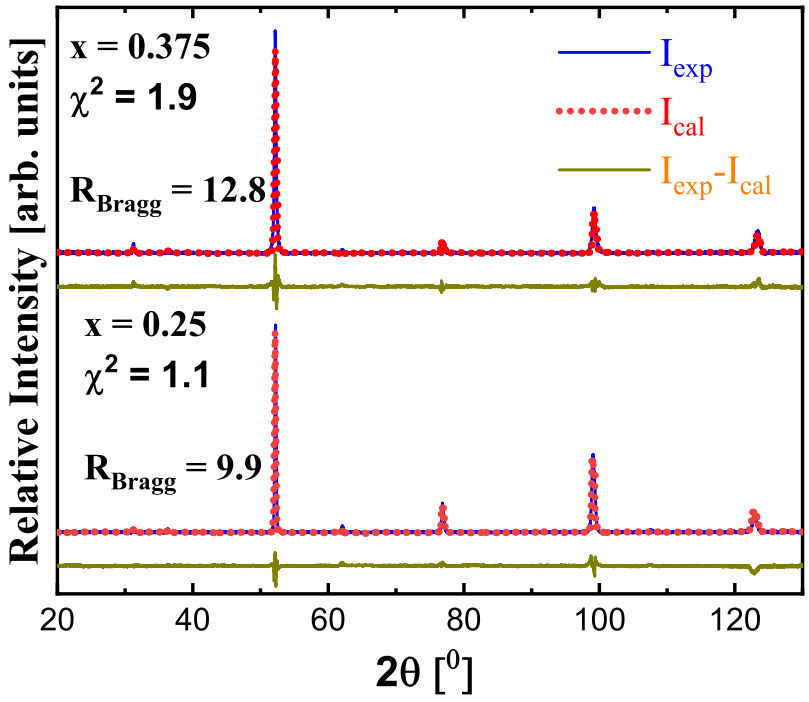

Figure 4.30: Rietveld refinement performed on $Co_2Fe_{1-x}V_xGe$ ($x = 0.25$ and $x = 0.375$) annealed at 1000°C for 9 days followed by ice/water mixture quenching considering first atomic configuration given in Table 4.9.

The Co_2-based Heusler alloys, which are half-metallic ferromagnets, show a Slater-Pauling-

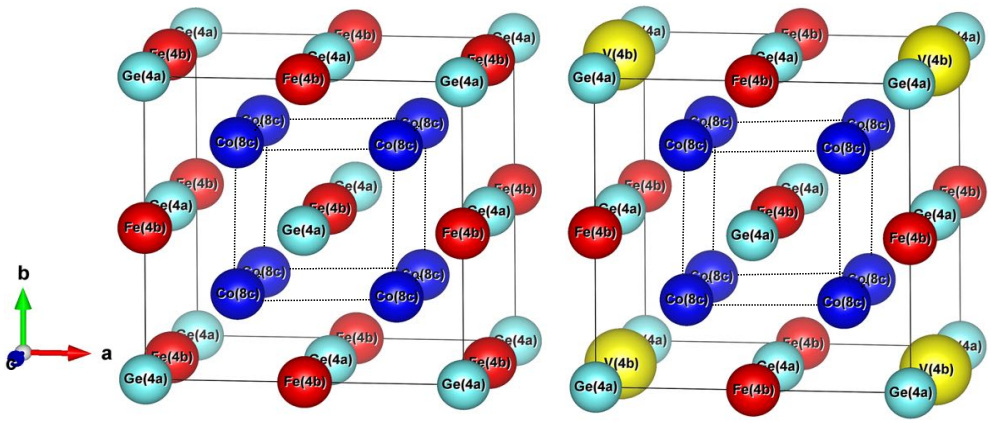

(a) (b)

Figure 4.31: Crystal structure in unit cells of a Heusler alloys (a) Co_2FeGe, and (b) $Co_2Fe_{0.75}V_{0.25}Ge$ assuming $L2_1$(I) structure.

like behavior for the magnetization. The Slater-Pauling rule describes the dependence of the saturation magnetization on the valence electron concentration (N_v) for ordered, half-metallic ferromagnetic Heusler compounds. This dependence is given by [1]

$$m = N_v - 24. \tag{4.11}$$

A saturation magnetic moment of

$$m(x) = 6 - 3x \tag{4.12}$$

is expected for $Co_2Fe_{1-x}V_xGe$.

Low-temperature magnetometry of the single-phase samples was performed by means of the VSM option of a Quantum design PPMS Dynacool. Fig. 4.32(a) shows the field dependent magnetization M(H) curves of the stable alloys with $x = 0.25$ and $x = 0.375$ in the $Co_2Fe_{1-x}V_xGe$ series at 5 K. The decrease of the saturation moment with increasing V concentration is clearly visible. In addition, it is found that stable $Co_2Fe_{1-x}V_xGe$ samples are soft ferromagnets with a small remanence and a small coercive field. The saturation moments at 5 K were extracted to be 5.21 $\mu_B/f.u.$ and 4.78 $\mu_B/f.u.$ for $Co_2Fe_{0.75}V_{0.25}Ge$ and $Co_2Fe_{0.625}V_{0.375}Ge$ respectively, in agreement with the values 5.25 $\mu_B/f.u.$ and 4.875 $\mu_B/f.u.$ expected from a Slater-Pauling-like behavior. The sat-

uration magnetic moments were extracted from an Arrot plot [207], *i.e.*, by extrapolating the linear part of M^2 versus H/M curve to H/M=0 (see inset to Fig. 4.32(a)). In Co_2YZ alloys, the local magnetic moment of low valence transition metal at Y site determines the nature of exchange coupling. If the transition element at Y site carries large moment (Y = Mn, Fe) the exchange coupling between Co−Y sublattices becomes dominant whereas for small moment at Y site (Y = Ti, V) the strongest coupling is between the Co−Co sublattices. In $Co_2Fe_{1-x}V_xGe$ series, magnetism in single phase samples is expected to arise due to dominant coupling from Co−Fe instead of Co−Co due to higher Fe concentration in Y site. The high temperature magnetization was measured by

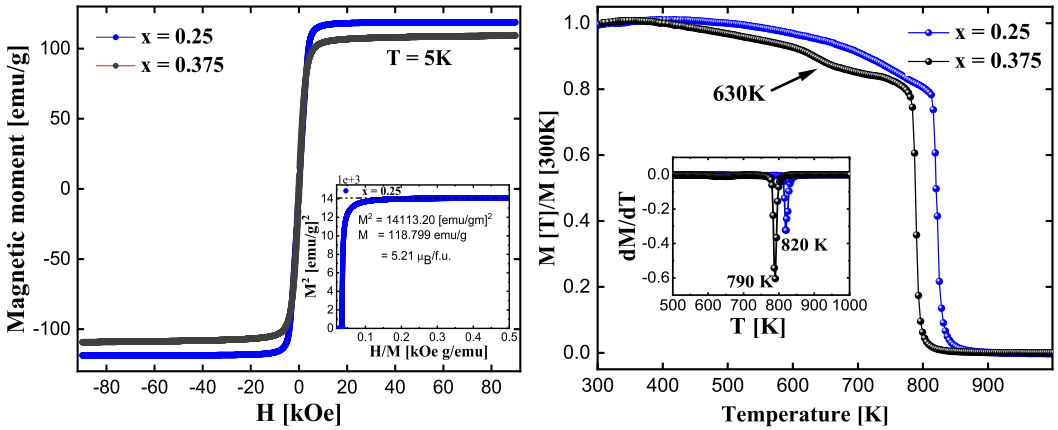

Figure 4.32: (a) The field-dependent magnetization at 5 K of $Co_2Fe_{1-x}V_xGe$ ($x = 0.25$ and 0.375) (b) Temperature dependence of magnetization at 100 Oe. The arrow shows the magnetic transition due to possible secondary phase formation in $x = 0.375$. The inset shows the first-order derivative of magnetization as a function of temperature, the minima of which is used to extract T_c.

means of a vibrating sample magnetometer VSM equipped with a high temperature stage. The plot of Fig. 4.32(b) shows the temperature dependence of magnetization M(T) curves in a constant field of 100 Oe for $Co_2Fe_{1-x}V_xGe$ ($x = 0.25$ and 0.375) showing the ferro-paramagnetic transition. The Curie temperatures were extracted from the inflection point *i.e.*, by taking the minima of the first-order derivative of M(T) curves. The estimated T_c values are about 820 K and 790 K, respectively for $x = 0.25$ and 0.375. In alloy $x = 0.375$, the magnetic transition around 630 K could be due to the formation of small amount of secondary phase (see Supplementary information) during vacuum annealing, as the alloy $x = 0.375$ is stable only after annealing at high temperature

followed by ice/water mixture quenching. The change in interatomic spacing in Co_2FeGe due to the substitution of a fourth element V is expected to lead to a change in magnetic interactions. The increase in lattice parameter with V concentration changes the distance between magnetic ions, leading a weaker exchange interaction between Co−(Fe, V) sublattices and hence giving lower T_c values compared to parent Co_2FeGe.

Resistivity ρ of the $Co_2Fe_{1-x}V_xGe$ ($x = 0.25$ and 0.375) alloys was measured using the van der Pauw method [179] in a PPMS Dynacool for samples with approximate dimensions 4 x 4 x 1.5 mm^3. Fig. 4.33 shows the resistivity ρ as a function of temperature T for zero magnetic field measured during cooling process in the temperature range from 2 K to 400 K. In zero field the resistivity is observed to show a clear metallic temperature dependence with a monotonic increase with increasing temperature and saturating at higher temperatures, indicating weak variation of resistivity resulting from the parallel contribution of the intrinsic resistivity and some limiting resistivity known as shunting with temperature [219, 220]. The total resistivity of magnetic alloys obeys the following Matthiessen's rule [99];

$$\rho(T) = \rho_0 + \rho_{e-ph}(T) + \rho_{e-m}(T) = \rho_0 + \alpha T + \beta T^2 \tag{4.13}$$

where ρ_0 is the temperature independent residual resistivity due to lattice imperfections, impurities *etc.*, ρ_{e-ph} and ρ_{e-m} are temperature dependent terms due to the scattering by phonons (linear temperature dependence) and magnons (quadratic temperature dependence) respectively. As reported in the literature [219, 220], a parallel shunting resistivity is also introduced to the total resistivity to include the contribution from grain boundaries, assuming a weak variation of the resistivity of the highly disordered grain boundaries with temperature, which leads to the following expression for the resistivity;

$$1/\rho_{tot}(T) = 1/\rho_i(T) + 1/\rho_{shunt} \tag{4.14}$$

However, the attempt to fit $\rho(T)$ of $Co_2Fe_{1-x}V_xGe$ ($x = 0.25$ and 0.375) alloys with a quadratic and a quadratic plus linear temperature dependence (for pure magnon and magnon plus phonon

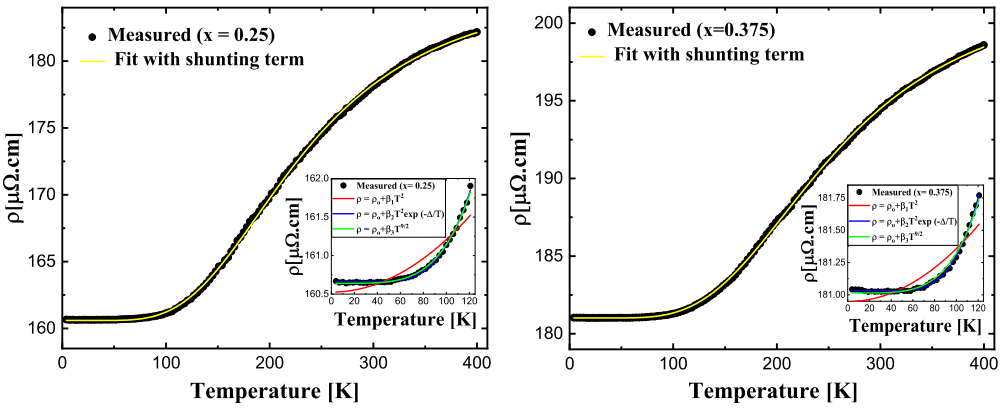

(a) (b)

Figure 4.33: Temperature dependence of electrical resistivity in $Co_2Fe_{1-x}V_xGe$ in zero magnetic field (a) $x = 0.25$, and (b) $x = 0.375$.

scattering of the electrons, respectively) as described in equation 4.13 fails completely (see insets in Fig. 4.33(a) & (b)). The observed temperature dependence of the resistivity can not be understood considering the conventional electron-magnon scattering of ferromagnets. The predicted half-metallic character of the material can be employed to better understand the transport properties (see details in theoretical section below). In half-metallic ferromagnets, due to the presence of a gap at the Fermi level in one of the spin channels (say, the minority spin channel), a minimum excitation energy $k_B\Delta$ of majority charge carriers is required to occupy empty minority states involving a spin flip. As a consequence, the usual quadratic magnonic term (ρ_{e-m}) is expected to be exponentially suppressed at low temperatures [101, 102]. Thus, the usual electron-magnon scattering term can be modified by adding a Boltzmann factor as [102–105],

$$\rho_{e-m}(T) = \beta T^2 e^{-\Delta/T} \tag{4.15}$$

where Δ is a measure of the energy gap between the Fermi level and the band edge of the un-

Table 4.10: Fitted parameters of resistivity data of $Co_2Fe_{1-x}V_xGe$ (x = 0.25 and 0.375).

x	ρ_0($\mu\Omega$-cm)	α ($\mu\Omega$-cm/K)	β ($\mu\Omega$-cm/K^2)	ρ_{shunt}($\mu\Omega$-cm)	Δ (K)	Reduced χ^2
0.25	160.66(4)	1.36(9) $\times 10^{-3}$	1.02(4) $\times 10^{-1}$	186.32(12)	340(6)	1.68 $\times 10^{-14}$
0.375	181.06(2)	1.98(9) $\times 10^{-3}$	1.06(7) $\times 10^{-1}$	203.08(18)	358(12)	1.97 $\times 10^{-14}$

occupied band. Fig. 4.33(a) & (b) show the plot of a nonlinear least-squares fit to this model over the entire temperature range, with fitting parameters summarized in Table 4.10. The fitting yields an energy gap of Δ = 29.30 meV and 30.85 meV, respectively for $x = 0.25$ and $x = 0.375$. The observed exponential suppression of one magnon scattering implies the possibility of HMF behavior.

The possibility of half-metallic ferromagnetism in Heusler alloys has also been studied by looking for the signature of two-magnon scattering in the low temperature resistivity [107–109] which should present a $T^{9/2}$ dependence [109, 221, 227]. The observed resistivity data at low temperature is found to fit this dependence well (see insets in Fig. 4.33(a) & (b)), using the following expression and *now eliminating* the shunt and electron-phonon terms: [107–109]

$$\rho(T) = \rho_0 + \beta T^{9/2} \tag{4.16}$$

In the insets to Fig. 4.33(a) & (b), we also fit the low-temperature data to $\rho(T) = \rho_0 + \beta T^2$ (again without the shunting or electron-phonon terms) to compare the $9/2$ and 2 power laws. That the $T^{9/2}$ behavior is a much better fit than T^2 behavior at low temperatures, not to mention the fact that only a single temperature-dependent term is necessary, suggests a strong contribution from two-magnon scattering, as expected in half metallic systems [109, 221]. However, one can seemingly always find a workable model for resistivity, either by restricting the range or adding parameters as we have done, so we should not say that either fitting result should be taken as more than suggestive on its own.

From the application point of view, the mechanical properties of Heusler alloys can also be an important factor for their final use. Most of the previous studies on mechanical properties are theoretical in nature and only few are verified experimentally. Hardness values reported here are the averages of data taken from at least 12 different regions of each sample with $F = 0.2\,\mathrm{kg}$ load and a 10 s loading time. The Vickers hardness is calculated from

$$HV = 1.8544F/D^2[\mathrm{kg/mm^2}] \tag{4.17}$$

Table 4.11: Possible atomic configurations and corresponding parameters calculated using GGA approach. The values in the parentheses represent the calculated values using GGA+U approach for the most stable configurations predicted from GGA approach. In the table E, E_L, M, M_{SP}, and $\langle a \rangle$ represent calculated energy, energy of most stable configuration, calculated magnetic moment, Slater-Pauling moment, and optimized lattice parameter. The last column shows the tetragonality in the structure.

Configurations	8c	4b	4a	E-E_L (eV)	M ($\mu_B/f.u.$)	M-M_{SP} ($\mu_B/f.u.$)	$\langle a \rangle$ (Å)	Tet. (a/c-1)
$x = 0$								
Co_8-Fe_4Ge_4	8Co	4Fe	4Ge	0	5.773(6.000)	-0.227(0)	5.747(5.758)	0.000
Co_4Fe_4-Co_4Ge_4	4Fe,4Co	4Co	4Ge	1.060	4.990	-1.010	5.719	0.012
Co_4Ge_4-Fe_4Co_4	4Ge,4Co	4Co	4Fe	2.210	4.932	-1.068	5.752	0.020
Co_8-Fe_4Ge_4	8Co	3Fe,1Ge	3Ge,1Fe	3.012	5.012	-0.988	5.739	0.020
$x = 0.25$								
Co_8-Fe_3VGe_4	8Co	1V,3Fe	4Ge	0	5.191(5.250)	-0.089(0)	5.758(5.759)	0.000
Co_5Fe_3- Co_3VGe_4	5Co,3Fe	1V,3Co	4Ge	1.261	3.397	-1.853	5.710	0.000
Co_4Fe_3V- Co_4Ge_4	4Co,3Fe,1V	4Co	4Ge	2.101	3.632	-1.618	5.705	-0.008
Co_8-Fe_3VGe_4	8Co	3Fe,1Ge	3Ge,1V	3.532	4.180	-1.070	5.736	0.050
Co_4Ge_4-Fe_3VCo_4	4Co,4Ge	3Fe,1V	4Co	3.900	3.818	-1.432	5.771	-0.030
x= 0.375								
Co_{64}-$Fe_{20}V_{12}Ge_{32}$	64Co	12V,20Fe	32Ge	-	4.750(4.875)	-0.125(0)	5.765(5.769)	0.005(0.003)

where, D is the diagonal length of the impression of the diamond probe. Relatively high hardness values (7.39 $\pm$ 0.22) GPa and (8.40 $\pm$ 0.07) GPa are measured for $Co_2Fe_{0.75}V_{0.25}Ge$ and $Co_2Fe_{0.625}V_{0.375}Ge$, respectively. Hardness values are comparable to the values reported for full Heusler alloys in the literature [105, 154, 155, 158, 163, 164, 209, 210]. The hardness is observed to increase with V concentration, as we also observed in $Fe_{3-x}V_xGe$ [163].

4.3.4.2 Theoretical Results and Discussions

From experiment, it is clear that only nominal V substitution to Fe stabilizes disordered Co_2FeGe system with XRD patterns consistent with $L2_1$ structure. But, small differences in the atomic scattering factors between the constituent 3d-metals Co, Fe, and V and the unknown degree of texturing in the samples make it difficult to determine the chemical order relying only on XRD data. In order to obtain further information about the stability and chemical ordering in $Co_2Fe_{1-x}V_xGe$ system, we have calculated the zero-temperature electronic structure, magnetic structure, and relative site preference energies for three different possible atomic configurations discussed in Table 4.9, considering the symmetry of $L2_1$ and other disordered structures. We used both GGA and GGA+U approach. Usually, Heusler alloys exhibit localized moments where electron-electron correlations

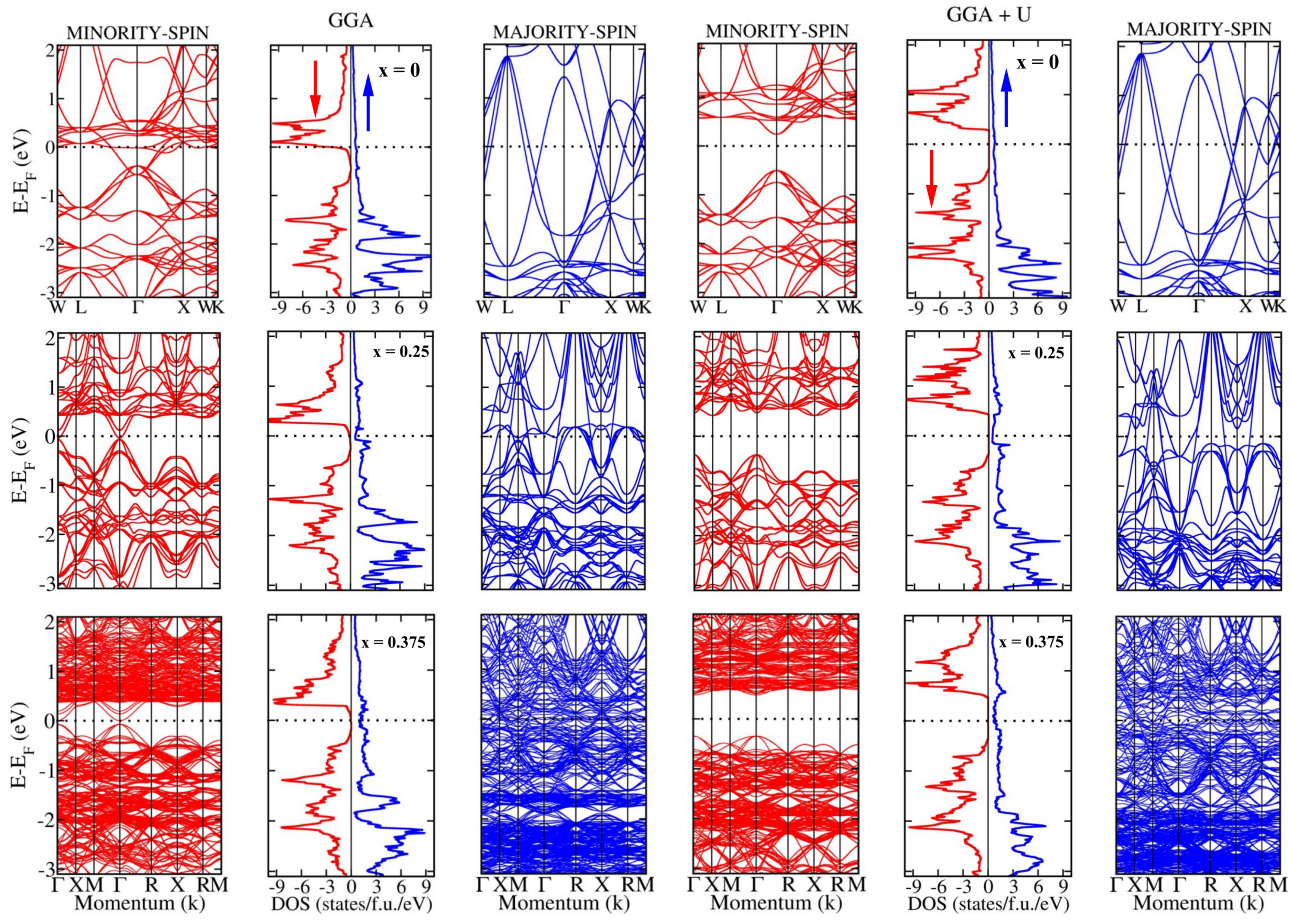

Figure 4.34: Spin polarized DOS for $Co_2Fe_{1-x}V_xGe$ ($x = 0$, 0.25, and 0.375, from top to bottom) calculated using both GGA (left) and GGA+U (right) approaches. Number of states in each DOS plots are scaled with respect to one formula unit. The horizontal dotted line represents Fermi level.

on localized d-states of Co, Fe, and V may play an important role. The GGA+U is used for calculation of the electronic structure to resolve the discrepancy between the theoretical and measured magnetic moment. The plain GGA calculations are considered not sufficient to explain the magnetic moments in Co_2FeZ systems.

We fixed the Ge atoms at the 4a position and permuted rest of the three atoms Co, Fe and V on 4b and 8c Wyckoff sites. To describe the atomic configurations, we have used the occupation of the Wyckoff positions of space group #225 (structure $L2_1$) referring 4a and 4b sites as A sublattice and 8c as B sublattice. Before relaxation, both A and B sublattices are simple cubic with every atom on A sublattice at the center of a cube with eight B sublattice atoms at the corners and every atom on the B sublattice at the center of a cube with eight A sublattice atoms at the corners. The distortion

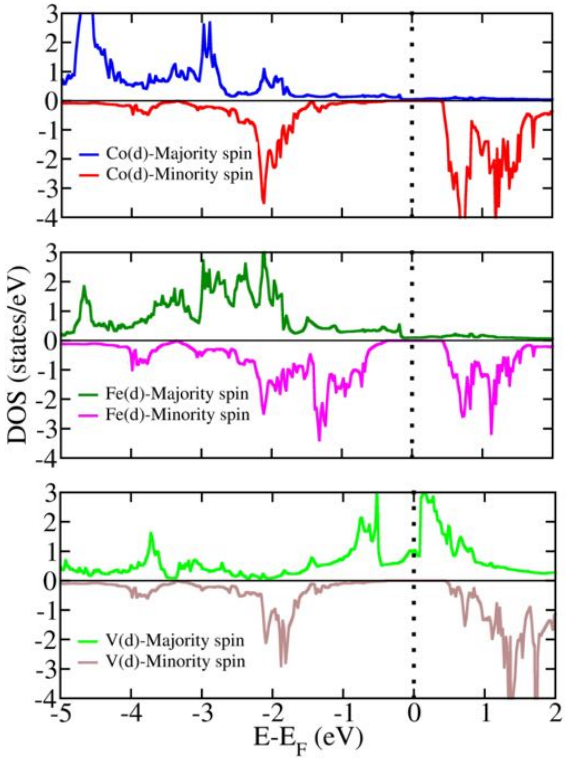

Figure 4.35: Atom-resolved DOS for $x = 0.25$ calculated using GGA+U approach. The vertical dotted line represents Fermi level. The d in parenthesis represents d-orbital.

from cubic symmetry in most of the considered configurations after relaxation to eliminate the forces on the atom is observed to be of the order of a few percents or less.

Out of three different possible configurations shown in Table 4.11, only the configuration with Co only on the B sublattice (8c site) and Fe, V and Ge on A sublattice (4a and 4b sites) is appeared to be energetically the most stable configuration, as also confirmed by experiment for $x = 0.25$, which is I configuration. This is also consistent with the electronegativity rule as V is the least electronegative in the series and more likely to form an ionic-type sublattice with most electronegative Ge rather than Co as discussed in XRD section above. The most stable configuration (I) observed in the alloy $x = 0.25$ is utilized to generate the electronic and magnetic structure of $x = 0.375$ alloy with bigger supercell $2 \times 2 \times 2$. Various calculated parameters are summarized in Table 4.11.

Fig. 4.34 shows the calculated spin resolved band structure and density of states (DOS) of the energetically most favorable configuration for $x = 0$, $x = 0.25$, and $x = 0.375$ respectively from

top to bottom. The electronic band structures are plotted along the high symmetry directions of $Co_2Fe_{1-x}V_xGe$ ($x = 0$, 0.25, and 0.375) Heusler compounds. The large number of bands in the case of $x = 0.375$ is due to the bigger ($2 \times 2 \times 2$) supercell involving 128 atoms/cell considered for the calculations. There is good agreement between band structure and DOS calculations. The DOS for other compositions which are not experimentally stable, are provided in Supplementary information. Our calculations using GGA approach show nearly half-metallic behavior for $x =$ 0.25 and 0.375 as the band gap is present in the vicinity of the Fermi level in minority spin channel as shown in Fig. 4.34 while Fermi level is observed to fall in conduction band edge for Co_2FeGe (see Fig. 4.34 ($x = 0$)) as reported in literatures [17, 105, 129, 212]. However, the inclusion of electron-electron correlation in GGA+U approach opened an energy gap, as expected in minority spin channel with calculated magnetic moments 6 $\mu_B/f.u.$ for Co_2FeGe (M_{expt} = 5.74 $\mu_B/f.u.$), 5.25 $\mu_B/f.u.$ (M_{expt} = 5.21 $\mu_B/f.u.$) for $x = 0.25$ and 4.875 $\mu_B/f.u.$ (M_{expt} = 4.78 $\mu_B/f.u.$) for $x = 0.375$, which follow Slater-Pauling rule for half-metals. In GGA approach, the energy gaps of 0.073 eV and 0.091 eV are calculated around Fermi level for $x = 0.25$ and $x = 0.375$ respectively while the energy gaps of 0.751 eV, 0.773 eV and 0.786 eV are calculated for $x = 0$, $x = 0.25$, and $x = 0.375$ respectively in GGA+U approach. Though the energy gaps extracted from resistivity analysis above are slightly smaller than those from DFT calculations, the half metallic characteristic with the electron transport being dominated by the spin-up electrons is expected from both theory and experiment in V substituted alloys.

Fig. 4.35 shows the atom-resolved DOS plots calculated using the GGA+U approach for Co, Fe, and V respectively from top to bottom in $x = 0.25$. V in this compounds plays an important role towards technological applications. While the Fe and Co atoms have vanishing majority-spin DOS at the Fermi level, V majority-spin DOS on the contrary is significant. Thus the spin-polarization at the Fermi level in the V-doped compounds increases considerably with respect to the parent compounds making possible the creation of a significant spin-polarized current. Second, there is a large exchange splitting between the occupied majority-spin and unoccupied minority-spin states of the V atom. This leads to large band gaps since the conduction minority-spin states are located

higher in energy with respect to the Fermi level when compared to Co or Fe atoms.

4.3.5 Conclusion

In summary, the substitutional series of the quaternary Heusler alloy $Co_2Fe_{1-x}V_xGe$ was synthesized and investigated, both experimentally and theoretically. Single phase microstructures were observed only for $x = 0.25$ and $x = 0.375$ from the series. All stable specimens of the substitutional series exhibit an $L2_1$ order. The saturation magnetic moments are in good agreement with the expectation from the Slater-Pauling rule of thumb for half-metals, a prerequisite for half metallicity. The alloys also show interesting temperature changes of resistivity which appears to be consistent with the band structure calculations. The *ab intio* calculations predict the half-metallic ferromagnetic state in all these alloys. Thus, half-metallic character with high T_c makes these alloys promising for room temperature spintronics applications. However, study of other properties such as current spin polarization is needed to confirm the above observations.

4.4 Effect of mixing the low-valence transition metal atoms Y = Co, Fe, Mn, Cr, V, Ti, or Sc on the properties of quaternary Heusler compounds $Co_{2-x}Y_xFeSi$ ($0 \leq x \leq 1$)

4.4.1 Abstract

In this paper, we report an experimental study of structural, magnetic, electrical transport, and mechanical properties of quaternary Heusler alloys $Co_{2-x}Y_xFeSi$ (Y = Co, Fe, Mn, Cr, V, Ti, or Sc, $0 \leq x \leq 1$) and the experimental findings are supported by *ab initio* electronic structure calculations. The alloys were synthesized using an arc-melting technique. Single phase microstructures are observed for all alloys substituted with low valence transition metals Y except Sc. X-ray powder diffraction patterns at room temperature show the presence of Heusler like face-centered cubic crystal structure in all single phase specimens. The low-temperature saturation magnetic moments, as determined from magnetization measurements, agree fairly well with our theoretical results and also follow the Slater-Pauling rule of thumb for half-metals, a prerequisite for half metallicity. The alloys are predicted to exhibit half-metallic ferromagnetism by *ab initio* electronic structure calculations using GGA+U approach. All stable compounds are observed to have high Curie temperatures with linear dependence with the valence electrons concentration in the alloys. Relatively high hardness values are also measured, approaching 15.72 GPa for Ti-substituted material, highest among the values reported for Heuslers so far. All these properties strongly suggest the alloys are promising for the spintronic applications at room temperature and above.

4.4.2 Introduction

Co_2-based full Heusler compounds with stoichiometric composition Co_2YZ, (Co,Y) being two transition metals, and Z being main group element, crystallizing in the $L2_1$ structure (space group $Fm\bar{3}m$, # 225 [64, 65]) belong to the most promising class of materials for magneto-electronics applications because of their half-metallic ferromagnetic (HMF) nature, high Curie temperatures,

PUBLISHED AS: R. Mahat*, U. Karki, S. KC, J. Law, V. Franco, I. Galanakis, A. Gupta & P. LeClair, *Effect of mixing the low-valence transition metal atoms Y = Co, Fe, Mn, Cr, V, Ti, or Sc on the properties of quaternary Heusler compounds $Co_{2-x}Y_xFeSi$ ($0 \leq x \leq 1$)*, Manuscript ready for submission (2022).

compatible lattice mismatch with conventional semiconductors, and 100% spin polarization at room temperature, arising from the exceptional electronic structure with a energy band gap at the Fermi level (E_F) for minority spin sub-band [20, 29–34]. But, there is a fact that the experimentally observed spin polarization of most of the Co_2-based ternary Heusler alloys are always much smaller than the theoretical values. The discrepancy between theory and experiment is expected due to the structural disorder in the crystal lattices [1, 41]. In many cases, improvements in various properties such as structure, magnetization, transport, critical temperature T_c, magnetoresistance as well as high spin polarization are realised in slightly disordered Heusler alloys by the substitution of a quaternary element, as quaternary element additions are observed to reduce the structural disorder and change the degree of hybridization between the $3d$ orbitals of different elements with consequent changes in the position of the Fermi level with respect to the spin sub-band [115–120]. In previous studies, the doping of low-valent transition metal atoms in ternary Heusler alloys has been reported to change the electronic structure opening the energy gap around Fermi level in minority states, which gives 100% spin polarization, stabilizing the half-metallic character [121]. So, doping is considered as one of the promising ways to stabilize Co_2-based new robust half-metals [122].

Among the various Heuslers, Co_2FeSi (CFS) system is suitable for spintronic device applications because of its large magnetic moment of 6 μ_B and high Curie temperature of 1100 K [20]. But, regarding the half-metallicity in CFS, both half-metallic [137] and non-half-metallic [7] properties have been reported theoretically. Kandpal *et al.* [137] have reported a half-metallic band structure calculations using local spin density approximation and generalized gradient approximation, including optimum effective coulomb exchange interaction (U_{eff}) while Galanakis *et al.* [7] have reported the non-half-metallic character by the full-potential screened Korringa-Kohn-Rostoker Green's function approach. In these approaches, the Fermi level falls on the edge of the minority conduction band, leading to an unstable half-metallicity. Half-metallic ferromagnets with a high thermal stability of energy gap in minority spin channel are desired for technical applications [107, 152]. For such robustness, compounds with Fermi level located at the middle of the energy

gap are highly preferred [107, 152]. If one of the Co atom in CFS is substituted by another low valence transition metal atom Y = Fe, Mn, Cr, V, Ti, or Sc, alloys with rich and useful properties can be tailored. Inverse Heusler alloy Fe_2CoSi has been reported to be zero-gap half-metal with very low Gilbert damping [138, 139]. The quaternary Heulser alloy CoFeMnSi has been observed theoretically and experimentally to be spin-gapless semiconductor [93, 140, 141], CoFeCrSi has been reported to be half-metallic with some structural disorder [133], while CoFeVSi and CoFeTiSi are reported theoretically to be nearly half-metallic and half-metallic respectively, but both have been observed experimentally to show multi-phase behavior in bulk form [142, 143]. In all these quaternary Heusler alloys, the Fermi level again lies on the edge of the minority valence band. So, as we go from CFS to CoFeYSi, Fermi level is shifted from lower edge of conduction band to upper edge of valence band in minority spin channel which is in accordance to the calculations by Galanakis *et al.* [128]. They have suggested that an expansion of the lattice should shift the Fermi level deeper in energy and the contraction should shift it higher in energy. If the Fermi energy is near one of the band edges, the energy gap may easily be smeared out at finite temperatures or destroyed by quasiparticle excitation [107, 152]. Therefore, one can expect robust half metallicity with Fermi level exactly at the middle of the band gap for some intermediate Y content in CFS due to the expansion of the lattice when Y atom with larger atomic radius substitutes for Co [153]. The substitution of Y atom to Co in CFS may be also seen as d-electron deficiency.

There have already been many achievements on CFS system where substitution plays an important role to realize useful electronic and magnetic properties tuning the Fermi level towards the minority band gap [107, 115, 228–230]. The band gap at the Fermi level can be tuned by substituting a fourth element at X/Y/Z site *i.e.*, $Co_{2-x}Y^*_xYZ$, $Co_2Y_{1-x}Y^*_xZ$ or $Co_2YZ_{1-x}Z^*_x$ where Y, Y* are low valence transition elements and Z, Z* are main group elements [41, 62, 123–127]. The substitution at X/Y site is more convincing as X/Y site element plays main role in tailoring the half-metallicity and magnetic properties compared to Z site [128]. Previously, Cr substitution for Fe on CFS has been observed to increase the spin polarization steeply from 0.57 to 0.64 due to the improvements in half-metallicity [115]. Low Gilbert damping has been observed in half-metallic

$Co_2Fe_xMn_{1-x}Si$ substitutional series [229]. The tuning of Fermi level for half-metallicity has been demonstrated in Heusler alloy $Co_2FeAl_{0.5}Si_{0.5}$ [228, 230]. It is the aim of this work to synthesize CFS, a potential candidate for spintronic applications due to promising temperature stability, and investigate the effect of low valence transition metal Y substitution for Co in CFS on structural, electronic, magnetic, electrical transport, and mechanical properties. In particular, we present results on the extent to which Y = Fe, Mn, Cr, V, Ti, or Sc substitution to Co can help to tune the half metallic character stabilizing the $L2_1$ structure in $Co_{2-x}Y_xFeSi$ (CFYS) Heusler system.

4.4.3 Methods

4.4.3.1 Experimental Methods

The polycrystalline $Co_{2-x}Y_xFeSi$ (Y = Co, Fe, Mn, Cr, V, Ti, or Sc, $0 \leq x \leq 1$) off-stoichiometric Heusler alloys were prepared by conventional arc melting of constituents of 99.99% purity on a Cu hearth provided with water cooling under argon flow at a base pressure of 10^{-4} mbar. The mixture was flipped and melted at least 6 times to ensure chemical homogeneity. As an oxygen absorber, Ti was melted inside the vacuum chamber separately before melting the compound to avoid oxygen contamination. The weight loss during the process was less than 1%. The resulting ingots were cut into pieces and examined using an energy dispersive X-ray spectroscopy (EDS) detector equipped in a JEOL 7000 field emission scanning electron microscope (FESEM) to ensure the target composition after the arc melting. These pieces were annealed in evacuated quartz tubes for different heat treatments, and cooled slowly in the furnace to get optimum crystallization to promote the formation of $L2_1$ structure. To make the comparison uniform across all compositions, only the samples annealed under similar heat treatments (*i.e.*, 900°C for 7 days) are reported. The heat treatments were followed by metallography (see details in the supplementary information of our previous publications [163, 164]) to produce a metallic shiny surface for microstructure analysis by optical and electron microscopes. After the heat treatment and metallography, the composition and homogeneity of the samples were again confirmed by using EDS.

The crystal structure was investigated by means of X-ray diffraction (XRD) using a Bruker D8 Discover X-ray diffractometer equipped with monochromatic Co-Kα (λ = 0.179 nm) radiation at room temperature. The specimens were crushed by hand using a mortar and the XRD measurements were carried out on crushed powder samples by rotating around the ϕ axis to minimize surface effects. It should be noted that steel ball milling results in a distortion in crystalline structure due to mechanical robustness of our alloys (discussed in forth coming session). CaRIne crystallography 4.0 software [78] as well as in-house PYTHON code [79] including the dispersive corrections to the atomic scattering factors were used to simulate the XRD patterns to compare with the experimental XRD patterns. Rietveld refinements of the XRD data were performed using a MATCH! software based on the FullProf algorithm [80]. Magnetization isotherms at 5 and 300 K were studied by means of Quantum Design Physical Properties Measurement System (PPMS) using small spherical sample pieces of $\sim$ 20-30 mg, while the high temperature magnetization was measured using LakeShore VSM 7407. The mechanical properties in terms of Vickers hardness were measured by using Buehler model 1600-6100 micro-hardness tester.

4.4.3.2 Computational Methods

Ab initio calculations are performed using density-functional theory (DFT) employing the projector augmented wave (PAW) pseudopotentials by Blöchl [180], implemented by Kresse and Furthmüller in the Vienna *ab initio* simulation package (VASP) [181]. We have adopted the generalized-gradient approximation (GGA) as formulated by Perdew, Bueke, and Ernzerhof (PBE) for the electronic exchange-correlation potential [182]. A 16-atom supercell, *i.e.*, 4 formula units of the underlying $L2_1$ structure adopted by the perfect full-Heusler compounds like Co_2MnGe is used in all of our calculations. The integrals in the reciprocal space of cubic systems was done considering a $20 \times 20 \times 20$ Γ-centered Monkhorst-Pack grid [200] using the linear tetrahedron method with Blöchl corrections. Total energies were converged upto 10^{-7}eV/cell with a cutoff for the kinetic energy of the plane waves of 520 eV. Full relaxation of cell (initially cubic) volume, shape and atomic positions were performed until the forces on each atom become less than 10^{-2}

meV/cell using the conjugate-gradient method. Spin-orbit interaction is ignored in our calculations as it is not crucial for the half-metallic properties of Heusler compounds [183].

Ab-initio electronic structure calculations using GGA approach in the case of parent compound CFS with 30 valence electrons per formula unit has been reported to predict a significantly reduced magnetic moment with respect to experiment and the Slater-Pauling value, due to the well-known on-site electronic correlations of the d-electrons and related fractional state occupation [225]. The observed half-metallic properties of CFS is reported to be recovered by introducing an appropriate Hubbard U term into the electronic Hamiltonian [225]. In our study, we have also presented GGA+U calculations on $Co_{2-x}Y_xFeSi$ system and explore how the CFS electronic properties are affected by low valence atomic substitutions.

The Hubbard U parameter cannot be calculated simultaneously with the minimization of the total energy because total energy remains constant with respect to the U term. Both experimental and computational determination of the U values is very difficult and tedious tasks and in 2013 Sasioglu and collaobrators employed the constrained random-phase approximation (CRPA) scheme to calculate the U values for several half-metals [190]. For the calculations presented in the rest of this work, we have used the semi-empirical values mentioned in Ref. kandpal2007calculated, where Kandpal *et al.* have employed the LDA+U scheme to study the electronic structure of several half-metallic Heusler compounds. The considered U values for the d-orbitals of Co, Fe, Mn, Cr, V, Ti, and Sc are 1.92 eV, 1.80 eV, 1.69 eV, 1.59 eV, 1.34 eV, 1.36 eV, and 1.30 eV respectively. Finally, it should be noted that the inclusion of U artificially opens a band-gap in the minority spin channel and only comparison to experimental data guarantees that the used U parameters in the calculations are adequate for a particular material.

4.4.4 Results and Discussions

4.4.4.1 Experimental results and Discussions

4.4.4.1.1 Microstructural and Compositional analysis

Optical microscopy and SEM of polished and etched samples are very helpful to characterize the microstructure specially when the impurity phase contents are either below the detection limit of XRD (less than roughly 5% of the overall volume) or amorphous in nature [105, 168, 169]. These methods provide a morphological image which can clearly figure out secondary phases and grain boundary segregation even for minor constituents. We can speculate the presence of impurity phases by observing different contrast in optical microscopy, and SEM with EDS can be utilized to quantify whether regions of different contrasts represent impurity phases or possible different crystallite orientations.

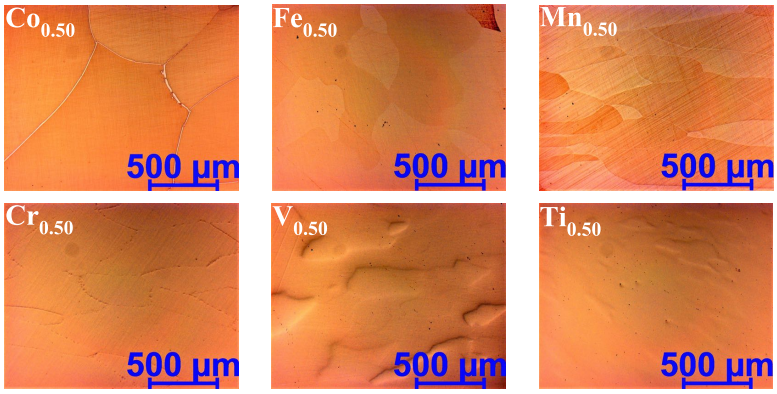

Figure 4.36: Optical micrograph of $Co_{2-x}Y_xFeSi$ (Y = Co, Fe, Mn, Cr, V, or Ti, $x = 0.50$) annealed at 900°C for 7 days followed by slow cooling showing the granular microstructure. The samples were etched for 60 seconds using the Adler etchant.

Fig. 4.36 shows the microstructures of all single phase specimens $Co_{2-x}Y_xFeSi$ (Y = Co, Fe, Mn, Cr, V, or Ti, $x = 0.50$) annealed at 900°C for 7 days, observed using optical microscope. With the substitution of 50% Y content (Co, Fe, Mn, Cr, V, Ti, or Sc) for Co in CFS, we observed single phase microstructures except for 50% Sc. Our results are in accordance with previous reports for 50% Co and Fe for Co in CFS. It is found that the grain size of the alloys decreased greatly with

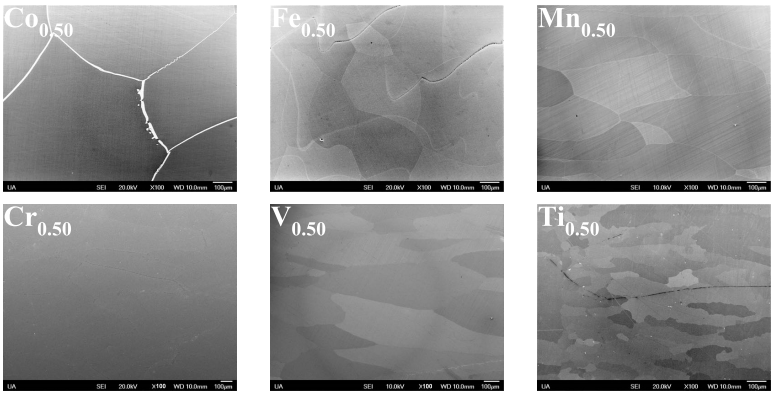

Figure 4.37: SEM micrograph of $Co_{2-x}Y_xFeSi$ (Y = Co, Fe, Mn, Cr, V, or Ti, $x = 0.50$) alloys annealed at 900°C for 7 days followed by slow cooling, showing the granular microstructure.

the substitution of less valence Y content. The contrast developed in micrograph (see details in Supplementary information) suggests significant compositional differences between phases in the case of 50% Sc for Co. The composition was measured to differ from the target composition by more than 5% with the secondary phase mainly located in grain boundaries. The stoichiometry within the grains of all the single-phase specimens was confirmed as the target composition within an instrumental uncertainty of $\sim$ 5% using EDS (see Supplementary information). Fig. 4.37 shows the typical electron images displaying the microstructure of single phase alloys. The optical and electron micrographs of all the remaining alloys in the series are presented in Supplementary information.

4.4.4.1.2 Crystal structure and atomic order analysis

The crystallographic order of the alloys is highly important for their use in any kind of spintronics applications. So, structural analysis has been performed with XRD as the standard method. Fig. 4.38 shows the powder XRD spectra of the studied alloys with $x = 0.50$, measured at room temperature, using a Co-K_α radiation source (see details in Supplementary information). All the alloys showed single phase behavior except for Sc, consistent with microstructures observed in previous section. The asterisks correspond to Heusler cubic peaks while others are from secondary phase/unknown impurity phase in the case of Sc based alloy. All the XRD peaks in single-phase al-

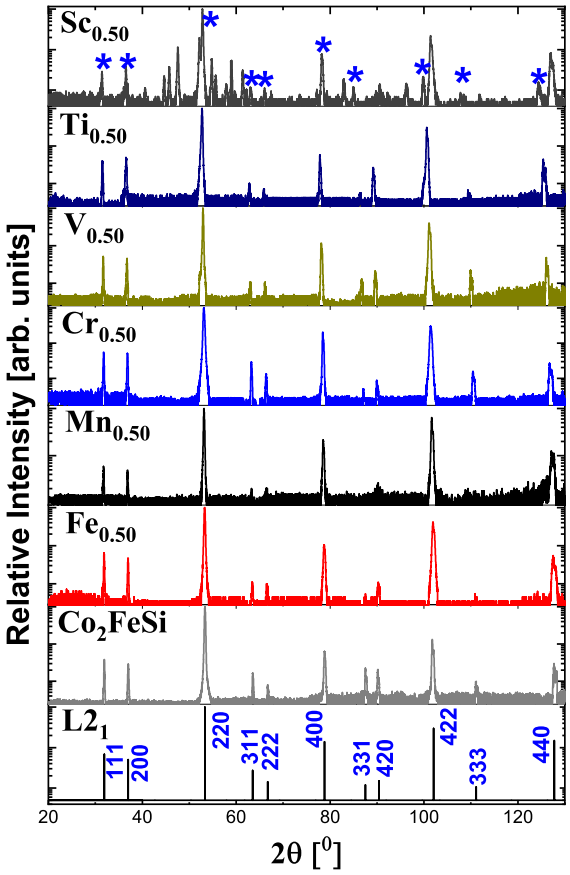

Figure 4.38: Experimental XRD patterns of $Co_{2-x}Y_xFeSi$ (Y = Co, Fe, Mn, Cr, V, Ti or Sc, $x = 0.50$) alloy series annealed at 900°C for 7 days investigated at room temperature, here, $*$ corresponds Heusler cubic peaks in Sc based alloy while others are from secondary phase/unknown impurity phase. The first from the bottom is the simulated XRD pattern for ordered $L2_1$ structure of CFS. The relative Intensity (y-axis) is plotted in log scale so that all the peaks can be seen clearly.

loys can be indexed as face centered cubic (*fcc*) structure. As expected only three distinct Heusler-like reflection peaks (h, k, l all odd or even) are observed; fundamental peaks with $h+k+l = 4n$, even superlattice peaks with $h+k+l = 4n+2$ and odd superlattice peaks with $h+k+l = 2n+1$. Heusler alloys in the ordered $L2_1$ structure are characterized by the presence of superlattice reflection (SR) peaks; the presence of (111) peak indicates the chemical ordering of atoms in octahedral positions, and (200) peak indicates the order for atoms in tetrahedral positions, while (220) peak is a principal reflection which is independent of the state of the order [72].

In full Heusler alloys (FHA) of the type X_2YZ ($L2_1$ structure), Z is the main group element with highest electronegativity which occupies 4a(0,0,0), Y is the low valence transition metal atom

with least electronegativity which occupies 4b($\frac{1}{2},\frac{1}{2},\frac{1}{2}$), and transition metal atoms X are of the intermediate electronegativity values and occupy 8c($\frac{1}{4},\frac{1}{4},\frac{1}{4}$) (or 4c($\frac{1}{4},\frac{1}{4},\frac{1}{4}$), and 4d($\frac{3}{4},\frac{3}{4},\frac{3}{4}$)) Wyckoff positions of the space group $Fm\bar{3}m$ [1, 61]. Hereafter, we refer 4a and 4b sites as A sublattice and 4c and 4d as B sublattice as shown in Fig. 4.40. The intensities of superstructure peaks are affected by various types of atomic disorders, *e.g.*, (i) A2-type disorder due to random distribution of atoms over lattice sites 4a, 4b, 4c, and 4d which results vanishing superstructure peaks, (ii) B2-type disorder due to random distribution between atoms in 4a and 4b sites which results only the (200) superstructure peak and vanishing (111) peak, and (iii) B32a-type when disorder is between atoms in 4a, and 4c sites, and 4b, and 4d sites [1, 73]. This disordered structure B32a results (111) peak with much higher intensity than the (200) peak. All these types of disorder would destroy the half-metallic property of the material by introducing density of states (DOS) at Fermi level in the minority spin channel [62] but the magnetic moment of the materials may still follow a Slater-Pauling rule.

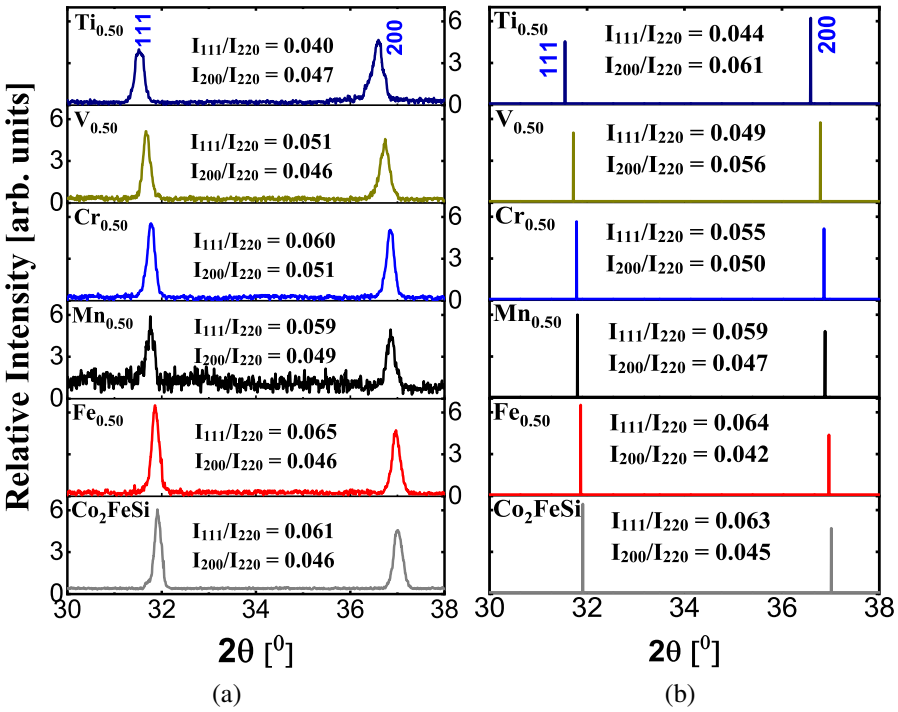

Figure 4.39: (a) Enlargement of (111) and (200) X-ray diffraction peaks of single phase alloys and (b) the corresponding simulated patterns for the ideal ordered structure.

Fig. 4.39(a) shows the enlargement of the experimental XRD patterns between 30° and 38° for all single phase specimens and Fig. 4.39(b) shows the corresponding simulated XRD patterns of ideal $L2_1$ structure for comparison. The superlattice reflections (111) and (200) are clearly visible as expected for the defect-free ordered Heusler structure, indicating the presence of a long range ordering in these samples. The measured and expected values for I_{111}/I_{220} and I_{200}/I_{220} are also labeled. These values agree with each other qualitatively. The degree of chemical ordering in $Co_{2-x}Y_xFeSi$ is evaluated by Webster's model [231] using factors S and α.

$$S = \sqrt{\frac{(I_{200}/I_{\text{fund}})_{\text{exp}}}{(I_{200}/I_{\text{fund}})_{\text{cal}}}} \tag{4.18}$$

$$(1-2\alpha)S = \sqrt{\frac{(I_{111}/I_{\text{fund}})_{\text{exp}}}{(I_{111}/I_{\text{fund}})_{\text{cal}}}} \tag{4.19}$$

where I_{111}, I_{200}, and I_{fund} are the integrated intensities of (111) and (200) superlattice reflection peaks and a fundamental peak, respectively. The numerator is an experimentally extracted value, and the denominator is the calculated value for the perfect-order case. The long range ordering parameter S = 0 indicates the A2-type disorder, and S = 1 indicates ordering of atoms in B sublattice sites. The factor α = 0 means ordering in A sublattice and α = 0.5 means disorder in A sublattice called B2-type disorder. Thus, $L2_1$ ordering is characterized by S = 1 and α = 0 while S = 1 and α = 0.5 indicate B2-type disorder. To minimize the effect of preferred orientation and texturing in our specimens, we have reported the average S and α values estimated using I_{fund} as (220), (400), (422), and (440) fundamental peaks in equations 4.18 and 4.19. As shown in Table 4.12, the extracted high S value and a low α value for all of the specimens indicates that the crystal structure of alloys is sufficiently ordered. A certain amount of disorder is expected in V and Ti substituted alloys.

meaning of $\alpha < 0$?

In order to gain more insight on chemical ordering, we performed Rietveld refinement of experimental XRD pattern for $Co_{2-x}Y_xFeSi$ (Y = Co, Fe, Mn, Cr, V, or Ti, $x = 0.50$) considering three non-degenerate configurations as presented in Table 4.13. Details of the refinements for

note with uncert. all are consistent with $\alpha = 0$

Table 4.12: Ordering parameters S and α with corresponding goodness of fit parameters (χ^2 and R_{Bragg} factor) obtained from Rietveld refinement for $Co_{2-x}Y_xFeSi$ (Y = Co, Fe, Mn, Cr, V, or Ti, $x = 0.50$) alloys. The numbers in parentheses are the standard deviation (SD), *e.g.*, $1.04(5) = 1.04 \pm 0.05$. The SD was calculated among values estimated using I_{fund} for the (220), (400), (422), and (440) fundamental peaks.

Y element	S	α	χ^2	R_{Bragg}
Co	1.01(5)	0.01(8)	1.1	5.3
Fe	1.04(7)	0.01(7)	1.3	6.9
Mn	1.02(9)	0.01(5)	1.5	11.2
Cr	1.01(4)	-0.02(4)	1.9	9.1
V	0.90(10)	-0.06(9)	1.6	8.3
Ti	0.88(12)	-0.04(4)	1.5	7.7

Table 4.13: Possible site assignments for cubic $Co_{2-x}Y_xFeSi$ (Y = Co, Fe, Mn, Cr, V, Ti, or Sc, $x = 0.50$) Heusler system.

Type	4a (0,0,0)	4b $(\frac{1}{2},\frac{1}{2},\frac{1}{2})$	4c $(\frac{1}{4},\frac{1}{4},\frac{1}{4})$	4d $(\frac{3}{4},\frac{3}{4},\frac{3}{4})$
I	Si	$Fe_{0.50}Y_{0.50}$	$Co_{0.50}Fe_{0.50}$	Co
II	Si	$Co_{0.50}Y_{0.50}$	Fe	Co
III	Si	Fe	$Co_{0.50}Y_{0.50}$	Co

the best fit configuration (I) are provided in Table 4.12. The observed, calculated and difference profiles for the best fit configuration (I) after performing the Rietveld refinement are provided in Supplementary information. The crystal structure for this configuration is shown in Fig. 4.40(b) (see Supplementary information for crystal structures for other possible configurations). In this configuration, we presumed that low-valence Y substitution (Y being least electronegative) in CFS with perfect $L2_1$ structure will displace half of the Fe atoms from 4b sites towards vacated Co sites and it will fill the site previously occupied by Fe forming an ionic-type sublattice with Si (which has a larger electronegativity) rather than with Co and Fe and becomes stable by donating its electrons to other elements in the alloy. The Co and displaced Fe atoms have intermediate electronegativities and occupy tetrahedral sites [1, 61]. In other word, Co and Fe atoms are assumed on the tetrahedral sublattice B (4c & 4d) and Fe, Y, and Si on the octahedral sublattice A (4a & 4b). This Hume-Rothery condition of phase stability of substitutional solid solution also supports this atomic configuration. According to this rule, the atomic size difference between two elements should be no larger than 15% and electron negativity difference no higher than 0.4 in order to form

the stable solid solution [202–204].

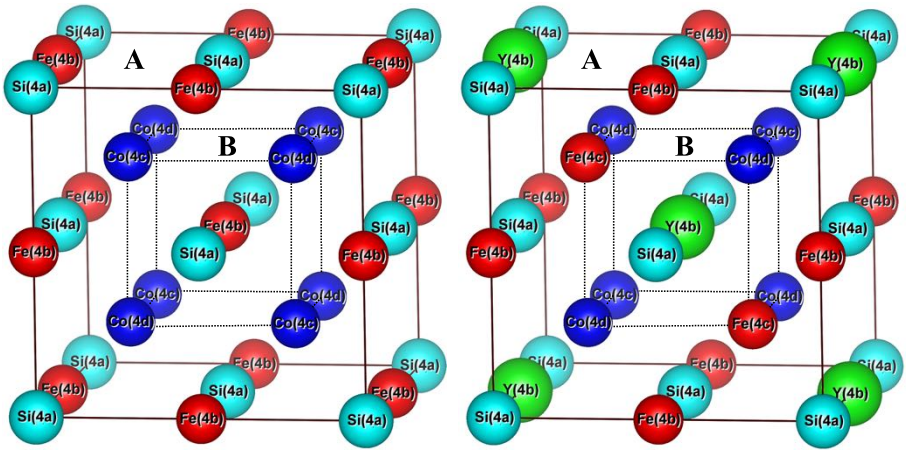

(a) (b)

Figure 4.40: Crystal structure in unit cell of (a) CFS and (b) $Co_{1.50}Y_{0.50}FeSi$ (Y = Fe, Mn, Cr, V, Ti, or Sc) (I) configuration mentioned in Table 4.13 assuming $L2_1$ structure. The structures are shown in their ideal, unrelaxed forms.

We have used Cohen's method with a Nelson-Riley extrapolation to accurately determine the lattice parameters [171]. The dependence of the lattice parameter a on the Y content for $Co_{2-x}Y_xFeSi$ (Y = Co, Fe, Mn, Cr, V, or Ti, $0 \leq x \leq 1$) is shown in Fig. 4.41(a) while Fig. 4.41(b) shows the variation of lattice parameter with atomic number of Y element in $Co_{1.50}Y_{0.50}FeSi$ (Y = Co, Fe, Mn, Cr, V, or Ti). It is noticed that the lattice parameter increases linearly with the substitution of less valence Y content, consistent with Vegard's law [205] as atomic radii decrease in the order Ti > V > Cr > Mn > Fe > Co [153].

4.4.4.1.3 Magnetic Characterization

Most of the Co-based half-metallic Heusler alloys show a Slater-Pauling-like behavior for the magnetization when crystallized in a fully ordered state [206]. The Slater-Pauling (SP) rule relates the dependence of the magnetic moment with the valence electron concentration (Z_t) following a simple electron counting scheme for ordered, half-metallic ferromagnetic Heusler compounds. If the value of the saturation magnetization changes with Y element according to the Slater-Pauling

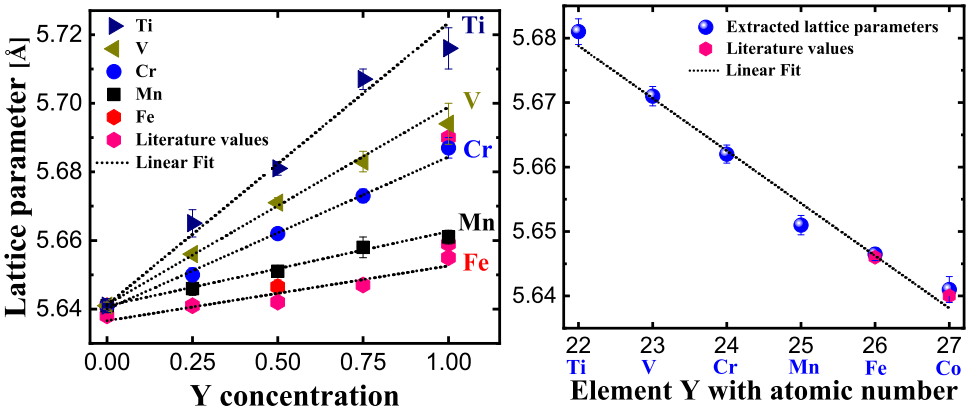

Figure 4.41: Variation of lattice parameter with (a) Y content in $Co_{2-x}Y_xFeSi$ (Y = Co, Fe, Mn, Cr, V, or Ti, $0 \leq x \leq 1$), and (b) atomic number of low valence transition metal element Y in $Co_{2-x}Y_xFeSi$ (Y = Co, Fe, Mn, Cr, V, or Ti, $x = 0.50$) showing linear behavior. The pink data points represent literature values [19, 20].

rule of thumb for half-metals, then we expect the total magnetization to be [1, 7]

$$M_t = [(2-x)Z_{Co} + xZ_Y + Z_{Fe} + Z_{Si}] - 24 \tag{4.20}$$

where, M_t is the total spin magnetic moment per f.u. in μ_B and Z_i is the number of valence electrons of each individual atom. In $Co_{2-x}Y_xFeSi$ (Y = Co, Fe, Mn, Cr, V, or Ti, $0 \leq x \leq 1$) system, the total number of valence electrons change from 30 in CFS to 25 in CoFeTiSi. Therefore, the SP behavior predicts that the saturation magnetic moment should decrease with the substitution of Y element for Co. A saturation magnetic moment of

$$M(Y) = 6 - x \times (Z_{Co} - Z_Y) \tag{4.21}$$

is expected for $Co_{2-x}Y_xFeSi$.

Here, we have utilized the VSM option of a Quantum design PPMS Dynacool working in the temperature range of T = 5 K to 400 K and with maximum possible magnetic field of 9 T to observe low temperature magnetisations for all single-phase alloys. Fig. 4.42(a) shows the isothermal

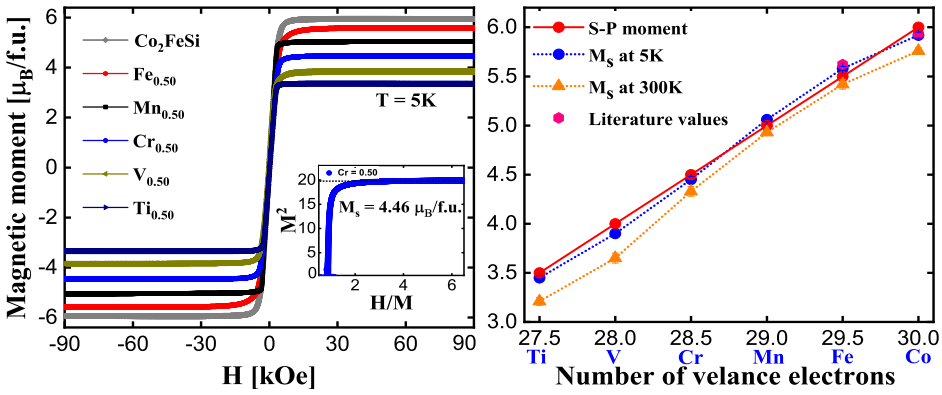

(a) (b)

Figure 4.42: (a) Isothermal magnetization curves of $Co_{2-x}Y_xFeSi$ (Y = Co, Fe, Mn, Cr, V, or Ti, $x = 0.50$) at 5 K, and (b) The saturation magnetic moment versus valence electron counts per formula units with element Y, both experimental(at 5 K and 300 K) and expected from Slater-Pauling rule for half metals. The pink data points represent reported literature values [19, 20].

magnetization curves measured at 5 K for $x = 0.50$ (see Supplementary information for magnetization curves of all other alloys in the series), as expected for ferromagnets. All the alloys are saturated in magnetic field of about 4 kOe which indicates small magnetocrystalline anisotropy in the specimens. Arrot plot method [207] (*i.e.*, by linear extrapolation to H/M=0 of M^2 versus H/M curve) is utilized to determine the spontaneous magnetizations (see inset to Fig. 4.42(a)). Total saturation magnetic moments (M_s) obtained from the spontaneous magnetization at 5 K are observed to follow the Slater-Pauling rule of thumb for half metals (see red data points) and decrease with the decrease of valence electrons in Y atoms (see Fig. 4.42(b)). The decrease of M_s is expected due to the decrease in number of Co atoms. The magnetic moment per formula unit for $x = 0$, *i.e.*, CFS is measured to be 5.92 μ_B, which is also in good agreement with reported results [19, 20]. Fig. 4.44(a) shows the systematic variation of saturation magnetic moment with Y atom concentration ($0 \leq x \leq 1$) in the series. The slight deviation of magnetic moments from expected Slater-Pauling values could be due to the slight variation in the stoichiometry of the alloys, weighing and measurement errors, partial surface oxidation, and the measurement temperature of 5 K. The experimentally determined spin magnetic moments are also in good agreement with those obtained from first-principle calculations (see Table 4.15), as discussed in the forthcoming section.

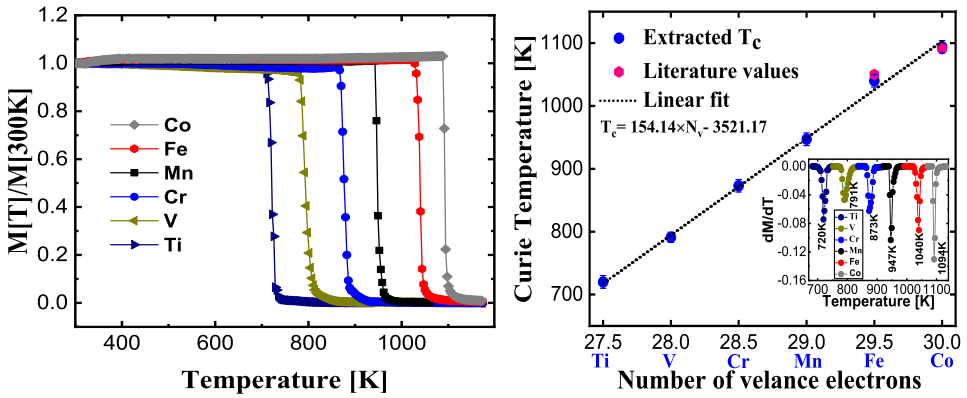

Figure 4.43: (a) Temperature dependence of magnetization at 100 Oe, and (b) Variation of Curie temperature as a function of valence electron counts per formula units with element Y ($x = 0.50$). The inset shows the first-order derivative of magnetization as a function of temperature, the minima of which is used to extract T_c. The pink data points represents reported literature values [19, 20].

Fig. 4.43(a) shows the temperature dependent specific magnetization of the alloys for $x = 0.50$ (see Supplementary information for all other alloys in the series), measured by means of a vibrating sample magnetometer (LakeShore VSM 7407) equipped with a high temperature stage. The measurements were not performed at saturation but in a constant magnetic field of 100 Oe. The Curie temperatures T_c were extracted from the inflection point *i.e.*, by taking the minima of the first-order derivative of M(T) curves (see inset in Fig. 4.43(b)). The Curie temperature is observed to decrease with the substitution of low valence transition metal element Y due to the weakening of the exchange interaction caused by small magnetic moment of substituted element Y compared to Co. The decrease in T_c can also be attributed to the increase in lattice parameter with the substitution of Y changing the distance between magnetic ions leading to a weak exchange interaction. A linear dependence is obtained when plotting T_c as a function of number of valence electron concentration, and hence M_s (see Fig. 4.43(b)), which is expected in half-metallic Co-based Heusler alloys [124]. According to this plot, T_c is the highest for those that exhibit a large magnetic moment, or equivalently for those with a high valence electron concentration as derived from the Slater-Pauling rule. The high values of T_c usually imply stable magnetism and half-metallicity over wide temperature range, necessary in practical applications. Fig. 4.44(b) shows

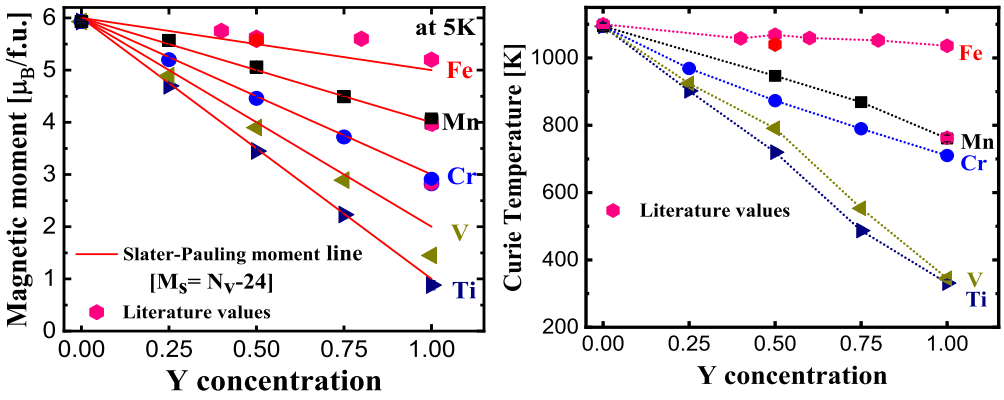

Figure 4.44: The variation of (a) saturation magnetic moment at 5 K, and (b) Curie temperature with Y content in $Co_{2-x}Y_xFeSi$ (Y = Co, Fe, Mn, Cr, V, or Ti, $0 \leq x \leq 1$). The solid lines in Fig. 4.44(a) represent the vaules expected from Slater Pauling rule for half metals. The pink data points represent reported literature values [19, 20].

the systematic variation of Curie temperature with Y atom concentration ($0 \leq x \leq 1$) in the series.

The experimental values of lattice parameters, saturation magnetic moments at 5 K, Curie temperatures, and corresponding mechanical hardness values of all single phase specimens in $Co_{2-x}Y_xFeSi$ (Y = Co, Fe, Mn, Cr, V, or Ti, $0 \leq x \leq 1$) alloy series are summarized in Table 4.14.

4.4.4.1.4 Vickers micro hardness

For industrial applications, materials require mechanical robustness to undergo repetitive thermal cycling and resist cracking from vibrations. Here, we have measured the mechanical properties in terms of Vickers hardness. Fig. 4.45(a) displays the variation of Vickers micro hardness with transition metals of increasing atomic number in $Co_{2-x}Y_xFeSi$ (Y = Co, Fe, Mn, Cr, V, or Ti) series with $0 \leq x \leq 1$ and Fig. 4.45(b) shows the variation for allows with $x = 0.50$, all measured at room temperature. The corresponding harness values are given in Table 4.14. The data were taken from at least 12 different regions of each sample with 0.2 kg load and 10 s loading time and

Table 4.14: Experimental lattice parameters and saturation magnetic moments at T = 5 K along with the Slater-Pauling (S-P) values, and the measured Curie temperature (T_c) of $Co_{2-x}Y_xFeSi$ (Y = Co, Fe, Mn, Cr, V, or Ti, $0 \leq x \leq 1$) alloy series. The numbers in parentheses are the uncertainty in the last digit, *e.g.*, $5.92(3) = 5.92 \pm 0.03$. The numbers in square brackets are the uncertainty

Series	Concentartion	Expt. lattice parameter (Å)	Expt. M_s (μ_B/f.u.)	S-P (μ_B/f.u.)	T_C (K)	Vickers Hardness (*GPa*)
Co_2FeSi	$x = 0$	a = 5.641(2)[5.636]	5.92(3)[6.00]	6.00	1094(10)[1100] [20, 109]	7.33(4)
$Co_{2-x}Fe_xFeSi$	$x = 0.25$	a = [5.641]	[5.75]	5.60	[1058][19, 109]	-
	$x = 0.50$	a = 5.646(2)[5.642]	5.58(2)[5.62]	5.50	1040(10)[1069][19, 109]	7.55(6)
	$x = 0.75$	a = [5.647]	[5.60]	5.20	[1052][19, 109]	-
	$x = 1$	a = [5.655]	[5.20]	5.00	[1036][19, 109]	-
$Co_{2-x}Mn_xFeSi$	$x = 0.25$	a = 5.646(2)	5.57(4)	5.50	-	7.51(4)
	$x = 0.50$	a = 5.651(2)	5.06(3)	5.00	947(10)	7.94(3)
	$x = 0.75$	a = 5.658(3)	4.49(2)	4.50	869(10)	8.51(5)
	$x = 1$	a = 5.661(2)	4.03(3) [3.99]	4.00	761(10)[763]	9.69(7)
$Co_{2-x}Cr_xFeSi$	$x = 0.25$	a = 5.650(2)	5.20(4)	5.25	969(10)	7.82(6)
	$x = 0.50$	a = 5.662(1)	4.46(3)	4.50	873(10)	8.61(8)
	$x = 0.75$	a = 5.673(2)	3.72(2)	3.75	790(10)	9.78(9)
	$x = 1$	a = 5.687(3)	2.91(2)[2.82]	3.00	710(10)	11.33(9)
$Co_{2-x}V_xFeSi$	$x = 0.25$	a = 5.656(1)	4.89(4)	5.00	924(10)	8.52(5)
	$x = 0.50$	a = 5.671(1)	3.90(3)	4.00	791(10)	9.85(7)
	$x = 0.75$	a = 5.683(3)	2.89(4)	3.00	553(10)	11.37(8)
	$x = 1^{\dagger}$	a = 5.694(6)	1.45(5)	2.00	345(10)	11.79(10)
$Co_{2-x}Ti_xFeSi$	$x = 0.25$	a = 5.665(4)	4.75(5)	4.75	902(10)	10.75(7)
	$x = 0.50$	a = 5.681(2)	3.45(2)	3.50	720(10)	12.58(3)
	$x = 0.75$	a = 5.707(3)	2.23(5)	2.25	487(10)	13.81(9)
	$x = 1^{\dagger}$	a = 5.716(6)	0.88(9)	1.00	331(10)	15.72(14)

† Multiphase specimen

average values are reported here. The Vickers hardness is calculated from

$$HV = 1.8544F/D^2[\mathrm{kg/mm^2}] \tag{4.22}$$

where, D is the diagonal length of the impression of the diamond probe. Relatively high hardness values are measured, approaching 15.72 GPa for CoFeTiSi, highest among the values reported for Heuslers so far [105, 154–156, 158, 163, 164, 209, 210]. The hardness is observed to increase with the substitution of Y element of increasing atomic radius and depends on phases present as reported in the literature [211].

4.4.4.2 Theoretical Results and Discussions

The parent compound CFS of the series $Co_{2-x}Y_xFeSi$ (Y = Co, Fe, Mn, Cr, V, Ti, or Sc, $x = 0.50$) is already reported in literatures to form the $L2_1$ structure with a low degree of chemical

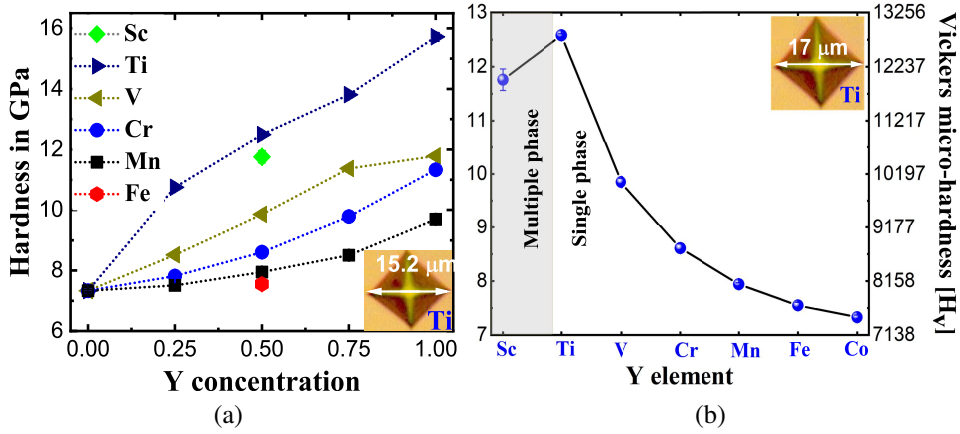

Figure 4.45: Vickers hardness versus Y content in $Co_{2-x}Y_xFeSi$ (Y = Co, Fe, Mn, Cr, V, Ti, or Sc), all annealed at 900°C for 7 days (a) for all the alloys $0 \leq x \leq 1$, and (b) for alloys with $x = 0.50$. The imprints of the indenter with radial cracks for Ti = 1 [bottom right of Fig. 4.45(a)] and Ti = 0.50 [top right of Fig. 4.45(b)] are shown.

disorder [107] and our experimental investigations confirmed the low valence transition metals Y substitution for Co in CFS also give stable single phases with XRD patterns consistent with the ordered $L2_1$ structure except for Scandium substituted alloy. These experimental facts allow us accurate comparison between experiment and theory. The fact that DFT using GGA approach predicts a significantly reduced magnetic moment with respect to experiment and the Slater-Pauling value and the introduction of Hubbard U terms in GGA approach *i.e.,* GGA+U resolves the discrepancy in CFS [107, 225]. In order to predict the size and nature of band gaps and magnetic moments, we have performed the electronic-structure calculations using both GGA and GGA+U approaches.

For theoretical calculations, bulk $Co_{1.50}Y_{0.50}FeSi$ (Y = Co, Fe, Mn, Cr, V, Ti, or Sc) cubic supercell structures consisting of 16 atoms were constructed using the Monte Carlo Special Quasirandom Structure (MCSQS) method [184] which is a part of the open source ATAT toolkit [185] accessible from [186]. The MCSQS method can handle double-site substitutions as described in experimental section above taking care of nearest neighbor interaction and predicts a special quasirandom structure by generating a set of clusters with specific correlations relative to a target random structure. The best MCSQS structures were confirmed after waiting for a long enough

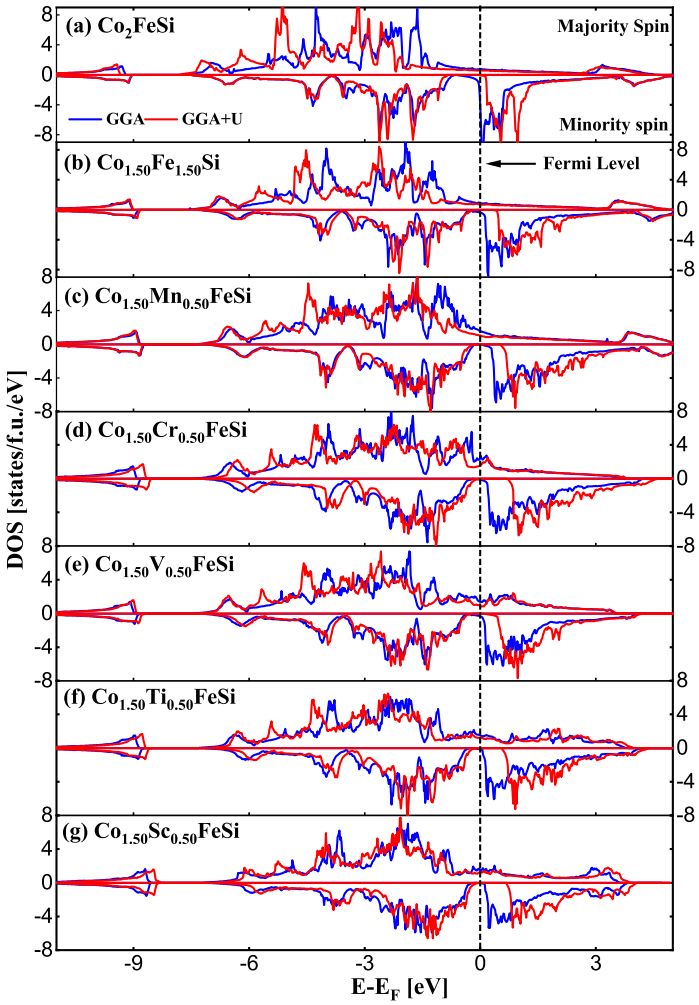

Figure 4.46: Spin polarized total density of states (TDOS) of $Co_{1.50}Y_{0.50}FeSi$ (Y = Co, Fe, Mn, Cr, V, Ti, or Sc) alloys using both GGA (Blue) and GGA+U (Red) methods. Number of states in each plot is scaled with respect to one formula unit.

time until a correlation difference relative to the target random structure approach to zero. The predicted MCSQS structures are in good agreement with configuration I predicted in Table 4.13 (see also Fig. 4.40(b)). The predicted MCSQS structures were then optimized using GGA method. The experimental lattice constants extracted in our experimental work were employed as starting values for the calculations. The optimized lattice parameters are in good agreement with experimental values, increasing with the substitution of atoms with low-valency. All the calculated parameters are presented in Table 4.15.

As shown in Fig. 4.46, Our calculations show the systematic shifting of Fermi level from

conduction band edge in parent compound CFS towards the energy gap in minority-spin channel after substituting low-valence transition metals. In GGA approach, only $Co_{1.50}Mn_{0.50}FeSi$ alloy is observed to be perfect half-metal with Fermi level at energy gap in minority-spin channel. The non-zero contribution to DOS from Fe(I) (which share the same sublattice A with Y atoms) at Fermi level in minority-spin channel is observed to play major-role to destroy the half-metallicity in all other alloys. The calculated magnetic moment in $Co_{1.50}Mn_{0.50}FeSi$ is also in good agreement with that extracted from experiment and expected from Slater-Pauling rule while the calculated moments are way less in other alloys (see Table 4.14 and Table 4.15), given that calculations are done at 0 K and experimental magnetic moments were measured at 5 K. However, the inclusion of electron-electron correlation in GGA+U approach opened the energy gap, as expected in minority spin channel with calculated magnetic moments in good agreement with the experiment and expected from Slater-Pauling rule. The Fermi level is observed to lie within energy gap in minority-spin channel making the systems half-metallic, however energy gap is observed to decrease after low-valence transition metal atom substitution for Co in CFS. The estimated energy gaps at Fermi level in all the alloys are provided in Table 4.15.

Table 4.15: Parameters extraced from DFT calculations (both GGA and GGA+U approach) for type I configuration. In the table M, M_{SP}, $\langle a \rangle$, and Δ represent calculated magnetic moment, Slater-Pauling moment, optimized lattice parameter, and energy gap at Fermi level. The last column shows the tetragonality in the structure. The values in the parentheses represent the calculated values using GGA approach.

Y element	Configurations	4d	4c	4b	4a	M ($\mu_B/f.u.$)	M_{SP} ($\mu_B/f.u.$)	$\langle a \rangle$ (Å)	Tet. (a/c-1)	Δ (eV)
Co	Co_8-Fe_4Si_4	4Co	4Co	4Fe	4Si	6.000(5.484)	6.000	5.636	0.012	0.791
Fe	Co_6Fe_2-Fe_4Si_4	4Co	2Fe,2Co	4Fe	4Si	5.502(5.369)	5.500	5.640	0.012	0.387
Mn	Co_6Fe_2-$Fe_2Mn_2Si_4$	4Co	2Fe,2Co	2Mn,2Fe	4Si	5.000(4.999)	5.000	5.645	0.012	0.575(0.138)
Cr	Co_6Fe_2-$Fe_2Cr_2Si_4$	4Co	2Fe,2Co	2Cr,2Fe	4Si	4.500(4.480)	4.500	5.657	0.012	0.626
V	Co_6Fe_2-$Fe_2V_2Si_4$	4Co	2Fe,2Co	2V,2Fe	4Si	3.999(3.856)	4.000	5.678	0.012	0.176
Ti	Co_6Fe_2-$Fe_2Ti_2Si_4$	4Co	2Fe,2Co	2Ti,2Fe	4Si	3.500(3.463)	3.500	5.690	0.012	0.597
Sc	Co_6Fe_2-$Fe_2Sc_2Si_4$	4Co	2Fe,2Co	2Sc,2Fe	4Si	3.000(2.994)	3.000	5.717	0.012	0.719

4.4.5 Conclusion

In summary, quaternary Heusler alloys $Co_{2-x}Y_xFeSi$ (Y = Co, Fe, Mn, Cr, V, Ti, or Sc, $0 \leq x \leq 1$) were synthesized and a combined experimental and theoretical study of structural,

electronic, magnetic and mechanical properties of quaternary Heusler alloys $Co_{2-x}Y_xFeSi$ (Y = Co, Fe, Mn, Cr, V, Ti, or Sc, $x = 0.50$) were carried out. The alloys were identified as potential half-metallic ferromagnets by *ab initio* electronic structure calculations using GGA+U approach while only $Co_{1.50}Mn_{0.50}FeSi$ is predicted to be potential half-metal in GGA approach. The structural analysis reveals that the alloys exist in cubic Heusler structure. A certain amount of disorder is observed in V and Ti substitued alloys. The magnetic properties were analyzed at both 5 K and 300 K. The saturation magnetic moments of the alloys measured at 5 K are in fair agreement with those expected from Slater-Pauling rule. The results are also in accordance with the electronic structure calculations, indicating the half-metallicity and high spin polarization required for spintronics applications. The Curie temperatures of all compounds ($x = 0.50$) are higher than 700 K, allowing use at room temperature and above. Robust mechanical properties with hardness values increasing with the substitution of Y element of increasing atomic radius are also observed. This way of substitution of low-valence transition metal atoms to design new quaternary Heusler compounds give enormous potential for many room temperature applications such as in spintronics or thermoelectrics and other areas of research, and clearly deserve further exploration on thin films in the future.

4.5 Structural, electronic, magnetic, and mechanical properties of $Co_{2-x}V_xFeSi$ Heusler alloys

4.5.1 Abstract

The influence of V substitution for Co on the structural, electronic, magnetic, and mechanical properties of quaternary Heusler alloys $Co_{2-x}V_xFeSi$ (x = 0, 0.25, 0.50, 0.75, 1) has been systematically investigated. The microstructural and the scanning profile using energy dispersive X-ray analysis suggests the single phase behavior in all alloys except for x = 1. The X-ray diffraction analysis at room temperature reveals $L2_1$ crystal structure promoting lattice expansion after V substitution. The low-temperature saturation magnetic moments, as determined from magnetization measurements, agree fairly well with our theoretical results and also obey the Slater-Pauling rule. Very high Curie temperature is also observed. The alloys are mechanically robust. First-principles calculation with the implementation of a Hubbard correction term (U) is observed to predict half-metallic behavior.

4.5.2 Introduction

Cobalt based full Heusler compounds with stoichiometric composition Co_2YZ, (Co,Y) being two transition metals, and Z being main group element, crystallizing in the $L2_1$ structure have received growing interest due to their potential to be half-metallic ferromagnets, having an energy band gap at the Fermi level (E_F) for minority spin sub-band [41]. The Co_2FeSi system is suitable for spintronic device applications because of its high Curie temperature of $T_C \approx 1100\,\mathrm{K}$ and high magnetic moment of $6\,\mu_B$/f.u. [20]. Standard *ab-initio* calculations fail to correctly describe the electronic band structure of Co_2FeSi since the on-site Coulomb interactions should be explicitly included [137]. The Fermi level in Co_2FeSi falls on the edge of the minority spin conduction band [137], but for applications it is highly desirable for the Fermi level to be located at the middle of the energy gap [107, 152]. This can be achieved either by doping with early transition metal atoms

PUBLISHED AS: 3. R. Mahat*, S. KC, U. Karki, S. Regmi, J. Law, V. Franco, I. Galanakis, A. Gupta & P. LeClair, *Structural, electronic, magnetic, and mechanical properties of $Co_{2-x}V_xFeSi$ Heusler alloys*, IEEE Transactions on Magnetics (2021).

which have larger atomic radius [121].

Several theoretical and experimental studies have been devoted to the partial substitution of the lower valence transition metal atoms in Co_2YZ to tune the electronic and magnetic properties of the parent compound [62, 107, 124, 126, 154, 229]. This has inspired us to synthesize Co_2FeSi, a potential candidate for spintronic applications and investigate the effect of V substitution for Co in Co_2FeSi on structural, electronic, magnetic and mechanical properties, as the experimental synthesis of other end member of the series CoFeVSi has not been reported yet in bulk form. In particular, as will be shown below, the V impurity atoms occupy Fe sites in the ideal Co_2FeSi structure, and the Fe atoms themselves move to the empty Co sites. That is, we propose that $Co_{2-x}V_xFeSi$ can be more accurately depicted as $(Co_{1-\frac{x}{2}}Fe_{\frac{x}{2}})_2(Fe_{1-x}V_x)Si$.

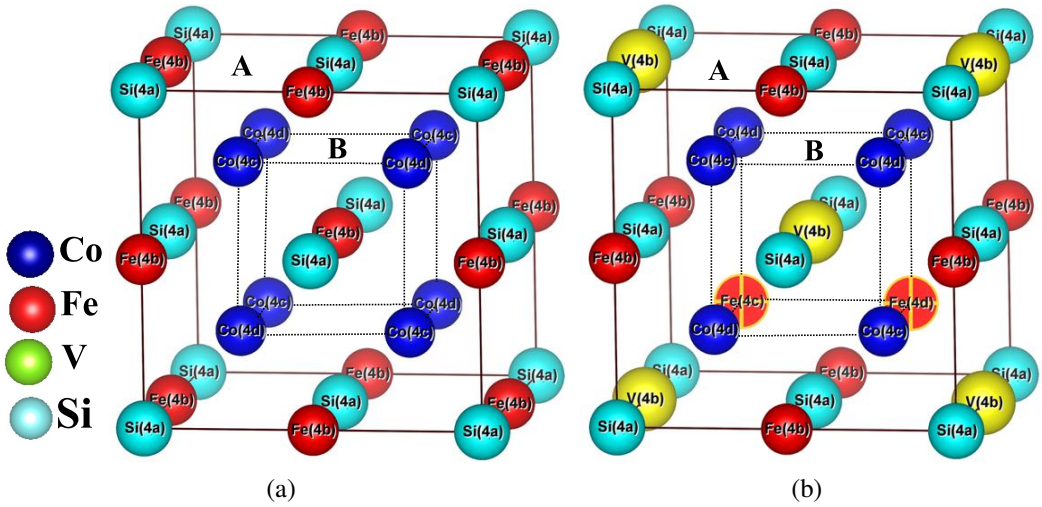

Figure 4.47: Crystal structure in unit cell of (a) Co_2FeSi and (b) $Co_{1.50}V_{0.50}FeSi$ (I) configuration mentioned in Table 4.16 assuming the $L2_1$ structure. The structures are shown in their ideal, unrelaxed forms.

4.5.3 Methods

4.5.3.1 Experimental Methods

The bulk ingots of $Co_{2-x}V_xFeSi$ Heusler alloys with x = 0, 0.25, 0.50, 0.75, 1 at% were prepared by arc melting of constituent elements (at least 99.99% purity) in argon atmosphere at a base pressure of 10^{-4} mbar. The mixture was melted at least 6 times to ensure chemical homogeneity. To further increase homogeneity, as-cast sample pieces were annealed under vacuum at 900°C for 7 days, and cooled slowly in the furnace for optimum crystallization and to promote formation of the $L2_1$ structure. The heat treatments were followed by metallography to produce a metallic shiny surface for microstructure analysis by optical and electron microscopes. After heat treatment and metallography, composition and homogeneity of the samples were again confirmed by using energy dispersive X-ray spectroscopy (EDS) in a JEOL 7000 Field Emission Scanning Electron Microscope. Details of our sample preparation techniques, and metallography can be found in Ref. [163, 164]. The crystal structure was investigated using X-ray diffraction (XRD) using a Bruker D8 Discover X-ray diffractometer equipped with monochromatic Co-Kα (λ = 0.179 nm) radiation. The XRD measurements were carried out on crushed powder samples by rotating around the ϕ axis to minimize surface effects. Rietveld refinement was done using a MATCH! software based on the FullProf algorithm [80]. The low temperature magnetic properties were studied in Quantum Design Physical Properties Measurement System (PPMS), while the high temperature magnetization was measured using LakeShore VSM 7407. The mechanical properties were studied in terms of Vickers hardness by using Buehler model 1600-6100 micro-hardness tester.

4.5.3.2 Computational Methods

For the calculations we have employed the projector-augmented wave (PAW) method by Blöchl [180] as implemented by Kresse and Furthmüller in the Vienna *ab initio* simulation package (VASP) [181]. We have used the generalized-gradient approximation (GGA) to the electronic exchange-correlation functional as parameterized in Ref. [182]. For the calculations we have used

the 16-atom supercell as shown in Fig. 4.47. For the integrations in the **k**-space we used a 64 points per Å^{-1} mesh. The Methfessel-Paxton [232] integration method with smearing width 0.05 eV was used, along with plane-wave cut-off energy of 520 eV and total energy convergence of 10^{-7}eV/cell. Full relaxation of cell volume, shape and atomic positions were performed until the forces on each atom become less than 10^{-2} meV/cell using the conjugate-gradient method. To account for the on-site electron correlations the GGA+U scheme has been employed [189]. Following the work by Kandpal *et al.* [137, 191], we have used for the d-orbitals of the three transition metal atoms (Co, Fe and V) the values 1.92 eV, 1.80 eV, and 1.34 eV, respectively, for the on-site effective Coulomb repulsion term U.

4.5.4 Results and Discussions

4.5.4.1 Experimental results and Discussions

4.5.4.1.1 Structural and atomic order analysis

When the impurity phase contents are either below the detection limit of XRD (less than roughly 5% of the overall volume) or amorphous in nature, optical microscopy and SEM of polished and etched samples are very helpful to characterize the microstructure [105, 154, 163, 164]. Single phase behavior was observed from optical and electron microscopy except for $x = 1$ in $Co_{2-x}V_xFeSi$ alloy series (not shown here). The stoichiometry of all the single-phase samples was confirmed as the target composition within an instrumental uncertainty of $\sim 5\%$ using EDS.

Table 4.16: Possible site assignments for cubic $Co_{2-x}V_xFeSi$ with corresponding goodness of fit parameter for $x = 0.50$.

Type	4a (0,0,0)	4b $(\frac{1}{2},\frac{1}{2},\frac{1}{2})$	4c $(\frac{1}{4},\frac{1}{4},\frac{1}{4})$	4d $(\frac{3}{4},\frac{3}{4},\frac{3}{4})$	$\chi^2_{x=0.50}$
I	Si	$Fe_{1-x}V_x$	$Co_{1-x/2}Fe_{x/2}$	$Co_{1-x/2}Fe_{x/2}$	1.6
II	Si	$Fe_{1-x}V_x$	$Co_{1-x}Fe_x$	Co	1.9
III	Si	$Co_{1-x}V_x$	Fe	Co	2.3
IV	Si	Fe	$Co_{1-x}V_x$	Co	2.7

Fig. 4.48 shows the powder XRD patterns for $Co_{2-x}V_xFeSi$ alloys annealed at 900°C for

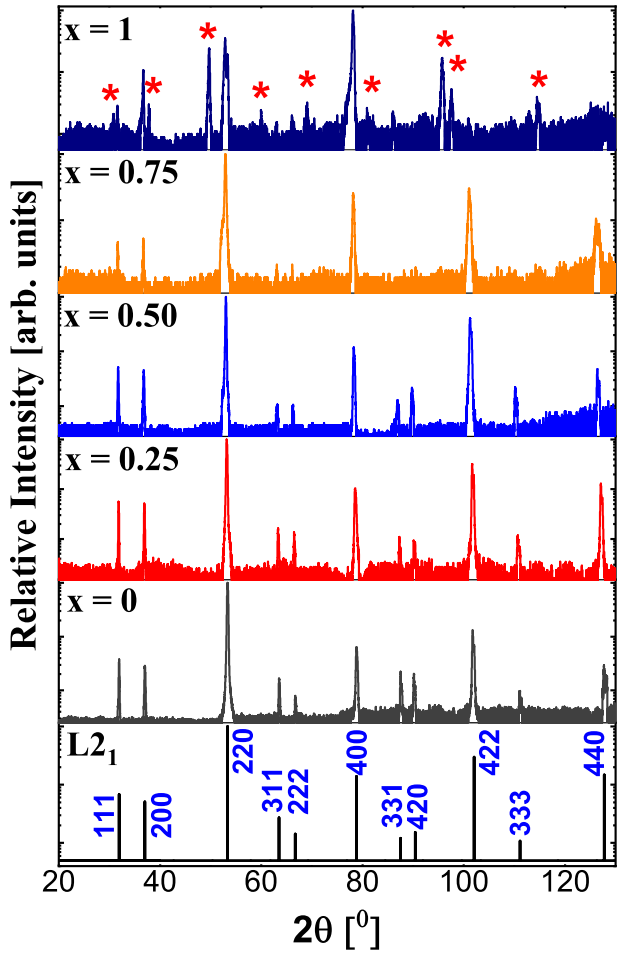

Figure 4.48: Experimental XRD patterns of $Co_{2-x}V_xFeSi$ alloy series, here, $*$ corresponds to the secondary phase/unknown impurity phase. The first from the bottom is the simulated XRD pattern for ordered $L2_1$ structure of CFS. The relative intensity (y-axis) is plotted in log scale so that all the peaks can be seen clearly.

7 days, measured at room temperature. Consistent with our microstructural and compositional analysis, single phase behavior can be seen only for $0 \leq x \leq 0.75$ while $x = 1$ contains several impurity peaks (represented by asterisks) which can not be indexed with its cubic $L2_1$ structure. Simple structural information of a cubic single phase can be gained by indexing all XRD peaks. For all cubic single-phase alloys, only three distinct Heusler-like reflection peaks (h, k, l all odd or even) are observed; fundamental peaks with $h+k+l = 4n$, even superlattice peaks with $h+k+l = 4n+2$ and odd superlattice peaks with $h+k+l = 2n+1$. Heusler alloys in the ordered $L2_1$ structure are characterized by the presence of superlattice diffraction peaks; the presence of (111)

peak indicates the chemical ordering of atoms in octahedral positions, and (200) peak indicates the order for atoms in tetrahedral positions, while (220) peak is a principal reflection which is independent of the state of the order [72]. The superlattice reflections are clearly observed in the single phase XRD patterns, which reveal that the alloy exists in ordered cubic Heusler structure (Cu_2MnAl type) with $Fm\bar{3}m$ space group (#225).

To further analyze the chemical ordering, we adopted the atomic configurations considered in [105, 154] and performed Rietveld refinement of experimental XRD pattern for $x = 0.50$ considering four non-degenerate configurations. These four non-degenerate configurations and corresponding goodness of fit parameters for $x = 0.50$ are shown in Table 4.16. The Rietveld refinement revealed that the best fit configuration is (I) and the corresponding crystal structure is shown in Fig. 4.47(b). In $Co_{2-x}V_xFeSi$, V is the least electronegative (1.63 Pauli units) [201]. Therefore, we presume that V will displace the Fe atoms towards vacated Co sites, and V will then fill the site previously occupied by Fe forming an ionic-type sublattice with Si, since it has a larger electronegativity (2.01 Pauli units) than Co and Fe (1.88 and 1.83 Pauli units, respectively). Stability is increased by V donating its electrons to other elements in the alloy. The Co and displaced Fe atoms with intermediate electronegativities then occupy the tetrahedral sites [61].

Lattice parameters were calculated using Cohen's method with a Nelson-Riley extrapolation [171]. There is a dependence of the lattice parameter on the V concentration, as one would expect given the larger atomic radius of V (171 pm) compared with Co (152 pm) [153]. The variation is essentially linear, consistent with Vegard's law [205], and slightly less than 1% over the entire composition range. The extracted lattice parameters are shown in Table 4.17.

4.5.4.1.2 Magnetic Characterization

Most of the Co-based half-metallic Heusler alloys show a Slater-Pauling-like behavior for the magnetization when crystallized in a fully ordered state [206]. In the $Co_{2-x}V_xFeSi$ system, the total number of valence electrons change from 30 in Co_2FeSi to 26 in CoFeVSi. Therefore, the Slater-Pauling behavior predicts that the saturation magnetic moment should decrease with the partial

substitution of V for Co, and specifically according to $M(x) = 6 - 4x\,[\mu_B/\text{f.u.}]$ for $Co_{2-x}V_xFeSi$.

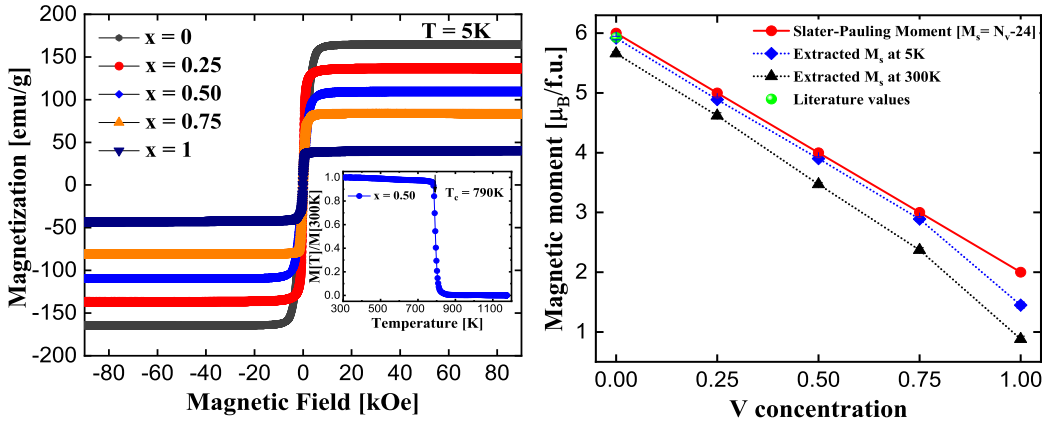

(a) (b)

Figure 4.49: (a) The field-dependent magnetization at 5 K of $Co_{2-x}V_xFeSi$ $(0 \leq x \leq 1)$. The inset shows the temperature dependence of magnetization at 100 Oe for $x = 0.50$. (b) The saturation magnetic moment versus V concentration, both experimental and expected from Slater Pauling rule for half metals. The green data point represents a reported literature value [20].

Table 4.17: Experimental lattice parameters and saturation magnetic moments at T = 5 K along with the Slater-Pauling (S-P) values of $Co_{2-x}V_xFeSi$ alloy series. The numbers in parentheses are the uncertainty in the last digit, *e.g.*, $5.92(3) = 5.92 \pm 0.03$.

x	Expt. lattice parameter (Å)	Expt. M_s (μ_B/f.u.)	S-P (μ_B/f.u.)	Hardness (GPa)
0	a = 5.641(1)	5.92(3)	6.00	7.33(4)
0.25	a = 5.656(1)	4.92(4)	5.00	8.52(5)
0.50	a = 5.673(1)	3.90(3)	4.00	9.85(7)
0.75	a = 5.683(3)	2.89(4)	3.00	11.37(8)
1[†]	a = 5.694(6)	1.45(5)	2.00	11.79(10)

[†] Multiphase specimen

Fig. 4.49(a) shows the magnetization curves measured at 5 K. The magnetization curves shown in Fig. 4.49(a) are characteristic for ferromagnets. All the alloys are saturated in magnetic field of about 5 kOe, indicating small magnetocrystalline anisotropy. The spontaneous magnetizations (M_s) were determined by the linear extrapolation to magnetic field (H) = 0 of magnetization curves. The saturation magnetic moments are in good agreement with those expected for Slater-Pauling half metals (see red data points) and decrease almost linearly with the increase of V content (see Fig. 4.49(b)). The decrease of the total saturation magnetic moment with the increase in V content

can only be attributed to the decrease in number of Co atoms. The magnetic moment per formula unit for $x = 0$, *i.e.*, Co_2FeSi is measured to be 5.92 μ_B, which is also in good agreement with reported results [20]. The slight deviation from integer value of magnetic moment could be due to the slight variation in the stoichiometry of the compounds, weighing and measurement errors, partial surface oxidation, and the measurement temperature of 5 K. All experimentally extracted saturation magnetic moments are also in good agreement with those obtained from first-principle calculations, as described in the forthcoming section. We also measured the saturation magnetization versus temperature under a constant magnetic field of 100 Oe for $x = 0.50$ (see inset in Fig. 4.49(a)) which shows an abrupt decrease at about 790 K which is the measured Curie temperature.

The experimentally-determined lattice parameters, saturation magnetic moments at 5 K along with the Slater-Pauling (S-P) values of all specimens in $Co_{2-x}V_xFeSi$ alloy series are summarized in Table 4.17.

4.5.4.1.3 Vickers micro hardness

Adaptation of materials to industrial applications requires mechanical robustness to undergo repetitive thermal cycling and resist cracking from vibrations. Fig. 4.50 shows the variation of Vickers micro hardness of the alloy series with V concentration measured at room temperature. Hardness values reported are the averages of data taken from at least 12 different regions of each sample with 0.2 kg load and 10 s loading time. The Vickers hardness is calculated from

$$HV = 1.8544F/D^2\,[\mathrm{kg/mm^2}] \tag{4.23}$$

where, D is the diagonal length of the impression of the diamond probe. Relatively high hardness values are measured, approaching 11.79 GPa for $x = 1$ (see Table 4.17) , comparable to the highest values reported for Heuslers in the literature [105, 154, 156, 158, 163, 164, 209]. The hardness is observed to increase almost linearly with increasing V concentration.

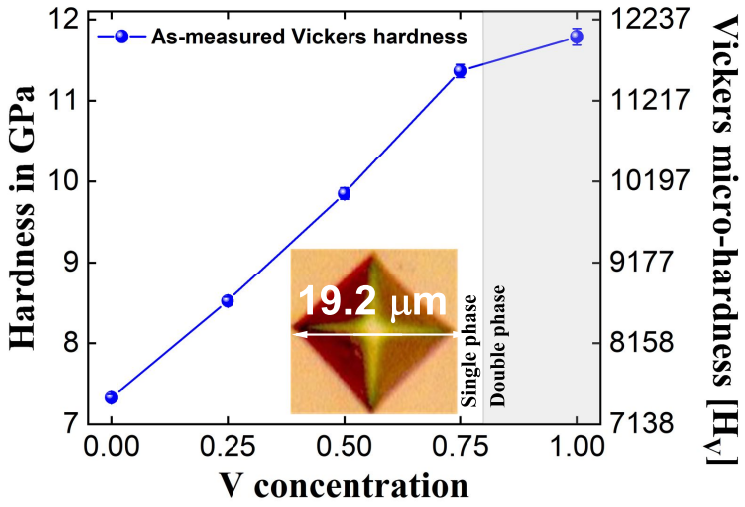

Figure 4.50: Vickers hardness versus V concentration in $Co_{2-x}V_xFeSi$, all annealed at 900°C for 7 days, with imprint of the indenter with radial cracks for $x = 0.50$ [bottom center].

4.5.4.2 Theoretical Results and Discussions

From our experiments, it is clear that V substitution for Co in Co_2FeSi gives stable single phases except for $x = 1$ with XRD patterns consistent with the $L2_1$ structure. In order to obtain further information about the electronic, and magnetic properties of the $Co_{2-x}V_xFeSi$ alloy series and better understand the experimental results, we created alloys structures using the Monte Carlo Special Quasirandom Structure (MCSQS) method for x = 0, 0.25, 0.50, 0.75, and 1. The MCSQS method can handle double-site substitutions taking care of nearest neighbor interaction which makes it ideal for predicting the atomic structure of each concentration. After constraining the supercell to be cubic, the best MCSQS structures were confirmed from negative maximum of correlation functions. Our MCSQS structures are in good agreement with configuration I predicted in Table 4.16 (see also Fig. 4.47(b)) and are composed of a 16 atoms supercell. This reinforces our idea that the system should be thought of as $(Co_{1-\frac{x}{2}}Fe_{\frac{x}{2}})_2(Fe_{1-x}V_x)Si$.

MCSQS candidate structures were then optimized using GGA method. The optimized lattice parameters are 5.637, 5.647, 5.658, 5.574, and 5.682 (Å) for x = 0, 0.25, 0.50, 0.75, and 1 respectively in good agreement with experimental values, increasing with the increase of V content. We used both GGA and GGA+U approach to study electronic and magnetic properties. Usu-

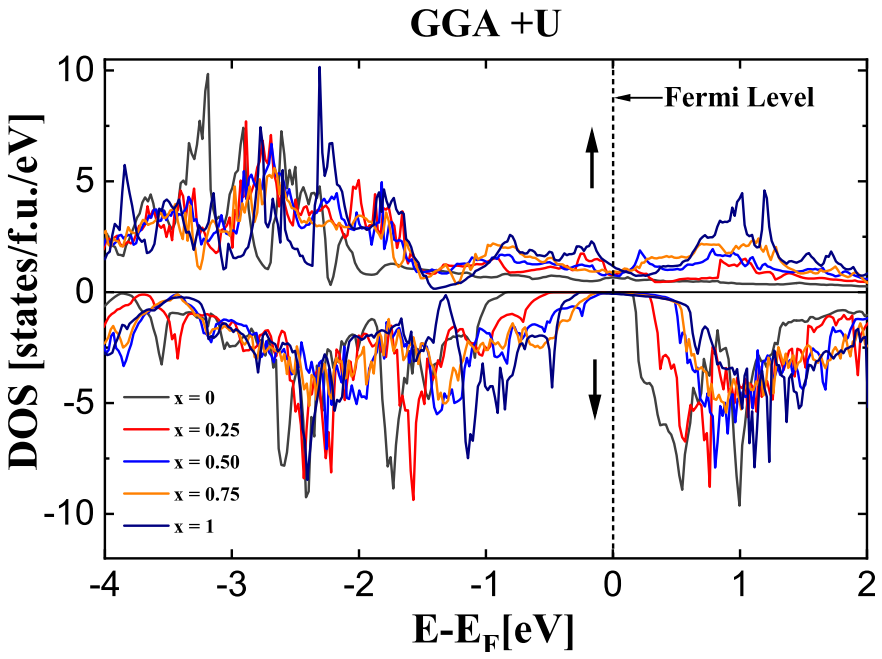

Figure 4.51: Spin polarized DOS for $Co_{2-x}V_xFeSi$ ($x = 0$, 0.25, 0.50, 0.75, and 1) calculated using the GGA+U approach. Number of states is scaled with respect to one formula unit. The vertical dotted line represents Fermi level. The up and down arrows represent majority and minority spin channels respectively.

ally, Heusler alloys exhibit localized moments where electron-electron correlations on localized d-states of Co, Fe, and V may play an important role. The GGA+U is used to resolve the discrepancy between the theoretical and measured magnetic moment observed in GGA approach. The plain GGA calculations are considered not sufficient to explain the magnetic moments in Co_2FeZ systems [137].

Fig. 4.51 shows the calculated spin resolved density of states (DOS) of $Co_{2-x}V_xFeSi$ alloys using the GGA+U method. Our calculations using GGA approach (not shown here) show nearly half-metallic behavior after V substitution as the band gap is present in the vicinity of the Fermi level in minority spin channel and Fermi level is observed to fall in conduction band edge for Co_2FeSi ($x = 0$) as reported in [7]. The calculated magnetic moments using GGA approach are found to be 5.44 $\mu_B/f.u.$, 4.82 $\mu_B/f.u.$, 3.84 $\mu_B/f.u.$, 2.86 $\mu_B/f.u.$, and 1.95 $\mu_B/f.u.$ for x = 0, 0.25, 0.50, 0.75, and 1 respectively. However, the inclusion of electron-electron correlation in GGA+U approach opened the energy gap, as expected in minority spin channel with calculated

magnetic moments 6.00 $\mu_B/f.u.$, 5.00 $\mu_B/f.u.$, 4.00 $\mu_B/f.u.$, 2.98 $\mu_B/f.u.$, and 1.99 $\mu_B/f.u.$ for x = 0, 0.25, 0.50, 0.75, and 1 respectively. Although, the energy gap is observed to decrease with the increase of V content, the half-metallicity is robust for $x = 0.25$ as Fermi level is observed to fall almost at the middle of energy gap in minority spin channel.

4.5.5 Conclusion

In conclusion, we performed a detailed experimental and theoretical study on the structural, electronic, magnetic and mechanical properties of V-substituted Co_2FeSi Heusler alloys. The alloys are found to crystallize in the face-centered cubic structure for $0 \leq x \leq 0.75$. The isothermal magnetization curves showed that the saturation magnetic moment decreases with the increase of V content and the values at 5 K are found in good agreement with the Slater-Pauling rule of thumb for half-metals. A high Curie temperature of T_c = 790 K is found for $x = 0.50$, allowing for applications at room temperature and above. First-principles calculations with GGA+U approach predicted half-metallic electronic structures which makes them suitable for spintronic device applications.

4.6 Tuneable structure and magnetic properties in $Fe_{3-x}V_xGe$ alloys

4.6.1 Abstract

We report a detailed experimental and theoretical study of the effects of V substitution for Fe atom on the structural, magnetic, transport, electronic and mechanical properties of an off-stoichiometric $Fe_{3-x}V_xGe$ intermetallic alloy series $(0 \leq x \leq 1)$. Single phase microstructures are observed for $x < 0.75$, whereas higher V content alloys $x \geq 0.75$ are multi-phased. Vanadium substitution is observed to induce a diffusionless martensitic phase transformation from a Heusler-like $L2_1$ structure to hexagonal DO_{19} structure, as corroborated by Differential Scanning Calorimetry results. The vanadium substitution is also found to decreases the grain size, inhibiting the grain growth by pinning the grain boundary migration. All the alloys in the series are found to be soft ferromagnets at 5 K with saturation magnetic moment and Curie temperature decreasing as V concentration increases. The low temperature saturation magnetic moment is in close agreement with the expected Slater-Pauling values for the $L2_1$ phases, while the hexagonal samples have markedly higher values of saturation moments. First-principle calculations agree with the experimental findings and reveal that V substitution energetically favours one of the Fe sites in Fe_3Ge. The electrical resistivity measured over the temperature range from 5 K to 400 K shows negative temperature coefficient of resistivity at high temperatures with increasing the V concentration. Relatively high mechanical hardness values are also observed, with the values increasing with increasing V content. Vanadium substitution is found to play a central role in tuning the mechanical properties, stabilising the $L2_1$ structure, and shifting the martensitic transformation temperature to higher values from that of parent Fe_3Ge.

PUBLISHED AS: R. Mahat*, S. KC, D. Wines, S. Regmi, U. Karki, R. White, F. Earsan, C. Ataca, P. Padhan, A. Gupta & P. LeClair, *Tuneable structure and magnetic properties in $Fe_{3-x}V_xGe$ alloys*, Journal of Alloys and Compounds, **830**, 154403(2020).

4.6.2 Introduction

Heusler alloys, first discovered by and named after Fritz Heusler in 1903 [48], are very useful for applications in information storage and spintronics as well as many other areas [1, 66, 88, 96, 233, 234]. For applications in magnetics and spintronics [66], the inherently low magnetocrystalline anisotropy in cubic Heusler alloys can be limiting factor [67]. Identifying a hexagonal Heusler analogue [233] that retains half metallicity and exhibits a high magneto-crystalline anisotropy may be very attractive for applications such as perpendicular media, current perpendicular to plane giant magnetoresistance (CPP-GMR), and spin-torque-transfer RAM (STT-RAM) [68–71, 235]. However, half-metallicity has been predicted for some Heusler analogues in the hexagonal DO_{19} ($P6_3/mmc$, space group no. 194 [64, 65]) crystal structure [174, 233, 236].

The intermetallic compound Fe_3Ge is well known to crystallize in two crystal structures, a cubic $L1_2$ phase ($Pm\bar{3}m$, space group no. 221 [64, 65]) at low temperatures ($< 700^{\circ}C$) and hexagonal DO_{19} phase at higher temperatures ($> 700^{\circ}C$) [237, 238]. In this compound, the forward $L1_2$ to DO_{19} structural transformation takes place easily but the reverse DO_{19} to $L1_2$ transformation is difficult to achieve under normal cooling conditions, and often one retains the high temperature DO_{19} crystal structure [21, 238, 239]. A few attempts have been made in the past on the substitution of V for Fe atom in Fe_3Ge alloy and structural transformations are studied. Nakagawa and Kanematsu [240], by means of X-ray and magnetic studies have suggested the hexagonal DO_{19} phase of parent Fe_3Ge transforms to a body centered cubic (A2) structure for $x \geq 0.50$. They have reported the structure to be A2 due to the absence of superlattice peaks in X-ray diffraction. However, later Beitollahi and Booth [241] have reported structure to be $L2_1$ ($Fm\bar{3}m$, space group no. 225 [64, 65]) based on the presence of (111) superlattice peak in their room temperature neutron diffraction patterns for nominally single phase samples with $x \geq 0.60$. In spite of several investigations [240, 241] aimed at understanding the structural phase transformation, the detailed mechanisms responsible for such transformations are still far from being understood. Further, they lack any microstructural analysis. Large magneto-optical Kerr rotations have also been observed in the same system [242].

To our best knowledge, there is not yet a detailed report of the structural, magnetic, transport, and mechanical properties of $Fe_{3-x}V_xGe$ in the bulk form, neither experimentally nor theoretically. Previous investigations focused on substituting V in one of Fe site in Fe_3Ge under higher temperature annealing conditions. Reports on low temperature annealing conditions are not available thus far. In this study, we have addressed different annealing conditions and systematically studied the microstructure and phase purity, magnetic properties, electrical transport, differential scanning calorimetry, and hardness in addition to structure determination to understand the structure-property relationships in this interesting family of Heusler-like compounds. Particular attention has been paid to metallography and microstructural analysis to determine which regions of the phase diagram yield single phase specimens.

4.6.3 Experimental details

$Fe_{3-x}V_xGe$ $(0 \leq x \leq 1)$ bulk samples with x varying in the steps of 0.125, were prepared by arc melting of stoichiometric amounts of the constituents in an argon atmosphere at 10^{-4} mbar (see details in Supplementary Information). Care was taken to avoid oxygen contamination. As an oxygen getter, Ti was melted inside the vacuum chamber separately before melting the compound to avoid oxygen contamination. The as-cast ingots were examined repeatedly using scanning electron microscopy (SEM) and energy dispersive X-ray spectroscopy (EDS) analysis in a JEOL 7000 Field Emission Scanning Electron Microscope (FESEM) to confirm homogeneity and correct composition. After confirming the anticipated target composition, the polycrystalline ingots were then annealed in an evacuated quartz tube at different temperatures ranging from 650°C to 1000°C for different dwell times (5 days to 25 days), and at the end of each annealing cycle, the samples were cooled slowly in the furnace to get optimum crystallization to promote the formation of $L2_1$ structure.

Annealed ingots were polished for spectroscopic investigations (see details in Supplementary Information). The polishing was done, first grinding using silicon carbide abrasive discs (120 through 1200 grit size) followed by diamond suspension polishing. Colloidal silica suspension of

grit size 0.02 μm was used at last for the finest polishing. After obtaining a smooth and reflective surface, the samples were etched with Adler etchant (9 g of $CuNH_3Cl$, 45 g of hydrated $FeCl_2$, 150 mL of HCl and 75 mL of DI Water) [243]. The purpose of etching is that etchant attacks different phases present in the samples at different rates, and provides high quality surface contrast for microstructure characterization.

The crystal structure was investigated by means of X-ray diffraction (XRD) using a Bruker D8 Discover X-ray diffractometer equipped with monochromatic Co-Kα (λ = 0.179 nm) radiation. The polished samples were rotated around the ϕ axis during the XRD measurement to minimise surface effects. CaRIne crystallography 4.0 software [78] as well as in-house PYTHON code [79] including the dispersive corrections to the atomic scattering factors were used to simulate the XRD patterns to compare with the experimental XRD patterns. XRD analysis (Rietveld refinement) was done using the CRYSTAL IMPACT MATCH! software based on the FULLPROF algorithm [80] that uses the least-square refinement between experimental and calculated intensities. The crystal structures determined from XRD were further confirmed using electron backscatter diffraction (EBSD) phase mapping analysis in a JEOL 7000 FESEM system. The low temperature magnetic and electrical transport properties were studied in Quantum Design Physical Properties Measurement System (PPMS), while the high temperature magnetization was measured using the Lakeshore VSM 7410. DSC measurements were carried out to confirm the diffusionless martensitic transformation (with a ramp rate 10°C/min during heating and cooling) in the temperature range up to 1200°C in a Setaram Labsys Evo. in Ar gas flux at the rate of 20 mL/min to prevent the possible oxidation of the samples. The temperature and the heat reaction were calibrated using high purity indium, aluminium, silver and nickel standards. The mechanical properties were studied in terms of Vicker's hardness by using Buehler model 1600-6100 micro-hardness tester.

4.6.4 Experimental Results and Discussions

4.6.4.1 Microstructural and Compositional analysis

XRD is not always sufficient to confirm the phase purity if the impurity phase content is less than 5% of the overall volume [105, 168]. In such case, optical microscopy and SEM of polished and etched samples are the most direct ways to characterise micro-structure by revealing grain boundaries, phase boundaries, and inclusion distribution. Observing different contrast in etched sample seen from optical microscopy, we can speculate the presence of impurity phases, and SEM with EDS/EBSD can be used to directly quantify whether areas of different contrast represent impurity phases or possible different crystallite orientations.

Starting from the fully stoichiometric Fe_2VGe, multi-phase microstructure was obtained in every heat treatment performed at 800, 900, 950, or 1000°C for different dwelling times; 3, 5, 7, or 14 days. However, with the substitution of Fe for V, the secondary phase began to disappear and uniform single phase behavior was observed in the V composition range $(0 \leq x \leq 0.625)$. All other higher V concentration produced multiphase behavior (see details in Supplementary Information). Fig. 4.52 shows microstructure of all single phase samples observed under high temperature annealing conditions *i.e.*, 7 days at 950°C using optical microscope. The microstructure of the high temperature (> 700°C) phase for $x = 0$ *i.e.*, the parent Fe_3Ge compound is also presented in Fig. 4.52 already known to be stable, annealed under similar conditions [21, 238, 239].

In addition to high temperature annealing, we also attempted to investigate low temperature annealing of our V-substituted alloys (see details in Supplementary Information) to check if the samples which showed single phase microstructure at high temperature annealing conditions were indeed stable at low temperature as well, as low temperature annealing is missing in previous works. Low temperature annealing is also necessary to shed more light on the structural phase transformation as this alloy series is reported to show structural phase transformation from low temperature $L1_2$ or $L2_1$ to high temperature DO_{19} phase, similar to parent Fe_3Ge [21, 238, 239]. Single phase granular microstructures was observed for the intermediate compositions $x = 0.50$ and

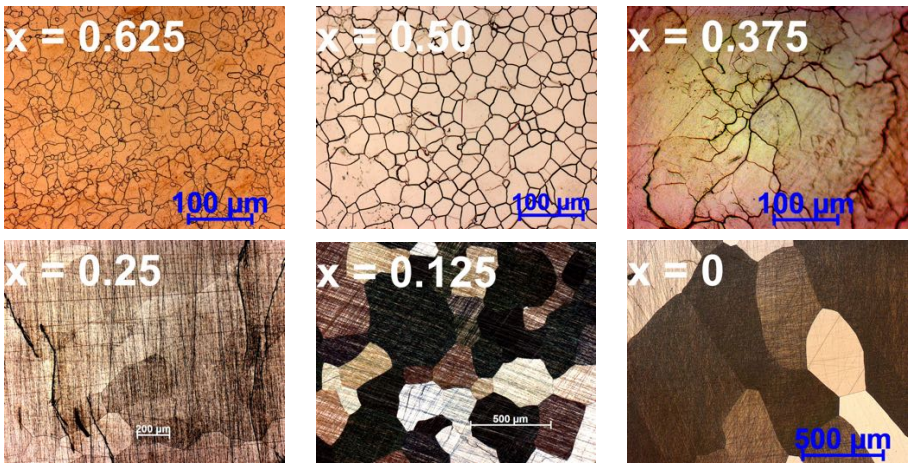

Figure 4.52: Optical micrograph of $Fe_{3-x}V_xGe$ ($0 \leq x \leq 1$) heat treated at 950°C for 7 days showing the grain structures. The samples were etched for 25 seconds using the Adler etchant.

0.25. In the case of Fe_3Ge ($x = 0$), small amounts of secondary phases were observed in agreement with detailed studies on the parent Fe_3Ge compound [67, 239, 240].

The composition of all the stable single phase samples in the series are confirmed to be close to the target composition within $\sim 5\%$ instrumental uncertainty range using EDS (see details in Supplementary Information). Fig. 4.53 shows the SEM images displaying the microstructure of

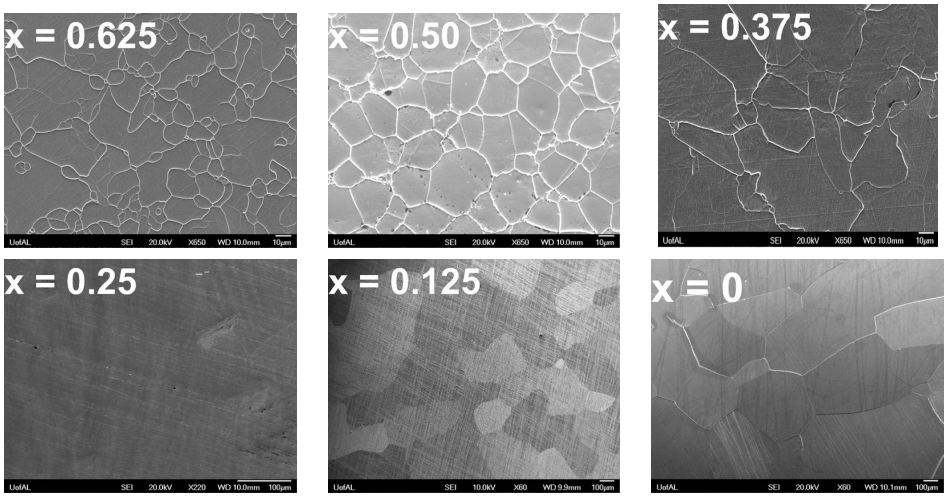

Figure 4.53: SEM micrograph of $Fe_{3-x}V_xGe$ ($0 \leq x \leq 1$) heat treated at 950°C for 7 days showing the granular microstructure. The magnification of each micrograph is indicated at the bottom, like $\times 650$ for $x = 0.50$.

all single phase samples (see Supplementary Information for SEM images of low temperature

annealed samples). Relatively small grains are observed compared to high temperature annealed samples. The effect of V substitution on the microstructure is substantial. The average grain size is observed to decrease dramatically with increasing the V content indicating the V substitution can effectively inhibit the grain boundary migration. The dramatic increase in grain size with decreasing V content is also accompanied by the increase of roughness of certain grains, producing different color contrast between neighboring grains in bright-field as reported in the literatures [244, 245].

4.6.4.2 Crystal structure and atomic order analysis

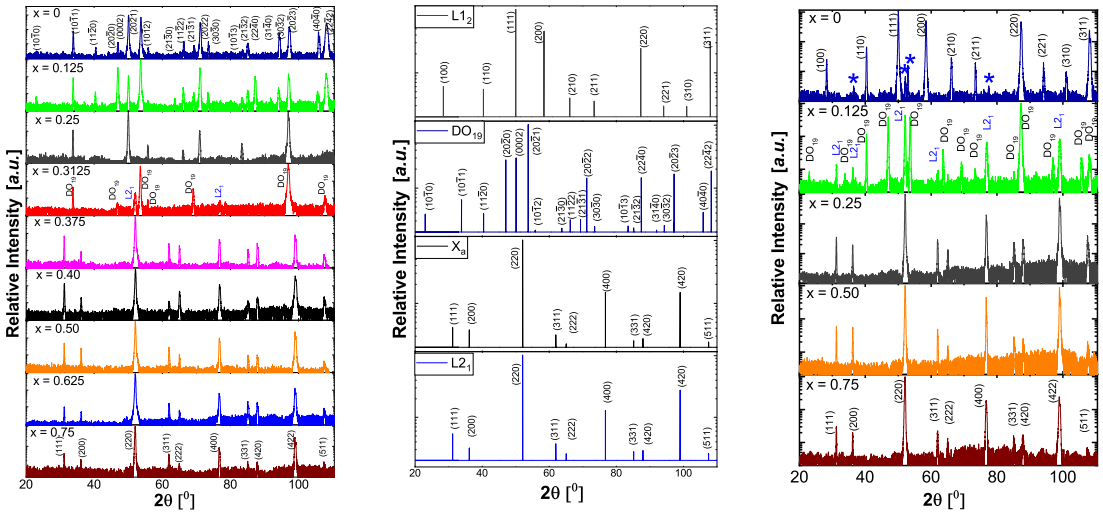

(a) (b) (c)

Figure 4.54: Experimental XRD patterns of $Fe_{3-x}V_xGe$ alloy series annealed at (a) 950°C for 7 days and (c) 650°C for 25 days using X-ray source, and (b) simulated powder XRD patterns using CaRIne. For (a), the upper indexing is for the DO_{19} structure and the lower indexing is for the $L2_1$ structure. For (c), the upper indexing is for the $L1_2$ structure and the lower indexing is for the $L2_1$ structure.

Fig. 4.54(a) shows the XRD patterns of the $Fe_{3-x}V_xGe$ alloy series annealed at 950°C for 7 days after polishing and etching, using a Co-K_α radiation source. The crystal structure obtained from the XRD data suggests the presence of $L2_1$ Heusler structure for $0.375 \leq x \leq 0.75$ and hexagonal DO_{19} structure for $0 \leq x \leq 0.25$, whereas the intermediate composition $Fe_{2.6875}V_{0.3125}Ge$

showed the co-existence of both phases and onset of structural phase transformation (see Fig. 4.54(a) fourth row from the top). Fig. 4.54(c) shows the XRD pattern of $Fe_{3-x}V_xGe$ alloys series annealed at 650°C for 25 days. Interestingly, for the lower temperature annealing it showed Heusler-like $L2_1$ ordering for $x = 0.25$, while at higher temperature annealing it showed DO_{19} ordering. The low temperature cubic $L1_2$ crystal phase of the parent Fe_3Ge compound is also observed with some impurity peaks (represented by asterisks) with lattice constant $a = 3.6667$ Å as reported in the literature [246].

For all cubic single-phase compositions $0.375 \leq x \leq 0.75$, only three distinct Heusler-like reflection peaks (h, k, l all odd or even) are observed; fundamental peaks with $h+k+l = 4n$, even superlattice peaks with $h+k+l = 4n+2$ and odd superlattice peaks $h+k+l = 2n+1$. In Heusler-like alloys, presence of (111) peak indicates the chemical ordering of atoms in octahedral positions, and (200) peak reflects the superlattice reflections due to atoms in tetrahedral positions, while (220) peak is a principal reflection. None of the low angle superlattice peaks are absent in all cubic structures which indicates a degree of sublattice ordering. No mixed odd/even indices are observed in reflection peaks indicting that all cubic samples are crystallised in the face-centred cubic Heusler-like structure. The intensity of superlattice peak (111) is greater than that of (200) peak in all stable cubic phases consistently, though as noted below texturing effects makes it difficult to rely on XRD peak intensities.

Considering the fact that Heusler-like compounds can crystallize in a number of structures, particularly the ordered $L2_1$ ($Fm\bar{3}m$, space group no. 225 [64, 65]) and X_a ($F\bar{4}3m$, space group no. 216 [64, 65]) as well as the disordered A2 and B2 phases, structure assignment should be undertaken carefully. We can argue here that there is no complete A2 and B2 disorder on the basis of presence of low angle superlattice peaks in all stable cubic compositions. Furthermore, the distinction between $L2_1$ and X_a structure is rather challenging from X-ray diffraction experiment if the participating elements in the alloy have similar X-ray scattering properties.

However, Beitollahi and Booth [241] previously proposed an $L2_1$ structure for x = 0.6 to 1.0, which we corroborate here (see Table 4.18). Our construction of possible structures is as follows;

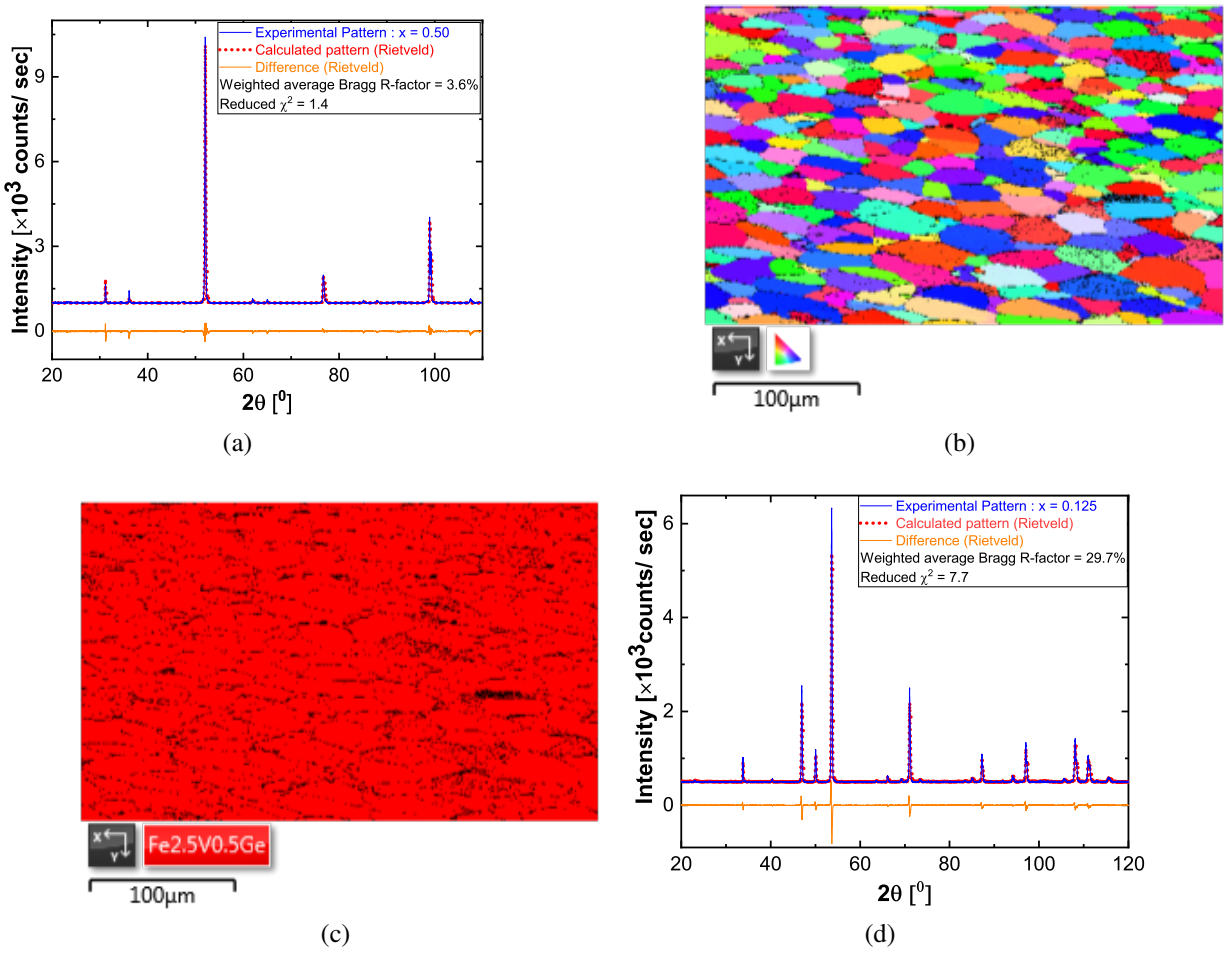

Figure 4.55: (a) The Rietveld refinement of XRD pattern showing a signature of good fit with the proposed crystal model $L2_1$, (b) IPF color map, (c) The corresponding EBSD phase color map of the same area of $Fe_{2.50}V_{0.50}Ge$ in SEM, and (d) The Rietveld refinement of XRD pattern for $Fe_{2.875}V_{0.125}Ge$ with the proposed DO_{19} crystal structure.

starting from parent Fe_3Ge compound, where Fe atoms occupy 4b and 8c (or 4c and 4d) sites whereas Ge atom fills 4a site. In this picture, the substituted V atom can have several possible ways to fill the crystal structure; it can replace the Fe atom on 4b site, or 4c site, or 4d site. It is also possible for V atom to replace Ge atom to other site and fill the vacant position, however in the experimental XRD pattern we confirm that the Ge atoms form an *fcc* superstructure on the underlying *bcc* superlattice. Hence, we argue that 4a site is completely ordered. Further, the replacement of Fe atom on 4c and 4d site doesn't alter the X-ray intensity as these sites belong to the same sublattice (with octahedral symmetry). In view of this, we are left with two possibilities

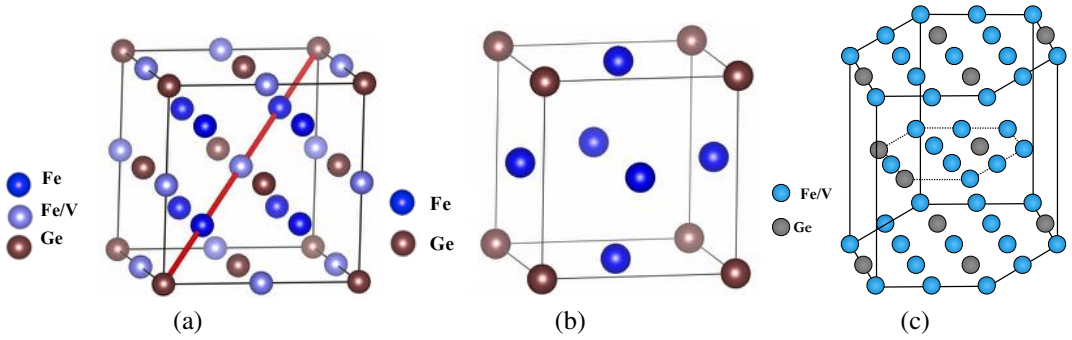

Figure 4.56: Various crystal structures (a) $L2_1$, (b) $L1_2$, and (c) DO_{19}

and we try to push further XRD based analysis to shed light on the exact atomic order of the alloys. To further narrow down the exact atomic ordering, we simulated the XRD patterns for $Fe_{2.50}V_{0.50}Ge$ considering different crystal structures (see Fig. 4.54(b)). The experimental XRD pattern observed matches to $L2_1$ structure generated in either CaRIne 4.0 simulations or CRYSTAL IMPACT MATCH, or our in-house python code for $Fe_{2.50}V_{0.50}Ge$. The superlattice peaks (111) and (200) have a little bit higher intensity than those generated from simulations, which might be due to texturing effects, given the large grain size we observe ($\sim 30\,\mu$m). As the crystal structure of parent Fe_3Ge is hexagonal DO_{19} at higher temperature ($> 700^{\circ}$C) and cubic ($L1_2$) at lower temperature ($< 700^{\circ}$C), the $L1_2$ crystal structure was also simulated using CaRIne 4.0 software, but none of the intensities and peak positions matched with the experimental pattern (see Fig. 4.54(b)).

Table 4.18: Possible site assignments for cubic $Fe_{3-x}V_xGe$ assuming two space groups; $L2_1$ ($Fm\bar{3}m$) and X_a ($F\bar{4}3m$).

Type	Ge	$Fe_{1-x}V_x$	Fe	Fe
$L2_1$	4a (0,0,0)	4b($\frac{1}{2},\frac{1}{2},\frac{1}{2}$)	8c ($\frac{1}{4},\frac{1}{4},\frac{1}{4}$)	8c ($\frac{1}{4},\frac{1}{4},\frac{3}{4}$)
X_a	4a (0,0,0)	4c ($\frac{1}{4},\frac{1}{4},\frac{1}{4}$)	4b($\frac{1}{2},\frac{1}{2},\frac{1}{2}$)	4d ($\frac{3}{4},\frac{3}{4},\frac{3}{4}$)

Rietveld refinement shows good agreement (reduced χ^2 = 1.4 and weighted average Bragg R-factor = 3.6) between the observed XRD pattern and the calculated pattern for the $L2_1$ (space group 225) structure with the experimental lattice parameter $a = 5.7632$ Å as shown in Fig. 4.55(a). The goodness of fit parameters (reduced χ^2 = 5.2 and weighted average Bragg R-factor = 9.7) are al-

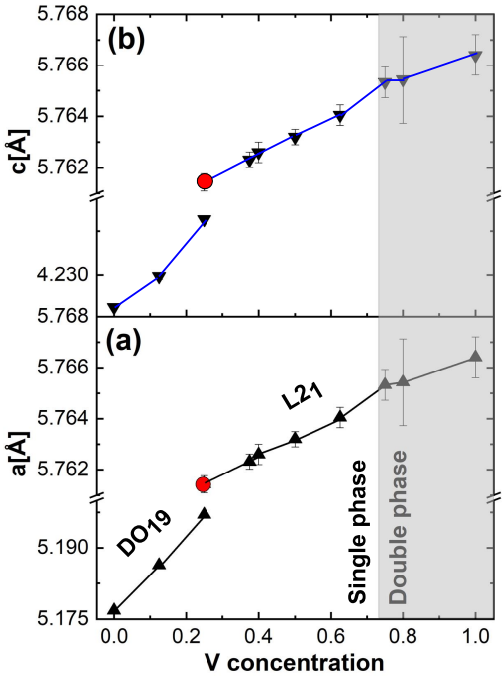

Figure 4.57: Variation of lattice parameters of $Fe_{3-x}V_xGe$ annealed at 950°C for 7 days (except the red data point representing $x = 0.25$ annealed at 650°C for 25 days) (a) a versus V concentration, and (b) c versus V concentration. The shaded region represents multiphase region.

Table 4.19: Proposed site assignment for the hexagonal DO_{19} $Fe_{3-x}V_xGe$.

	Wyckoff position	Coordinates	Occupancy
Fe	$6h, y = \frac{5}{6}$	$(y, 2y, \frac{1}{4})$ $(-2y, -y, \frac{1}{4})$ $(y, -y, \frac{1}{4})(-y, -2y, \frac{3}{4})$ $(2y, y, \frac{3}{4})$ $(-y, y, \frac{3}{4})$	$\frac{3-x}{3}$
V	$6h, y = \frac{5}{6}$	$(y, 2y, \frac{1}{4})$ $(-2y, -y, \frac{1}{4})(y, -y, \frac{1}{4})(-y, -2y, \frac{3}{4})$ $(2y, y, \frac{3}{4})$ $(-y, y, \frac{3}{4})$	$\frac{x}{3}$
Ge	$2c$	$(\frac{1}{3}, \frac{2}{3}, \frac{1}{4})$ $(\frac{2}{3}, \frac{1}{4}, \frac{3}{4})$	1

ways higher for X_a (space group 216) structure considered in Table 4.18. Having no evidence to the contrary, we presume Fe and V mix randomly on the 4b sites. This is also in good agreement with the Pauling electronegativity rule. Because V and Ge have a higher electronegativity difference, they will tend to form a rock-salt (NaCl) type lattice and coordinate octahedrally due to ionic nature of their interactions. EBSD inverse pole figure (IPF) map and phase map of $Fe_{2.50}V_{0.50}Ge$ were also performed to determine the degree of texturing and purity of phase considered. Relatively large grains with some preferred orientation is revealed from IPF as shown in Fig. 4.55(b). Almost 95% of the selected microstructure is observed to match the proposed $L2_1$ structure (red color in the EBSD map (see Fig. 4.55(c)) with some zero solution regions (black spots) mainly in grain

boundaries due to the artefact of polishing and some nominal Ge segregation. All these experimentally observed facts support that the crystal structure of all stable cubic samples $0.375 \leq x \leq 0.75$ is $L2_1$, in agreement with Beitollahi and Booth [241]. The $L2_1$ structure is shown in Fig. 4.56(a).

In order to determine the atomic ordering in hexagonal samples, $x = 0.125$ is chosen for Rietveld refinement due to the visibility of all hexagonal peaks in XRD. Even though the texturing effect from larger grains ($\sim 300\,\mu$m) is evident in peak intensities, a final reduced χ^2 = 7.7 is found. This single digit goodness of fit parameter between the observed XRD pattern and the calculated pattern for the hexagonal DO_{19} (space group 194) indicates the reliability of the fit (see Fig. 4.55(d)). According to Rietveld refinement, the 6h sites (with the parameter y = 5/6) are shared by Fe and V with occupancy 0.958 and 0.042, respectively, in agreement with the nominal composition, and the 2c sites are occupied by Ge. Again, with no evidence to the contrary, we presume that Fe and V mix randomly on the 6h sites. This DO_{19} structure is shown in FIG 4.56(c). The proposed site assignments are summarised for DO_{19} $Fe_{3-x}V_xGe$ in Table 4.19 [174].

Lattice parameters of all cubic stable phases, calculated using Cohen's method with a Nelson-Riley error function [171], are observed to increase linearly with increasing V concentration (see Fig. 4.57(c)) which is expected according to Vegard's law [205] as the lattice constant of bcc V (0.3024 nm) is greater than that of bcc Fe (0.2867 nm) [247]. Both lattice parameters a and c increase with the increase of V concentration for all hexagonal stable phases as shown in Fig. 4.57. The lattice parameters of all stable samples along with different annealing conditions for $Fe_{3-x}V_xGe$ alloy series are presented in Table 4.20.

4.6.4.3 Phase transformation behavior and thermal stability

Differential Scanning Calorimetry (DSC) is a simple but an effective tool to identify phase transformation temperatures. Since the local composition of our samples does not change in going from one structure to another, this serves to indicate that the transformation is a diffusionless martensitic transformation, as observed in the parent compound Fe_3Ge. Continuous heating and cooling DSC curves of $Fe_{3-x}V_xGe$ annealed at 950°C for 7 days measured at a heating/cooling

Table 4.20: Experimental lattice parameters of $Fe_{3-x}V_xGe$ alloy series of different crystal structures with annealing conditions, the experimental saturation magnetic moments at T = 5 K along with the theoretical and Slater-Pauling (S-P) values, and the measured Curie temperature (T_c). The numbers in parentheses are the uncertainty in the last digit, *e.g.*, $3.2(2) = 3.2 \pm 0.2$.

x	Crystal structure	Experimental lattice (Å)	Theoretical lattice (Å)	Expt. M_s at $T = 5K$ ($\mu_B/f.u.$)	Theor. M_s ($\mu_B/f.u.$)	S-P M_s ($\mu_B/f.u.$)	T_C (K)
0	DO_{19}[†]	$a = 5.1768(2)$	$a = 5.134$	6.55(9)	6.48	4.00	640
		$c = 4.2246(3)$	$c = 4.222$				
0	$L1_2$[‡*]	$a = 3.6667(1)$	$a = 3.638$	6.55(9)	6.45	4.00	-
0.125	DO_{19}[†]	$a = 5.1863(5)$	$a = 5.146$	5.88(2)	6.07	3.63	620(10)
		$c = 4.2298(5)$	$c = 4.220$				
0.125	$L2_1 + DO_{19}$[‡*]	-	-	-	-	-	
0.25	DO_{19}	$a = 5.1970(4)$	$a = 5.159$	5.33(3)	5.72	3.25	603(12)
		$c = 4.2395(3)$	$c = 4.220$				
0.25	$L2_1$[‡]	$a = 5.7614(3)$	$a = 5.753$	3.91(3)	3.77	3.25	-
0.375	$L2_1$[†]	$a = 5.7623(3)$	$a = 5.767$	3.18(2)	-	2.88	590(9)
0.40	$L2_1$[†]	$a = 5.7626(1)$	-	3.09(3)	-	2.80	-
0.50	$L2_1$[†]	$a = 5.7632(3)$	$a = 5.788$	2.64(3)	2.47	2.50	509(8)
0.625	$L2_1$[†]	$a = 5.7640(4)$	$a = 5.802$	2.24(2)	-	2.13	450(5)
0.75	$L2_1$[†*]	$a = 5.7653(6)$	$a = 5.806$	-	1.62	1.75	-

[†] annealed at 950°C for 7 days, [‡] annealed at 650°C for 25 days, [*] multi-phased samples.

rate of 10°C/min are shown in Fig. 4.58(a). Fig. 4.58(b) shows the DSC curves at heating/cooling rate 10°C/min for $x = 0$ and $x = 0.25$ annealed at 650°C for 25 days. The phase evolution is clearly seen from the DSC curves. The large, sharp endothermic peaks around 1120°C corresponds to the melting point which is in agreement with the reported melting point $\sim$ 1100°C of parent Fe_3Ge. Additionally, small endothermic peaks are seen in addition to the prominent melting point peaks for all compositions having $L2_1$ structures, indicating the signature of first order phase transformations.

No peaks are observed in those compositions which were already crystallized in hexagonal DO_{19} structure at room temperature. Small endothermic peaks are also observed for $x = 0$ ($L1_2$) and x = 0.25 ($L2_1$) annealed at 650°C for 25 days during heating cycle only. All these experimentally observed facts indicate that transforming the $L1_2$ or $L2_1$ structure to the DO_{19} structure is relatively easy, but the reverse transition is relatively difficult for low V concentration [238, 239]. Additionally, XRD on samples with $x = 0.25$ annealed at 950°C for 7 days and at 650°C for 25 days showed a DO_{19} structure and a $L2_1$ structure, respectively, corroborating the DSC measurements. Thus, we conclude that the small DSC peaks observed correspond to the structural phase transformation from cubic $L1_2$ or $L2_1$ to hexagonal DO_{19}. The linear shifting of the peak positions

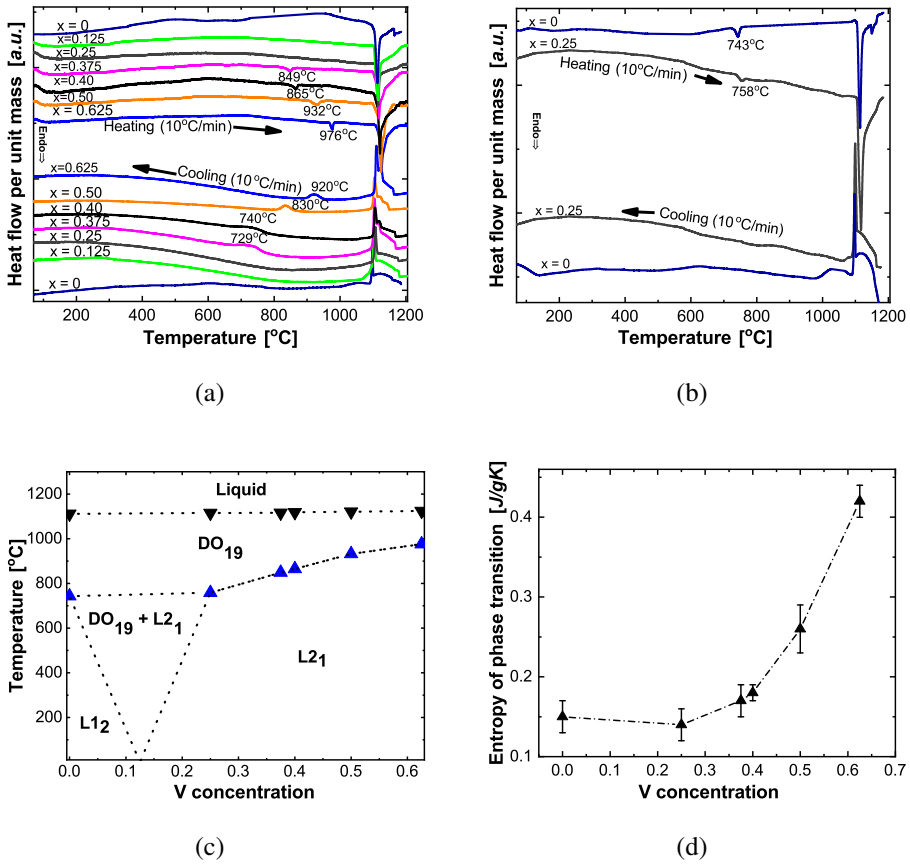

Figure 4.58: (a) DSC scans of $Fe_{3-x}V_xGe$ alloy series heat-treated at 950°C for 7 days measured at heating/cooling rate 10°C/min. (b) DSC scans for $x = 0$ and $x = 0.25$ heat-treated at 650°C for 25 days at heating/cooling rate 10°C/min. (c) Temperature versus V concentration phase diagram of $Fe_{3-x}V_xGe$ alloy system. Martensitic phase transformation temperature: blue data pints, Melting point: red data points, and dashed lines: proposed phase boundaries. (d) The total entropy of phase transformation with V concentration.

with increasing vanadium concentration, as shown in Fig. 4.58(c), indicates an improvement of the stability of the low temperature $L2_1$ structure with increasing V content. Notably, this low temperature $L2_1$ phase with V substitution is completely different from the low temperature $L1_2$ phase of the parent Fe_3Ge. The reproducibility of those peaks on cooling (with some hysteresis) and the lack of local composition variation suggests the transformation to be of the diffusionless martensitic type. We note that the hysteresis may be due to super-cooling (recall the heating/cooling rate of 10°C/min). The total entropy of phase transformation also changes significantly with V concentration (see Fig. 4.58(d)).

The onset temperatures (T_1), temperatures (T_p) and total entropy change (ΔS_p) of the phase transformation peaks, and melting points (T_m), measured at heating rate 10°C/min for samples annealed at 950°C for 7 days with different vanadium concentrations are presented in Table 4.21.

Table 4.21: The values T_1, T_p, ΔS_p, and T_m of $Fe_{3-x}V_xGe$ annealed at 950°C for 7 days measured in continuous heating at the rate 10°C/min. (The subscripts 1, p and m denote for on-set, $L2_1$ to DO_{19} transformation, and melting point, respectively.) The numbers in parentheses are the uncertainty in the last digit.

x	T_1(°C)	T_p(°C)	ΔS_p (J/g·K)	T_m(°C)
0*	721	743	0.15(2)	1112
0.125	-	-	-	1115
0.25*	737	758	0.14(2)	1116
0.375	828	849	0.17(2)	1118
0.40	842	865	0.18(1)	1121
0.50	905	932	0.26(3)	1124
0.625	965	976	0.42(2)	1126

*Samples annealed at 650°C for 25 days.

Thus, the $L2_1$ to DO_{19} martensitic phase transformation is observed to depend on V concentration as well as annealing temperature conditions in off-stoichiometric $Fe_{3-x}V_xGe$ intermetallic alloys, distinct from the temperature driven $L1_2$ to DO_{19} transformation of the parent compound Fe_3Ge. After annealing at 950°C for 7 days, alloys for $0.375 \leq x \leq 0.75$ are found to crystallize in the Heusler-like $L2_1$ structure, and alloys with $0 \leq x \leq 0.25$, crystallize in the hexagonal DO_{19} structure, which is the high temperature structure of the parent Fe_3Ge. On the other hand, alloys with $0.25 \leq x \leq 0.75$ annealed at 650°C for 25 days are observed to crystallize in $L2_1$ structure. Clearly two distinct crystal structures are observed at room temperatures in $x = 0.25$; $L2_1$ for sample annealed at 650°C for 25 days and DO_{19} for sample annealed at 950°C for 7 days, confirming the $L2_1$ to DO_{19} *fcc* to *hcp* phase transformation, likely similar to those widely studied in cobalt and ferrous alloys [248, 249]. According to the Shoji-Nishiyama mechanism, the atomic arrangements of the $(111)_{fcc}$ plane and the $(0001)_{hcp}$ planes are parallel [248]. Since, both *fcc* and *hcp* are close-packed structures, the only difference is in the stacking sequence of atoms normal to these planes. The transformation from *fcc* to *hcp* only requires the deformation of the atoms along the (111) plane to form a stacking sequence from *ABCABC*... to *ABABA*... type [6].

4.6.4.4 Magnetic Characterisation

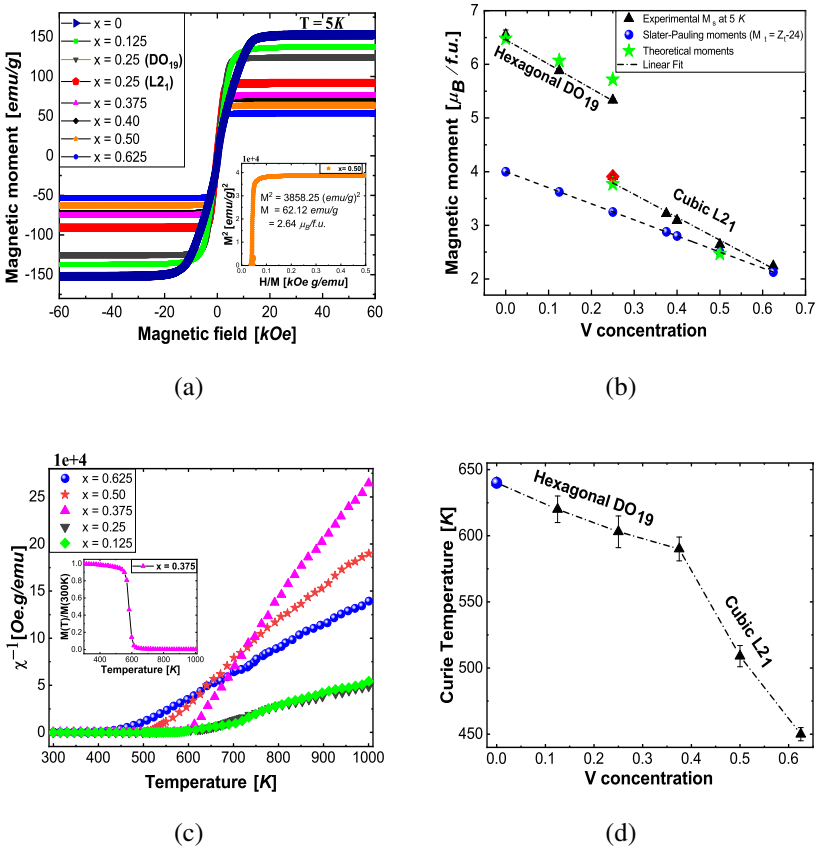

Figure 4.59: (a) The field-dependent magnetisation at 5 K of $Fe_{3-x}V_xGe$ alloy series annealed at 950°C for 7 days except the sample $x = 0.25$ ($L2_1$) which was annealed at 650°C for 25 days. The inset indicates the Arrot plot. (b) The magnetic moment versus V concentration both experimental and expected from Slater Pauling rule. (c) Inverse susceptibility as a function of temperature for the alloys ($0.125 \leq x \leq 0.625$) annealed at 950°C for 7 days. The inset is temperature dependent magnetisation for $x = 0.375$ with H = 1000 Oe. (d) The variation of T_c with V concentration (The blue data point is literature value of parent Fe_3Ge [21, 22]).

The magnetic measurements for all single-phase samples were done using the VSM module of a Quantum design PPMS Dynacool. Fig. 4.59(a) shows the field dependent magnetisation M(H) curves of all stable samples in the $Fe_{3-x}V_xGe$ series at 5 K. All the samples appeared to be ferromagnetic at 5 K. The saturation magnetizing field is observed to decrease with increasing V content, though all samples are magnetically very soft. The saturation magnetic moments (M_s) were extracted from an Arrot plot [207], *i.e.*, by extrapolating the linear part of M^2 versus to H/M

to H/M = 0 (see inset to Fig. 4.59(a)). The extracted M_s at 5 K is observed to decrease linearly with increasing V content, however two different trendlines are observed (see Fig. 4.59(b). This anomaly can be attributed due to different crystal structures (DO_{19} structure for low V content and $L2_1$ for high V content) consistent with our microstructural and XRD analysis. The extracted values of saturation magnetic moment (M_s) versus V concentration plot presented in Fig. 4.59(b) shows linear behavior for all stable $L2_1$ phases, in good agreement with Slater-Pauling rule (shown in blue data points). The Slater-Pauling rule describes the dependence of the magnetic moment on the valence electron concentration (N_v) for ordered, half-metallic ferromagnetic Heusler compounds. This dependence is given by [1]

$$m = N_v - 24. \tag{4.24}$$

The slightly higher extracted saturation magnetic moments in the Fe rich members of $L2_1$ series are not unusual. Similar deviations from the theoretical values have been reported previously for Fe based Heusler compounds elsewhere [1, 20]. The plot also shows linear behavior for DO_{19} compositions, but the values are much higher than values from Slater-Pauling rule which simply indicates that the Slater-Pauling rule is not expected to hold for the hexagonal structure. Dramatic changes in magnetic moment are observed at $x = 0.25$ depending on the annealing condition, where we clearly observed two distinct pure crystal structures, DO_{19} for sample annealed at 950°C for 7 days and $L2_1$ for sample annealed at 650°C for 25 days. The red coloured solid square data point in Fig. 4.59(b) represents the magnetic moment for $x = 0.25$ ($L2_1$) annealed at 650°C for 25 days. All experimentally extracted saturation magnetic moments are in good agreement with those obtained from first-principle calculations (see Fig. 4.59(b)) (discussed in theory section below).

The high temperature magnetization of a series of heat-treated $Fe_{3-x}V_xGe$ alloy were measured by means of a vibrating sample magnetometer VSM equipped with a high temperature stage. The Curie temperatures of inter-metallic alloy series were extracted taking the average of values obtained from linear fitting of the inverse susceptibility versus temperature graph as shown in Fig.

4.59(c) and the values obtained by plotting dM/dT as a function of temperature. The inset in Fig. 4.59(c) shows the specific magnetization as a function of temperature for $x = 0.375$. The measurements were performed with a constant magnetic field of 1000 Oe in the temperature range of 300 K to 1000 K. Even though the ferromagnetic Curie temperature T_c of these alloys are all observed to be above room temperature, and decrease with increasing x as shown in Fig. 4.59(d), the linear decrease of T_c of hexagonal samples $x = 0.125$ and $x = 0.25$ has different slope than that of cubic ones. The T_c values are well below the melting point and martensitic phase transition temperatures obtained by means of differential scanning calorimetry.

The saturation magnetic moments at 5 K and corresponding Curie temperature of all stable samples along with different annealing conditions for $Fe_{3-x}V_xGe$ alloy series are presented in Table 4.20 above.

4.6.4.5 Electrical resistivity

The electrical resistivity data were collected using the van der Pauw method [179] in a PPMS Dynacool for samples with approximate dimensions 4 x 4 x 1.5 mm^3. Fig. 4.60 shows the temperature dependence of the electrical resistivity for $Fe_{3-x}V_xGe$ measured during heating process in the temperature range from 5 K to 400 K. The electrical resistivity is observed to be sensitive to the composition change. An increase of V substitution for Fe is found to increase the residual resistivity that could be attributed due to atomic disorder arising from the substitution or sample quality. For x = 0.25 the variation of resistivity with temperature is purely metallic (see Fig. 4.60), but for higher V concentrations, a typical metallic behaviour is observed only for the low temperature range from 5 K up to 200 K. The resistivity is observed to saturate at higher temperatures for $x = 0.50$, suggesting a parallel contribution of the intrinsic resistivity and a weakly-varying shunting resistance, possibly due to grain boundaries [219, 250]. The pseudo gap near Fermi level present in the minority spin channel of total density of state (see Fig. 4.64) for $x = 0.50$ might be responsible for this saturation effect. According to Allen and Chakraborty [250], the resistivity of a sub-band of electrons with an energy gap at the Fermi level is high and independent of

temperature while the other sub-band has metallic character and resistivity increases with temperature and saturates at high temperature. The downturn in resistivity at higher temperature for $x = 0.625$ indicates the semiconducting nature of the material. This kind of anomalous behavior of resistivity is quite similar to those observed in $Fe_{2-x}V_{1+x}Al$, $Fe_{2-x}Ti_{1+x}Sn$, $(Fe_{1-x}V_x)_3Ga$, and $(Fe_{1-x}Ti_x)_3Ga$ systems, where the tendency toward negative temperature dependence of electrical resistivity increases markedly with increasing x [251–254]. The anomaly that the resistivity

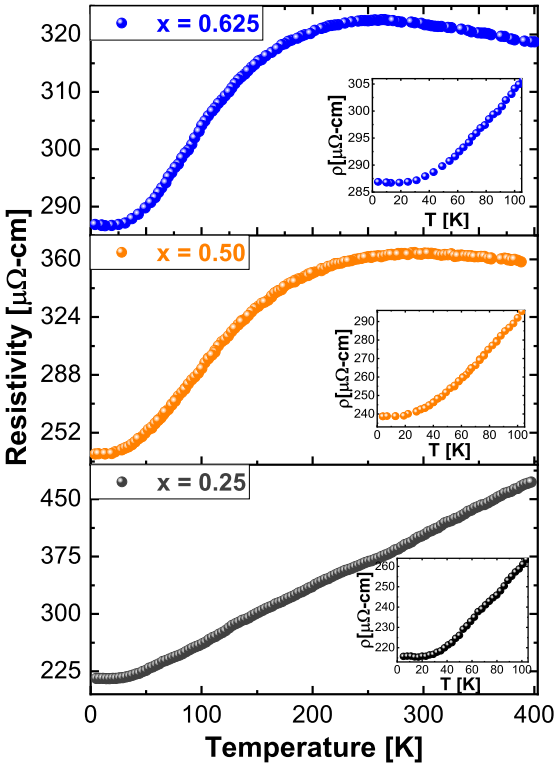

Figure 4.60: (color online) Temperature dependence of electrical resistivity in $Fe_{3-x}V_xGe$ (x = 0.25, 0.50, and 0.625, all annealed at 950°C for 7 days, respectively from bottom to top) in zero magnetic field.

reaches the maximum value quickly at $T \leq T_c$, decreases after that and reaches saturation at higher temperature is observed in many half-metallic Heusler alloys where the resistivity of one of the spin polarized sub-band with energy gap at Fermi level is expected to have a semiconductor character at high temperature [255–262]. The energy gap in down spin sub-band is observed to fall at Fermi level for $x = 0.75$ (see Fig. 4.64). The existence of a gap in one of the spin-polarized

sub-band near Fermi level in total density of state for higher V concentration in $Fe_{3-x}V_xGe$ can be considered as the anomalous decrease of resistivity with increasing temperature. Elucidating the true bulk transport properties unambiguously would ideally require single crystal or highly ordered thin films.

4.6.4.6 Vickers micro hardness

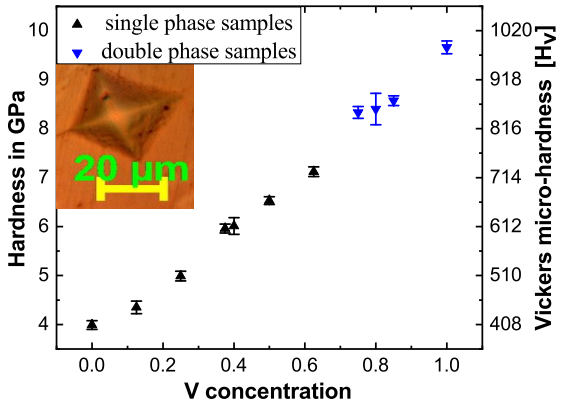

Figure 4.61: Vickers hardness versus V concentration in $Fe_{3-x}V_xGe$ with imprint of the indenter with radial cracks for $x = 0$ [top left]. The black data points represent the single phase compositions.

During specimen preparation, we found the samples to be unusually hard, as evidenced by the polishing time required. For this reason, we decided to investigate the Vickers hardness of our alloy series, since most of the previous studies on mechanical properties are theoretical in nature [263–267] and only few are verified experimentally. The variation of Vickers micro hardness of our alloy series (all annealed at 950°C for 7 days) with V concentration is presented in Fig. 4.61 with corresponding values in Table 4.22. Hardness values reported are the averages of data taken from at least 12 different regions of each sample with 0.2 kg load and 10 s loading time. Relatively high hardness values are measured, approaching 10 GPa for $x = 1$, comparable with highest value 12 GPa reported for $Co_{2-x}Ti_xFeGe$ Heusler system [105] and higher than values reported for full Heuslers in the literature, *e.g.*, $\sim$ 8.5 GPa for powder Fe_2VAl [268], $\sim$ 8.5 GPa

for nanocrystalline Co_2FeAl [209], ~ 7.3 GPa and ~ 7.9 GPa for bulk polycrystalline Co_2MnGe and Co_2MnSi respectively [210]. The hardness is observed to increase almost linearly in going from hexagonal DO_{19} phases (with low V concentration) to $L2_1$ phases (with higher vanadium concentration) and depend on grains size and phases present as reported in the literature [211]. The grain size of the hexagonal phases at low V concentration are bigger than those of cubic phases at higher concentrations, and the cubic structure shows better toughness than the hexagonal structure, presumably as the *fcc* structure has more slip planes in which the atoms are packed most closely relative to each other, and hence most tightly bonded to each other [269].

Table 4.22: Vicker's micro-hardness of the $Fe_{3-x}V_xGe$ alloy series.

x	Vickers Hardness (GPa)
0	3.99 ± 0.09
0.125	4.35 ± 0.13
0.25	4.99 ± 0.10
0.3125	4.81 ± 0.37
0.375	5.96 ± 0.09
0.40	6.01 ± 0.17
0.50	6.53 ± 0.08
0.625	7.12 ± 0.10
0.75	8.33 ± 0.12
0.80	8.40 ± 0.32
0.85	8.57 ± 0.10
1	9.66 ± 0.13

4.6.5 Theoretical Calculations

4.6.5.1 Computational Methodology

The Vienna *Ab initio* Simulation Package (VASP) was used for our density functional theory calculations (DFT) [181]. We used potentials from the projector augmented-wave (PAW) method and used the Perdew-Burke-Ernzerhof (PBE) functional [180, 182, 217]. The Monkhorst-Pack scheme was used to sample the Brillouin zone using a 9 x 9 x 9 k-point grid for cubic structures and a 9 x 9 x 5 grid for hexagonal structures in addition to a plane wave basis set with a cutoff energy of 400 eV [200]. Self-consistent field calculations of the total and projected electronic

density of states were carried out with a Gaussian-type Fermi-level smearing width of 0.05 eV. To generate $Fe_{3-x}V_xGe$ structures with varying V concentrations, we used the Special Quasi-random Structures (SQS) method implemented in the ATAT package [270, 271]. The formation energy E_{form} (in eV/atom) of $Fe_{3-x}V_xGe$ is defined as $E_{form} = (E_{Fe_{3-x}V_xGe} - (1-x)E_{Fe_3Ge} - xE_{V_3Ge})$, where $E_{Fe_{3-x}V_xGe}$ is the energy of a $Fe_{3-x}V_xGe$ cell, E_{Fe_3Ge} is the energy of a Fe_3Ge cell, and E_{V_3Ge} is the energy of a V_3Ge cell, all per formula unit. We then normalized the x axis to start from $x = 0$ (Fe_3Ge) to $x = 1$ (Fe_2VGe). To obtain the charge distribution on the atoms in the simulation cells, we used Bader charge analysis [272, 273]. The VESTA program was used to visualize of atomic structures [274].

4.6.5.2 Theoretical Results and Discussion

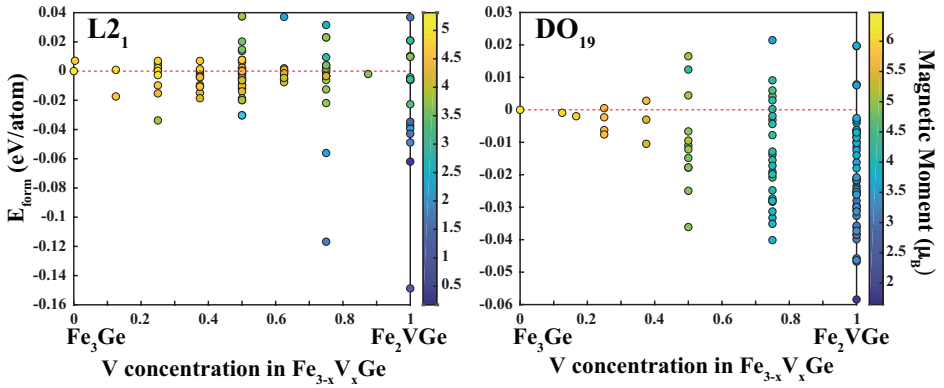

Figure 4.62: The formation energy (in eV/atom) as a function of V concentration for the $L2_1$ and DO_{19} alloys created with the SQS method. Each data point represents a different structure and the color axis indicates the magnetic moment value for each structure.

Previously, first-principles DFT has been used to successfully calculate the electronic and magnetic properties of Heusler alloys [275–277]. In order to confirm experimental results and further investigate the electronic structure of this particular $Fe_{3-x}V_xGe$ alloy system, we employed the Special Quasi-random Structures (SQS) method to generate structures between $x = 0$ and $x = 1$ for the $L2_1$ and DO_{19} phases. When comparing with experiment, we were able to generate structures with all of the same alloying ratios as Table 4.20 except $x = 0.40$ for the $L2_1$ phase. We note

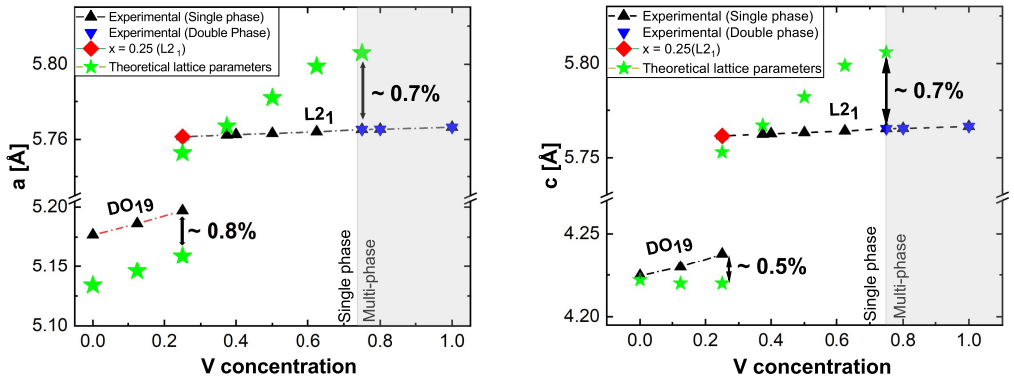

(a) (b)

Figure 4.63: Comparison plot between experimentally extracted lattice parameters and theoretical values from First-principles calculations of $Fe_{3-x}V_xGe$ (a) a versus V concentration, and (b) c versus V concentration.

that for certain alloying ratios for the $L2_1$ phase such as $x = 0.375$, $x = 0.40$, and $x = 0.625$, the SQS method requires a larger supercell to preserve such concentrations. We propose that the SQS method being unable to create structures near $x = 0.40$ is due to the requirement of a significantly large supercell, beyond the capability of DFT. For $x = 0.375$ and $x = 0.625$, the quasi-random structures are forced to be confined to a rectangular supercell rather than a cubic supercell to preserve such alloying ratios without approaching the DFT limit (a much larger cubic supercell). However, from these rectangular structures, we are still able to obtain accurate lattice parameters to compare with experiment where only the long edges of the rectangular cell (b) are almost two times larger than the (a) lattice constant.

Fig. 4.62 shows the formation energy as a function of V concentration x of the $L2_1$ and DO_{19} phases respectively. The magnetic moment value is also depicted in the color axis of Fig. 4.62. We observe that at $x = 0.25$, the $L2_1$ phase is more energetically favorable than the DO_{19} phase. As expected for both phases, the increase of V concentration results in a decrease in magnetic moment with Fe_2VGe ($x = 1$) being the least magnetic alloying concentration. As can be seen in Table 4.20, calculated magnetic moments are in good agreement with the experimentally measured values. The calculated values of magnetic moment for $x = 0.375$ ($M_{S,avg}$ = 4.48 μ_B) and $x = 0.625$ ($M_{S,avg}$ =

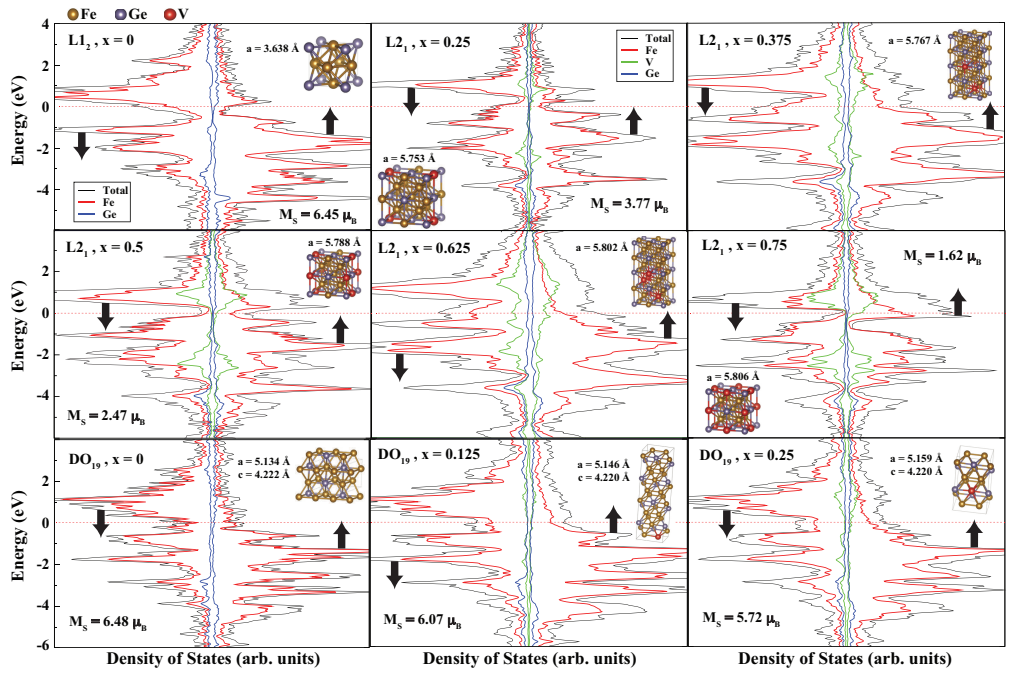

Figure 4.64: The DOS and PDOS of the lowest energy structure at specific concentration ratios for $L2_1$, DO_{19}, and $L1_2$. The black arrows depict the spin up and spin down contributions and the red dotted line represents the Fermi level. The figure insets include the optimised structures, magnetic moment values and average lattice constants.

3.61 μ_B) are almost 1 μ_B bigger than the experimental results due to considered supercells being rectangular instead of cubic. For the lowest energy structure (most energetically favorable) at each experimentally observed alloying concentration, we calculated the electronic density of states (DOS). Fig. 4.64 depicts the atom projected DOS of the experimentally observed alloys for $L2_1$ ($x = 0.25$, $x = 0.375$, $x = 0.50$, $x = 0.625$, $x = 0.75$), DO_{19} ($x = 0$, $x = 0.125$, $x = 0.25$) and $L1_2$ ($x = 0$). The spin up and spin down contributions to the DOS are indicated by the black arrows. The insets of Fig. 4.64 also include the optimized geometry, the lattice constants and magnetic moment values (excluding M_S for $x = 0.375$, and $x = 0.625$) for the considered alloys. All the experimentally extracted lattice parameters are within $\sim$ 1% of theoretical values (see Fig. 4.63). Because the experiments were done at a finite temperatures, this can cause the lattice parameters of the crystal structure to change from the 0 K structures due to the thermal expansion coefficient of the material and one might need longer annealing time yet to reach the true ground state. This

also creates a margin of error such that all the structures generated with SQS lie in the range of thermal fluctuation at a given concentration. Due to this fact, we report an average value for lattice constant given at each concentration. In comparison to experiment, DFT calculations confirm that increasing V concentration increases the lattice constant on average (see Fig. 4.63). The metallic characteristics of the DO_{19} and $L1_2$ (for $x = 0$) Fe_3Ge structures arise from the orbital contribution of Fe atoms. Vanadium substitution can give different contributions to the density of states according to its position inside the material. For instance, if the V atom is positioned close to Ge atoms, it gives a contribution similar to the Ge contribution (see Fig. 4.64 $L2_1$ for $x = 0.50$, and $x = 0.75$). When V atoms are placed far from the Ge atoms, specifically if they are surrounded by Fe atoms, their DOS look similar to the DOS of Fe atoms (see Fig. 4.64 $L2_1$ for $x = 0.375$, $x = 0.50$, and $x = 0.625$). For the DO_{19} structures, V atom substitution does not significantly effect the DOS of the bare Fe_3Ge structure due to low V concentration.

To understand the bonding type between the atoms and to gain insight on the electronic mechanism of these structures, we performed Bader charge transfer analysis of the $Fe_{3-x}V_xGe$ alloys. Bader charge analysis indicates that while 0.10 electrons (e^-) transfer to Ge from Fe atoms for $L1_2$, 0.30 e^- transfer for DO_{19} at x = 0. This amount of electron transfer, in addition to the electronegativity difference between Fe and Ge atoms (0.18 according to the Pauling scale) indicate that there is non-polar covalent bonding between them. For DO_{19} at $x = 0.125$, and $x = 0.25$, V (which has a lower electronegativity than Fe and Ge) loses 1.38 e^- and the three Ge atoms that are binding with this V atom gain 0.50 e^-. Bader charge analysis for $L2_1$ at $x = 0$ indicates that charge transfer is different from DO_{19} and $L1_2$ structures. Some Fe atoms which are binding with Ge donate 0.30 e^- and each Ge atoms take 0.13 e^- while some Fe atoms take 0.07 e^-. With the substitution of V atoms instead of Fe atoms, polarization increases between the Fe atoms. For $x = 0.50$, Fe atoms that are close to Ge atoms donate 0.35 e^- while the remaining Fe atoms gain 0.35 e^-. The increasing of stability can be attributed to this increased polarization.

4.6.6 Conclusion

In summary, an off-stoichiometric polycrystalline bulk $Fe_{3-x}V_xGe$ inter-metallic alloys series ($0 \leq x \leq 1$) was synthesized by arc-melting and the structural, magnetic, electrical transport and mechanical properties were investigated under different heat-treatment conditions. V substitution was observed to favor one of the Fe site in Fe_3Ge energetically to form $L2_1$ structure for higher V concentration and DO_{19} structure for lower V concentrations, corroborated by first-principles calculations. The $L2_1$ to DO_{19} martensitic phase transformation was observed to depend on V concentration as well as annealing conditions. DSC results also confirmed the diffusionless martensitic phase transformation in the alloy series. All the alloys in the series were found to be soft ferromagnets at 5 K with decreasing saturation magnetic moment with increasing V concentration. The sample with $x = 0.25$ crystallized in two different crystal structures $L2_1$ and DO_{19} at two different annealing conditions, and they were found to exhibit two different saturation magnetizations at 5 K, with the magnetization in the hexagonal phase being substantially larger. In contrast to DO_{19} structures, the saturation magnetic moments of all $L2_1$ structures were observed to decrease linearly with V concentration in close agreement with the expected Slater-Pauling values. The hexagonal samples were in all cases observed to have markedly higher values of saturation moments. The saturation magnetic moments extracted from experiment are found to be in good agreement with those obtained from first-principles calculations. The ferromagnetic Curie temperature T_c of these alloys were observed to decrease with increasing V concentration. The electrical resistivity measured over the temperature range from 5 K to 400 K showed a negative temperature coefficient of resistivity at high temperatures, more so with increasing the V concentration. The residual resistivity value is also found to increase with V substitution. Relatively high mechanical hardness values are also measured, increasing as V content increased. Vanadium is found to play a central role in tuning rich physical properties in $Fe_{3-x}V_xGe$, changing the mechanical properties, stabilizing the $L2_1$ structure not found in the parent Fe_3Ge compound, and shifting the martensitic transformation temperature to higher values compared to that of parent Fe_3Ge.

4.7 Influence of Cr-substitution on the structural, magnetic, electron transport, and mechanical properties of $Fe_{3-x}Cr_xGe$ Heusler alloys

4.7.1 Abstract

We performed combined experimental and theoretical studies of the effect of Cr substitution for Fe on the structural, magnetic, transport, electronic, and mechanical properties of $Fe_{3-x}Cr_xGe$ ($0 \leq x \leq 1$) intermetallic alloys. Single phase microstructures are observed for $x \leq 0.70$. Higher Cr concentrations $x > 0.70$ are multi-phased. A hexagonal $D0_{19}$ structure is found for all Cr concentrations, with the lattice parameters increasing systematically with an increasing Cr content. All the alloys in the series are found to be ferromagnets with large magnetization values of about 6 $\mu_B/f.u.$ and high Curie temperature above room temperature. The low-temperature saturation magnetic moments agree fairly well with our theoretical results and also obey the Slater-Pauling rule. The density functional theory calculation reveals that Cr substitution energetically favours one of the Fe sites in Fe_3Ge. The electrical resistivity measured over the temperature range from 5 K to 400 K shows metallic behavior, with a residual resistivity ratio that decreases with Cr content. Vicker's hardness values are observed to increase with increasing Cr content to approximately 5 GPa.

4.7.2 Introduction

Heusler compounds include a large family of interesting materials exhibiting a wide range of properties of both fundamental and potential technological interest such as half metallic ferromagnets, high perpendicular magnetic anisotropy materials, shape-memory alloys, spingapless semiconductors, skyrmions, topological insulators, and magnetocalorics [66, 96, 278–284]. Half metallic Heusler alloys are the most suitable materials in the field of information storage and spintronics as well as many other areas [1, 66, 233, 285] because the electrical current is perfectly spin

PUBLISHED AS: R. Mahat*, S. KC, D. Wines, S. Regmi, U. Karki, Z. Li, F. Earsan, J. Law, C. Ataca, V. Franco, A. Gupta & P. LeClair, *Influence of Cr-substitution on the structural, magnetic, electron transport, and mechanical properties of $Fe_{3-x}Cr_xGe$ Heusler alloys*, Journal of Magnetism and Magnetic Materials, **521**,167398(2021).

polarized in these materials. For applications in magnetics and spintronics [66], the inherently low magnetocrystalline anisotropy in cubic Heusler alloys can be limiting factor [67]. Identifying a hexagonal Heusler analogue [233] that exhibits a high magneto-crystalline anisotropy may be very attractive for applications such as perpendicular media, current perpendicular to plane giant magnetoresistance (CPP-GMR), and spin-torque-transfer RAM (STT-RAM) [68–71].

The extensive tunability of the Heusler compounds through chemical substitutions makes the family especially interesting. The intermetallic compound Fe_3Ge is an iron rich ferromagnet, well known to crystallize in two crystal structures, a cubic $L1_2$ phase (Cu_3Au type, $Pm\bar{3}m$, space group no. 221 [64, 65]) at low temperatures ($< 700^{\circ}$C) and hexagonal $D0_{19}$ phase (Mg_3Cd type, $P6_3/mmc$, space group no. 194 [64, 65]) at higher temperatures ($> 700^{\circ}$C) [237, 238]. High magnetizations, with moments of about $2\mu_B$/Fe, high Curie temperatures of 640 K along with crystallographic anisotropy, makes the hexagonal phase of Fe_3Ge substantial interest as a permanent magnet [64, 286]. As 3d transition metals exhibit large magnetic moments and high Curie temperatures, and compounds in cubic phase generally exhibit weak magnetocrystalline anisotropy, identifying magnetic compounds with high Fe concentrations in hexagonal or tetragonal crystal structures is very helpful to discover new potential permanent magnets.

To our best knowledge, in spite of investigations aimed at understanding the magnetocrystalline anisotropy by substituting nominal Cr ($x = 0.099$) in hexagonal $Fe_{3.3}Ge$ [287], there is not yet a detailed report of the structural, magnetic, electron transport, and mechanical properties of $Fe_{3-x}Cr_xGe$ in the bulk form, neither experimentally nor theoretically. Our interest in this compound stems from a recent theoretical prediction that Fe_2CrGe has the high density-of-state at the Fermi energy in the majority-spin state and exhibits high spin polarization (almost 100%) insensitive to Fe$-$Cr chemical disorder [288]. In this paper, we present our systematic experimental investigation of the microstructure and phase purity, magnetic properties, electrical transport, and hardness in addition to structure determination to understand the structure-property relationships in this interesting family of Heusler-like compounds and compare the experimental data with results of first principles calculation. Particular attention has been paid to metallography and microstruc-

tural analysis to determine which regions of the phase diagram yield single phase specimens.

4.7.3 Experimental details

$Fe_{3-x}Cr_xGe$ ($0 \leq x \leq 1$) bulk samples were prepared by arc melting of stoichiometric amounts of the constituents in an argon atmosphere at 10^{-4} mbar (see details in Supplementary). Care was taken to avoid oxygen contamination. As an oxygen getter, Ti was melted inside the vacuum chamber separately before melting the compound to avoid oxygen contamination. The as-cast ingots were examined repeatedly using scanning electron microscopy (SEM) and energy dispersive X-ray spectroscopy (EDS) analysis in a JEOL 7000 Field Emission Scanning Electron Microscope (FESEM) to confirm homogeneity and correct composition. After confirming the anticipated target composition, the polycrystalline ingots were then annealed in an evacuated quartz tube at different temperatures ranging from 650°C to 1000°C for different dwell times (5 days to 25 days), and at the end of each annealing cycle, the samples were cooled slowly in the furnace to get optimum crystallization.

Annealed ingots were polished for spectroscopic investigations (see details in Supplementary). The polishing was done, first grinding using silicon carbide abrasive discs (120 through 1200 grit size) followed by diamond suspension polishing. Colloidal silica suspension of grit size 0.02 μm was used at last for the finest polishing. After obtaining a smooth and reflective surface, the samples were etched with Adler etchant (9 g of $CuNH_3Cl$, 45 g of hydrated $FeCl_2$, 150 mL of HCl and 75 mL of DI Water) [243]. The purpose of etching is that etchant attacks different phases present in the samples at different rates, and provides high quality surface contrast for microstructure characterization.

Structural analyzes were carried out by means of X-ray diffraction (XRD) using a Bruker D8 Discover X-ray diffractometer equipped with monochromatic Co-Kα (λ = 0.179 nm) radiation. The polished samples were rotated around the ϕ axis during the XRD measurement to minimize surface effects. CaRIne crystallography 4.0 software [78] as well as in-house PYTHON code [79] including the dispersive corrections to the atomic scattering factors were used to simulate the XRD

patterns to compare with the experimental XRD patterns. XRD analysis (Rietveld refinement) was done using the CRYSTAL IMPACT MATCH! software based on the FULLPROF algorithm [80] that uses the least-square refinement between experimental and calculated intensities. The low temperature magnetic and electrical transport properties were studied in Quantum Design Physical Properties Measurement System (PPMS), while the high temperature magnetization was measured using the Lakeshore VSM 7407. DC electrical resistivity measurements were carried out using van der Pauw method [179]. Al wire bonding was used to make the contacts. The mechanical properties were studied in terms of Vicker's hardness by using Buehler model 1600-6100 micro-hardness tester.

4.7.4 Experimental Results and Discussions

4.7.4.1 Microstructural and Compositional analysis

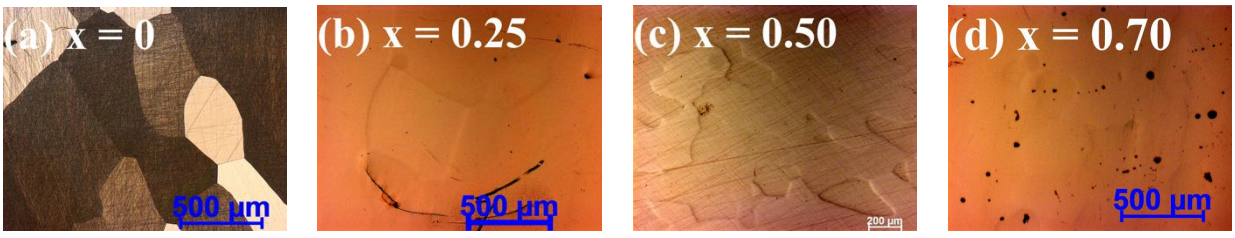

Figure 4.65: Optical micrograph of $Fe_{3-x}Cr_xGe$ ($0 \leq x \leq 1$) heat treated at 1000°C for 15 days showing the grain structures. The samples were etched for 1 minutes using the Adler etchant.

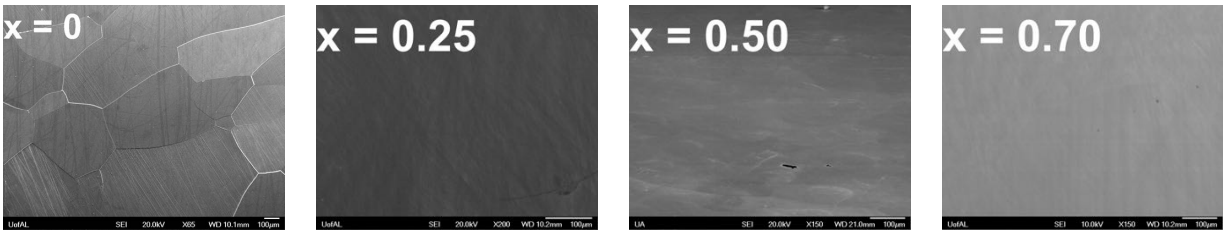

Figure 4.66: SEM micrograph of $Fe_{3-x}Cr_xGe$ ($0 \leq x \leq 1$) heat treated at 1000°C for 15 days.

Optical microscopy and SEM of polished and etched samples are the most direct ways to

characterize micro-structure by revealing grain boundaries, phase boundaries, and inclusion distribution as XRD is not always sufficient to confirm the phase purity if the impurity phase content is less than 5% of the overall volume [105, 163, 168, 169]. We can speculate the presence of impurity phases observing different contrast in optical images, and SEM with EDS/EBSD can be used to directly quantify whether areas of different contrast represent impurity phases or possible different crystallite orientations.

Starting from the full stoichiometric Fe_2CrGe, multi-phase microstructure was obtained in every heat treatments performed at 650, 800, 900, or 1000°C for different dwelling times; 3, 5, 7, 15 or 25 days. However, with the substitution of Fe for Cr, the secondary phase began to disappear and uniform single phase behavior was observed in the Cr composition range $(0 \leq x \leq 0.70)$. All other higher Cr concentration produced multiphase behaviour (see details in Supplementary Information). Fig. **??** shows microstructure of all single phase samples heat treated at 1000°C for 15 days. The microstructure of the high temperature (> 700°C) phase for x = 0 *i.e.*, the parent Fe_3Ge compound is presented in Fig. 4.65(a) already known to be stable, annealed under similar conditions [21, 238].

The composition of all the stable single phase samples in the series are confirmed to be close to the target composition within $\sim 5\%$ instrumental uncertainty range using EDS (see details in Supplementary information). SEM images displaying the microstructure are shown in Fig. 4.66, all annealed at 1000°C for 15 days.

4.7.4.2 Crystal structure and atomic order analysis

XRD patterns taken from the $Fe_{3-x}Cr_xGe$ alloy series annealed at 1000°C for 15 days after polishing and etching, using a Co-K_α radiation source at room temperature are shown in Fig. 4.67(a). All the diffraction peaks can be indexed as corresponding to the hexagonal $D0_{19}$ structure for all single phase specimens, though as noted below texturing effect makes it difficult to rely on XRD peak intensities. Lattice parameters of all stable phases, both along a-axis and c-axis, extracted using Cohen's method with a Nelson-Riley extrapolation function [171], are observed to

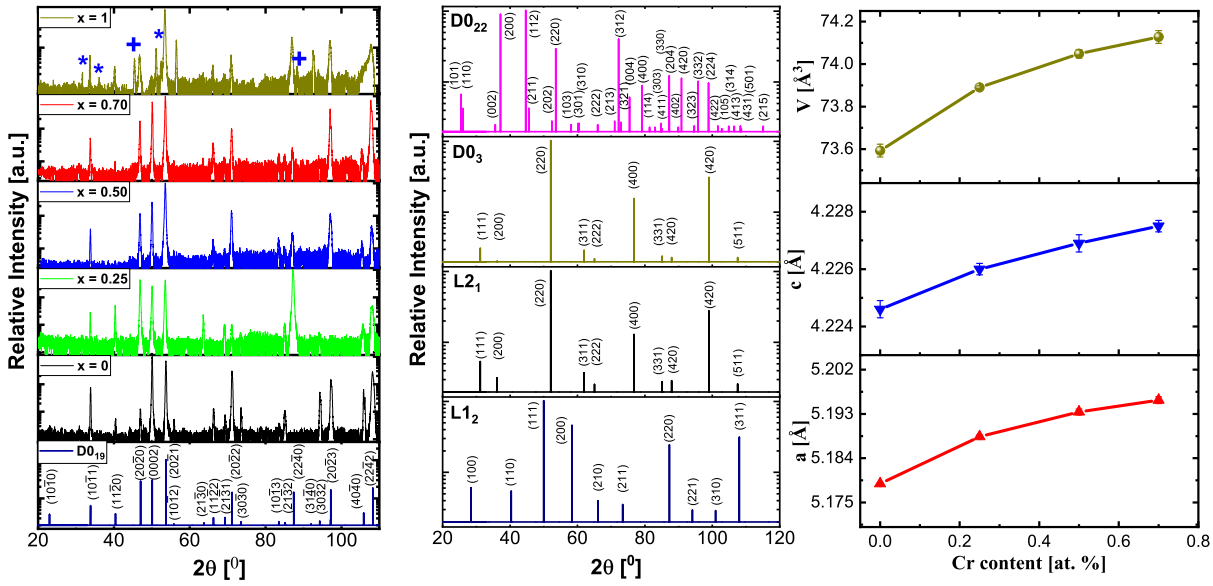

Figure 4.67: (a) Experimental XRD patterns of $Fe_{3-x}Cr_xGe$ alloy series annealed at 1000°C for 15 days, here, * and + correspond to the secondary cubic phase and unknown impurity phase, respectively. The first from bottom is simulated XRD pattern for $D0_{19}$ structure. (b) The simulated powder XRD patterns considering different crystal structures using CaRIne, and (c) The composition dependent lattice parameters a and c and unit cell volume of $Fe_{3-x}Cr_xGe$ (x = 0, 0.25, 0.50, 0.70) alloys investigated at room temperature.

increase systematically with increasing Cr content which leads to an overall increase in the unit cell volume (see Fig. 4.67(c)). The reason for the increase in unit cell is in accordance to Vegard's law [205] as the atomic radius of Cr (200 pm) is comparatively larger compared with that of the Fe atom (156 pm) [153]. The lattice parameters of all stable samples in $Fe_{3-x}Cr_xGe$ alloy series are presented in Table 4.24.

Considering the fact that Heusler-like compounds can crystallize in a number of structures, particularly the ordered $L2_1$ ($Fm\bar{3}m$, space group no. 225 [64, 65]) and its possible disordered phases $D0_3$ ($Fm\bar{3}m$, space group no. 225 [64, 65]), $D0_{19}$ ($P6_3/mmc$, space group no. 194 [64, 65]) [172–174], and $D0_{22}$ (I4/mmm, space group no. 139 [64, 65]), structure assignment should be undertaken carefully. The structural deformation through compression or elongation along one of the cubic (100) axes forms a tetragonal lattice while a similar deformation along the (111) direction

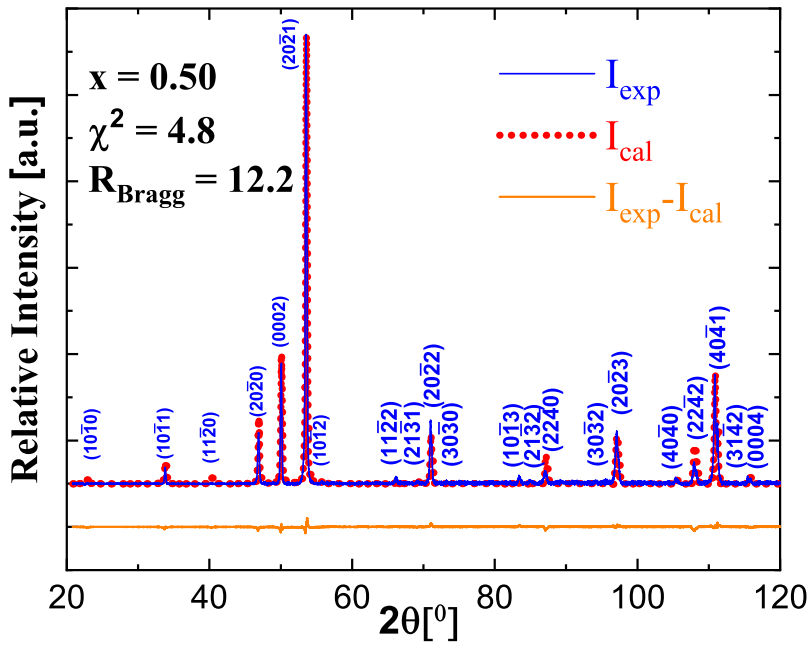

Figure 4.68: The Rietveld refinement of XRD pattern for $x = 0.50$ showing a signature of good fit with the proposed crystal model $D0_{19}$.

results in a hexagonal structure [6]. In order to avoid a selection bias, we first determined the crystal class from the XRD data alone, following the procedure in Ref. [171]. From the observed XRD peaks, the values of $\sin^2\theta$ were tabulated. If the structure is in the cubic system, then these values, when properly normalized, will yield a set of integers. Omissions in the list of integers distinguish the type of cubic lattice (*sc, bcc, fcc*). If there is no overall normalization of the values that results in only integral values, the system is not cubic. For the $Fe_{3-x}Cr_xGe$ alloy series shown in Fig. 4.67(a), We easily ruled out the possibility of cubic $L2_1$, Xa and complete A2 and B2 disordered structures due to the presence of more number of reflection peaks than those required for cubic structures. A similar but slightly more involved procedure [171] can be used to test the XRD data against hexagonal systems. We observed that the XRD data presented in Fig. 4.67(a) derive from a hexagonal crystal system, and after indexing all peaks, lattice parameters (see Table 4.24) were extracted for all alloys in the series using Cohen's method with a Nelson-Riley extrapolation function [171]. So, from our initial list of structures, only $D0_{19}$ structure is remained to be a plausible crystal structure.

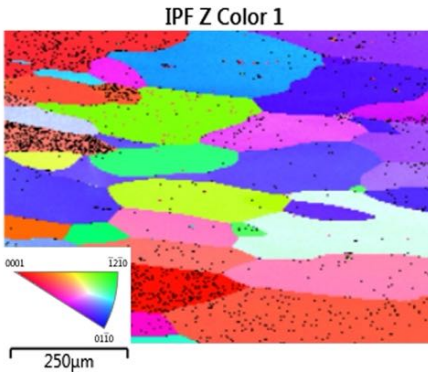

(a)

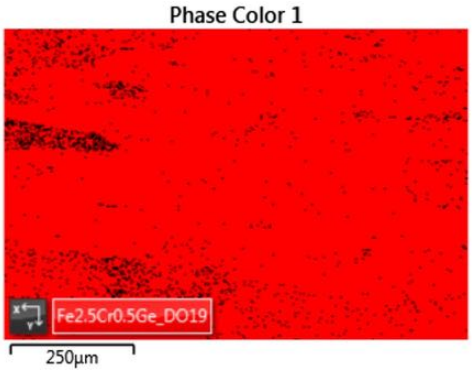

(b)

Figure 4.69: (a) Inverse pole figure (IPF) color map of $x = 0.50$ taken using EBSD in SEM showing grain orientation with preferred texture. The insert shows the color map of crystallographic orientation. (b) The corresponding EBSD phase map of the same area showing single-phase behavior.

Table 4.23: Proposed site assignment for the hexagonal $D0_{19}$ $Fe_{3-x}Cr_xGe$.

	Wyckoff position	Coordinates	Occupancy
Fe	$6h, y = \frac{5}{6}$	$(y, 2y, \frac{1}{4})$ $(-2y, -y, \frac{1}{4})$ $(y, -y, \frac{1}{4})$ $(-y, -2y, \frac{3}{4})$ $(2y, y, \frac{3}{4})$ $(-y, y, \frac{3}{4})$	$\frac{3-x}{3}$
Cr	$6h, y = \frac{5}{6}$	$(y, 2y, \frac{1}{4})$ $(-2y, -y, \frac{1}{4})$ $(y, -y, \frac{1}{4})$ $(-y, -2y, \frac{3}{4})$ $(2y, y, \frac{3}{4})$ $(-y, y, \frac{3}{4})$	$\frac{x}{3}$
Ge	$2c$	$(\frac{1}{3}, \frac{2}{3}, \frac{1}{4})$ $(\frac{2}{3}, \frac{1}{4}, \frac{3}{4})$	1

As a secondary check, all above postulated crystal structures $L2_1$ and its possible disordered phases (*e.g.*, $D0_3$), the hexagonal $D0_{19}$, and the tetragonal $D0_{22}$ were simulated using either CaRIne 4.0 simulations or CRYSTAL IMPACT MATCH, or an in-house PYTHON code [79] including both the real and imaginary dispersive corrections to the atomic scattering factors [289]. The simulated XRD patterns using CaRIne 4.0 for different crystal structures are presented in Fig. 4.67(b) with details including their prototypes and Wyckoff positions listed in Table 4.24. Again, among all the simulated XRD patterns, only the hexagonal $D0_{19}$ structure provides a good match to the experimental XRD pattern observed for all single phase compositions in the alloy series. There is some variation in experimental XRD peak intensities than those generated from simulations, which might be due to texturing effects, given the large grain size we observe ($\sim 300\ \mu m$). As the crystal structure of parent Fe_3Ge is hexagonal $D0_{19}$ at higher temperature ($> 700°C$) and cubic ($L1_2$, $Pm\bar{3}m$, space group no. 221 [64, 65]) at lower temperature ($< 700°C$), the $L1_2$ crys-

Table 4.24: Experimental lattice parameters and saturation magnetic moments at $T = 5$ K, both experimental and theoretical, and Curie temperature of $Fe_{3-x}Cr_xGe$ alloy series, all annealed at 1000°C for 15 days ($D0_{19}$ phases). The numbers in parentheses are the uncertainty in the last digit, *e.g.*, $6.55(9) = 6.55 \pm 0.09$.

x	Experimental lattice (Å)	Theoretical lattice (Å)	Expt. M_s at $T = 5$ K ($\mu_B/f.u.$)	Theor. M_s ($\mu_B/f.u.$)	T_c (K)
0	$a = 5.1768(2)$ $c = 4.2246(3)$	$a = 5.134$ $c = 4.222$	6.55(9)	6.48	640 [21]
0.25	$a = 5.1885(2)$ $c = 4.2260(3)$	$a = 5.144$ $c = 4.202$	5.79(5)	5.98	546
0.50	$a = 5.1934(2)$ $c = 4.2269(2)$	$a = 5.153$ $c = 4.195$	5.11(5)	5.52	446
0.70	$a = 5.1958(1)$ $c = 4.2275(3)$	$a = 5.155$ $c = 4.195$	4.44(7)	4.98	364

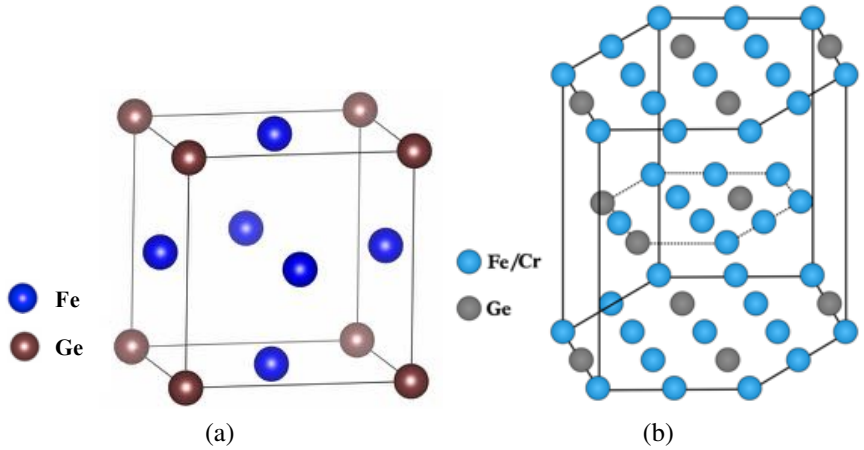

Figure 4.70: Crystal structures (a) $L1_2$, and (b) $D0_{19}$

tal structure was also simulated, but none of the intensities and peak positions matched with the experimental pattern (see Fig. 4.67).

XRD is a powerful analytical tool to determine the structures and phases present, however, the unknown degree of texturing as evident from larger grains ($\sim$ 300 μm) (in our case) alters the relative intensities of the XRD peaks and makes it difficult to rely only on the experimental XRD to determine the exact chemical order. In an attempt to determine the possible atomic ordering, we have performed Rietveld refinement. Fig. 4.68 shows the Rietveld refinement for $x = 0.50$ (see Supplementary information for $x = 0$, $x = 0.25$ and $x = 0.70$). Rietveld refinement showed reasonably good agreement (reduced χ^2 = 4.8 and weighted average Bragg R-factor = 12.2) between the observed XRD pattern and the calculated pattern for the hexagoanl $D0_{19}$ structure with the

experimental lattice parameters $a = 5.1934\,\text{Å}$ and $c = 4.2269\,\text{Å}$. However, slightly higher fitting parameters than those expected for a perfect fit can be attributed to the sample texture altering the relative intensities of the peaks compared to the calculated pattern. According to Rietveld refinement, the 6*h* sites (with the parameter $y = 5/6$) are shared by Fe and Cr with occupancy 0.833 and 0.167, respectively, in agreement with the nominal composition, and the 2*c* sites are occupied by Ge. Here, with no evidence to the contrary, we presume that Fe and Cr mix randomly on the 6*h* sites. This $D0_{19}$ structure is shown in Fig. 4.70(b). The proposed site assignments are summarized for $D0_{19}$ $Fe_{3-x}Cr_xGe$ in Table 4.23 [174].

Five hour continuous EBSD scan of $Fe_{2.50}Cr_{0.50}Ge$ sample with the step size of $\sim$0.5 μm was performed to determine the degree of texturing and purity of phase considered. Relatively large grains with some preferred orientation is revealed from IPF color map as shown in Fig. 4.69(a). The different color assigned is based on the orientation of grains. Almost 96% of the selected microstructure is observed to match the proposed structure (red color in the EBSD map (see Fig. 4.69(b)) with some zero solution regions (approximately 4%, black spots) which seem to be from the sudden changes in the roughness of the sample at grain boundaries or from artifacts caused by the metallography and chemical etching procedures. This indicates that the phase present in $Fe_{2.50}Cr_{0.50}Ge$ is proposed $D0_{19}$ phase. All these experimentally observed facts support that the crystal structure of all stable samples $0 \leq x \leq 0.70$ could be $D0_{19}$.

4.7.4.3 Magnetic Characterization

Bulk magnetic properties of all single-phase samples, measured using the VSM module of a Quantum design PPMS Dynacool are presented in Fig. 4.71 and the main parameters are summarized in Table 4.24. Fig. 4.71(a) shows the field dependent magnetization M(H) curves of all stable samples in the $Fe_{3-x}Cr_xGe$ series at 5 K. All the samples appeared to be ferromagnetic at 5 K. The saturation magnetizing field is observed to decrease with increasing Cr concentration consistent with the Slater-Pauling rule, though all samples are magnetically very soft. The Slater-Pauling rule describes the dependence of the magnetic moment on the valence electron concentration [82, 290].

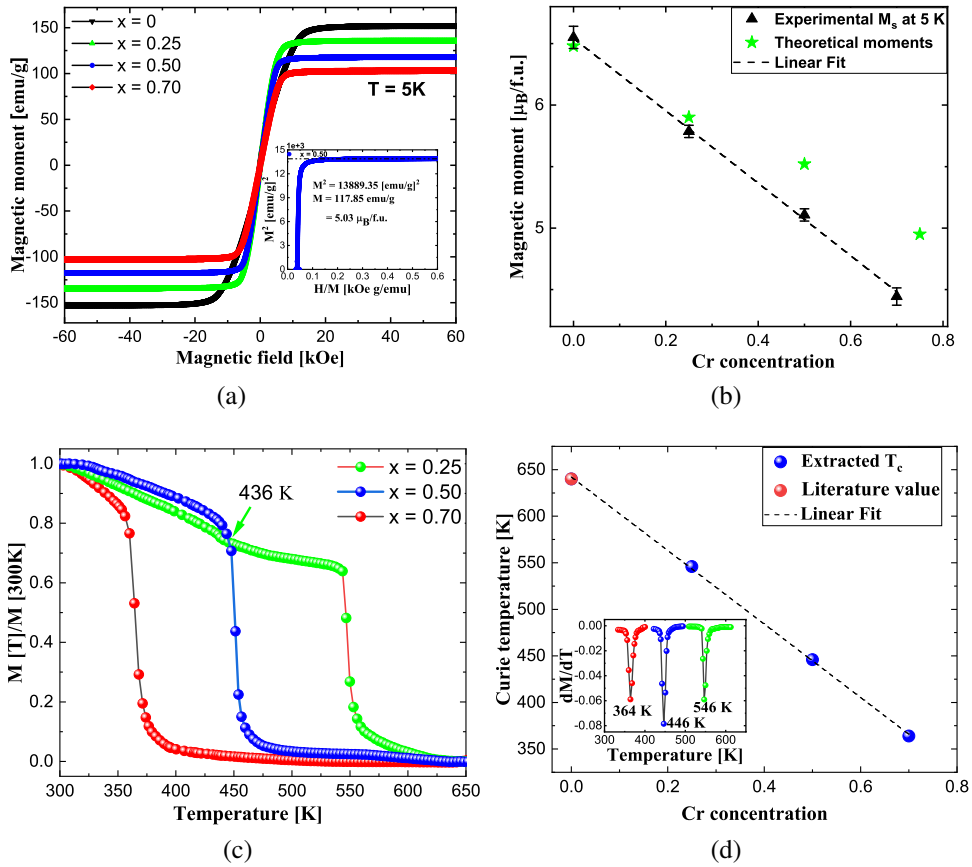

Figure 4.71: (a) The field-dependent magnetization at 5 K of $Fe_{3-x}Cr_xGe$ alloy series annealed at 1000°C for 15 days. The inset shows the Arrot plot for $x = 0.50$. (b) The magnetic moment versus Cr concentration both experimental and theoretical. (c) Temperature dependence of magnetization M at 100 Oe.The green arrow shows possible order-disorder phase transition at 436 K for $x = 0.25$. (d) The variation of T_c with Cr concentration. The inset shows the first-order derivative of magnetization as a function of temperature, the minima of which is used to extract T_c.

The saturation magnetic moments (M_s) were extracted from an Arrot plot [207], *i.e.*, by extrapolating the linear part of M^2 versus H/M to $H/M = 0$ (see inset to Fig. 4.71(a)). The obtained values of saturation magnetic moment (M_s) versus Cr concentration plot presented in Fig. 4.71(b) shows linear behavior for all stable $D0_{19}$ phases, in good agreement with those obtained from first principles calculations (shown in green data points).

The high temperature magnetization was measured by means of a vibrating sample magnetometer (LakeShore VSM 7407) equipped with a high temperature stage. The temperature of the sample was ramped at 5 K/min and measurements were taken in heating mode under an applied

field of 100 Oe. The plots of Fig. 4.71(c) show the temperature dependence of magnetization M(T) curves for $Fe_{3-x}Cr_xGe$ alloy series showing the ferro-paramagnetic transition. As shown in Fig. 4.71(c), the sample with $x = 0.25$ shows two magnetic transitions (see details in Supplementary information). The magnetic transition at 546 K corresponds to the Curie temperature but the origin of the transition at 436 K is not clear. One possible reason could be order-disorder phase transition introduced by the substitution of Cr on parent Fe_3Ge. Although the possibility of secondary phase formation (small amount) due to vacuum annealing cannot be completely ruled out, the composition measured using EDS was within $\sim 5\%$ instrumental uncertainty range. The extracted Curie temperature is observed to decrease linearly with the increase of Cr content (see Fig. 4.71(d)). The change in interatomic spacing in Fe_3Ge due to the substitution of a third element Cr leads to change in magnetic interaction. The increase in lattice parameter with Cr concentration is expected to change the distance between magnetic ions leading a weak exchange interaction between Fe-(Fe,Cr) sublattices and hence giving lower T_c values compared to parent Fe_3Ge (640 K) [21]. The inset in Fig. 4.71(d) shows the first-order derivative of magnetization as a function of temperature.

The saturation magnetic moments at 5 K and corresponding Curie temperature of all stable samples in $Fe_{3-x}Cr_xGe$ alloy series are presented in Table 4.24.

4.7.4.4 Electrical resistivity

Temperature dependence of electrical resistivity ρ of the $Fe_{3-x}Cr_xGe$ alloy series was measured using the van der Pauw method [179] in a PPMS Dynacool for samples with approximate dimensions 4 x 4 x 1.5 mm^3. Fig. 4.72 shows the variation of normalized electrical resistivity (in zero magnetic field) as a function of temperature for all samples measured during cooling process in the temperature range from 5 K to 400 K. The residual resistivity ratio (RRR) ρ_{300K}/ρ_{5K} for $Fe_{3-x}Cr_xGe$ series is found to be 7.22, 4.36, 3.16, and 2.13 for $x = 0$, 0.25, 0.50 and 0.70 respectively. A higher RRR values usually indicate to good chemical ordering, while a lower values can be attributed to scattering from impurities or anti-site defects [291]. In the present alloys, lower RRR values after Cr substitution indicates the presence of atomic disorder. Also, an increase of

Cr substitution for Fe results a substantial decrease of RRR value which suggests that the disorder increases with the increase of Cr concentration.

The resistivity upto 25 K is found to be almost independent of temperature, called residual resistivity due to lattice imperfections, impurities, *etc.* which increases with an increasing Cr content. After that, the resistivity is observed to increase with an increasing temperature and saturated at higher temperatures after Cr substitution, indicating weak variation of resistivity resulting from the parallel contribution of the intrinsic resistivity and some limiting resistivity (*e.g.,* disordered grain boundaries) known as shunting with temperature [219, 250]. The details of the nonlinear least-squares fit to resistivity including shunting term is provided in Supplementary information.

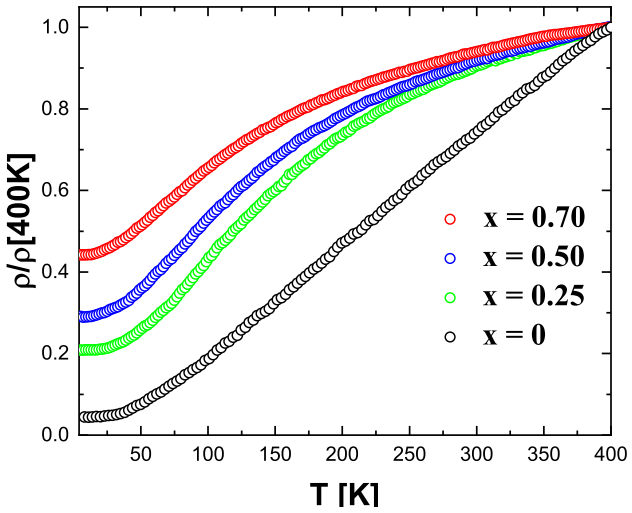

Figure 4.72: (color online) Variation of normalised electrical resistivity for $Fe_{3-x}Cr_xGe$ alloys.

4.7.4.5 Vickers micro hardness

Most previous studies on mechanical properties of Heusler alloys are theoretical in nature [263–265, 267] and only few are verified experimentally. Therefore, we decided to investigate the Vickers hardness of our alloy series as evidenced by the polishing time required during specimen preparation. The variation of Vickers micro hardness of our alloy series (all annealed at 1000°C for 15 days) with Cr concentration is presented in Fig. 4.73 with corresponding values

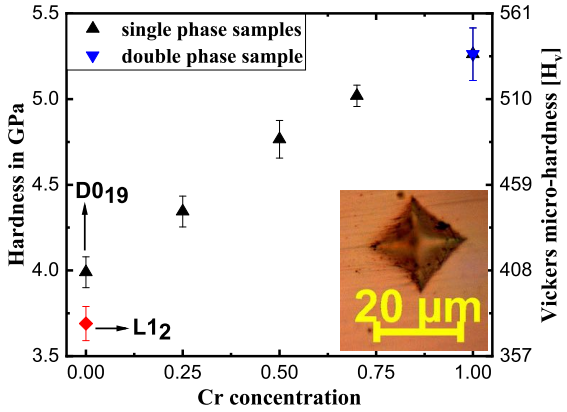

Figure 4.73: Vickers hardness versus Cr concentration in $Fe_{3-x}Cr_xGe$, all annealed at 1000°C for 15 days, with imprint of the indenter with radial cracks [bottom right]. The black data points represent the single phase compositions and diamond shaped solid red data point represent the hardness of low temperature $L1_2$ phase of parent Fe_3Ge annealed at 650°C for 25 days.

in Table 4.25. Hardness values reported are the averages of data taken from at least 12 different regions of each sample with 0.2 kg load and 10 s loading time. $Fe_{3-x}Cr_xGe$ system is observed to be softer than those reported for Heusler systems in the literatures [105, 158, 163, 209, 210, 268], respectively. The hardness is observed to increase almost linearly with increasing Cr concentration and depend on grains size and phases present as reported in the literature [211]. An enhancement of hardness is expected with the substitution of atoms with larger atomic radius for the atoms with lower atomic radius, consistent with our substitution of Cr for Fe [292]. The observed hardness values are found to agree well with those calculated theoretically (see details in Supplementary information). From the microstructure analysis of all single phase compositions, a decrease in grain size was observed with the increase of Cr concentration. We argue that grain size reduction was one key factor in the enhancement of hardness.

Table 4.25: Vickers micro-hardness of the $Fe_{3-x}Cr_xGe$ alloy series.

x	Vickers Hardness (GPa)
0	3.99 ± 0.09
0.25	4.34 ± 0.09
0.50	4.77 ± 0.11
0.70	5.02 ± 0.06
1	5.26 ± 0.15

4.7.5 Theoretical Calculations

4.7.5.1 Computational Methodology

We performed first-principle calculations within the density functional theory (DFT) framework as implemented in the Vienna Ab-initio Simulation Package (VASP) [181]. We used potentials from the projector augmented-wave (PAW) method and used the Perdew-Burke-Ernzerhof (PBE) functional [180, 182, 217]. The valence states of the atoms are as follows: Fe: $3d^7\ 4s^1$, Ge: $4s^2\ 4p^2$, Cr: $3d^5\ 4s^1$. To sample the Brillouin zone, The Monkhorst-Pack scheme was used with a 9 x 9 x 9 k-point grid for cubic structures and a 9 x 9 x 5 grid for hexagonal structures in addition to a plane wave basis set with a cutoff energy of 400 eV [200]. Self-consistent field calculations of the total and projected electronic density of states were carried out with a Gaussian-type Fermi-level smearing width of 0.05 eV. In order to generate $Fe_{3-x}Cr_xGe$ structures with varying Cr concentrations, we used the Special Quasirandom Structures (SQS) method implemented in the ATAT package [166, 270, 271]. The formation energy E_{form} (in eV/atom) of $Fe_{3-x}Cr_xGe$ is defined as $E_{\text{form}} = (E_{Fe_{3-x}Cr_xGe} - (1-x)E_{Fe_3Ge} - xE_{Cr_3Ge})$, where $E_{Fe_{3-x}Cr_xGe}$ is the energy of a $Fe_{3-x}Cr_xGe$ cell, E_{Fe_3Ge} is the energy of a Fe_3Ge cell, and E_{Cr_3Ge} is the energy of a Cr_3Ge cell, all per formula unit. We then normalized the x axis to start from x = 0 (Fe_3Ge) to x = 1 (Fe_2CrGe). We used Bader charge analysis [272, 293] to obtain the charge distribution on the atoms. The VESTA program was used to visualize atomic structures [274].

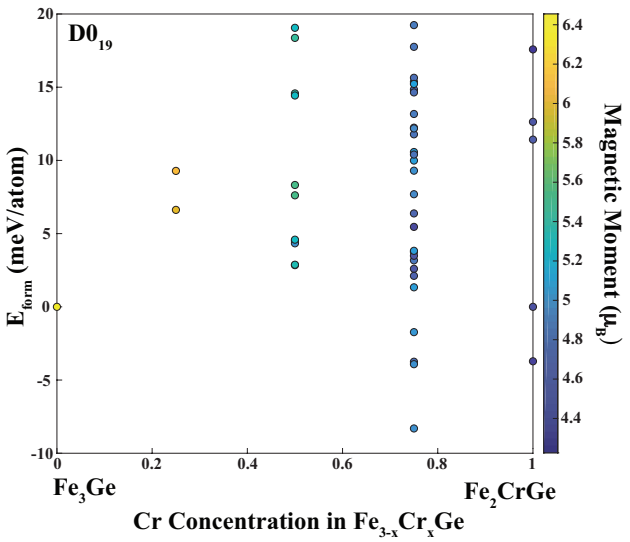

Figure 4.74: The formation energy (in eV/atom) as a function of Cr concentration for the $D0_{19}$ alloys created with the SQS method. Each data point represents a different structure and the color axis indicates the magnetic moment value for each structure.

4.7.5.2 Theoretical Results and Discussion

For the sake of comparison, we calculated the electronic, magnetic and mechanical properties of Fe_3Ge alloys for the space group of $L1_2$ and $D0_{19}$. The calculated lattice constants and magnetic moments for Fe_3Ge alloys in $L1_2$ and $D0_{19}$ phases are $a = b = c = 3.638$ Å 6.45 μ_B, and $a = b =$ 5.134 Å $c = 4.222$ Å and 6.48 μ_B, respectively. These results are in good agreement with our experimental data. In order to investigate Cr atom substitution with Fe in the Fe_3Ge structure, we employed the Special Quasirandom Structures (SQS) method to generate $Fe_{3-x}Cr_xGe$ structures between $x = 0$ and $x = 1$ for the $D0_{19}$ phases. Fig. 4.74 shows the formation energy as a function of Cr concentration x of the $D0_{19}$ phases. The magnetic moment value is also illustrated in the color axis of Fig. 4.74.

As depicted in Fig. 4.74, the $Fe_{3-x}Cr_xGe$ alloys for $x = 0.25$ and $x = 0.50$ are energetically less favorable than Fe_3Ge. However, some $Fe_{2.25}Cr_{0.75}Ge$ alloys are energetically preferable structures when compared to the alloys at $x = 0.25$ and $x = 0.50$. Substitution of Cr atoms instead of Fe atoms has little effect on the lattice parameters of the $Fe_{3-x}Cr_xGe$ structures. For instance, for $Fe_{2.25}Cr_{0.75}Ge$ the percent difference of the $a = b$ lattice parameters with respect to the Fe_3Ge case

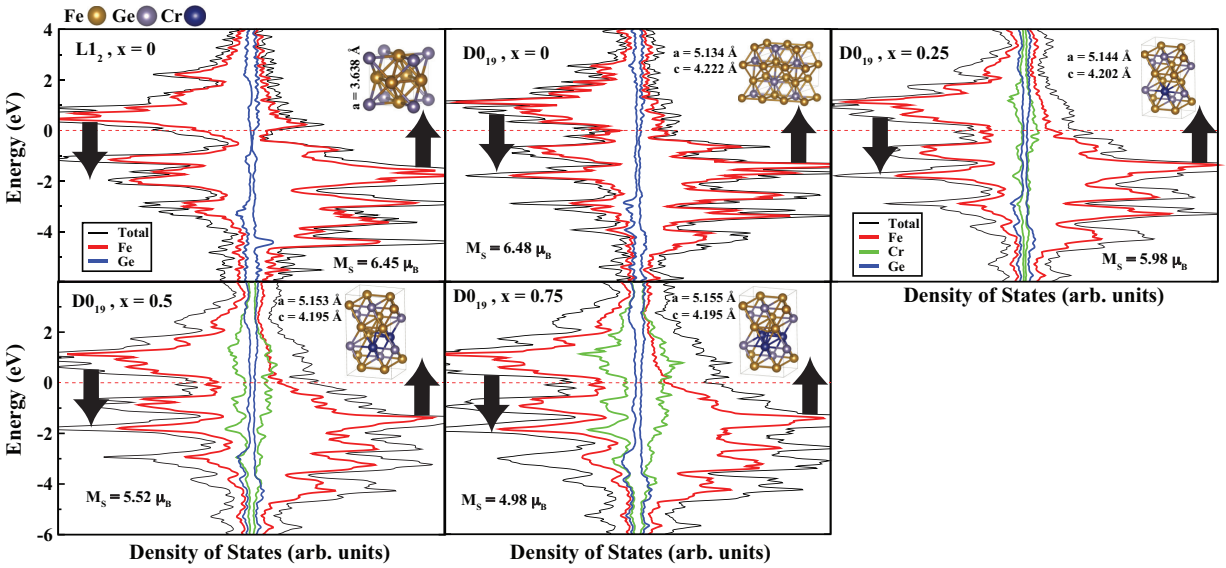

Figure 4.75: The DOS and PDOS of the lowest energy structure at specific concentration ratios for $L1_2$ and $D0_{19}$. The black arrows depict the spin up and spin down contributions and the red dotted line represents the Fermi level. The figure insets include the optimized structures, magnetic moment values and average lattice constants.

is only 0.41% and the decrease for the c lattice parameter is 0.64%. The obtained lattice parameters are in good agreement with the experimental results (see Table II). The obtained magnetic moment value for Fe_3Ge decreases with the increasing of Cr concentration, which is in accordance with Hund's rule. We observed that for the each $x = 0.25$ increment of Cr concentration in the $Fe_{3-x}Cr_xGe$ alloys results in around a 0.5 $\mu_B/f.u.$ decrease for the magnetic moment value. As can be seen in Table 4.24, calculated magnetic moments are also in good agreement with the experimentally measured values. The total and atomic magnetic moments in a unit cell for the $Fe_{3-x}Cr_xGe$ alloy series are presented in Supplementary information.

For the lowest energy structure (most energetically favorable) at each experimentally observed alloying concentration, we calculated the electronic density of states (DOS). Fig. 4.75 depicts the atom projected DOS of the experimentally observed alloys for $L1_2$ ($x = 0$) and $D0_{19}$ ($x = 0$, $x = 0.25$, $x = 0.50$, and $x = 0.75$). The spin up and spin down contributions to the DOS are indicated by the black arrows. The insets of each DOS also include the optimized geometry, the lattice constants and magnetic moment values for the considered alloys. The metallic characteristics of the $D0_{19}$ and

$L1_2$ (for $x = 0$) Fe_3Ge structures arise from the dominant orbital contribution of Fe atoms, while the Ge atom contribution around the Fermi level is negligible. As can be seen from the insets, increasing of the number of Cr atom inside the $Fe_{3-x}Cr_xGe$ alloy results in Cr clusters instead of separately placed Cr atoms. Density of states calculations show that the orbital contributions of Cr atoms are similar to the Fe orbital contribution, especially for the spin-down channel. In summary, substitution of Cr does not change the electronic properties of the $Fe_{3-x}Cr_xGe$ alloys except for the magnetic moment value.

Bader charge transfer analysis for the $Fe_{3-x}Cr_xGe$ alloys were performed to investigate the bonding type between the atoms and to gain insight on the electronic mechanism of these alloys. Bader charge analysis indicates that totally 0.30 electrons (e^-) transfer to each Ge atom from Fe atoms in Fe_3Ge for the $D0_{19}$ phase. According to the Pauling scale, the electronegativity difference between Fe and Ge atoms is 0.18, and the small amount of the charge transfer between these atoms indicate that there is non-polar covalent bonding between Fe and Ge atoms. Substitution of Cr atoms instead of Fe atoms results in a new charge distribution inside the $Fe_{3-x}Cr_xGe$ alloys. For instance, the substituted Cr atom donates 0.39 e^- and a majority of these donated electrons (0.30 e^-) are shared by the surrounding Fe atoms for the $x = 0.25$ ratio. This is expected because according to the Pauling scale of electronegativity, Fe has a value of 1.83 while Cr has a value of 1.66. With this charge transfer, some Fe atoms make their valence states similar to the initial non-alloyed states ($3d^7\ 4s^1$). Increasing of the Cr concentration slightly decreases the charge transfer from Cr atoms. For instance at $x = 0.50$, two Cr atoms donate 0.35 e^- while for $x = 0.75$, one Cr atom donates 0.37 e^- and the remaining two Cr atoms donate 0.26 e^- to the surrounding Fe and Ge atoms.

The attempt to calculate the mechanical hardness using the approaches described in references [294, 295] results in a wrong dependence on the Cr composition (see details in Supplementary information).

4.7.6 Conclusion

In conclusion, an off-stoichiometric polycrystalline bulk $Fe_{3-x}Cr_xGe$ intermetallic alloys series ($0 \leq x \leq 1$) was synthesized by arc-melting and the structural, magnetic, electron transport and mechanical properties were investigated by means of theory and experiment. Single phase microstructure in the $Fe_{3-x}Cr_xGe$ alloy series were confirmed by substituting Cr for Fe, up to $x = 0.70$. Cr substitution was observed to favor one of the Fe site in Fe_3Ge energetically to form $D0_{19}$ structure, corroborated by Ab-initio simulations. All the alloys in the series were found to be soft ferromagnets at 5 K with decreasing saturation magnetic moment as the Cr concentration increases. These hexagonal samples were in all cases observed to have markedly higher values of saturation moments. The ferromagnetic Curie temperature T_c was observed to decrease linearly with the addition of Cr concentration. The electrical resistivity measured over the temperature range from 5 K to 400 K showed purely a metallic behavior showing saturation at high temperatures. The residual resistivity ratio is also found to decrease with Cr substitution. Mechanical hardness values are measured to increase as Cr content increased. These findings may be interesting for magnetic applications where large saturation magnetization and high Curie temperature are desired.

4.8 Possible half-metallic and spin-gapless semiconducting behavior in quaternary Heusler compounds $Co_{2-x}Y_xFeGa$ (Y = Ti, V, Cr, Mn, Fe, or Co, $x = 0.50$)

4.8.1 Abstract

Recent discovery of a new class of semiconductor materials, called spin gapless semiconductors that bridge the gap between semiconductors and half-metallic ferromagnets, has attracted considerable attention in spintronics primarily because they are expected to provide a high degree of spin polarization in electron transport. In this work, we investigate the structural, electronic, magnetic, and mechanical properties of quaternary Heusler alloys $Co_{2-x}Y_xFeGa$ (Y = Ti, V, Cr, Mn, Fe, or Co, $x = 0.50$) with promising half metallic and spin gapless behavior using various experimental techniques. X-ray diffraction patterns at room temperature reveal that these alloys consist of $L2_1$ ordered phase. The magnetization study show that saturation magnetic moments measured at 5 K obey the Slater-Pauling rule of thumb for half-metals, a prerequisite for half metallicity. All alloys are observed to have high Curie temperatures that scale linearly with the saturation magnetic moments. Electrical transport measurements are performed to explain the electronic structure of the alloys. The temperature dependence of electrical resistivity in the complete temperature regime (5 K-400 K) for Mn substituted alloy strongly support the view that $Co_{1.50}Mn_{0.50}FeGa$ is a spin gapless semiconductor. *Ab initio* calculations are currently underway to understand the experimental findings.

4.8.2 Introduction

Full Heusler alloys consist of a large family of intermetallic ternary compounds designed in the stoichiometric composition X_2YZ, where X and Y represent transition metals and Z is a main group element. Heusler alloys have drawn considerable attention due to their high Curie temperature and easily tunable structural, electronic, or magnetic properties. Co-based Heusler compounds belong

PUBLISHED AS: R. Mahat*, U. Karki, S. KC, J. Law, V. Franco, I. Galanakis, A. Gupta & P. LeClair, *Possible half-metallic and spin-gapless semiconducting behavior in quaternary Heusler compounds $Co_{2-x}Y_xFeGa$ (Y = Ti, V, Cr, Mn, Fe, or Co, $x = 0.50$)*, Work in progress (2022).

to the most promising candidates of this family due to so-called half-metallicity with full spin polarization at the Fermi level, which is demandable for their potential use in spintronics devices applications *e.g.,* magnetic tunnel junctions, spin polarized field effect transistors etc [1, 29, 30, 66, 84–91, 296, 297]. Co-based Heusler alloys are supposed to be excellent candidates to examine itinerant electron ferromagnetism, exhibiting varying magnetic moments ranging from 0.3 μ_B to 1.0 μ_B at the Co site (depending on the constituents Y and Z), compatible lattice mismatch with conventional semiconductors, and 100% spin polarization at room temperature, arising from the exceptional electronic structure with a energy band gap at the Fermi level (E_F) for minority spin sub-band [20, 29–34].

The search of half metallic system with 100% spin polarization is always a center of attention because the experimentally observed spin polarization of most of the ternary Heusler alloys is always much smaller than the theoretical value. The discrepancy between theory and experiment is expected due to the structural disorder in the crystal structure [1, 41]. Many studies have been performed to tune the spin polarization, other electronic and magnetic properties reducing the structural disorder by means of various external stimuli, such as mechanical strain, chemical substitution, surface/interface termination, and temperature [53, 62, 105, 154, 206, 298–300]. In particular, in our recent work, we introduced new substitutional approach to tune electronic and magnetic properties of disordered Heusler alloys Co2FeGe and Co2FeSi [105, 154, 155]. The quaternary element additions are observed to reduce the structural disorder and change the degree of hybridization between the 3*d* orbitals of different elements with consequent changes in the position of the Fermi level with respect to the spin sub-band [115–120]. In our approach, the band gap at the Fermi level can be tuned by substituting a fourth element at X site *i.e.*, $Co_{2-x}Y^*_xYZ$, where Y, Y* are low valent transition elements and Z, Z* are main group elements [105, 154, 155] and is more convincing as X/Y site element plays main role in tailoring the half-metallicity and magnetic properties compared to Z site [122, 128]. Here, we follow a somewhat similar approach and show that it is indeed a viable mechanism for inducing a half-metallic or spin-gapless semiconducting properties in Co2FeGa (CFGa) Heusler alloy. Spin gapless semiconductors exhibit a band gap in

one of the spin channels and a zero band gap in the other and hence allow for tunable spin transport.

Further, CFGa has been reported to be stable, crystallizing in the $L2_1$ structure with high $T_c >$ 1100 K, large magnetic moment of 5.05 $\mu_B/f.u.$, and excellent transport properties [32, 144, 301]. However, the spin-polarization of 59% with Fermi level falling on the edge of the minority conduction band has been reported which makes the system shy from being half metallic [144, 302]. The quaternary Heulser alloy CoFeMnGa has been observed theoretically and experimentally to be nearly half-metallic [136] with possibility to tune spin gapless semiconducting behavior with chemical substitution , CoFeCrGa has been reported to be spin gapless semiconductor [92], while CoFeVGa and CoFeTiGa are reported theoretically to be nearly half-metallic and semiconductor respectively [142]. So, in ternary Heusler compound CFGa, it has been reported that the Fermi level lies near the conduction band edge of minority spin channel in their reported spin-polarized density of states (DOS) [144, 302]. If one of the Co atom in CFGa is replaced by another low valence transition metal atoms like Ti, V, Cr, Mn, then the Fermi level in resulting quaternery Heusler compounds has been reported to fall near the valence band edge in DOS with interesting half-metallic and spin-gapless behavior [92, 136, 142]. So, as we go from ternary CFGa to quaternary CoFeYGa (Y = Ti, V, Cr, Mn), Fermi level is observed to shift from lower edge of conduction band to upper edge of valence band in minority spin channel which is in accordance to the calculations by Galanakis *et al.* [128]. They have suggested that an expansion of the lattice should shift the Fermi level deeper in energy and the contraction should shift it higher in energy. If the Fermi energy is near one of the band edges, the energy gap may easily be smeared out at finite temperatures or destroyed by quasiparticle excitation [107, 152]. Therefore, one can expect robust half metallic and spin gapless behavior with Fermi level exactly at the middle of the band gap for some intermediate Y content in $Co_{2-x}Y_xFeGa$ (Y = Ti, V, Cr, Mn, Fe, Co; $0 \leq x \leq 1$) due to the expansion of the lattice when Y atom with larger atomic radius substitutes for Co [153]. The substitution of Y atom for Co may be also seen as d-electron deficiency.

In this work, we have introduced the substitution of all low valence transition metals atoms Y = Ti, V, Cr, Mn, and Fe to Co atoms in the parent Co_2FeGa system, and examined the structural,

electronic, magnetic, electron transport and mechanical properties of quaternary Heusler compounds $Co_{2-x}Y_xFeGa$ ($x = 0.50$), both experimentally and theoretically to get a global overview of the structural, electronic, magnetic, electron transport and mechanical properties, promising candidates for spintronics applications.

4.8.3 Experimental Methods

High purity (> 99.99 wt.%) raw materials of Ti, V, Cr, Mn, Fe, Co, and Ga in elemental form were used for arc melting of bulk $Co_{2-x}Y_xFeGa$ (Y = Ti, V, Cr, Mn, Fe, or Co, $x = 0.50$) alloys in an arc furnace on a Cu hearth provided with water cooling under argon atmosphere at a base pressure of 10^{-4} mbar. Each alloy (5g) was melted and re-melted six times to ensure chemical homogeneity. The weight loss in the alloy ingot was found to be less than 1% of the initial weight except for Mn substituted alloy. An extra 5% of the initially calculated mass was added to compensate the loss of volatile elements Mn. As an oxygen getter, Ti was melted inside the vacuum chamber separately before melting the compound to avoid oxygen contamination. The resulting ingots were cut into pieces and examined using an energy dispersive X-ray spectroscopy (EDS) detector equipped in a JEOL 7000 field emission scanning electron microscope (FESEM) to ensure the target composition after the arc melting. These as-cast alloys were heat-treated in evacuated quartz tubes at 850 K for 7 days in a furnace followed by slow cooling to room temperature to get optimum crystallization promoting the formation of $L2_1$ structure. The heat treatments were followed by metallography (see details in [163, 164]) to produce a metallic shiny surface for microstructural analysis by optical and electron microscopes. The composition and homogeneity of the specimens were again confirmed by using EDS after metallography.

The X-ray powder diffraction patterns taken on a Bruker D8 Discover X-ray diffractometer equipped with monochromatic Co-Kα (λ = 0.179 nm) radiation were used to investigate the crystal structure of the phases present at room temperature. The specimens were crushed by hand using a mortar and the XRD measurements were carried out on crushed powder samples by rotating around the ϕ axis to minimize surface effects. CaRIne crystallography 4.0 software [78] as

well as in-house PYTHON code [79] including the dispersive corrections to the atomic scattering factors were used to simulate the XRD patterns to compare with the experimental XRD patterns. Further, X-ray diffraction patterns were analyzed by Rietveld refinement technique to study the crystal structure of constituent phases using a MATCH! software based on the FullProf algorithm [80]. The low temperature magnetization curves were measured using a VSM option of Quantum Design Physical Properties Measurement System (PPMS) at 5 K and 300 K in magnetic field varying from 0 to 9 T, while the high temperature magnetization was measured using LakeShore VSM 7407. Temperature dependent of dc electrical resistivity measurements were performed using van der Pauw method [179] in PPMS. Al wire bonding was used to make the contacts. The Vickers hardness values were measured by using Buehler model 1600-6100 micro-hardness tester.

4.8.4 Experimental results and Discussions

4.8.4.0.1 Microstructural and Compositional analysis

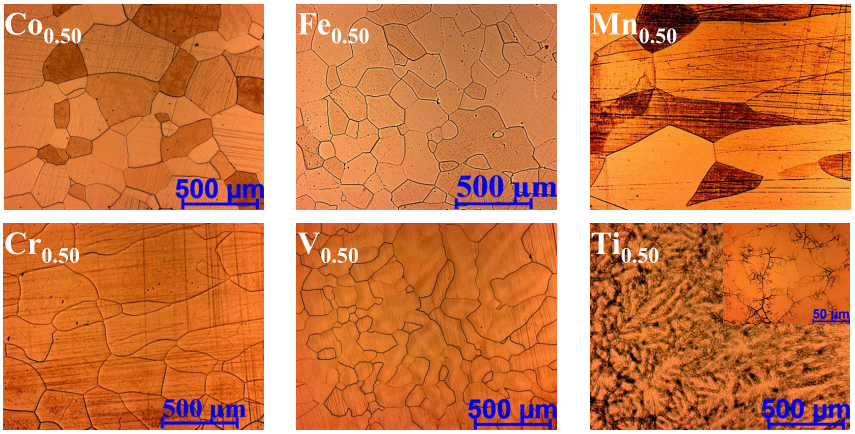

Figure 4.76: Optical micrograph of $Co_{2-x}Y_xFeGa$ (Y = Ti, V, Cr, Mn, Fe, or Co, $x = 0.50$) annealed at 850°C for 7 days followed by slow cooling showing the granular microstructure. The insert in optical image of Ti (last) shows the zoomed version. The samples were etched for 30 seconds using the Adler etchant.

Fig. 4.76 and 4.77 respectively show the optical and electron micrographs of single phase specimens from $Co_{2-x}Y_xFeGa$ (Y = Co, Fe, Mn, Cr, V, or Ti, $x = 0.50$) alloy series, all annealed

at 850°C for 7 days. 50% Y content (Co, Fe, Mn, Cr, V, or Ti) substitution for Co in CFGa is observed to get single phase microstructures. We also observed the decrease of grain size in the alloys series with the substitution of less valence Y content. The composition within the grains of all the single-phase specimens is confirmed as the target composition within an instrumental uncertainty of $\sim 5\%$ using EDS as shown in Table 4.26.

Table 4.26: Average composition of $Co_{2-x}Y_xFeGa$ (Y = Co, Fe, Mn, Cr, V, or Ti, $x = 0.50$) alloy series as determined from EDS analysis (annealed at 850°C for 7 days followed by normal cooling in the furnace).

Y content	Main phase	Composition in grain boundary	Target
Co	$Co_{1.991}Fe_{1.015}Ga_{0.994}$	$Co_{2.012}Fe_{0.982}Ga_{1.006}$	Co_2FeGa
Fe	$Co_{1.493}Fe_{1.510}Ga_{0.997}$	$Co_{1.511}Fe_{1.485}Ga_{1.004}$	$Co_{1.500}Fe_{1.500}Ga$
Mn	$Co_{1.495}Mn_{0.510}Fe_{1.010}Ga_{0.985}$	$Co_{1.503}Mn_{0.511}Fe_{0.994}Ga_{0.992}$	$Co_{1.500}Mn_{0.500}FeGa$
Cr	$Co_{1.496}Cr_{0.507}Fe_{1.003}Ga_{0.994}$	$Co_{1.507}Cr_{0.491}Fe_{0.988}Ga_{1.014}$	$Co_{1.500}Cr_{0.500}FeGa$
V	$Co_{1.491}V_{0.507}Fe_{1.011}Ga_{0.991}$	$Co_{1.497}V_{0.492}Fe_{0.990}Ga_{1.021}$	$Co_{1.500}V_{0.500}FeGa$
Ti	$Co_{1.493}Ti0.507Fe_{1.010}Ga_{0.990}$	$Co_{1.505}Ti_{0.492}Fe_{0.993}Ga_{1.010}$	$Co_{1.500}Ti_{0.500}FeGa$

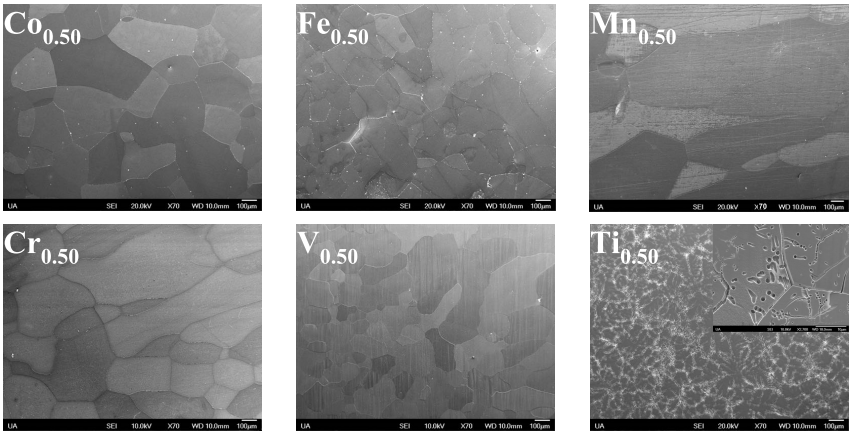

Figure 4.77: SEM micrograph of $Co_{2-x}Y_xFeGa$ (Y = Ti, V, Cr, Mn, Fe, or Co, $x = 0.50$) annealed at 850°C for 7 days followed by slow cooling showing the granular microstructure. The insert in SEM image of Ti (last) shows the zoomed version.

4.8.4.0.2 Crystal structure and atomic order analysis

Fig. 4.78(a) shows the powder XRD patterns for $Co_{2-x}Y_xFeGa$ (Y = Ti, V, Cr, Mn, Fe, or Co, $x = 0.50$) alloy series annealed at 850°C for 7 days, measured at room temperature, using a Co-K_α radiation source. All the diffraction features can be indexed to the $L2_1$ structure (first from

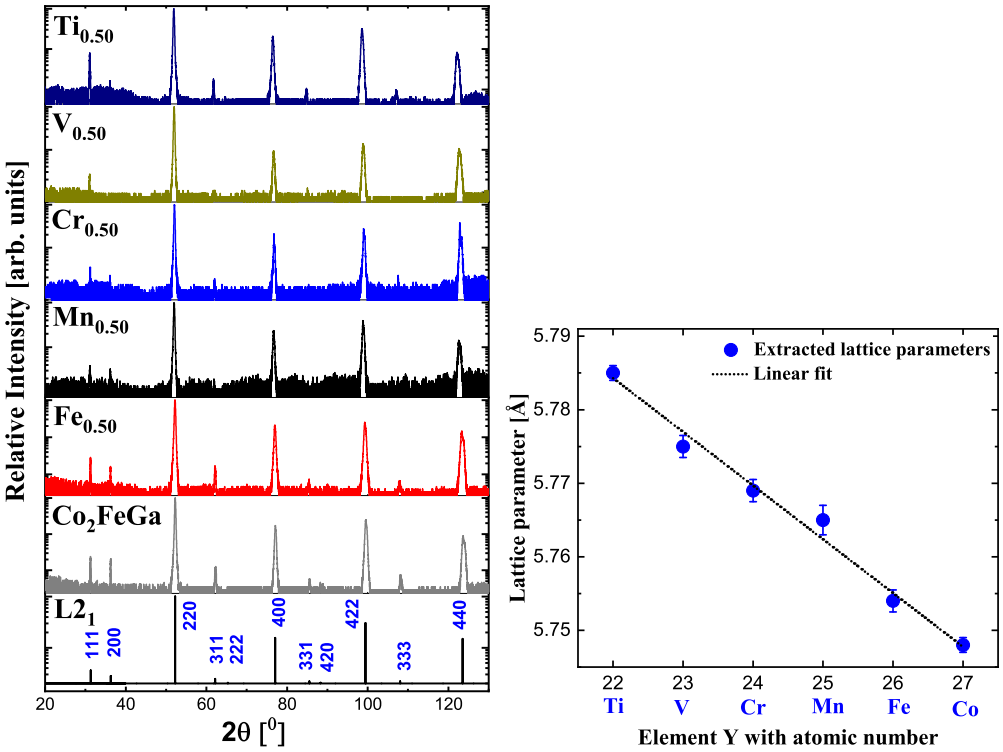

Figure 4.78: (a) Experimental XRD patterns of $Co_{2-x}Y_xFeGa$ (Y = Ti, V, Cr, Mn, Fe, or Co, $x = 0.50$) alloy series annealed at 850°C for 7 days investigated at room temperature. The first from the bottom is the simulated XRD pattern for ordered $L2_1$ structure of CFGa. The relative Intensity (y-axis) is plotted in log scale so that all the peaks can be seen clearly. (b) Variation of lattice parameter with Y element showing linear behavior.

the bottom) where only three distinct Heusler-like reflection peaks (h, k, l all odd or even) are observed; fundamental peaks with $h+k+l = 4n$, even superlattice peaks with $h+k+l = 4n+2$ and odd superlattice peaks with $h+k+l = 2n+1$. The analysis of the relative intensities of the superstructure reflection peaks (111) and (200) can be used to get important structural information concerning atomic disorder. In CFGa, the ordering of the Fe and Ga sublattices is characterized by the presence of the (111) superlattice diffraction peak and ordering of the Co sublattice is indicated by the presence of the (200) superlattice diffraction peak.

In full Heusler alloys (FHA) of the type X_2YZ with ordered $L2_1$ structure, the most electronegative main group element Z occupies 4a(0,0,0), the low valence transition metal atom Y with least electronegativity occupies 4b($\frac{1}{2},\frac{1}{2},\frac{1}{2}$), and the transition metal atoms X with intermediate

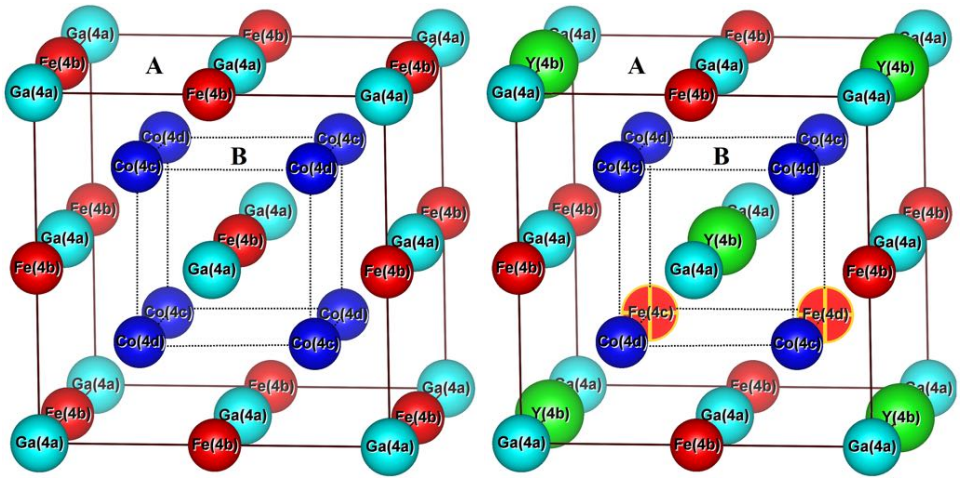

(a) (b)

Figure 4.79: Crystal structure in unit cell of (a) CFGa, and (b) $Co_{1.50}Y_{0.50}FeGa$ assuming $L2_1$ structure. The structures are shown in their ideal, unrelaxed forms.

electronegativity values occupy 8c($\frac{1}{4},\frac{1}{4},\frac{1}{4}$) (or 4c($\frac{1}{4},\frac{1}{4},\frac{1}{4}$), and 4d($\frac{3}{4},\frac{3}{4},\frac{3}{4}$)) Wyckoff positions of the space group $Fm\bar{3}m$ [1, 61]. Hereafter, we refer octahedral sites 4a and 4b as A sublattice and tetrahedral sites 4c and 4d as B sublattice as shown in Fig. 4.79. The intensities of superlattice peaks are very sensitive to any kind of atomic disorders. When the Y and Z atoms in A sublattice occupy their sites absolutely at random, this leads to B2-type disorder with only the (200) superstructure peak and vanishing (111) peak [18]. Similarly, if the X atoms occupying one of the *fcc* sublattices are mixed with the Y atoms, and the X atoms on the second sublattice are mixed with the Z atoms, this leads to B32a type disordered structure resulting (111) superstructure peak with much higher intensity than the (200) peak

Both (111) and (200) superlattice diffraction peaks are clearly visible as expected for the defect-free ordered Heusler structure in Fe, Mn, and Cr substituted alloys. However, the absence (or weak) of (200) peak in the pattern of V, and Ti substituted alloys suggests that the specimens contain strong B32a-type disorder. Further detail about possible chemical orderings in the crystal structure for this type of substitution is described in our previous publications [105, 154, 155]. Here also, we have considered that the Ga atoms occupy the 4a position, a statistical distribution of the Fe and the Y atom which substitute Co atoms in the chemical formula is expected at 4b, the

Fe atoms initially at these site in the perfect $L2_1$ structure migrate to the tetrahedral sublattice B initially occupied purely by Co, *i.e.*, Co and Fe are on the tetrahedral sublattice B (4c & 4d) and Fe, Y, and Ga on the octahedral sublattice A (4a & 4b).

Cohen's method with a Nelson-Riley extrapolation [171] was used to extract the lattice parameters. Fig. 4.78(b) displays the linear dependence of the lattice parameter a with the atomic number of Y element in $Co_{2-x}Y_xFeGa$ ($x = 0.50$), as expected from Vegard's law [205] due to the fact that Ti > V > Cr > Mn > Fe > Co [153].

4.8.4.0.3 Magnetic Characterization

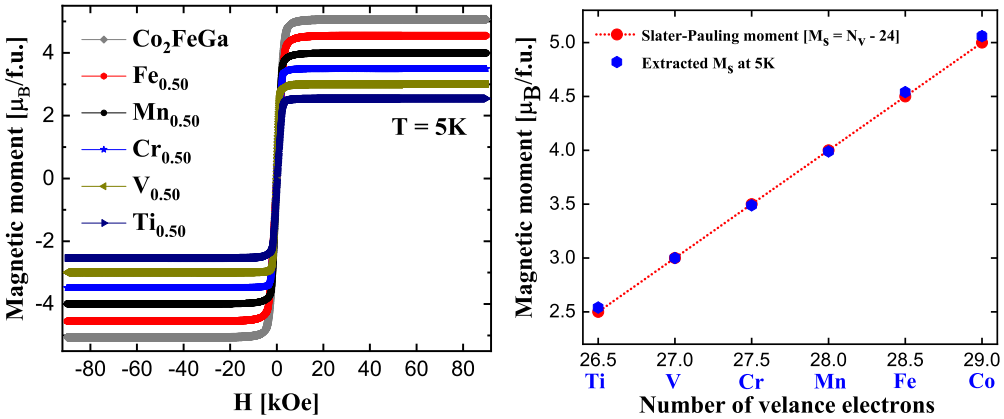

(a) (b)

Figure 4.80: (a) The field-dependent magnetization at 5 K of $Co_{2-x}Y_xFeGa$ (Y = Ti, V, Cr, Mn, Fe, or Co, $x = 0.50$). (b) The saturation magnetic moment versus number of valence electrons in the alloy series, both experimental and expected from Slater Pauling rule for half metals.

The saturation magnetization of the half-metallic Heusler alloys when crystallized in a fully ordered $L2_1$ structure are reported to follow a Slater-Pauling rule [206]. The Slater-Pauling (SP) rule relates the dependence of the magnetic moment with the valence electron concentration as [1, 7];

$$M_t = [1.50Z_{Co} + 0.50Z_Y + Z_{Fe} + Z_{Ga}] - 24 \tag{4.25}$$

where, M_t is the total spin magnetic moment per f.u. in μ_B and Z_i is the number of valence electrons of each individual atom. In $Co_{2-x}Y_xFeGa$ (Y = Co, Fe, Mn, Cr, V, or Ti, $x = 0.50$) system, the total

number of valence electrons change from 29 in CFGa to 26.5 in $Co_{1.50}Ti_{0.50}FeGa$. Therefore, the SP behavior predicts that the saturation magnetic moment should decrease with the substitution of Y element for Co. A saturation magnetic moment of

$$M(Y) = 5 - 0.50 \times (Z_{Co} - Z_{Y}) \tag{4.26}$$

is expected for $Co_{1.50}Y_{0.50}FeGa$.

Fig. 4.80(a) shows the magnetization curves for all single-phase alloys measured at 5 K using the VSM option of a Quantum design PPMS Dynacool working in the temperature range of T = 1.8 K to 400 K and with maximum possible magnetic field of 9 T. The M versus H curves shown in Fig. 4.80(a) are characteristic for ferromagnets. All the alloys are saturated in quite a low magnetic field of about 1000 Oe, indicating a low magneto-crystalline anisotropy. The spontaneous magnetic moments (M_s) at 5 K obtained by linear extrapolation to H/M=0 of M^2 versus H/M curve [207] are observed in good agreement with those expected from Slater-Pauling rule of thumb for half metals (see red data points) and decrease almost linearly with the substitution of low valence Y content (see Fig. 4.80(b)). The decrease of the total saturation magnetic moment with the substitution of low valence Y content can only be attributed to the decrease in number of Co atoms. The slight deviation from integer value of magnetic moment could be due to the slight variation in the stoichiometry of the compounds, weighing and measurement errors, partial surface oxidation, and the measurement temperature of 5 K.

The experimentally extracted values of lattice parameters, saturation magnetic moments at 5 K along with the Slater-Pauling (S-P) values, and the measured hardness values of all single phase specimens in $Co_{2-x}Y_xFeGa$ (Y = Co, Fe, Mn, Cr, V, or Ti, $x = 0.50$) alloy series are summarized in Table 4.27.

4.8.4.0.4 Electrical resistivity

Resistivity ρ of the alloys was measured using the van der Pauw method [179] in a PPMS Dynacool for samples with approximate dimensions 4 x 4 x 2 mm^3. The specific temperature

Table 4.27: Experimental lattice parameters and saturation magnetic moments at T = 5 K along with the Slater-Pauling (S-P) values, and the Vickers Hardness values of $Co_{2-x}Y_xFeGa$ (Y = Co, Fe, Mn, Cr, V, or Ti, $x = 0.50$) alloy series. The numbers in parentheses are the uncertainty in the last digit, *e.g.*, $5.06(4) = 5.06 \pm 0.04$.

Y element	Expt. lattice parameter (Å)	Expt. M_s (μ_B/f.u.)	S-P (μ_B/f.u.)	Hardness (*GPa*)
Co	a = 5.748(1)	5.06(4)	5.00	2.85(4)
Fe	a = 5.754(2)	4.54(3)	4.5	3.25(4)
Mn	a = 5.765(2)	3.99(3)	4.00	3.52(3)
Cr	a = 5.769(2)	3.49(2)	3.50	3.78(8)
V	a = 5.775(2)	3.00(2)	3.00	3.98(9)
Ti	a = 5.785(1)	2.54(3)	2.50	4.46(83)

dependencies of electrical resistivity for $Co_{2-x}Y_xFeGa$ (Y= Co, Mn, Cr, or V, $x = 0.50$) with zero applied field are shown in Fig. 4.81 (a). In zero field, the resistivity is observed to show a clear metallic temperature dependence with a monotonic increase with increasing temperature for Co, Cr, and V doped alloys. But, Mn doped $Co_{1.50}Mn_{0.50}FeGa$ alloy shows semiconducting behavior with a negative temperature coefficient ($d\rho/dT < 0$). The electrical resistivity decreases almost linearly with increasing temperature, which clearly indicates a semiconducting behaviour. The temperature coefficient of resistivity (TCR) is extracted to be -8.0 x 10^{-10} Ω m/K which is much smaller than that of classical semiconductor Si *e.g.* TCR = -8.0 x 10^{-2} Ω m/K. The extracted TCR value is also comparable with the values -7.0 x 10^{-10} Ω m/K, -1.4 x 10^{-9} Ω m/K, and -5.0 x 10^{-9} Ω m/K reported for spin gapless semiconductors (SGS) CoFeMnSi, Mn_2CoAl and CoFeCrAl, respectively which are also known to exhibit linear resistivity behaviour [53, 303, 304]. The value of conductivity is found to be 3058 S/cm at 300 K, which is slightly higher than the value 2440 S/cm obtained for SGS Heusler alloys Mn_2CoAl [53] and comparable to the value 3233 S/cm reported for SGS CoFeCrGa [92].

We also synthesized $Co_{2-x}Mn_xFeGa$ ($0 \leq x \leq 1$) alloy series to understand the transport behavior more. Fig. 4.81 (b) shows the specific temperature dependencies of electrical resistivity for $Co_{2-x}Mn_xFeGa$ ($0 \leq x \leq 1$) alloy series with zero applied field. All alloys except $Co_{1.50}Mn_{0.50}FeGa$ show metallic behavior in the resistivity measurements. So far, the electronic transport properties strongly support the view that $Co_{1.50}Mn_{0.50}FeGa$ is a spin gapless semiconductor.

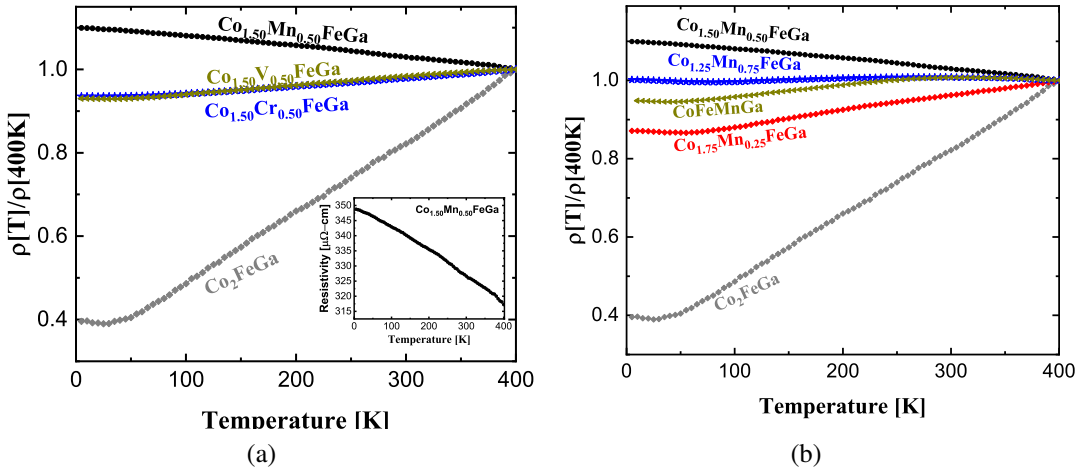

Figure 4.81: Variation of electrical resistivity with temperature in zero field for (a) $Co_{2-x}Y_xFeGa$ (Y= Co, Mn, Cr, or V, $x = 0.50$), and (b) $Co_{2-x}Mn_xFeGa$ ($0 \leq x \leq 1$). The values are normalized with the value at 400 K. The inset in FIG 4.81 (a) shows the temperature dependence of resistivity for $Co_{1.50}Mn_{0.50}FeGa$.

4.8.4.0.5 Vickers micro hardness

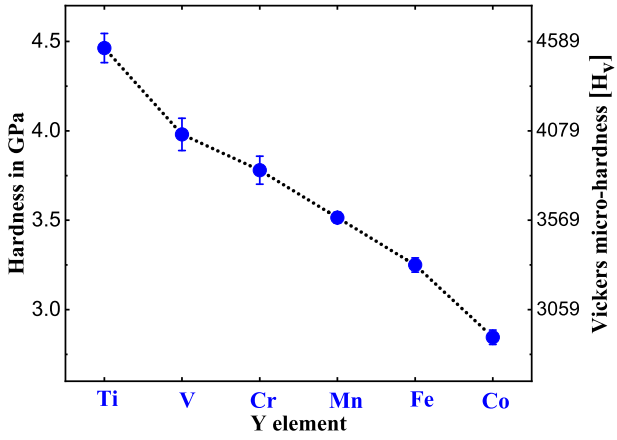

Figure 4.82: Vickers hardness versus Y atom in $Co_{2-x}Y_xFeGa$ (Y = Ti, V, Cr, Mn, Fe, or Co, $x = 0.50$), all annealed at 850°C for 7 days.

Mechanical robustness of materials is one of the key factor to undergo repetitive thermal cycling and resist cracking from vibrations in industrial applications. Here, the Vickers indentation test is utilized to characterize the hardness of the materials as these experiments are simple to perform, need a small quantity of material, are generally non-destructive. Fig. 4.82 shows the vari-

ation of Vickers micro hardness of the alloy series with substituted Y element measured at room temperature with corresponding values in Table 4.27. Hardness values reported are the averages of data taken from at least 12 different regions of each sample with 0.2 kg load and 10 s loading time. The Vickers hardness is calculated from

$$HV = 1.8544F/D^2[\mathrm{kg/mm^2}] \tag{4.27}$$

where, D is the diagonal length of the impression of the diamond probe. The alloys from the series are relatively soft when compared to the values reported for Heuslers in the literature [105, 154–156, 158, 163, 164, 209, 210]. The hardness is observed to increase with the decrease of atomic number of substituted Y element.

4.8.5 Conclusion

In conclusion, we performed a detailed experimental study on the structural, magnetic, electron transport, and mechanical properties of $Co_{2-x}Y_xFeGa$ (Y = Ti, V, Cr, Mn, Fe, or Co, $x = 0.50$) Heusler alloys. The alloys are found to crystallize in the face-centered cubic structure with some B32a-type disorder in V, and Ti substituted alloys. The saturation magnetization is found to be in fair agreement with the value expected from Slater-Pauling rule of thumb for half-metals, which is a prerequisite for spintronic materials. Resistivity measurements confirm the metallic behavior except for $Co_{1.50}Mn_{0.50}FeGa$ alloy. $Co_{1.50}Mn_{0.50}FeGa$ is observed to show semiconducting behavior. The absence of exponential dependence of resistivity on temperature indicates the semiconducting nature, but with spin gapless behavior. So far, the electronic transport properties, together with the predicted and measured magnetic moment of ~ 4 μ_B/f.u. strongly support the view that $Co_{1.50}Mn_{0.50}FeGa$ is a spin gapless semiconductor. *Ab initio* calculations are currently underway to understand the experimental findings.

CHAPTER 5

SUMMARY

5.1 Conclusions

In this dissertation, at first we have utilized the Heusler database and literature survey to screen potential Heusler compounds for their use in spintronics device applications and introduced a new approach of novel material design. Our research focused mainly on finding new candidates for stable half-metallic Heusler compounds from experimental and theoretical aspects. Our new approach of designing novel Heuselr compounds by substituting low valence transition metal atoms Sc, Ti, V, Cr, Mn, or Fe on X site of full Heulser alloys (X_2YZ) is observed to exhibit exceptional tunability in the electronic and magnetic properties compared to other existing substitutional schemes.

For our study, we focused mainly on Co- and Fe-based Hesuler compounds because most of them are predicted to show robust half-metallicity at room temperature due to their observed high Curie temperature and large interinsic magnetic moments. Our work utilizes the substitution of low valence transition metal atoms Y = Sc, Ti, V, Cr, Mn, or Fe for Co in series of ternary Heusler alloys $Co_{2-x}Y_xFeZ$ (Z = Ge, Si, Ga, Al, $0 \leq x \leq 1$) to understand the substitutional effect on structural, electronic, magnetic, electron transport and mechanical properties, both experimentally and theoretically. The low valence transition metal atoms substitution for Co is observed to bring the Fermi level toward the center of energy gap in minority spin channel and increase the majority spin density of states near the Fermi level, responsible for achieving 100% spin polarization. The low valence transition metal atoms (bigger atomic size) substitution for Co can also be taken as electron deficiency and increase of unit cell. To investigate these new materials experimentally,

we synthesized them in the polycrystalline bulk form. A comprehensive discussion of our experimental and analytical approach to synthesize and characterize these new materials can be found in Chapter 2 and theoretical methods in Chapter 3 of this dissertation. The unique part of our work is metallography followed by detailed microstructural (optical and electron) analysis, which is missing in most of the literature. The fact that XRD can not detect the impurity phase contents either below the detection limit of XRD (less than roughly 5% of the overall volume) or amorphous in nature, in such case the microstructural analysis is the most direct way to characterize the stability of the alloys. Another unique part in our theoretical calculations is the use of the Monte Carlo Special Quasirandom Structure (MCSQS) method to accurately construct the cubic supercell structures consisting of 16 atoms which can handle double-site substitutions as expected for our substitutional series taking care of nearest neighbor interaction. Our experimental and theoretical findings for investigated systems are reported in Chapter 4 in published paper format.

Our investigations of $Co_{2-x}Y_xFeGe$ (Y = V, or Cr, $0 \leq x \leq 1$) system revealed that Cr and V substitutions for Co stabilized the disordered Co_2FeGe system with tunable electronic and magnetic properties. Our magnetic and electron transport measurements along with DFT calculations showed that Cr and V are ideal dopant for achieving robust half-metallic behavior in Co_2FeGe. These results inspired us to investigate another Heusler system $Co_{2-x}Y_xFeSi$ (Y = Sc, Ti, V, Cr, Mn, or Fe, $0 \leq x \leq 1$), because the parent compound Co_2FeSi is known to have highest Curie temperature of 1100 K and magnetic moment of 6 μ_B. The system is reported to be half-metallic only after including effective coulomb exchange interaction (DFT+U approach). Our experimental investigation revealed that all the alloys from the series showed promising half-metallic behavior with very high Curie temperatures, except Sc substituted alloys. But, only Mn and Cr substituted alloys appeared to show half-metallic behavior in DFT calculations while half-metallicity is predicted in all the alloys after introducing Hubbard U correction to DFT and the results are consistent with experiment. This confirmed that $Co_{2-x}Y_xFeSi$ is strongly correlated system. Further, our investigations for finding half-metallic Heuslers led us to synthesize $Co_{2`x}Y_xFeGa/Al$ (Y = Ti, V, Cr, Mn, or Fe, $x = 0.50$) compounds. So far, the magnetic and electronic transport properties

strongly support the view that $Co_{1.50}Mn_{0.50}FeGa$ is a spin gapless semiconductor and *ab initio* calculations are currently underway to understand the experimental findings. Our search for the half-metallic Heuslers also led us to the discovery of a new phase of materials $Fe_{3-x}Y_xGe$ (Y = V, or Cr, $0 \leq x \leq 1$) with the hexagonal crystal structure which makes them potential in perpendicular media and CPP-GMR because these materials possess high magnetic moment and high magneto-crystalline anisotropy.

The half-metallicity and spin-gapless semiconductiong behavior, with a confirmation from both theory and experiment, make the investigated alloys promising material for spintronics application. However, experimental study of other properties such as current spin polarization is needed to confirm the above observations.

5.2 Outlook

The half-metallicity and spin-gapless semiconductiong behavior, with a confirmation from both theory and experiment, make the investigated alloys promising materials for spintronics application. However, experimental study of other properties such as current spin polarization using Point Contact Andreev Reflection (PCAR) is needed to confirm the above observations. One can study the magnetoresistance in the materials to gain more insights. The greatest challenge to our substitutional series is to identify the exact chemical ordering in the crystal structure. The fact that the Heusler systems that we investigated $Co_{2-x}Y_xFeZ$ (Y = Sc, Ti, V, Cr, Mn, Fe or Co, Z = Ge, Si, Ga, or Al, $0 \leq x \leq 1$) contain constituent $3d$-metals with very small differences in the atomic scattering factors, X-ray powder diffraction technique might not be a sufficient method to identify the exact chemical ordering as discussed in our work. The unknown degree of texturing in the specimens might alter the relative intensity of XRD peaks. One can use methods such as Mössbauer spectroscopy to locate the position of Fe atoms and Fe vacancies because Fe is expected to occupy two different crystal cites as an indirect substitution scheme in our study. More theoretical and experimental investigations are necessary to understand the spin-gapless semiconducting behavior in $Co_{1.50}Mn_{0.50}FeGa$ alloy.

Our work covered the theoretical calculations and experimental investigations of bulk properties revealing some applicable potentiality of series of Heusler alloys. In order to gain more insights on the properties and implement these materials into the spintronics devices, it is then apparent to fabricate them in thin films form. Gilbert damping parameters, and magnetic anisotropies can be experimentally studied using ferromagnetic resonance (FMR). Nevertheless, we have already started to fabricate $Co_{1.50}Cr_{0.50}FeGe$ and $Co_{1.50}Cr_{0.50}FeAl$ Heusler alloys in thin film form using magnetron sputtering technique. From our initial investigation, alloys are observed to have very low damping constants ($\sim 10^{-3}$) as expected for half-metallic systems.

REFERENCES

[1] T. Graf, C. Felser, and S. S. Parkin, *Simple rules for the understanding of Heusler compounds*, Progress in solid state chemistry **39**, 1 (2011).

[2] Y. Waseda, E. Matsubara, and K. Shinoda, *X-ray diffraction crystallography: introduction, examples and solved problems* (Springer Science & Business Media, 2011).

[3] https://www.mram-info.com/stt-mram, Accessed 01 Jan 2022 .

[4] https://www.nims.go.jp/mmu/tutorials/SpinFET.html , Accessed 01 Jan 2022 .

[5] https://www.cpfs.mpg.de/felser, Accessed 08 Jan 2022 .

[6] K. Manna, Y. Sun, L. Muechler, J. Kübler, and C. Felser, *Heusler, weyl and berry*, Nature Reviews Materials **3**, 244 (2018).

[7] I. Galanakis, P. H. Dederichs, and N. Papanikolaou, *Slater-Pauling behavior and origin of the half-metallicity of the full-Heusler alloys*, Phys. Rev. B **66**, 174429 (2002).

[8] I. Galanakis, P. Mavropoulos, and P. H. Dederichs, *Electronic structure and Slater–Pauling behaviour in half-metallic Heusler alloys calculated from first principles*, Journal of Physics D: Applied Physics **39**, 765 (2006).

[9] https://www.struers.com/Search?q=labopress .

[10] IndianFace, *Wikipedia commons images under Creative Commons Licence*, `https://commons.wikimedia.org/wiki/File:Electron-beam_interaction_and_transmission_with_sample.jpg` (2013).

[11] A. S. Ali, *Application of nanomaterials in environmental improvement*, in *Nanotechnology and the Environment* (IntechOpen, 2020).

[12] Claudionico, *Wikipedia commons images under Creative Commons Licence*, `https://en.wikipedia.org/wiki/File:Electron_Interaction_with_Matter.svg` (2015).

[13] S. Nasir, M. Z. Hussein, Z. Zainal, N. A. Yusof, S. A. M. Zobir, and I. M. Alibe, *Potential valorization of by-product materials from oil palm: A review of alternative and sustainable carbon sources for carbon-based nanomaterials synthesis*, BioResources **14**, 2352 (2019).

[14] https://sites.fct.unl.pt/labanalises/AnalyticalFields/MaterialsCharacterization, Accessed 01 Jan 2022 .

[15] https://commons.wikimedia.org/w/index.php?curid=12958389, Accessed 10 Oct 2021 ().

[16] Á. Morales-García, R. Valero, and F. Illas, *An empirical, yet practical way to predict the band gap in solids by using density functional band structure calculations*, The Journal of Physical Chemistry C **121**, 18862 (2017).

[17] K. R. Kumar, K. K. Bharathi, J. A. Chelvane, S. Venkatesh, G. Markandeyulu, and N. Harishkumar, *First-principles calculation and experimental investigations on full-Heusler alloy Co_2FeGe*, IEEE Transactions on Magnetics **45**, 3997 (2009).

[18] Enamullah, Y. Venkateswara, S. Gupta, M. R. Varma, P. Singh, K. G. Suresh, and A. Alam, *Electronic structure, magnetism, and antisite disorder in CoFeCrGe and CoMnCrAl quaternary Heusler alloys*, Phys. Rev. B **92**, 224413 (2015).

[19] J. E. Fischer, J. Karel, S. Fabbrici, P. Adler, S. Ouardi, G. H. Fecher, F. Albertini, and C. Felser, *Magnetic properties and Curie temperatures of disordered Heusler compounds:* $Co_{1+x}Fe_{2-x}Si$, Phys. Rev. B **94**, 024418 (2016).

[20] S. Wurmehl, G. H. Fecher, H. C. Kandpal, V. Ksenofontov, C. Felser, and H.-J. Lin, *Investigation of Co_2FeSi: The Heusler compound with highest Curie temperature and magnetic moment*, Applied physics letters **88**, 032503 (2006).

[21] J. Drijver, S. Sinnema, and F. Van der Woude, *Magnetic properties of hexagonal and cubic Fe_3Ge*, Journal of Physics F: Metal Physics **6**, 2165 (1976).

[22] T. Kaneko, T. Kanomata, Y. Kawazoe, and Y. Uwatoko, *Magnetic Properties of d-Elements, Alloys and Compounds Under Pressure* (Springer, 2014).

[23] M. N. Baibich, J. M. Broto, A. Fert, F. N. Van Dau, F. Petroff, P. Etienne, G. Creuzet, A. Friederich, and J. Chazelas, *Giant Magnetoresistance of (001)Fe/(001)Cr Magnetic Superlattices*, Phys. Rev. Lett. **61**, 2472 (1988).

[24] G. Binasch, P. Grünberg, F. Saurenbach, and W. Zinn, *Enhanced magnetoresistance in layered magnetic structures with antiferromagnetic interlayer exchange*, Phys. Rev. B **39**, 4828 (1989).

[25] B. Terris and T. Thomson, *Nanofabricated and self-assembled magnetic structures as data storage media*, Journal of physics D: Applied physics **38**, R199 (2005).

[26] S. Bhatti, R. Sbiaa, A. Hirohata, H. Ohno, S. Fukami, and S. Piramanayagam, *Spintronics based random access memory: a review*, Materials Today **20**, 530 (2017).

[27] E. E. Fullerton and I. K. Schuller, *The 2007 Nobel Prize in physics: Magnetism and transport at the nanoscale*, ACS nano **1**, 384 (2007).

[28] A. Hirohata and K. Takanashi, *Future perspectives for spintronic devices*, Journal of Physics D: Applied Physics **47**, 193001 (2014).

[29] R. A. de Groot, F. M. Mueller, P. G. v. Engen, and K. H. J. Buschow, *New Class of Materials: Half-Metallic Ferromagnets*, Phys. Rev. Lett. **50**, 2024 (1983).

[30] I. Galanakis, P. Dederichs, and N. Papanikolaou, *Slater-Pauling behavior and origin of the half-metallicity of the full-Heusler alloys*, Physical Review B **66**, 174429 (2002).

[31] K. Ziebeck and P. Webster, *A neutron diffraction and magnetization study of Heusler alloys containing Co and Zr, Hf, V or Nb*, Journal of Physics and Chemistry of Solids **35**, 1 (1974).

[32] P. Brown, K.-U. Neumann, P. Webster, and K. Ziebeck, *The magnetization distributions in some Heusler alloys proposed as half-metallic ferromagnets*, Journal of Physics: Condensed Matter **12**, 1827 (2000).

[33] A. Jezierski, *Magnetic properties of partially ordered $Co_{2-x}Pd_xTiSn$ alloys*, Journal of magnetism and magnetic materials **164**, 381 (1996).

[34] A. Yamasaki, S. Imada, R. Arai, H. Utsunomiya, S. Suga, T. Muro, Y. Saitoh, T. Kanomata, and S. Ishida, *Orbital angular momentum and interpretation of core-absorption magnetic circular dichroism on the band picture in Co-based Heusler alloys* $\mathrm{Co_2}Y\mathrm{Sn}$ ($Y =$ Ti, Zr, *and* Nb), Phys. Rev. B **65**, 104410 (2002).

[35] K. Schwarz, *CrO_2 predicted as a half-metallic ferromagnet*, Journal of Physics F: Metal Physics **16**, L211 (1986).

[36] A. Yanase and K. Siratori, *Band structure in the high temperature phase of Fe_3O_4*, Journal of the Physical Society of Japan **53**, 312 (1984).

[37] Y. Okimoto, T. Katsufuji, T. Ishikawa, A. Urushibara, T. Arima, and Y. Tokura, *Anomalous Variation of Optical Spectra with Spin Polarization in Double-Exchange Ferromagnet:* $\mathrm{La_{1-x}Sr_xMnO_3}$, Phys. Rev. Lett. **75**, 109 (1995).

[38] G. A. Prinz, *Magnetoelectronics*, Science **282**, 1660 (1998).

[39] D. Awschalom, D. Loss, and N. Samarth, *Semiconductor spintronics and quantum computation* (Springer Science & Business Media, 2002).

[40] T. Dietl, o. H. Ohno, a. F. Matsukura, J. Cibert, and e. D. Ferrand, *Zener model description of ferromagnetism in zinc-blende magnetic semiconductors*, science **287**, 1019 (2000).

[41] C. Felser and A. Hirohata, *Heusler alloys*, Vol. 222 (2015).

[42] A. Hirohata, M. Kikuchi, N. Tezuka, K. Inomata, J. Claydon, Y. Xu, and G. Van der Laan, *Heusler alloy/semiconductor hybrid structures*, Current Opinion in Solid State and Materials Science **10**, 93 (2006).

[43] A. Hirohata, H. Sukegawa, H. Yanagihara, I. Žutić, T. Seki, S. Mizukami, and R. Swaminathan, *Roadmap for emerging materials for spintronic device applications*, IEEE Transactions on Magnetics **51**, 1 (2015).

[44] K. E. H. M. Hanssen, P. E. Mijnarends, L. P. L. M. Rabou, and K. H. J. Buschow, *Positron-annihilation study of the half-metallic ferromagnet NiMnSb: Experiment*, Phys. Rev. B **42**, 1533 (1990).

[45] K. E. H. M. Hanssen and P. E. Mijnarends, *Positron-annihilation study of the half-metallic ferromagnet NiMnSb: Theory*, Phys. Rev. B **34**, 5009 (1986).

[46] M. Kirillova, A. Makhnev, E. Shreder, V. Dyakina, and N. Gorina, *Interband Optical Absorption and Plasma Effects in Half-Metallic XMnY Ferromagnets*, physica status solidi (b) **187**, 231 (1995).

[47] M. Jourdan, J. Minár, J. Braun, A. Kronenberg, S. Chadov, B. Balke, A. Gloskovskii, M. Kolbe, H.-J. Elmers, G. Schönhense, *et al.*, *Direct observation of half-metallicity in the Heusler compound Co_2MnSi*, Nature communications **5**, 1 (2014).

[48] F. Heusler, *über magnetische manganlegierungen.*, Verhandlungen der Deutschen physikalischen Gesellschaft **5**, 219 (1903).

[49] S. Khmelevskyi, *Antiferromagnetic ordering on the frustrated fcc lattice in the intermetallic compound GdPtBi*, Phys. Rev. B **86**, 104429 (2012).

[50] R. Weht and W. E. Pickett, *Half-metallic ferrimagnetism in* Mn_2VAl, Phys. Rev. B **60**, 13006 (1999).

[51] R. Zhang, Z. Gercsi, M. Venkatesan, K. Rode, and J. M. D. Coey, *Pauli paramagnetism of cubic* V_3Al*, CrVTiAl, and related 18-electron Heusler compounds with a group-13 element*, Phys. Rev. B **103**, 174407 (2021).

[52] H. Nakamura, Y. Kitaoka, K. Asayama, Y. Ōnuki, and T. Komatsubara, *Observation of two phase transitions in the Heusler heavy fermion system CeInCu2*, Journal of magnetism and magnetic materials **76**, 467 (1988).

[53] S. Ouardi, G. H. Fecher, C. Felser, and J. Kübler, *Realization of Spin Gapless Semiconductors: The Heusler Compound* Mn_2CoAl, Phys. Rev. Lett. **110**, 100401 (2013).

[54] T. Krenke, E. Duman, M. Acet, E. F. Wassermann, X. Moya, L. Mañosa, and A. Planes, *Inverse magnetocaloric effect in ferromagnetic Ni-Mn-Sn alloys*, Nature materials **4**, 450 (2005).

[55] R. Carey, D. M. Newman, and M. L. Wears, *Giant low-temperature enhancement of magneto-optic Kerr effects in PtMnSb*, Phys. Rev. B **62**, 1520 (2000).

[56] S. K. Malik, A. M. Umarji, and G. K. Shenoy, *Depression of the superconducting transition temperature of the Heusler alloy* Pd_2YSn *with the addition of magnetic rare-earth metals*, Phys. Rev. B **32**, 4426 (1985).

[57] N. Shutoh and S. Sakurada, *Thermoelectric properties of the* $Ti_x(Zr_{0.5}Hf_{0.5})_{1-x}NiSn$ *half-Heusler compounds*, Journal of alloys and compounds **389**, 204 (2005).

[58] H. Lin, L. A. Wray, Y. Xia, S. Xu, S. Jia, R. J. Cava, A. Bansil, and M. Z. Hasan, *Half-Heusler ternary compounds as new multifunctional experimental platforms for topological quantum phenomena*, Nature materials **9**, 546 (2010).

[59] Z. Wang, M. G. Vergniory, S. Kushwaha, M. Hirschberger, E. V. Chulkov, A. Ernst, N. P. Ong, R. J. Cava, and B. A. Bernevig, *Time-Reversal-Breaking Weyl Fermions in Magnetic Heusler Alloys*, Phys. Rev. Lett. **117**, 236401 (2016).

[60] S. Sakurada and N. Shutoh, *Effect of Ti substitution on the thermoelectric properties of (Zr, Hf) NiSn half-Heusler compounds*, Applied Physics Letters **86**, 082105 (2005).

[61] T. J. Burch, T. Litrenta, and J. I. Budnick, *Hyperfine Studies of Site Occupation in Ternary Systems*, Phys. Rev. Lett. **33**, 421 (1974).

[62] Y. Miura, K. Nagao, and M. Shirai, *Atomic disorder effects on half-metallicity of the full-Heusler alloys* $Co_2(Cr_{1-x}Fe_x)Al$ *: A first-principles study*, Phys. Rev. B **69**, 144413 (2004).

[63] P. J. Webster, *Heusler alloys*, Contemporary Physics **10**, 559 (1969).

[64] T. Hahn, *The 230 space groups*, in *International Tables for Crystallography Volume A: Space-Group Symmetry* (Springer, 2006) pp. 112–717.

[65] M. J. Mehl, D. Hicks, C. Toher, O. Levy, R. M. Hanson, G. Hart, and S. Curtarolo, *The AFLOW library of crystallographic prototypes: part 1*, Computational Materials Science **136**, S1 (2017).

[66] C. Felser and G. H. Fecher, *Spintronics: from materials to devices* (Springer Science & Business Media, 2013).

[67] K. V. Shanavas, M. A. McGuire, and D. S. Parker, *Electronic and magnetic properties of Si substituted* Fe_3Ge, Journal of Applied Physics **118**, 123902 (2015).

[68] Y. Sakuraba, K. Izumi, T. Iwase, S. Bosu, K. Saito, K. Takanashi, Y. Miura, K. Futatsukawa, K. Abe, and M. Shirai, *Mechanism of large magnetoresistance in* $Co_2MnSi/Ag/Co_2MnSi$ *devices with current perpendicular to the plane*, Phys. Rev. B **82**, 094444 (2010).

[69] T. Nakatani, N. Hase, H. Goripati, Y. Takahashi, T. Furubayashi, and K. Hono, *Co-based Heusler alloys for CPP-GMR spin-valves with large magnetoresistive outputs*, IEEE Transactions on Magnetics **48**, 1751 (2012).

[70] K. Yakushiji, K. Saito, S. Mitani, K. Takanashi, Y. Takahashi, and K. Hono, *Current-perpendicular-to-plane magnetoresistance in epitaxial* $Co_2MnSi/Cr/Co_2MnSi$ *trilayers*, Applied physics letters **88**, 222504 (2006).

[71] M. Kratochvílová, D. Král, M. Dušek, J. Valenta, R. Colman, O. Heczko, and M. Veis, Fe_2MnSn*-experimental quest for predicted heusler alloy*, Journal of Magnetism and Magnetic Materials , 166426 (2020).

[72] P. Webster, *Magnetic and chemical order in Heusler alloys containing cobalt and manganese*, Journal of Physics and Chemistry of Solids **32**, 1221 (1971).

[73] C. Guillemard, S. Petit-Watelot, T. Devolder, L. Pasquier, P. Boulet, S. Migot, J. Ghanbaja, F. Bertran, and S. Andrieu, *Issues in growing Heusler compounds in thin films for spintronic applications*, Journal of Applied Physics **128**, 241102 (2020).

[74] B. Ravel, M. P. Raphael, V. G. Harris, and Q. Huang, *EXAFS and neutron diffraction study of the Heusler alloy* Co_2MnSi, Phys. Rev. B **65**, 184431 (2002).

[75] S. Wurmehl, A. Alfonsov, J. T. Kohlhepp, H. J. M. Swagten, B. Koopmans, M. Wójcik, B. Balke, V. Ksenofontov, C. G. F. Blum, and B. Büchner, *^{55}Mn NMR study of quaternary half-metallic ferromagnetic $Co_2Mn_{1-x}Fe_xSi$ Heusler compounds*, Phys. Rev. B **88**, 134424 (2013).

[76] V. Jung, G. H. Fecher, B. Balke, V. Ksenofontov, and C. Felser, *Electronic structure, magnetic properties and order-disorder phenomena in $Co_2Mn_{1-x}Fe_xAl$*, Journal of Physics D: Applied Physics **42**, 084007 (2009).

[77] B. Ravel, J. O. Cross, M. P. Raphael, V. G. Harris, R. Ramesh, and L. V. Saraf, *Atomic disorder in Heusler Co_2MnGe measured by anomalous X-ray diffraction*, Applied physics letters **81**, 2812 (2002).

[78] C. Boudias and D. Monceau, *CaRIne Crystallography: The Crystallographic Software for Research and Teaching* (CaRIne Crystallography, 2006).

[79] P. LeClair, *X-ray Diffraction Calculation Software*, (2018).

[80] A. Putz and H. Brandenburg, *Phase Identification from Power Diffraction*, Crystal Impact **Kreuzherrenstr. 102, 53227 Bonn, Germany**.

[81] J. C. Slater, *The Ferromagnetism of Nickel. II. Temperature Effects*, Phys. Rev. **49**, 931 (1936).

[82] L. Pauling, *The Nature of the Interatomic Forces in Metals*, Phys. Rev. **54**, 899 (1938).

[83] J. Kübler, *First principle theory of metallic magnetism*, Physica B+ C **127**, 257 (1984).

[84] K. Buschow and P. Van Engen, *Magnetic and magneto-optical properties of Heusler alloys based on aluminium and gallium*, Journal of Magnetism and Magnetic Materials **25**, 90 (1981).

[85] C. Felser, G. H. Fecher, and B. Balke, *Spintronics: a challenge for materials science and solid-state chemistry*, Angewandte Chemie International Edition **46**, 668 (2007).

[86] J. Kübler, A. R. William, and C. B. Sommers, *Formation and coupling of magnetic moments in Heusler alloys*, Phys. Rev. B **28**, 1745 (1983).

[87] D. Kieven, R. Klenk, S. Naghavi, C. Felser, and T. Gruhn, *I-II-V half-Heusler compounds for optoelectronics: Ab initio calculations*, Phys. Rev. B **81**, 075208 (2010).

[88] S. A. Khandy and D. C. Gupta, *dft investigations on mechanical stability, electronic structure and magnetism in co_2taz (z = al, ga, in) heusler alloys*, Semiconductor Science and Technology **32**, 125019 (2017).

[89] H. Mori, Y. Odahara, D. Shigyo, T. Yoshitake, and E. Miyoshi, *Electronic band structure calculations on thin films of the $L2_1$ full Heusler alloys X_2YSi (X, Y = Mn, Fe, and Co): Toward spintronic materials*, Thin Solid Films **520**, 4979 (2012).

[90] D. Serrate, J. De Teresa, R. Cordoba, and S. Yusuf, *Magnetoresistance and magnetostriction of $Co_2Cr_{0.6}Fe_{0.4}Al$ Heusler alloy*, Solid state communications **142**, 363 (2007).

[91] S. Picozzi, A. Continenza, and A. J. Freeman, *Role of structural defects on the half-metallic character of* Co_2MnGe *and* Co_2MnSi *Heusler alloys*, Phys. Rev. B **69**, 094423 (2004).

[92] L. Bainsla, A. I. Mallick, M. M. Raja, A. A. Coelho, A. K. Nigam, D. D. Johnson, A. Alam, and K. G. Suresh, *Origin of spin gapless semiconductor behavior in CoFeCrGa: Theory and Experiment*, Phys. Rev. B **92**, 045201 (2015).

[93] L. Bainsla, A. I. Mallick, M. M. Raja, A. K. Nigam, B. S. D. C. S. Varaprasad, Y. K. Takahashi, A. Alam, K. G. Suresh, and K. Hono, *Spin gapless semiconducting behavior in equiatomic quaternary CoFeMnSi Heusler alloy*, Phys. Rev. B **91**, 104408 (2015).

[94] P. D. Patel, S. Shinde, S. D. Gupta, S. D. Dabhi, and P. K. Jha, *The first principle calculation of structural, electronic, magnetic, elastic, thermal and lattice dynamical properties of fully compensated ferrimagnetic spin-gapless heusler alloy Zr_2MnGa*, Computational Condensed Matter **15**, 61 (2018).

[95] I. Galanakis, K. Özdoğan, and E. Şaşıoğlu, *Spin-filter and spin-gapless semiconductors: The case of Heusler compounds*, AIP Advances **6**, 055606 (2016).

[96] L. Fan, F. Chen, C.-m. Li, X. Hou, X. Zhu, J.-l. Luo, and Z.-Q. Chen, *Promising spintronics: Mn-based Heusler alloys Mn_3Ga, Mn_2YGa (Y= V, Nb, Ta), ScMnVGa*, Journal of Magnetism and Magnetic Materials **497**, 166060 (2020).

[97] R. Soulen, J. Byers, M. Osofsky, B. Nadgorny, T. Ambrose, S. Cheng, P. R. Broussard, C. Tanaka, J. Nowak, J. Moodera, *et al.*, *Measuring the spin polarization of a metal with a superconducting point contact*, science **282**, 85 (1998).

[98] S. N. Okuno, T. Kishi, and K. Tanaka, *Spin-Polarized Tunneling Spectroscopy of Co(0001) Surface States*, Phys. Rev. Lett. **88**, 066803 (2002).

[99] H. Wiesmann, M. Gurvitch, H. Lutz, A. Ghosh, B. Schwarz, M. Strongin, P. B. Allen, and J. W. Halley, *Simple Model for Characterizing the Electrical Resistivity in $A-15$ Superconductors*, Phys. Rev. Lett. **38**, 782 (1977).

[100] B. Raquet, M. Viret, E. Sondergard, O. Cespedes, and R. Mamy, *Electron-magnon scattering and magnetic resistivity in 3d ferromagnets*, Phys. Rev. B **66**, 024433 (2002).

[101] J. Moodera and D. Mootoo, *Nature of half-metallic ferromagnets: Transport studies*, Journal of Applied Physics **76**, 6101 (1994).

[102] D. Bombor, C. G. F. Blum, O. Volkonskiy, S. Rodan, S. Wurmehl, C. Hess, and B. Büchner, *Half-Metallic Ferromagnetism with Unexpectedly Small Spin Splitting in the Heusler Compound* Co_2FeSi, Phys. Rev. Lett. **110**, 066601 (2013).

[103] A. Barry, J. Coey, L. Ranno, and K. Ounadjela, *Evidence for a gap in the excitation spectrum of CrO_2*, Journal of applied physics **83**, 7166 (1998).

[104] D. A. Goodings, *Electrical Resistivity of Ferromagnetic Metals at Low Temperatures*, Phys. Rev. **132**, 542 (1963).

[105] S. KC, R. Mahat, S. Regmi, A. Mukherjee, P. Padhan, R. Datta, W. H. Butler, A. Gupta, and P. LeClair, *Tunable properties and potential half-metallicity in* $(Co_{2-x}Ti_x)$FeGe *Heusler alloys: An experimental and theoretical investigation*, Phys. Rev. Materials **3**, 114406 (2019).

[106] K. Elphick, W. Frost, M. Samiepour, T. Kubota, K. Takanashi, H. Sukegawa, S. Mitani, and A. Hirohata, *Heusler alloys for spintronic devices: review on recent development and future perspectives*, Science and Technology of Advanced Materials **22**, 235 (2021).

[107] B. Balke, G. H. Fecher, H. C. Kandpal, C. Felser, K. Kobayashi, E. Ikenaga, J.-J. Kim, and S. Ueda, *Properties of the quaternary half-metal-type Heusler alloy* $Co_2Mn_{1-x}Fe_xSi$, Phys. Rev. B **74**, 104405 (2006).

[108] L. Singh, Z. Barber, Y. Miyoshi, W. Branford, and L. Cohen, *Structural and transport studies of stoichiometric and off-stoichiometric thin films of the full Heusler alloy* Co_2 *MnSi*, Journal of applied physics **95**, 7231 (2004).

[109] K. Srinivas, T. Prasanna Kumari, M. Manivel Raja, and S. Kamat, *Effect of Fe substitution for Co on structure, electrical resistivity, and magnetic properties of Heusler type* $Co_{2-x}Fe_{1+x}Si$ *alloys*, Journal of Applied Physics **114**, 033911 (2013).

[110] D. Rani, L. Bainsla, A. Alam, and K. Suresh, *Spin-gapless semiconductors: Fundamental and applied aspects*, Journal of Applied Physics **128**, 220902 (2020).

[111] S. Wurmehl, G. H. Fecher, H. C. Kandpal, V. Ksenofontov, C. Felser, H.-J. Lin, and J. Morais, *Geometric, electronic, and magnetic structure of* Co_2FeSi*: Curie temperature and magnetic moment measurements and calculations*, Phys. Rev. B **72**, 184434 (2005).

[112] J. Schmalhorst, A. Thomas, S. Kämmerer, O. Schebaum, D. Ebke, M. D. Sacher, G. Reiss, A. Hütten, A. Turchanin, A. Gölzhäuser, and E. Arenholz, *Transport properties of magnetic tunnel junctions with* Co_2MnSi *electrodes: The influence of temperature-dependent interface magnetization and electronic band structure*, Phys. Rev. B **75**, 014403 (2007).

[113] C. Herbort, E. A. Jorge, and M. Jourdan, *Morphology induced magnetoresistance enhancement of tunneling junctions with the Heusler electrode* $Co_2Cr_{0.6}Fe_{0.4}Al$, Applied Physics Letters **94**, 142504 (2009).

[114] Y. Sakuraba, a. M. Hattori, M. Oogane, Y. Ando, H. Kato, A. Sakuma, T. Miyazaki, and H. Kubota, *Giant tunneling magnetoresistance in* Co_2MnSi*/Al-O/* Co_2MnSi *magnetic tunnel junctions*, Applied Physics Letters **88**, 192508 (2006).

[115] S. Karthik, A. Rajanikanth, T. Nakatani, Z. Gercsi, Y. Takahashi, T. Furubayashi, K. Inomata, and K. Hono, *Effect of Cr substitution for Fe on the spin polarization of* $Co_2Cr_xFe_{1-x}Si$ *Heusler alloys*, Journal of Applied Physics **102**, 043903 (2007).

[116] N. Tezuka, N. Ikeda, S. Sugimoto, and K. Inomata, *Giant tunnel magnetoresistance at room temperature for junctions using full-Heusler* $Co_2FeAl_{0.5}Si_{0.5}$ *electrodes*, Japanese journal of applied physics **46**, L454 (2007).

[117] B. C. S. Varaprasad, A. Rajanikanth, Y. Takahashi, and K. Hono, *Enhanced spin polarization of Co2MnGe Heusler alloy by substitution of Ga for Ge*, Applied physics express **3**, 023002 (2010).

[118] T. Nakatani, A. Rajanikanth, Z. Gercsi, Y. Takahashi, K. Inomata, and K. Hono, *Structure, magnetic property, and spin polarization of $Co_2FeAl_xSi_{1-x}$ Heusler alloys*, Journal of Applied Physics **102**, 033916 (2007).

[119] B. Deka, A. Srinivasan, R. Singh, B. C. S. Varaprasad, Y. Takahashi, and K. Hono, *Effect of Co substitution for Mn on spin polarization and magnetic properties of ferrimagnetic Mn_2VAl*, Journal of Alloys and Compounds **662**, 510 (2016).

[120] B. C. S. Varaprasad, A. Srinivasan, Y. Takahashi, M. Hayashi, A. Rajanikanth, and K. Hono, *Spin polarization and Gilbert damping of $Co_2Fe(Ga_xGe_{1-x})$ Heusler alloys*, Acta Materialia **60**, 6257 (2012).

[121] K. Özdoğan, B. Aktaş, I. Galanakis, and E. Şaşıoğlu, *Influence of mixing the low-valent transition metal atoms (Y, Y^*=Cr, Mn, Fe) on the properties of the quaternary Co_2 $[Y_{1-x}Y^*_x]$ Z (Z=Al, Ga, Si, Ge, or Sn) Heusler compounds*, Journal of Applied Physics **101**, 073910 (2007).

[122] I. Galanakis, K. Özdoğan, B. Aktaş, and E. Şaşıoğlu, *Effect of doping and disorder on the half metallicity of full Heusler alloys*, Applied physics letters **89**, 042502 (2006).

[123] N. Tezuka, N. Ikeda, F. Mitsuhashi, and S. Sugimoto, *Improved tunnel magnetoresistance of magnetic tunnel junctions with Heusler $Co_2FeAl_{0.5}Si_{0.5}$ electrodes fabricated by molecular beam epitaxy*, Applied Physics Letters **94**, 162504 (2009).

[124] G. H. Fecher, H. C. Kandpal, S. Wurmehl, C. Felser, and G. Schönhense, *Slater-Pauling rule and Curie temperature of Co_2-based Heusler compounds*, Journal of applied physics **99**, 2167629 (2006).

[125] K. Kobayashi, R. Umetsu, R. Kainuma, K. Ishida, T. Oyamada, A. Fujita, and K. Fukamichi, *Phase separation and magnetic properties of half-metal-type $Co_2Cr_{1-x}Fe_xAl$ alloys*, Applied physics letters **85**, 4684 (2004).

[126] R. Y. Umetsu, K. Kobayashi, A. Fujita, K. Oikawa, R. Kainuma, K. Ishida, N. Endo, K. Fukamichi, and A. Sakuma, *Half-metallic properties of* $Co_2(Cr_{1-x}Fe_x)Ga$ *Heusler alloys*, Phys. Rev. B **72**, 214412 (2005).

[127] I. Galanakis, *Appearance of half-metallicity in the quaternary Heusler alloys*, Journal of Physics: Condensed Matter **16**, 3089 (2004).

[128] I. Galanakis, P. H. Dederichs, and N. Papanikolaou, *Origin and properties of the gap in the half-ferromagnetic Heusler alloys*, Phys. Rev. B **66**, 134428 (2002).

[129] M. Kumar, T. Nautiyal, and S. Auluck, *Full potential results on the magneto-optical properties of the Heusler compounds Co_2FeX (X= Al, Ga, Si and Ge)*, Journal of Physics: Condensed Matter **21**, 196003 (2009).

[130] B. Venkateswarlu, P. Midhunlal, P. Babu, and N. H. Kumar, *Magnetic and anomalous electronic transport properties of the quaternary Heusler alloys $Co_2Ti_{1-x}Fe_xGe$*, Journal of Magnetism and Magnetic Materials **407**, 142 (2016).

[131] B. Varaprasad, A. Srinivasan, Y. Takahashi, M. Hayashi, A. Rajanikanth, and K. Hono, *Spin polarization and Gilbert damping of $Co_2Fe(Ga_xGe_{1-x})$ Heusler alloys*, Acta Materialia **60**, 6257 (2012).

[132] G. Gao, L. Hu, K. Yao, B. Luo, and N. Liu, *Large half-metallic gaps in the quaternary Heusler alloys CoFeCrZ (Z= Al, Si, Ga, Ge): A first-principles study*, Journal of Alloys and Compounds **551**, 539 (2013).

[133] Y. Jin, P. Kharel, P. Lukashev, S. Valloppilly, B. Staten, J. Herran, I. Tutic, M. Mitrakumar, B. Bhusal, A. O'Connell, *et al.*, *Magnetism and electronic structure of CoFeCrX (X= Si, Ge) Heusler alloys*, Journal of Applied Physics **120**, 053903 (2016).

[134] Z. Cui, B. Wu, X. Ruan, Q. Zhou, Z. Liu, X. Fu, and Y. Feng, *Enhancing the half-metallicity of equiatomic quaternary Heusler compound CoFeCrGe via atomic doping*, Results in Physics **15**, 102533 (2019).

[135] L. Bainsla, K. Suresh, A. Nigam, M. Manivel Raja, B. C. S. Varaprasad, Y. Takahashi, and K. Hono, *High spin polarization in CoFeMnGe equiatomic quaternary Heusler alloy*, Journal of Applied Physics **116**, 203902 (2014).

[136] V. Alijani, S. Ouardi, G. H. Fecher, J. Winterlik, S. S. Naghavi, X. Kozina, G. Stryganyuk, C. Felser, E. Ikenaga, Y. Yamashita, S. Ueda, and K. Kobayashi, *Electronic, structural, and magnetic properties of the half-metallic ferromagnetic quaternary Heusler compounds CoFeMnZ (Z = Al, Ga, Si, Ge)*, Phys. Rev. B **84**, 224416 (2011).

[137] H. C. Kandpal, G. H. Fecher, C. Felser, and G. Schönhense, *Correlation in the transition-metal-based Heusler compounds* Co_2MnSi *and* Co_2FeSi, Phys. Rev. B **73**, 094422 (2006).

[138] Y. Du, G. Xu, X. Zhang, Z. Liu, S. Yu, E. Liu, W. Wang, and G. Wu, *Crossover of magnetoresistance in the zero-gap half-metallic Heusler alloy Fe_2CoSi*, EPL (Europhysics Letters) **103**, 37011 (2013).

[139] C. Sterwerf, S. Paul, B. Khodadadi, M. Meinert, J.-M. Schmalhorst, M. Buchmeier, C. K. Mewes, T. Mewes, and G. Reiss, *Low Gilbert damping in Co_2FeSi and Fe_2CoSi films*, Journal of Applied Physics **120**, 083904 (2016).

[140] L. Bainsla, K. Z. Suzuki, M. Tsujikawa, H. Tsuchiura, M. Shirai, and S. Mizukami, *Magnetic tunnel junctions with an equiatomic quaternary CoFeMnSi Heusler alloy electrode*, Applied Physics Letters **112**, 052403 (2018).

[141] X. Dai, G. Liu, G. H. Fecher, C. Felser, Y. Li, and H. Liu, *New quarternary half metallic material CoFeMnSi*, Journal of Applied Physics **105**, 07E901 (2009).

[142] L. Xiong, L. Yi, and G. Gao, *Search for half-metallic magnets with large half-metallic gaps in the quaternary Heusler alloys CoFeTiZ and CoFeVZ (Z= Al, Ga, Si, Ge, As, Sb)*, Journal of magnetism and magnetic materials **360**, 98 (2014).

[143] Y. Zhang, Z. Liu, G. Li, X. Ma, and G. Liu, *Magnetism, band gap and stability of half-metallic property for the quaternary Heusler alloys CoFeTiZ (Z= Si, Ge, Sn)*, Journal of alloys and compounds **616**, 449 (2014).

[144] M. Zhang, E. Brück, F. R. de Boer, Z. Li, and G. Wu, *The magnetic and transport properties of the Co_2FeGa Heusler alloy*, Journal of Physics D: Applied Physics **37**, 2049 (2004).

[145] W. Wang, H. Sukegawa, R. Shan, S. Mitani, and K. Inomata, *Giant tunneling magnetoresistance up to 330% at room temperature in sputter deposited Co_2FeAl/MgO/CoFe magnetic tunnel junctions*, Applied Physics Letters **95**, 182502 (2009).

[146] W. Wang, E. Liu, M. Kodzuka, H. Sukegawa, M. Wojcik, E. Jedryka, G. H. Wu, K. Inomata, S. Mitani, and K. Hono, *Coherent tunneling and giant tunneling magnetoresistance in $Co_2FeAl/MgO/CoFe$ magnetic tunneling junctions*, Phys. Rev. B **81**, 140402 (2010).

[147] S. Mizukami, D. Watanabe, M. Oogane, Y. Ando, Y. Miura, M. Shirai, and T. Miyazaki, *Low damping constant for Co_2FeAl Heusler alloy films and its correlation with density of states*, Journal of Applied Physics **105**, 07D306 (2009).

[148] R. Choudhary, P. Kharel, S. R. Valloppilly, Y. Jin, A. O' Connell, Y. Huh, S. Gilbert, A. Kashyap, D. J. Sellmyer, and R. Skomski, *Structural disorder and magnetism in the spin-gapless semiconductor CoFeCrAl*, AIP Advances **6**, 056304 (2016).

[149] T. Tsuchiya, T. Roy, K. Elphick, J. Okabayashi, L. Bainsla, T. Ichinose, K. Z. Suzuki, M. Tsujikawa, M. Shirai, A. Hirohata, and S. Mizukami, *Magnetic tunnel junctions with a B2-ordered CoFeCrAl equiatomic Heusler alloy*, Phys. Rev. Materials **3**, 084403 (2019).

[150] T. Lin, X. Dai, L. Wang, X. Wang, X. Liu, Y. Cui, and G. Liu, *Anti-site-induced diluted magnetism in semiconductive CoFeTiAl alloy*, Journal of Alloys and Compounds **657**, 519 (2016).

[151] Y. Takahashi, Y. Miura, R. Choi, T. Ohkubo, Z. Wen, K. Ishioka, R. Mandal, R. Medapalli, H. Sukegawa, S. Mitani, *et al.*, *Increased magnetic damping in ultrathin films of Co_2FeAl with perpendicular anisotropy*, Applied Physics Letters **110**, 252409 (2017).

[152] G. H. Fecher and C. Felser, *Substituting the main group element in cobalt-iron based Heusler alloys: $Co_2FeAl_{1-x}Si_x$*, Journal of Physics D: Applied Physics **40**, 1582 (2007).

[153] *http://periodictable.com/Properties/A/AtomicRadius.an. pr.html*, .

[154] R. Mahat, S. KC, U. Karki, J. Y. Law, V. Franco, I. Galanakis, A. Gupta, and P. LeClair, *Possible half-metallic behavior of $Co_{2-x}Cr_xFeGe$ Heusler alloys: Theory and experiment*, Phys. Rev. B **104**, 014430 (2021).

[155] R. Mahat, K. Shambhu, U. Karki, S. Regmi, J. Y. Law, V. Franco, I. Galanakis, A. Gupta, and P. LeClair, *Structural, electronic, magnetic, and mechanical properties of $Co_{2-x}V_xFeSi$ Heusler alloys*, IEEE Transactions on Magnetics , 1 (2021).

[156] R. Mahat, S. KC, U. Karki, S. Regmi, J. Y. Law, V. Franco, I. Galanakis, A. Gupta, and P. LeClair, *Structural, electronic, magnetic, transport and mechanical properties of the half-metal-type quaternary Heusler alloy $Co_2Fe_{1-x}V_xGe$*, Journal of Magnetism and Magnetic Materials **539**, 168352 (2021).

[157] R. Mahat, D. Wines, S. KC, U. Karki, J. Y. Law, F. Ersan, V. Franco, C. Ataca, A. Gupta, and P. LeClair, *Experimental and theoretical study on the possible half-metallic behavior of $Co_{2-x}V_xFeGe$ Heusler alloys*, sumbitted for publication **–**, (2022).

[158] R. Mahat, S. KC, D. Wines, S. Regmi, U. Karki, F. Ersan, C. Ataca, A. Gupta, and P. LeClair, *Effect of V substitution on structural, magnetic, transport and mechanical properties of the half-metal-type Heusler alloy Co_2FeGe*, Bulletin of the American Physical Society (2020).

[159] R. Mahat, U. Karki, S. KC, J. Y. Law, V. Franco, I. Galanakis, A. Gupta, and P. LeClair, *Effect of mixing the low-valence transition metal atoms Y = Co, Fe, Mn, Cr, V, Ti, or Sc on the properties of quaternary Heusler compounds $Co_{2-x}Y_xFeSi$ ($0 \leq x \leq 1$)*, To be submitted **–**, (2022).

[160] R. Mahat, S. KC, U. Karki, S. Regmi, J. Y. Law, V. Franco, I. Galanakis, A. Gupta, and P. LeClair, *Influence of mixing the low-valent transition metal atoms Y = Sc, Ti, V, Cr, Mn and Fe on the properties of possible half-metallic Heusler compounds $Co_{1.5}Y_{0.5}FeSi$*, Bulletin of the American Physical Society **2021** (2021).

[161] R. Mahat, U. Karki, S. KC, J. Y. Law, V. Franco, I. Galanakis, A. Gupta, and P. LeClair, *Possible half-metallic and spin-gapless semiconducting behavior in quaternary Heusler compounds $Co_{2-x}Y_xFeGa$ (Y = Ti, V, Cr, Mn, Fe, or Co; x = 0.50)*, in progress **–**, (2022).

[162] R. Mahat, U. Karki, S. KC, J. Y. Law, V. Franco, I. Galanakis, A. Gupta, and P. LeClair, *Effect of B2-type disorder in materials properties in quaternary Heusler compounds $Co_{2-x}Y_xFeAl$ (Y = Ti, V, Cr, Mn, Fe, or Co; x = 0.50)*, in progress **–**, (2022).

[163] R. Mahat, K. Shambhu, D. Wines, F. Ersan, S. Regmi, U. Karki, R. White, C. Ataca, P. Padhan, A. Gupta, and P. LeClair, *Tuneable structure and magnetic properties in $Fe_{3-x}V_xGe$ alloys*, Journal of Alloys and Compounds **830**, 154403 (2020).

[164] R. Mahat, S. KC, D. Wines, S. Regmi, U. Karki, Z. Li, F. Ersan, J. Law, C. Ataca, V. Franco, A. Gupta, and P. LeClair, *Influence of Cr-substitution on the structural, magnetic, electron transport, and mechanical properties of $Fe_{3`x}Cr_xGe$ Heusler alloys*, Journal of Magnetism and Magnetic Materials **521**, 167398 (2021).

[165] R. Mahat, *Tuning structural and magnetic properties by vanadium substitution in Fe_3Ge*, in *APS March Meeting Abstracts*, Vol. 2019 (2019) pp. G70–212.

[166] D. Wines, F. Ersan, R. Mahat, S. KC, S. Regmi, U. KARKI, P. Padhan, A. Gupta, P. LeClair, and C. Ataca, *Tuning the electronic and magnetic properties of Heusler alloys: A theoretical and experimental investigation*, Bulletin of the American Physical Society **65** (2020).

[167] G. F. Vander Voort, S. R. Lampman, B. R. Sanders, G. J. Anton, C. Polakowski, J. Kinson, K. Muldoon, S. D. Henry, and W. W. Scott Jr, *ASM handbook*, Metallography and microstructures **9**, 44073 (2004).

[168] H. S. Nalwa, *Handbook of nanostructured materials and nanotechnology, five-volume set* (Academic Press, 1999).

[169] M. Che and J. C. Védrine, *Characterization of solid materials and heterogeneous catalysts: From structure to surface reactivity* (John Wiley & Sons, 2012).

[170] B. Warren, *X-ray Diffraction*, New York **253** (1990).

[171] B. Cullity and S. Stock, *Elements of X-ray Diffraction, pp* (2014).

[172] L. Zhang, E. Brück, O. Tegus, K. Buschow, and F. De Boer, *The crystallization of amorphous Fe_2MnGe powder prepared by ball milling*, Journal of alloys and compounds **352**, 99 (2003).

[173] L. Zhang, E. Brück, O. Tegus, K. J. Buschow, and F. De Boer, *The crystallographic phases and magnetic properties of $Fe_2MnSi_{1-x}Ge_x$*, Physica B: Condensed Matter **328**, 295 (2003).

[174] S. Keshavarz, N. Naghibolashrafi, M. E. Jamer, K. Vinson, D. Mazumdar, C. L. Dennis, W. Ratcliff II, J. A. Borchers, A. Gupta, and P. LeClair, *Fe_2MnGe: A hexagonal Heusler analogue*, Journal of Alloys and Compounds **771**, 793 (2019).

[175] J. Rodríguez-Carvajal, *Recent advances in magnetic structure determination by neutron powder diffraction*, Physica B: Condensed Matter **192**, 55 (1993).

[176] http://www.mrl.ucsb.edu/sites/default/files/mrl$_d$ocs/instruments/VSMmanualB0.pdf, Accessed 10Oct202

[177] S. Okamura, R. Goto, S. Sugimoto, N. Tezuka, and K. Inomata, *Structural, magnetic, and transport properties of full-Heusler alloy $Co_2(Cr_{1-x}Fe_x)Al$ thin films*, Journal of applied physics **96**, 6561 (2004).

[178] S. Majumdar, M. K. Chattopadhyay, V. K. Sharma, K. J. S. Sokhey, S. B. Roy, and P. Chaddah, *Transport properties of the ferromagnetic Heusler alloy* Co_2TiSn, Phys. Rev. B **72**, 012417 (2005).

[179] L. J. van der Pauw, *A method of measuring specific resistivity and Hall effect of discs of arbitrary shape*, Philips Res. Rep **13**, 1 (1958).

[180] P. E. Blöchl, *Projector augmented-wave method*, Phys. Rev. B **50**, 17953 (1994).

[181] G. Kresse and J. Furthmüller, *Efficient iterative schemes for ab initio total-energy calculations using a plane-wave basis set*, Phys. Rev. B **54**, 11169 (1996).

[182] J. P. Perdew, K. Burke, and M. Ernzerhof, *Generalized Gradient Approximation Made Simple*, Phys. Rev. Lett. **77**, 3865 (1996).

[183] P. Mavropoulos, I. Galanakis, V. Popescu, and P. Dederichs, *The influence of spin-orbit coupling on the band gap of Heusler alloys*, Journal of Physics: Condensed Matter **16**, S5759 (2004).

[184] A. Van de Walle, P. Tiwary, M. De Jong, D. Olmsted, M. Asta, A. Dick, D. Shin, Y. Wang, L.-Q. Chen, and Z.-K. Liu, *Efficient stochastic generation of special quasirandom structures*, Calphad **42**, 13 (2013).

[185] A. Van De Walle, M. Asta, and G. Ceder, *The alloy theoretic automated toolkit: A user guide*, Calphad **26**, 539 (2002).

[186] *Alloy Theoretic Automated Toolkit (ATAT) Home Page. [Online]*, https://www.brown.edu/Departments/Engineering/Labs/avdw/atat/, Accessed 01 Jan 2021 .

[187] M. Guezlane, H. Baaziz, F. E. H. Hassan, Z. Charifi, and Y. Djaballah, *Electronic, magnetic and thermal properties of $Co_2Cr_xFe_{1-x}X$ (X= Al, Si) Heusler alloys: First-principles calculations*, Journal of Magnetism and Magnetic Materials **414**, 219 (2016).

[188] D. Rai, A. Shankar, Sandeep, M. Ghimire, and R. Thapa, *A comparative study of a Heusler alloy Co_2FeGe using LSDA and LSDA+U*, Physica B: Condensed Matter **407**, 3689 (2012).

[189] S. A. Tolba, K. M. Gameel, B. A. Ali, H. A. Almossalami, and N. K. Allam, *The DFT+U: Approaches, Accuracy, and Applications*, in *Density Functional Calculations*, edited by G. Yang (IntechOpen, Rijeka, 2018) Chap. 1.

[190] E. Şaşıoğlu, I. Galanakis, C. Friedrich, and S. Blügel, *Calculated electronic and magnetic properties of the half-metallic, transition metal based Heusler compounds*, Phys. Rev. B **88**, 134402 (2013).

[191] H. C. Kandpal, G. H. Fecher, and C. Felser, *Calculated electronic and magnetic properties of the half-metallic, transition metal based Heusler compounds*, Journal of Physics D: Applied Physics **40**, 1507 (2007).

[192] J. Heyd, G. E. Scuseria, and M. Ernzerhof, *Hybrid functionals based on a screened Coulomb potential*, The Journal of Chemical Physics **118**, 8207 (2003), https://doi.org/10.1063/1.1564060 .

[193] D. Rani, J. Kangsabanik, K. G. Suresh, N. Patra, D. Bhattacharyya, S. N. Jha, and A. Alam, *Origin of Local Atomic Order and Disorder in* $Co_2Fe_{1-x}Cr_xSi$ *Heusler Alloys: Theory and Experiment*, Phys. Rev. Applied **10**, 054022 (2018).

[194] F. Shi, M. Si, J. Xie, K. Mi, C. Xiao, and Q. Luo, *Hybrid density functional study of bandgaps for 27 new proposed half-Heusler semiconductors*, Journal of Applied Physics **122**, 215701 (2017).

[195] S. Grimme, *Semiempirical GGA-type density functional constructed with a long-range dispersion correction*, Journal of Computational Chemistry **27**, 1787 (2006), https://onlinelibrary.wiley.com/doi/pdf/10.1002/jcc.20495 .

[196] https://vaspkit.com/, Accessed 01 May 2020 .

[197] http://www.p4vasp.at//download, Accessed 01 May 2020 .

[198] https://www.originlab.com/, Accessed 01 April 2016 .

[199] B. Balke, S. Wurmehl, G. H. Fecher, C. Felser, M. d. C. M. Alves, F. Bernardi, and J. Morais, *Structural characterization of the Co_2FeZ (Z= Al, Si, Ga, and Ge) Heusler compounds by x-ray diffraction and extended x-ray absorption fine structure spectroscopy*, Applied physics letters. New York. Vol. 90, no. 17 (Apr. 2007), 172501, 3 p. (2007).

[200] H. J. Monkhorst and J. D. Pack, *Special points for Brillouin-zone integrations*, Phys. Rev. B **13**, 5188 (1976).

[201] https://periodictable.com/Properties/A/Electronegativity.an.html .

[202] W. Hume-Rothery, *Researches on the nature, properties, and conditions of formation of intermetallic compounds, with special reference to certain compounds of tin*, Ph.D. thesis, University of London (1926).

[203] A.-P. Tsai, *A test of Hume-Rothery rules for stable quasicrystals*, Journal of non-crystalline solids **334**, 317 (2004).

[204] M.-x. Ren, B.-s. Li, and H.-z. Fu, *Formation condition of solid solution type high-entropy alloy*, Transactions of Nonferrous Metals Society of China **23**, 991 (2013).

[205] A. R. Denton and N. W. Ashcroft, *Vegard's law*, Phys. Rev. A **43**, 3161 (1991).

[206] T. Block, M. J. Carey, B. A. Gurney, and O. Jepsen, *Band-structure calculations of the half-metallic ferromagnetism and structural stability of full- and half-Heusler phases*, Phys. Rev. B **70**, 205114 (2004).

[207] A. Arrott, *Criterion for Ferromagnetism from Observations of Magnetic Isotherms*, Phys. Rev. **108**, 1394 (1957).

[208] S. H. Aly and R. M. Shabara, *First principles calculation of elastic and magnetic properties of Cr-based full-Heusler alloys*, Journal of magnetism and magnetic materials **360**, 143 (2014).

[209] M. Hakimi, P. Kameli, H. Salamati, and Y. Mazaheri, *Evolution of microstructural and mechanical properties of nanocrystalline Co_2FeAl Heusler alloy prepared by mechanical alloying*, Powder Metallurgy **56**, 111 (2013).

[210] S. Ouardi, G. H. Fecher, B. Balke, A. Beleanu, X. Kozina, G. Stryganyuk, C. Felser, W. Klöß, H. Schrader, F. Bernardi, J. Morais, E. Ikenaga, Y. Yamashita, S. Ueda, and K. Kobayashi, *Electronic and crystallographic structure, hard X-ray photoemission, and mechanical and transport properties of the half-metallic Heusler compound Co_2MnGe*, Phys. Rev. B **84**, 155122 (2011).

[211] G. Rogl, A. Grytsiv, M. Gürth, A. Tavassoli, C. Ebner, A. Wünschek, S. Puchegger, V. Soprunyuk, W. Schranz, E. Bauer, *et al.*, *Mechanical properties of half-Heusler alloys*, Acta Materialia **107**, 178 (2016).

[212] D. Rai, A. Shankar, M. Ghimire, R. Thapa, *et al.*, *A comparative study of a Heusler alloy Co_2FeGe using LSDA and LSDA+ U*, Physica B: Condensed Matter **407**, 3689 (2012).

[213] K. Yao, G. Gao, Z. Liu, and L. Zhu, *Half-metallic ferromagnetism of zinc-blende CrS and CrP: a first-principles pseudopotential study*, Solid state communications **133**, 301 (2005).

[214] X. Wang, Z. Cheng, J. Wang, L. Wang, Z. Yu, C. Fang, J. Yang, and G. Liu, *Origin of the half-metallic band-gap in newly designed quaternary Heusler compounds ZrVTiZ (Z= Al, Ga)*, RSC advances **6**, 57041 (2016).

[215] S. Yamada, S. Kobayashi, K. Arima, and K. Hamaya, *Magnetic and Transport Properties of $Co_{(1+x)}FeV_{(1-x)}Si$ Epitaxial Films Grown by Molecular Beam Epitaxy*, IEEE Transactions on Magnetics **55**, 1 (2019).

[216] R. Mahat, K. Shambhu, D. Wines, F. Ersan, S. Regmi, U. Karki, R. White, C. Ataca, P. Padhan, A. Gupta, and P. LeClair, *Tuneable structure and magnetic properties in $Fe_{3-x}V_xGe$ alloys*, Journal of Alloys and Compounds , 154403 (2020).

[217] G. Kresse and D. Joubert, *From ultrasoft pseudopotentials to the projector augmented-wave method*, Phys. Rev. B **59**, 1758 (1999).

[218] J.-M. Hyun and M. Kim, *The half-metallicity of Co_2FeGe full Heusler alloy in (001) thin film: First principles study*, Journal of the Korean Physical Society **72**, 276 (2018).

[219] P. L. Rossiter, *The electrical resistivity of metals and alloys*, Vol. 6 (Cambridge University Press, 1991).

[220] P. B. Allen and B. Chakraborty, *Infrared and dc conductivity in metals with strong scattering: Nonclassical behavior from a generalized Boltzmann equation containing band-mixing effects*, Phys. Rev. B **23**, 4815 (1981).

[221] G. Prathiba, S. Venkatesh, M. Rajagopalan, and N. H. Kumar, *Half metallic Co_2TiGe-a theoretical and experimental investigation*, Journal of Magnetism and Magnetic Materials **323**, 22 (2011).

[222] Z. Gercsi and K. Hono, *Ab initio predictions for the effect of disorder and quarternary alloying on the half-metallic properties of selected Co_2Fe-based Heusler alloys*, Journal of Physics: Condensed Matter **19**, 326216 (2007).

[223] J. Caballero, A. Reilly, Y. Hao, J. Bass, W. Pratt Jr, F. Petroff, and J. Childress, *Effect of deposition parameters on the CPP-GMR of NiMnSb-based spin-valve structures*, Journal of magnetism and magnetic materials **198**, 55 (1999).

[224] K. Özdoğan, E. Şaşıoğlu, and I. Galanakis, *Engineering the electronic, magnetic and gap-related properties of the quinternary half-metallic Heusler alloys*, J. Appl. Phys. **103**, 023503 (2008).

[225] H. C. Kandpal, G. H. Fecher, C. Felser, and G. Schñhense, *Correlation in the transition-metal-based Heusler compounds Co_2MnSi and Co_2FeSi*, Phys. Rev. B **73**, 094422 (2006).

[226] V. I. Anisimov, F. Aryasetiawan, and A. Lichtenstein, *First-principles calculations of the electronic structure and spectra of strongly correlated systems: the LDA+ U method*, Journal of Physics: Condensed Matter **9**, 767 (1997).

[227] M. R. Paudel, C. S. Wolfe, H. Patton, I. Dubenko, N. Ali, J. A. Christodoulides, and S. Stadler, *Magnetic and transport properties of $Co_2MnSn_xSb_{1x}$ Heusler alloys*, Journal of Applied Physics **105**, 013716 (2009).

[228] M. Wójcik, E. Jedryka, H. Sukegawa, T. Nakatani, and K. Inomata, *^{59}Co NMR experiment as a probe of electron doping in $Co_2FeAl_{1-x}Si_x$ Heusler alloys*, Phys. Rev. B **85**, 100401 (2012).

[229] T. Kubota, S. Tsunegi, M. Oogane, S. Mizukami, T. Miyazaki, H. Naganuma, and Y. Ando, *Half-metallicity and Gilbert damping constant in $Co_2Fe_xMn_{1-x}Si$ Heusler alloys depending on the film composition*, Applied Physics Letters **94**, 122504 (2009).

[230] R. Shan, H. Sukegawa, W. H. Wang, M. Kodzuka, T. Furubayashi, T. Ohkubo, S. Mitani, K. Inomata, and K. Hono, *Demonstration of Half-Metallicity in Fermi-Level-Tuned Heusler Alloy* $Co_2FeAl_{0.5}Si_{0.5}$ *at Room Temperature*, Phys. Rev. Lett. **102**, 246601 (2009).

[231] P. Webster and K. Ziebeck, *Magnetic and chemical order in Heusler alloys containing cobalt and titanium*, Journal of Physics and Chemistry of Solids **34**, 1647 (1973).

[232] M. Methfessel and A. T. Paxton, *High-precision sampling for Brillouin-zone integration in metals*, Phys. Rev. B **40**, 3616 (1989).

[233] F. Casper, C. Felser, R. Seshadri, C. P. Sebastian, and R. Pöttgen, *Searching for hexagonal analogues of the half-metallic half-Heusler XYZ compounds*, Journal of Physics D: Applied Physics **41**, 035002 (2008).

[234] Q. Zhang, H. Cui, C. Tian, H. Chen, J. Wang, and H. Yuan, *Thickness and composition dependencies of magnetization and perpendicular magnetic anisotropy of Heusler-like alloys based Mn_xGa| Co_2FeAl superlattices*, Journal of Alloys and Compounds **773**, 327 (2019).

[235] F. Xin, C. You, H. Fu, L. Ma, Z. Cheng, and N. Tian, *Mechanically tuning magnetism and transport property in spin gapless semiconductor CoFeMnSi flexible thin film*, Journal of Alloys and Compounds **813**, 152207 (2020).

[236] X. Wang, Z. Cheng, Y. Jin, Y. Wu, X. Dai, and G. Liu, *Magneto-electronic properties and tetragonal deformation of rare-earth-element-based quaternary Heusler half-metals: A first-principles prediction*, Journal of Alloys and Compounds **734**, 329 (2018).

[237] A. F. Cabrera and F. H. Sánchez, *Mössbauer study of ball-milled Fe-Ge alloys*, Phys. Rev. B **65**, 094202 (2002).

[238] Q. Chen, A. Ngan, and B. Duggan, *An in-situ TEM study of the $L1_2$ to DO_{19} phase transformation in the intermetallic compound Fe_3Ge*, Intermetallics **6**, 105 (1998).

[239] Q. Chen, A. Ngan, and B. Duggan, *The $L1_2 \rightarrow DO_{19}$ transformation in the intermetallic compound Fe_3Ge*, Journal of materials science **33**, 5405 (1998).

[240] H. Nakagawa and K. Kanematsu, *Magnetic and X-Ray Studies on $(Fe_{1-x}V_x)_3Ge$*, Japanese Journal of Applied Physics **18**, 1959 (1979).

[241] A. Beitollahi and J. Booth, *Structural and magnetic properties of $Fe_{3-x}V_xGe$ alloys*, Journal of Physics: Condensed Matter **2**, 2997 (1990).

[242] K. v. Buschow, P. Van Engen, and R. Jongebreur, *Magneto-optical properties of metallic ferromagnetic materials*, Journal of magnetism and magnetic materials **38**, 1 (1983).

[243] P. Walker and W. H. Tarn, *CRC handbook of metal etchants* (CRC press, 1990).

[244] M. Mohammadtaheri, *A new metallographic technique for revealing grain boundaries in aluminum alloys*, Metallography, Microstructure, and Analysis **1**, 224 (2012).

[245] Y. El Hachi, B. Malard, S. Berveiller, and J. Wright, *Measurement of lattice rotations and internal stresses in over one hundred individual grains during a stress-induced martensitic transformation*, in *MATEC Web of Conferences*, Vol. 33 (EDP Sciences, 2015) p. 02003.

[246] H. P. Wijn, *Magnetic Properties of Metals: d-elements, alloys and Compounds* (Springer Science & Business Media, 2012).

[247] J. R. Rumble, *CRC Handbook of Chemistry and Physics 100th Edition (Internet Version 2019) CRC Press*.

[248] Z. Nishiyama, *Martensitic transformation* (Elsevier, 2012).

[249] R. M. Wentzcovitch and P. K. Lam, *fcc-to-hcp transformation: A first-principles investigation*, Phys. Rev. B **44**, 9155 (1991).

[250] P. B. Allen and B. Chakraborty, *Infrared and dc conductivity in metals with strong scattering: Nonclassical behavior from a generalized Boltzmann equation containing band-mixing effects*, Phys. Rev. B **23**, 4815 (1981).

[251] Y. Nishino, M. Kato, S. Asano, K. Soda, M. Hayasaki, and U. Mizutani, *Semiconductorlike behavior of electrical resistivity in Heusler-type Fe_2VAl compound*, Phys. Rev. Lett. **79**, 1909 (1997).

[252] C.-S. Lue and Y.-K. Kuo, *Thermal and transport properties of the Heusler-type compounds $Fe_{2-x}Ti_{1+x}Sn$*, Journal of applied physics **96**, 2681 (2004).

[253] N. Kawamiya, Y. Nishino, M. Matsuo, and S. Asano, *Electrical-resistance maximum near the Curie point in $(Fe_{1-x}V_x)_3Ga$ and $(Fe_{1-x}Ti_x)_3Ga$*, Phys. Rev. B **44**, 12406 (1991).

[254] C. S. Lue and Y.-K. Kuo, *Thermoelectric properties of the semimetallic Heusler compounds $Fe_{2-x}V_{1+x}M$ (M = Al, Ga)*, Phys. Rev. B **66**, 085121 (2002).

[255] N. Kourov, A. Korolev, V. Marchenkov, A. Lukoyanov, and K. Belozerova, *Magnetic and electrical properties of the half-metallic ferromagnets Co_2CrAl*, Physics of the Solid State **55**, 977 (2013).

[256] S. Majumdar, M. K. Chattopadhyay, V. K. Sharma, K. J. S. Sokhey, S. B. Roy, and P. Chaddah, *Transport properties of the ferromagnetic Heusler alloy* Co_2TiSn, Phys. Rev. B **72**, 012417 (2005).

[257] J. Barth, G. H. Fecher, B. Balke, S. Ouardi, T. Graf, C. Felser, A. Shkabko, A. Weidenkaff, P. Klaer, H. J. Elmers, H. Yoshikawa, S. Ueda, and K. Kobayashi, *Itinerant half-metallic ferromagnets* Co_2TiZ $(Z = Si,\ Ge,\ Sn)$*: Ab initio calculations and measurement of the electronic structure and transport properties*, Phys. Rev. B **81**, 064404 (2010).

[258] N. Kourov, V. Marchenkov, V. Pushin, and K. Belozerova, *Electrical properties of ferromagnetic* Ni_2MnGa *and* Co_2CrGa *Heusler alloys*, Journal of Experimental and Theoretical Physics **117**, 121 (2013).

[259] N. Kourov, A. Lukoyanov, and V. Marchenkov, *Specific features of the electrical resistance of half-metallic ferromagnetic alloys* Co_2CrAl *and* Co_2CrGa, Physics of the Solid State **55**, 2487 (2013).

[260] N. Kourov, V. Marchenkov, K. Belozerova, and H. Weber, *Specific features of the electrical resistivity of half-metallic ferromagnets* Fe_2MeAl *(Me= Ti, V, Cr, Mn, Fe, Ni)*, Journal of Experimental and Theoretical Physics **118**, 426 (2014).

[261] H. Kurt, K. Rode, P. Stamenov, M. Venkatesan, Y.-C. Lau, E. Fonda, and J. M. D. Coey, *Cubic* Mn_2Ga *Thin Films: Crossing the Spin Gap with Ruthenium*, Phys. Rev. Lett. **112**, 027201 (2014).

[262] L. Jodin, J. Tobola, P. Pecheur, H. Scherrer, and S. Kaprzyk, *Effect of substitutions and defects in half-Heusler* FeVSb *studied by electron transport measurements and KKR-CPA electronic structure calculations*, Phys. Rev. B **70**, 184207 (2004).

[263] M. I. Khan, H. Arshad, M. Rizwan, S. Gillani, M. Zafar, S. Ahmed, and M. Shakil, *Investigation of structural, electronic, magnetic and mechanical properties of a new series of equiatomic quaternary Heusler alloys CoYCrZ (Z= Si, Ge, Ga, Al): A DFT study*, Journal of Alloys and Compounds , 152964 (2019).

[264] S. Yousuf and D. C. Gupta, *Insight into half-metallicity, spin-polarization and mechanical properties of* $L2_1$ *structured* MnY_2Z *(Z= Al, Si, Ga, Ge, Sn, Sb) Heusler alloys*, Journal of Alloys and Compounds **735**, 1245 (2018).

[265] M. Elahmar, H. Rached, D. Rached, R. Khenata, G. Murtaza, S. B. Omran, and W. Ahmed, *Structural, mechanical, electronic and magnetic properties of a new series of quaternary Heusler alloys CoFeMnZ (Z= Si, As, Sb): a first-principle study*, Journal of Magnetism and Magnetic Materials **393**, 165 (2015).

[266] K. Benkaddour, A. Chahed, A. Amar, H. Rozale, A. Lakdja, O. Benhelal, and A. Sayede, *First-principles study of structural, elastic, thermodynamic, electronic and magnetic properties for the quaternary Heusler alloys CoRuFeZ (Z= Si, Ge, Sn)*, Journal of Alloys and Compounds **687**, 211 (2016).

[267] L. Zhang, X. Wang, and Z. Cheng, *Electronic, magnetic, mechanical, half-metallic and highly dispersive zero-gap half-metallic properties of rare-earth-element-based quaternary Heusler compounds*, Journal of Alloys and Compounds **718**, 63 (2017).

[268] K.-D. Kim and C.-H. Lee, *Fabrication and densification of Heusler Fe_2VAl alloy powders by mechanical alloying*, Journal of the Korean Crystal Growth and Crystal Technology **23**, 51 (2013).

[269] Z. Xie, S. Ni, and M. Song, *Effect of Y_2O_3 doping on FCC to HCP phase transformation in cobalt produced by ball milling and spark plasma sintering*, Powder Technology **324**, 1 (2018).

[270] A. Zunger, S.-H. Wei, L. G. Ferreira, and J. E. Bernard, *Special quasirandom structures*, Phys. Rev. Lett. **65**, 353 (1990).

[271] A. van de Walle, *Multicomponent multisublattice alloys, nonconfigurational entropy and other additions to the Alloy Theoretic Automated Toolkit*, Calphad **33**, 266 (2009).

[272] R. F. W. Bader, *Atoms in Molecules*, in *Encyclopedia of Computational Chemistry* (American Cancer Society, 2002).

[273] G. Henkelman, A. Arnaldsson, and H. Jónsson, *A fast and robust algorithm for Bader decomposition of charge density*, Computational Materials Science **36**, 354 (2006).

[274] K. Momma and F. Izumi, *Vesta 3 for three-dimensional visualization of crystal volumetric and morphology data*, Journal of Applied Crystallography **44**, 1272 (2011).

[275] Y. Zhang, Z. Liu, Z. Wu, and X. Ma, *Prediction of fully compensated ferrimagnetic spin-gapless semiconducting FeMnGa/Al/In half Heusler alloys*, IUCrJ **6**, 10.1107/S2052252519005062 (2019).

[276] T. Samanta, S. Chaudhuri, S. Singh, V. Srihari, A. Nigam, and P. Bhobe, *Structural, electronic, magnetic, and transport properties of the equiatomic Ni-based quaternary Heusler alloys*, Journal of Alloys and Compounds , 153029 (2019).

[277] A. Candan, G. Uğur, Z. Charifi, H. Baaziz, and M. Ellialtıoğlu, *Electronic structure and vibrational properties in cobalt-based full-Heusler compounds: A first principle study of Co_2MnX (X= Si, Ge, Al, Ga)*, Journal of Alloys and Compounds **560**, 215 (2013).

[278] S. Ouardi, G. H. Fecher, C. Felser, and J. Kübler, *Realization of Spin Gapless Semiconductors: The Heusler Compound* Mn_2CoAl, Phys. Rev. Lett. **110**, 100401 (2013).

[279] M. Franz, *Topological insulators: Starting a new family*, Nature materials **9**, 536 (2010).

[280] C. Felser, L. Wollmann, S. Chadov, G. H. Fecher, and S. S. Parkin, *Basics and prospective of magnetic Heusler compounds*, APL materials **3**, 041518 (2015).

[281] D. Rani, L. Bainsla, K. Suresh, and A. Alam, *Experimental and theoretical investigation on the possible half-metallic behaviour of equiatomic quaternary Heusler alloys: CoRuMnGe and CoRuVZ (Z = Al, Ga)*, Journal of Magnetism and Magnetic Materials **492**, 165662 (2019).

[282] D. S. Kuchin, E. T. Dilmieva, Y. S. Koshkid'ko, A. P. Kamantsev, V. V. Koledov, A. V. Mashirov, V. G. Shavrov, J. Cwik, K. Rogacki, and V. V. Khovaylo, *Direct measurement of shape memory effect for $Ni_{54}Mn_{21}Ga_{25}$, $Ni_{50}Mn_{41.2}In_{8.8}$ Heusler alloys in high magnetic field*, Journal of Magnetism and Magnetic Materials **482**, 317 (2019).

[283] A. Ghosh, R. Rawat, A. Bhattacharyya, G. Mandal, A. Nigam, and S. Nair, *Measurement independent magnetocaloric effect in Mn-rich Mn-Fe-Ni-Sn (Sb/In) Heusler alloys*, Journal of Magnetism and Magnetic Materials **476**, 92 (2019).

[284] Y. Li, H. Wang, Y. Yao, J. Xu, Z. Han, Y. Fang, L. Zhang, C. Zhang, B. Qian, and X. Jiang, *Magnetic phase diagram, magnetocaloric effect, and exchange bias in $Ni_{43}Mn_{46}Sn_{11-x}Ga_x$ Heusler alloys*, Journal of Magnetism and Magnetic Materials **478**, 161 (2019).

[285] X.-P. Wei, Q. Gao, P. Gao, Y.-L. Zhang, and X. Tao, *Investigations on Gilbert damping, electronic, magnetic and Curie temperature for equiatomic quaternary Heusler alloys CrScCoZ*, Journal of Magnetism and Magnetic Materials **512**, 166986 (2020).

[286] H. Nakagawa and K. Kanematsu, *Magnetic Properties and Phase Transition of Fe_3Ge*, Journal of the Physical Society of Japan **18**, 920 (1963).

[287] M. A. McGuire, K. Shanavas, M. S. Kesler, and D. S. Parker, *Tuning magnetocrystalline anisotropy by cobalt alloying in hexagonal Fe_3Ge*, Scientific reports **8**, 14206 (2018).

[288] S. Ishida, S. Mizutani, S. Fujii, and S. Asano, *Effect of chemical disorder on half-metallicity of Fe_2CrZ (Z= IIIb, IV, Vb element)*, .

[289] D. Creagh, *X-ray dispersion corrections*, (2006).

[290] J. C. Slater, *Electronic structure of alloys*, Journal of Applied Physics **8**, 385 (1937).

[291] M. Raphael, B. Ravel, M. Willard, S. Cheng, B. Das, R. Stroud, K. Bussmann, J. Claassen, and V. Harris, *Magnetic, structural, and transport properties of thin film and single crystal Co_2MnSi*, Applied Physics Letters **79**, 4396 (2001).

[292] L. Zhang, G. Rogl, A. Grytsiv, S. Puchegger, J. Koppensteiner, F. Spieckermann, H. Kabelka, M. Reinecker, P. Rogl, W. Schranz, *et al.*, *Mechanical properties of filled antimonide skutterudites*, Materials Science and Engineering: B **170**, 26 (2010).

[293] G. Henkelman, A. Arnaldsson, and H. Jónsson, English (US)*A fast and robust algorithm for Bader decomposition of charge density*, Computational Materials Science **36**, 354 (2006).

[294] X.-Q. Chen, H. Niu, D. Li, and Y. Li, *Modeling hardness of polycrystalline materials and bulk metallic glasses*, Intermetallics **19**, 1275 (2011).

[295] Y. Tian, B. Xu, and Z. Zhao, *Microscopic theory of hardness and design of novel superhard crystals*, International Journal of Refractory Metals and Hard Materials **33**, 93 (2012).

[296] S. Regmi, Z. Li, A. Srivastava, R. Mahat, S. Kc, A. Rastogi, Z. Galazka, R. Datta, T. Mewes, and A. Gupta, *Structural and magnetic properties of $NiFe_2O_4$ thin films grown on isostructural lattice-matched substrates*, Applied Physics Letters **118**, 152402 (2021).

[297] F. Y. Acquaye, R. Mahat, and S. Street, *Synthesis of FePt Nanoparticles by Photoreduction and Chemical Reduction in Poly (ethyleneimine)*, Langmuir **37**, 11750 (2021).

[298] Y. V. Kudryavtsev, V. N. Uvarov, V. A. Oksenenko, Y. P. Lee, J. B. Kim, Y. H. Hyun, K. W. Kim, J. Y. Rhee, and J. Dubowik, *Effect of disorder on various physical properties of Co_2CrAl Heusler alloy films: Experiment and theory*, Phys. Rev. B **77**, 195104 (2008).

[299] M. Jourdan, E. A. Jorge, C. Herbort, M. Kallmayer, P. Klaer, and H.-J. Elmers, *Interface and bulk magnetism of $Co_2Cr_{0.6}Fe_{0.4}Al$ and Co_2CrAl thin films*, Applied Physics Letters **95**, 172504 (2009).

[300] J. Herran, R. Dalal, P. Gray, P. Kharel, and P. V. Lukashev, *Atomic disorder induced modification of magnetization in MnCrVAl*, Journal of Applied Physics **122**, 153904 (2017).

[301] P. Chen, G. Wu, and X. Zhang, *Magnetic, transport and thermal properties of single crystal Co_2FeGa*, Journal of alloys and compounds **454**, 52 (2008).

[302] A. Deb, M. Itou, Y. Sakurai, N. Hiraoka, and N. Sakai, *Magnetic Compton scattering study of the* Co_2FeGa *Heusler alloy: Experiment and theory*, Phys. Rev. B **63**, 064409 (2001).

[303] D. Rani, Enamullah, L. Bainsla, K. G. Suresh, and A. Alam, *Spin-gapless semiconducting nature of Co-rich* $Co_{1+x}Fe_{1-x}CrGa$, Phys. Rev. B **99**, 104429 (2019).

[304] M. E. Jamer, B. A. Assaf, T. Devakul, and D. Heiman, *Magnetic and transport properties of Mn_2CoAl oriented films*, Applied Physics Letters **103**, 142403 (2013).

[305] K. Özdoğan, I. V. Maznichenko, S. Ostanin, E. Şaşıoğlu, A. Ernst, I. Mertig, and I. Galanakis, *High spin polarization in all-3d-metallic Heusler compounds: the case of Fe_2CrZ and $CoCrZ$ (Z = Sc, Ti, V)*, Journal of Physics D: Applied Physics **52**, 205003 (2019).

[306] I. Galanakis, *Towards half-metallic interfaces: Co_2CrAl/InP contacts*, Journal of Physics: Condensed Matter **16**, 8007 (2004).

[307] R. Gaillac, P. Pullumbi, and F.-X. Coudert, *ELATE: an open-source online application for analysis and visualization of elastic tensors*, Journal of Physics: Condensed Matter **28**, 275201 (2016).

[308] W. Voigt, *Lehrbuch der Kristallphysik* (1966).

[309] A. L. Greaves, G. N. snd Greer, R. S. Lakes, and T. Rouxel, *Poisson's ratio and modern materials*, Nature Materials **10**, 986 (2011).

APPENDIX A

SUPPLEMENTARY MATERIALS

A.1 Supplementary Information: Possible half-metallic behavior of $Co_{2-x}Cr_xFeGe$ Heusler alloys: Theory and Experiment

A.1.1 Experimental details

A.1.1.1 Synthesis and Thermal treatments

$Co_{2-x}Cr_xFeGe$ bulk samples were prepared, each with a mass of ~ 5 g, by repeated arc melting of stoichiometric amounts of pure Co (99.98%, Alfa Aesar), Fe (99.98%, Alfa Aesar), Cr (99.7%, Alfa Aesar), and Ge (99.999%, Alfa Aesar) under an ultrahigh purity Argon (99.999%) at pressure of 10^{-4} mbar using an Edmund Buehler compact arc melter MAM-1. The mixture of constituent elements Co, Cr, Fe and Ge in a ratios $2-x:x:1:1$ was melted at least 6 times, turning the specimen over before each melting cycle, to ensure sufficient homogeneity. The as-cast cut pieces were examined repeatedly using scanning electron microscopy (SEM) and energy dispersive X-ray spectroscopy (EDS) analysis in a JEOL 7000 Field Emission Scanning Electron Microscope (FESEM) to confirm homogeneity and correct composition. After confirming the anticipated target composition, the resulting polycrystalline ingots were annealed in evacuated quartz tubes at different temperatures; 900°C and 1000°C for different dwell times 3, 7, or 15 days, and at the end of each annealing cycle, the samples were cooled slowly in the furnace to get optimum crystallization and granular structures. To make the comparison uniform across all compositions, only the samples annealed under similar heat treatment *e.g.*, 1000°C for 15 days are chosen for this work.

A.1.1.2 Metallography

A hot mounting technique was used to mount the annealed samples in conductive graphite powder prior to metallography to observe the surface morphology on a microscopic level. The graphite powder avoids charge accumulation by providing conductive path during SEM/EDS analysis. The metallography begins with grinding using silicon carbide abrasive discs (120 through 1200 grit size) followed by diamond suspension polishing. Colloidal silica suspension of grit size $0.02\,\mu m$ was used at last for the finest polishing. After obtaining a smooth and reflective surface, the samples were etched with Adler etchant (9 g of $CuNH_3Cl$, 45 g of hydrated $FeCl_2$, 150 mL of HCl and 75 mL of DI Water). The purpose of etching is that etchant attacks different phases present in the samples at different rates, and provides high quality surface contrast for microstructure characterization.

A.1.2 Experimental Results

A.1.2.1 Microstructural and Compositional analysis

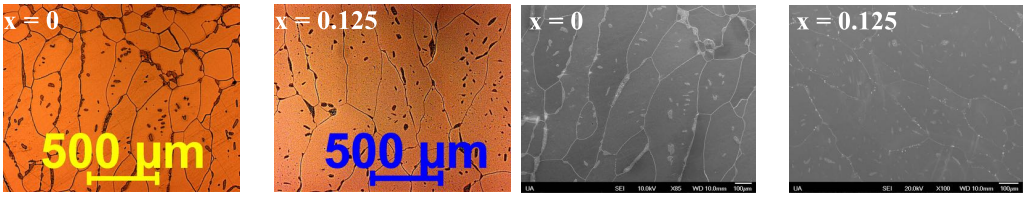

Figure A.1: Optical and electron micrographs of $Co_{2-x}Cr_xFeGe$ series for multiphase samples $x = 0$ and $x = 0.125$ respectively, heat treated at 1000°C for 15 days followed by normal cooling in the furnace.

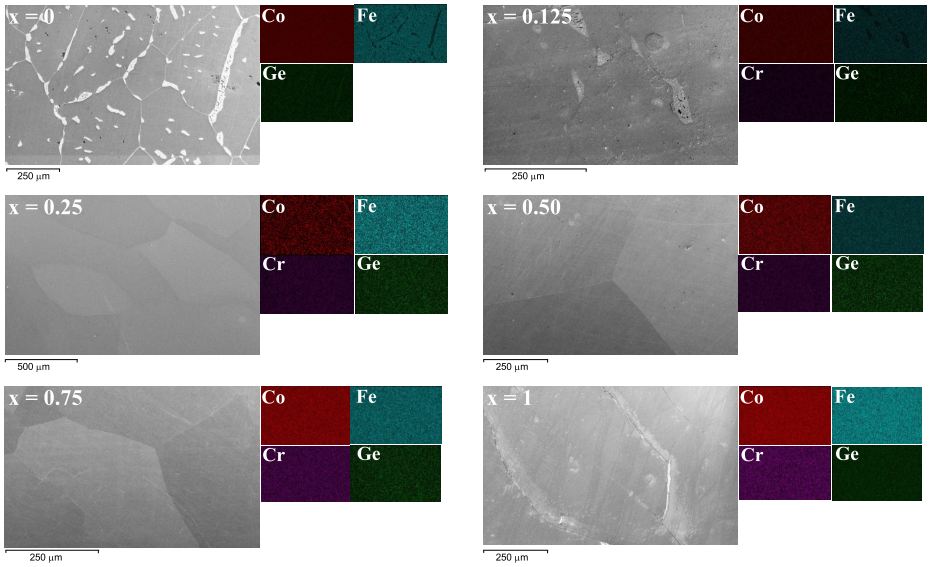

Figure A.2: SEM images and elemental mapping images of constituent elements in $Co_{2-x}Cr_xFeGe$ series

Starting of the full stoichiometric Co_2FeGe, substitution was made with x in steps of 0.25. Out of all, stable single phase is observed for Cr in the range ($0.25 \leq x \leq 1$). The sample $x = 0.125$ was also prepared to check the stability at even lower Cr concentration but multiphase behavior was observed. Microstructure of all single phase specimens are already presented in main manuscript, Fig. A.1 above shows the optical and SEM micrographs for multi-phase specimens.

To examine the approximate composition of grain boundaries and separated phases, composition analyses were performed. Fig. A.2 displays SEM images, and elemental mapping images of constituent elements in homogenized $Co_{2-x}Cr_xFeGe$ alloys. It is obvious from Fig. A.2 that the separated phase with Fe deficiency is mainly located in grain boundaries in parent Co_2FeGe. After Cr substitution $x = 0.125$ in place of Co, the major granular phase was identified to be close to target and nominal secondary phase was observed to segregate in grain boundaries. On further

Table A.1: Average composition of $Co_{2-x}Cr_xFeGe$ ($0 \leq x \leq 1$) alloy series as determined from EDS analysis (annealed at 1000°C for 15 days followed by normal cooling in the furnace).

	Main phase	Secondary phase	Composition in grain boundary	Target
x = 0†	$Co_{1.961}Fe_{1.063}Ge_{0.976}$	$Co_{2.170}Fe_{0.503}Ge_{1.327}$	$Co_{2.170}Fe_{0.503}Ge_{1.327}$	Co_2FeGe
x = 0.125†	$Co_{1.831}Cr_{0.139}Fe_{1.009}Ge_{1.021}$	$Co_{2.055}Cr_{0.061}Fe_{0.527}Ge_{1.357}$	$Co_{2.055}Cr_{0.061}Fe_{0.527}Ge_{1.357}$	$Co_{1.875}Cr_{0.125}FeGe$
x = 0.25	$Co_{1.747}Cr_{0.257}Fe_{1.002}Ge_{0.999}$	-	$Co_{1.757}Cr_{0.261}Fe_{0.928}Ge_{1.054}$	$Co_{1.75}Cr_{0.25}FeGe$
x = 0.50	$Co_{1.496}Cr_{0.507}Fe_{1.003}Ge_{0.994}$	-	$Co_{1.518}Cr_{0.493}Fe_{0.975}Ge_{1.014}$	$Co_{1.500}Cr_{0.500}FeGe$
x = 0.75	$Co_{1.249}Cr_{0.753}Fe_{0.995}Ge_{1.003}$	-	$Co_{1.263}Cr_{0.742}Fe_{0.987}Ge_{1.108}$	$Co_{1.250}Cr_{0.750}FeGe$
x = 1	$Co_{1.007}Cr0.994Fe_{1.002}Ge_{0.997}$	-	$Co_{0.998}Cr_{1.002}Fe_{0.992}Ge_{1.008}$	CoCrFeGe

† Multiphase specimen

substitution for Co by Cr in the range ($0.25 \leq x \leq 1$), stable phases were obtained. Relatively very large grains are observed. The composition of all the specimens in the series was analysed using EDS and the average composition of all specimens studied are presented in Table A.1.

A.1.2.2 Crystal structure

The Crystal structures in unit cells of a Heusler alloy $Co_{2-x}Cr_xFeGe$ as described in main manuscript are provided in Fig. A.3. Fig. A.4(a) shows the variation of lattice parameter, both experimental and theoretical, with Cr concentration. The calculated lattice parameters are in good agreement with values extracted from experiment (within $\sim 0.1\%$). Due to the fact that these experiments were done at a finite temperature, the experimental lattice parameters are slightly higher than those calculated from DFT (at 0 K) due to the thermal expansion coefficient of the material. One might also need a longer annealing time to reach the true ground state.

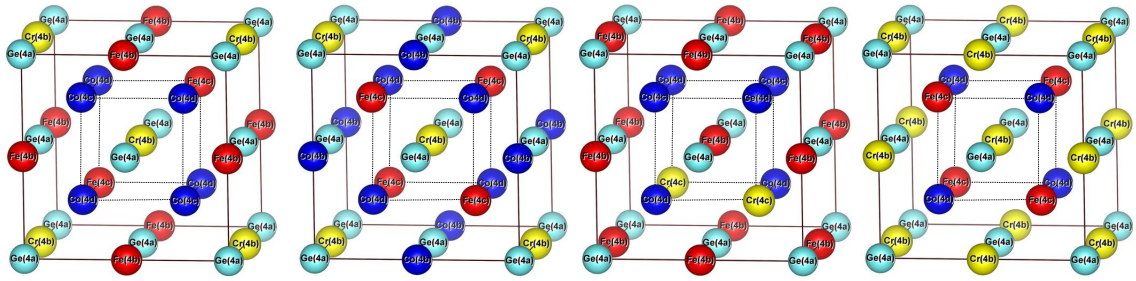

(a) (b) (c) (d)

Figure A.3: Crystal structure in unit cells of a Heusler alloy $Co_{2-x}Cr_xFeGe$ (a) $x = 0.50$ (II configuration), (b) $x = 0.50$ (III configuration), (c) $x = 0.50$ (IV configuration), and (d) CFCG (Y). The structures are shown in their ideal, unrelaxed forms.

A.1.2.3 Magnetic Characterization

Fig. A.4(b) shows the isothermal magnetization curves for all single-phase alloys measured at room temperature (300 K). All the single phase alloys are observed to be ferromagnets at room temperature as well with slightly small saturation magnetization values than those observed at 1.8 K.

Table A.2: The calculated total (and normalized per formula unit indicated in the parenthesis) and atomic spin-magnetic moments of the 16 atoms supercell of theoretically predicted most stable configurations in $Co_{2-x}Cr_xFeGe$ alloy series.

sites	Atoms ($x=0$)	M (μ_B)	Atoms ($x=0.25$)	M (μ_B)	Atoms ($x=0.50$)	M (μ_B)	Atoms ($x=0.75$)	M (μ_B)	Atoms ($x=1$)	M (μ_B)
4d	Co	1.421	Co	1.154	Fe	1.308	Fe	0.604	Co	0.998
	Co	1.421	Co	1.193	Co	0.975	Co	0.937	Co	0.998
	Co	1.421	Co	1.193	Co	1.027	Co	0.965	Co	0.998
	Co	1.421	Co	1.193	Co	1.027	Co	0.965	Co	0.998
4c	Co	1.421	Fe	1.732	Fe	1.308	Fe	0.532	Fe	0.225
	Co	1.421	Co	1.222	Co	0.975	Fe	0.858	Fe	0.225
	Co	1.421	Co	1.222	Co	1.027	Co	0.920	Fe	0.225
	Co	1.421	Co	1.222	Co	1.027	Co	0.920	Fe	0.225
4b	Fe	2.893	Fe	2.860	Fe	2.795	Fe	2.807	Cr	1.821
	Fe	2.893	Fe	2.860	Fe	2.795	Cr	1.873	Cr	1.821
	Fe	2.893	Fe	2.861	Cr	1.964	Cr	1.904	Cr	1.821
	Fe	2.893	Cr	2.396	Cr	1.964	Cr	1.904	Cr	1.821
4a	Ge	-0.001	Ge	0.004	Ge	-0.034	Ge	-0.065	Ge	-0.046
	Ge	-0.001	Ge	-0.047	Ge	-0.034	Ge	-0.043	Ge	-0.046
	Ge	-0.001	Ge	-0.047	Ge	-0.063	Ge	-0.043	Ge	-0.046
	Ge	-0.001	Ge	-0.047	Ge	-0.063	Ge	-0.043	Ge	-0.046
Total		22.936 (5.734)		20.972 (5.243)		17.997 (4.499)		14.998 (3.750)		11.992 (2.998)

The extracted saturation magnetic moments at room temperature are 5.54 μ_B/f.u., 5.18 μ_B/f.u., 4.45 μ_B/f.u., 3.69 μ_B/f.u., and 2.89 μ_B/f.u., respectively for $x = 0$, 0.25, 0.50, 0.75, and 1.

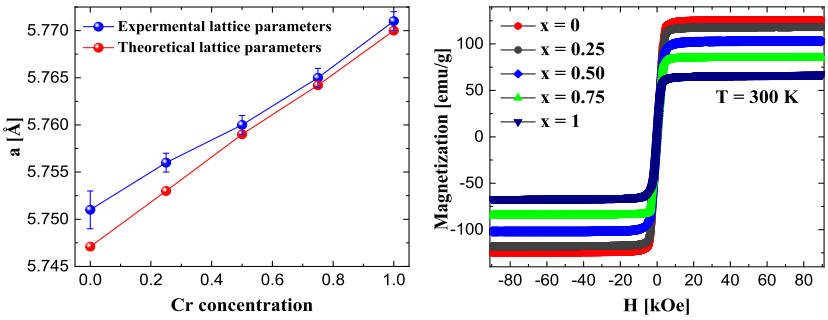

(a) (b)

Figure A.4: (a) The variation of lattice parameter, both experimental and theoretical, with Cr concentration; (b) The isothermal M-H curves measured at room temperature. The behavior is similar to that observed in low temperature case.

A.1.3 Theoretical Results

The atomic spin magnetic moments of theoretically predicted most stable configurations (see main manuscript) in $Co_{2-x}Cr_xFeGe$ alloy series are given in Table A.2;

A.2 Supplementary Information: Experimental and theoretical study on the possible half-metallic behavior of $Co_{2-x}V_xFeGe$ Heusler alloys

A.2.1 Experimental Results

A.2.1.1 Microstructural and Compositional analysis

Starting of the full stoichiometric Co_2FeGe, substitution was made with x in steps of 0.125. Out of all, stable single phase is observed for V in the range ($0.25 \leq x \leq 0.625$). Microstructure of all single phase specimens are already presented in main manuscript, Fig. A.5 and Fig. A.6 here show the micrographs for multi-phase specimens.

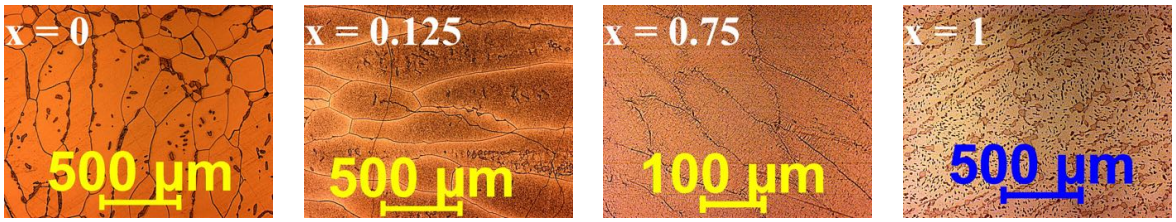

Figure A.5: Optical micrograph of $Co_{2-x}V_xFeGe$ ($0 \leq x \leq 1$) heat treated at 950°C for 7 days followed by normal cooling in the furnace. The samples were etched for 5 seconds using the Adler etchant.

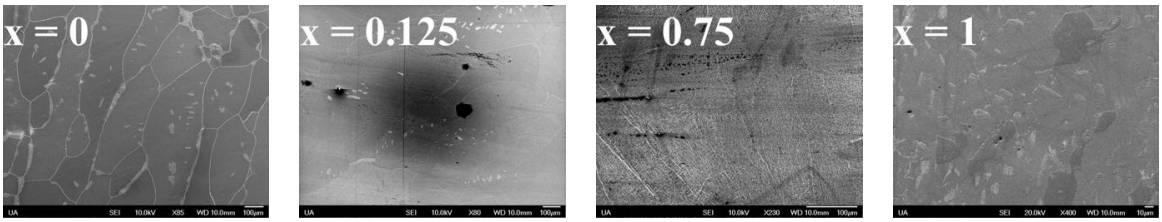

Figure A.6: SEM micrograph of $Co_{2-x}V_xFeGe$ ($0 \leq x \leq 1$) heat treated at 950°C for 7 days followed by ice/water mixture quenching. The samples were etched for 5 seconds using the Adler etchant.

As depicted in micrographs, the secondary phase is mainly located in grain boundaries in parent Co_2FeGe, and same trend is observed with the vanadium substitution $x = 0.125$ in place of Co, though the major granular phase was identified to be close to target and nominal secondary phase was observed to segregate in grain boundaries. On further substitution for Co by V in the range ($0.25 \leq x \leq 0.625$), most stable phases were obtained. Upon reaching $x = 0.75$, still the specimen was observed to be granular but more dendritic features with composition deviated from target composition result impurity peaks in XRD as a signature of secondary phase. Therefore, $x = 0.625$ is taken as an upper limit of V concentration for this alloy system to get a single phase specimen. The evolution of the grain size can be observed in the micrographs. Relatively very large grains are observed. The composition of all the specimens in the series was analyzed using EDS and the average composition of all specimens studied are presented in Table A.3.

The Crystal structures in unit cells of a Heusler alloy $Co_{2-x}V_xFeGe$ as described in main manuscript are provided in Fig. A.7.

Table A.3: Average composition of $Co_{2-x}V_xFeGe$ ($0 \leq x \leq 1$) alloy series as determined from EDS analysis (annealed at 950°C for 7 days followed by normal cooling in the furnace).

	Main phase	Secondary phase	Composition in grain boundary	Target
x = 0†	$Co_{1.961}Fe_{1.063}Ge_{0.976}$	$Co_{2.170}Fe_{0.503}Ge_{1.327}$	$Co_{2.170}Fe_{0.503}Ge_{1.327}$	Co_2FeGe
x = 0.125†	$Co_{1.835}V_{0.143}Fe_{1.015}Ge_{1.007}$	$Co_{2.070}V_{0.053}Fe_{0.615}Ge_{1.262}$	$Co_{2.070}V_{0.053}Fe_{0.615}Ge_{1.262}$	$Co_{1.875}V_{0.125}FeGe$
x = 0.250	$Co_{1.754}V_{0.256}Fe_{0.996}Ge_{0.994}$	-	$Co_{1.767}V_{0.291}Fe_{0.793}Ge_{1.149}$	$Co_{1.75}V_{0.25}FeGe$
x = 0.375	$Co_{1.623}V_{0.379}Fe_{0.991}Ge_{1.007}$	-	$Co_{1.632}V_{0.381}Fe_{0.944}Ge_{1.043}$	$Co_{1.625}V_{0.375}FeGe$
x = 0.500	$Co_{1.497}V_{0.508}Fe_{1.001}Ge_{0.994}$	-	$Co_{1.514}V_{0.515}Fe_{0.953}Ge_{1.018}$	$Co_{1.500}V_{0.500}FeGe$
x = 0.625	$Co_{1.373}V_{0.627}Fe_{0.992}Ge_{1.008}$	-	$Co_{1.384}V_{0.633}Fe_{0.951}Ge_{1.032}$	$Co_{1.375}V_{0.625}FeGe$
x = 0.750†	$Co_{1.262}V_{0.735}Fe_{1.035}Ge_{0.968}$	$Co_{1.223}V_{0.786}Fe_{0.884}Ge_{1.107}$	-	$Co_{1.250}V_{0.750}FeGe$
x = 1 †	$Co_{1.064}V_{0.953}Fe_{1.047}Ge_{0.936}$	$Co_{0.731}V_{1.400}Fe_{0.752}Ge_{1.117}$	-	CoVFeGe

† Multiphase specimen

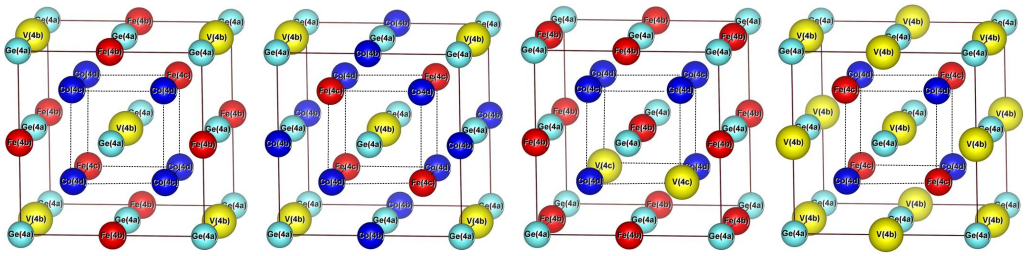

(a) (b) (c) (d)

Figure A.7: Crystal structure in unit cells of a Heusler alloy $Co_{2-x}Cr_xFeGe$ (a) CFVG (Y), (b) $x = 0.50$ (II configuration), (c) $x = 0.50$ (III configuration), and (d) $x = 0.50$ (IV configuration)

A.2.1.2 Electrical resistivity

Fig. A.8 shows the plot of a nonlinear least-squares fit with insets showing low temperature resistivity data fitting

A.2.2 Theoretical Results

Table A.4 shows the extracted (experimentally) and calculated (using PBE and PBE-D2) lattice parameters. The DOS and PDOS and magnetic moments of the MCSQS structure for $x = 0.25$, 0.375, 0.50 and 0.625 in the $Co_{2-x}V_xFeGe$ series, calculated using the PBE functional are shown in Fig. A.9. The calculated magnetic moments using PBE functional are less than those expected from Slater-Pauling rule and experimental values which requires the necessity of the hybrid functional HSE06 as discussed in main manuscript. Fig. A.10 shows the DOS and PDOS and magnetic moments of the Co_2FeGe structure calculated with PBE and HSE06. Table A.5 shows the calculated (with HSE06) total (and normalized per formula unit indicated in the parenthesis) and atomic spin-magnetic moments of the 16 atoms supercell of MCSQS structures of $x = 0$, 0.25, and 0.50 in $Co_{2-x}Cr_xGe_xGe$ alloy series. The alloys $x = 0.375$ and $x = 0.625$ contain 128 atoms in the supercell, so their atomic spin-magnetic moments are not shown here.

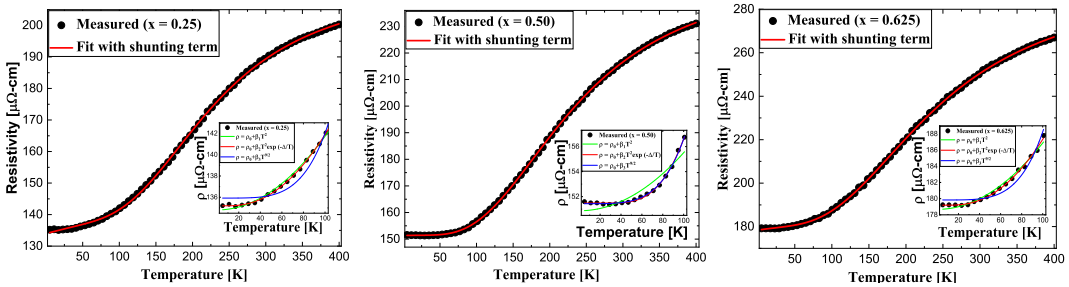

(a) (b) (c)

Figure A.8: Temperature dependence of electrical resistivity in $Co_{2-x}V_xFeGe$ in zero magnetic field for $x = 0.25$, $x = 0.50$, and $x = 0.625$. The fit is using Eqs. **??-??**.

Table A.4: Experimental and theoretical lattice parameters calculated with PBE and PBE-D2 (vdW correction) of the $Co_{2-x}V_xFeGe$ alloy series. The numbers in parentheses are the uncertainty in the last digit.

x	Expt. a (Å)	PBE a (Å)	PBE-D2 a (Å)
0	5.751(3)	5.735	5.667
0.25	5.760(1)	5.741	5.678
0.375	5.765(1)	5.742	5.680
0.50	5.769(1)	5.742	5.682
0.625	5.773(1)	5.743	5.684

Table A.5: The calculated total (and normalized per formula unit indicated in the parenthesis) and atomic spin-magnetic moments of the 16 atoms supercell of MCSQS structures of $x = 0$, 0.25, and 0.50 in $Co_{2-x}Cr_xGe_xGe$ alloy series.

	Concentration x = 0		Concentration x = 0.25		Concentration x = 0.50
Atom	Magnetic Moment	Atom	Magnetic Moment	Atom	Magnetic Moment
Co	1.238	Fe	3.577	V	-0.255
Co	1.235	Fe	3.546	V	-0.255
Co	1.236	Fe	3.559	Fe	3.583
Co	1.237	Fe	1.649	Fe	3.584
Co	1.237	V	0.175	Fe	1.571
Co	1.24	Co	1.194	Fe	1.571
Co	1.239	Co	1.201	Co	1.154
Co	1.237	Co	1.186	Co	1.154
Fe	3.683	Co	1.145	Co	1.061
Fe	3.677	Co	1.127	Co	1.061
Fe	3.677	Co	1.083	Co	1.019
Fe	3.682	Co	1.127	Co	1.019
Ge	-0.055	Ge	-0.055	Ge	-0.007
Ge	-0.043	Ge	-0.046	Ge	-0.038
Ge	-0.054	Ge	-0.097	Ge	-0.038
Ge	-0.042	Ge	-0.076	Ge	-0.007
Total	24.424 (6.106)	Total	20.296 (5.074)	Total	16.177 (4.044)

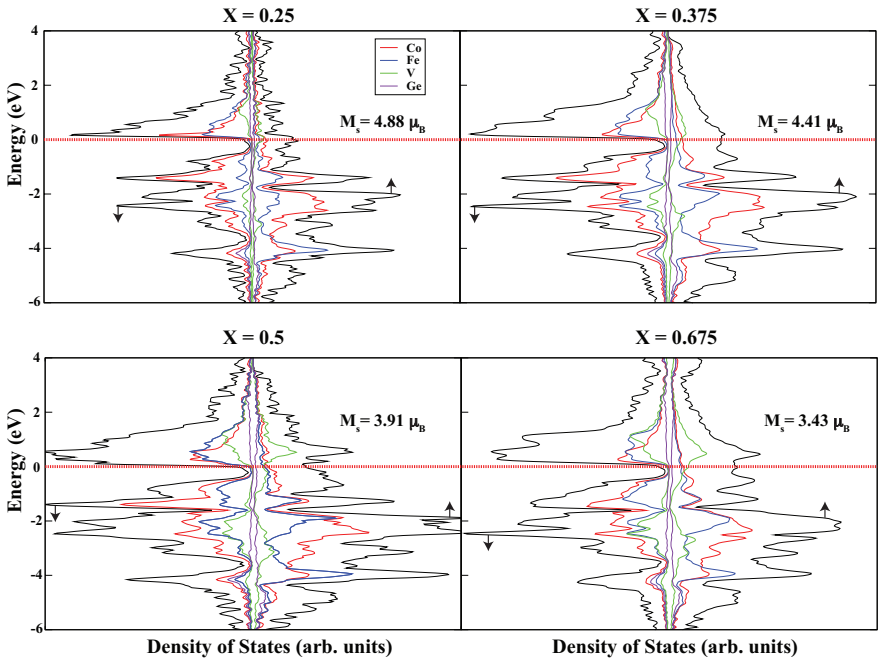

Figure A.9: The DOS and PDOS and magnetic moments of the MCSQS structure for $x = 0.25$, 0.375, 0.50 and 0.625 for the $Co_{2-x}V_xFeGe$ series. The black arrows depict the spin up and spin down contributions and the red dotted line represents the Fermi level. All results depicted involving electronic and magnetic properties are carried out using the PBE functional.

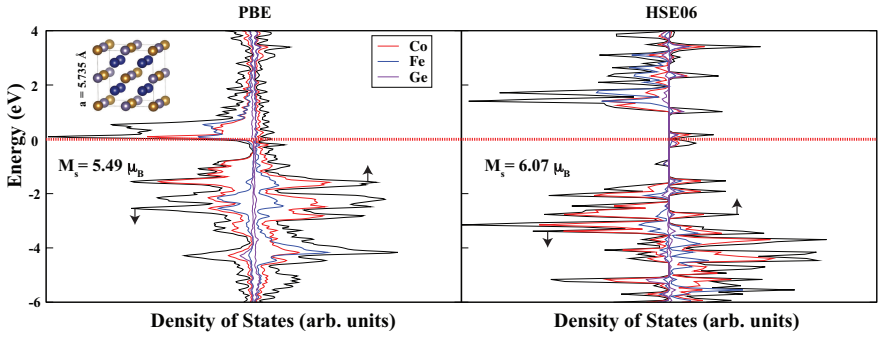

Figure A.10: The DOS and PDOS and magnetic moments of for the Co_2FeGe structure calculated with PBE and HSE06. The PBE optimized structure and lattice constant are included in the inset. The black arrows depict the spin up and spin down contributions and the red dotted line represents the Fermi level.

A.3 Supplementary Information: Structural, electronic, magnetic, transport and mechanical properties of the half-metal-type quaternary Heusler alloy $Co_2Fe_{1-x}V_xGe$

A.3.1 Synthesis and Thermal treatment

We have synthesized polycrystalline $Co_2Fe_{1-x}V_xGe$ alloy series in bulk form, each with a mass of ~ 5 g, by repeated arc-melting of pure Co (99.98%, Alfa Aesar), Fe (99.98%, Alfa Aesar), V (99.7%, Alfa Aesar), and Ge (99.999%, Alfa Aesar) under an ultrahigh purity Argon (99.999%) pressure of 0.02 Pa using an Edmund Buehler compact arc melter MAM-1. The mixture of constituent elements Co, Fe, V and Ge in a ratios $2 : 1-x : x : 1$ was melted at least 6 times, turning the specimen over before each melting cycle, in order to improve homogeneity of the samples. The as-cast cut pieces were examined repeatedly using scanning electron microscopy (SEM) and energy dispersive X-ray spectroscopy (EDS) analysis in a JEOL 7000 Field Emission Scanning Electron Microscope (FESEM) to confirm homogeneity and correct composition. After confirming the anticipated target composition, as-cast samples were sealed in quartz tubes under vacuum for thermal treatments. The samples were annealed in a furnace at different temperatures; 900°C, 950°C, and 1000°C for different dwell times (5 days to 15 days), and at the end of each annealing cycle, the samples were cooled slowly in the furnace as well as quenched in ice-water to get optimum crystallization and granular structures.

A.3.2 Experimental Results

As mentioned in main manuscript, only the alloy with $x = 0.25$ is observed to be stable phase in slow cooling method, while $x = 0.375$ in addition to $x = 0.25$ is found to be stable in rapid ice quenched method. All the reported optical images shown in Fig. A.11 are for specimens heat treated at 1000°C for 9 days followed by ice/water mixture quenching while optical images shown in Fig. A.12 are for specimens heat treated at 1000°C for 9 days followed by slow cooling in the furnace.

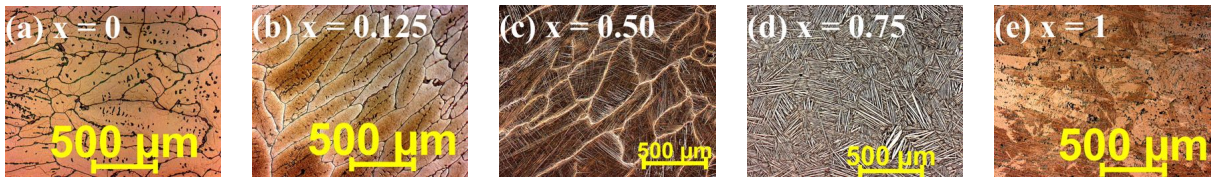

Figure A.11: Optical micrograph of $Co_2Fe_{1-x}V_xGe$ ($0 \leq x \leq 1$) heat treated at 1000°C for 9 days followed by ice/water mixture quenching. The samples were etched for 5 seconds using the Adler etchant.

In parent CFG, the secondary phase is mainly located in grain boundaries and same trend is observed with the vanadium substitution $x = 0.125$ in place of Fe, though the major granular phase was identified to be close to target and nominal secondary phase was observed to segregate in grain boundaries. On further substitution for Fe by V with $x = 0.25$, most stable phase was obtained on both slow cooling in the furnace as well as quenched in ice-water. We only observed the single phase microstructure for $x = 0.375$ after quenching in ice-water. All other higher V concentration produced multiphase behavior with micrographs revealing the elongated strips rearranged in dis-

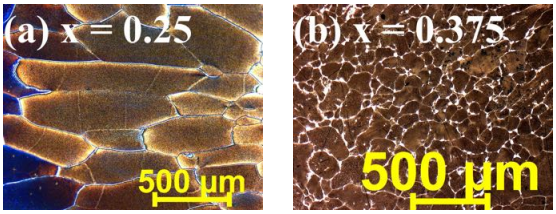

Figure A.12: Optical micrograph of (a) $Co_2Fe_{0.75}V_{0.25}Ge$, and (b) $Co_2Fe_{0.625}V_{0.375}Ge$ heat treated at 1000°C for 9 days followed by normal cooling in the furnace. The samples were etched for 5 seconds using the Adler etchant.

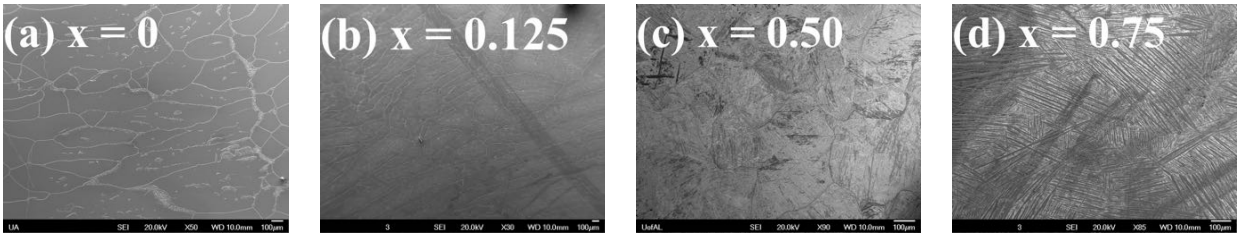

Figure A.13: SEM micrograph of $Co_2Fe_{1-x}V_xGe$ $(0 \leq x \leq 1)$ heat treated at 1000°C for 9 days followed by ice/water mixture quenching. The samples were etched for 5 seconds using the Adler etchant.

tinctive patterns. SEM images displaying the microstructure are shown in Fig. A.13 & A.14, both for single as well as multiphase specimens. The composition of all the specimens in the series was analysed using EDS (see Table A.6).

A.3.2.1 Crystal structure

Fig. A.15 shows the XRD patterns of the $Co_2Fe_{1-x}V_xGe$ alloy series heat treated at 1000°C for 9 days followed by ice/water mixture quenching, using a Co-K_α radiation source. The crystal structure obtained from the XRD data suggests the presence of pure $L2_1$ Heusler structure for $x = 0.25$ and 0.375 only. All other compositions are observed to have $L2_1$ crystal phase with some impurity. For all cubic single-phase compositions $x = 0.25$, and $x = 0.375$, only three distinct Heusler-like reflection peaks (h, k, l all odd or even) are observed; fundamental peaks with $h+$

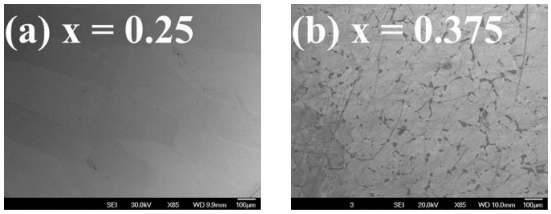

Figure A.14: SEM micrograph of (a) $Co_2Fe_{0.75}V_{0.25}Ge$, and (b) $Co_2Fe_{0.625}V_{0.375}Ge$ heat treated at 1000°C for 9 days followed by normal cooling in the furnace. The samples were etched for 5 seconds using the Adler etchant.

Table A.6: Average composition of $Co_2Fe_{1-x}V_xGe$ ($0 \leq x \leq 1$) alloy series as determined from EDS analysis (annealed at 1000°C for 9 days followed by ice/water mixture quenching).

	Main phase	Secondary phase	Composition in grain boundary	Target
x = 0	$Co_{1.96}Fe_{1.06}Ge_{0.98}$	$Co_{2.17}Fe_{0.5}Ge_{1.33}$	$Co_{2.17}Fe_{0.5}Ge_{1.33}$	Co_2FeGe
x = 0.125	$Co_{1.96}Fe_{0.91}V_{0.13}Ge$	$Co_{2.14}Fe_{0.38}V_{0.04}Ge_{1.44}$	$Co_{2.14}Fe_{0.38}V_{0.04}Ge_{1.44}$	$Co_2Fe_{0.875}V_{0.125}Ge$
x = 0.25	$Co_{1.99}Fe_{0.76}V_{0.26}Ge_{0.99}$	-	$Co_{2.03}Fe_{0.69}V_{0.22}Ge_{1.06}$	$Co_2Fe_{0.75}V_{0.25}Ge$
x = 0.375	$Co_{1.99}Fe_{0.63}V_{0.38}Ge$	-	$Co_{2.08}Fe_{0.53}V_{0.30}Ge_{1.09}$	$Co_2Fe_{0.625}V_{0.375}Ge$
x = 0.375†	$Co_{1.95}Fe_{0.60}V_{0.43}Ge_{1.02}$	$Co_{2.14}Fe_{0.42}V_{0.13}Ge_{1.31}$	$Co_{2.14}Fe_{0.42}V_{0.13}Ge_{1.31}$	$Co_2Fe_{0.625}V_{0.375}Ge$
x = 0.50	$Co_{1.99}Fe_{0.46}V_{0.54}Ge_{1.01}$	$Co_{1.98}Fe_{0.52}V_{0.47}Ge_{1.03}$	$Co_{2.11}Fe_{0.42}V_{0.37}Ge_{1.10}$	$Co_2Fe_{0.50}V_{0.50}Ge$
x = 0.75	$Co_{1.96}Fe_{0.28}V_{0.77}Ge_{0.99}$	$Co_{2.05}Fe_{0.13}V_{0.70}Ge_{1.12}$	-	$Co_2Fe_{0.25}V_{0.75}Ge$
x = 1	$Co_{1.95}V_{1.23}Ge_{0.82}$	$Co_{2.15}V_{0.62}Ge_{1.23}$	-	Co_2VGe

† annealed at 1000°C for 9 days followed by normal cooling in the furnace

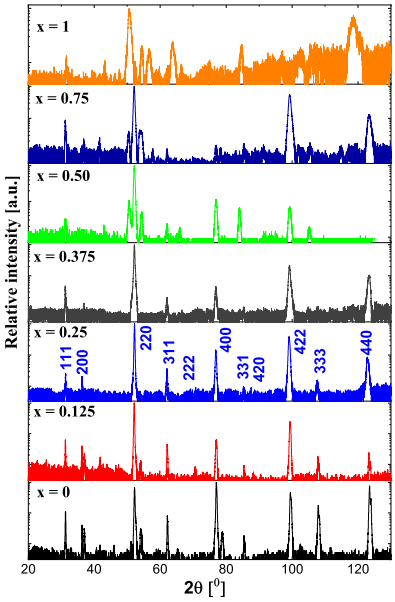

Figure A.15: Experimental XRD patterns of $Co_2Fe_{1-x}V_xGe$ ($0 \leq x \leq 1$) alloy series annealed at 1000°C for 9 days followed by ice/water mixture quenching. All the peaks corresponding to the indexed peaks are from $L1_2$ structure while all other peaks are impurity peaks.

$k+l=4n$, even superlattice peaks with $h+k+l=4n+2$ and odd superlattice peaks $h+k+l=2n+1$. In Heusler-like alloys, presence of (111) peak indicates the chemical ordering of atoms in octahedral positions, and (200) peak reflects the superlattice reflections due to atoms in tetrahedral positions, while (220) peak is a principal reflection. None of the low angle superlattice peaks are absent in single phase cubic structures which indicates a degree of sublattice ordering. No mixed odd/even indices are observed in reflection peaks indicting that single phase cubic samples are crystallized in the face-centered cubic Heusler-like structure. The intensity of superlattice peak (111) is greater than that of (200) peak in all stable cubic phases consistently, though the texturing effects makes it difficult to rely on XRD peak intensities.

Though the impurity peaks are clearly visible in $x=0$, $x=0.50$, $x=0.75$, and $x=1$ alloys, we extracted approximate lattice parameters considering only the visible Heusler cubic peaks in XRD patterns to be 5.745 , 5.765 , 5.773 , and 5.782 respectively.

Fig. A.17 shows the field dependent magnetization M(H) curves of the stable alloys with

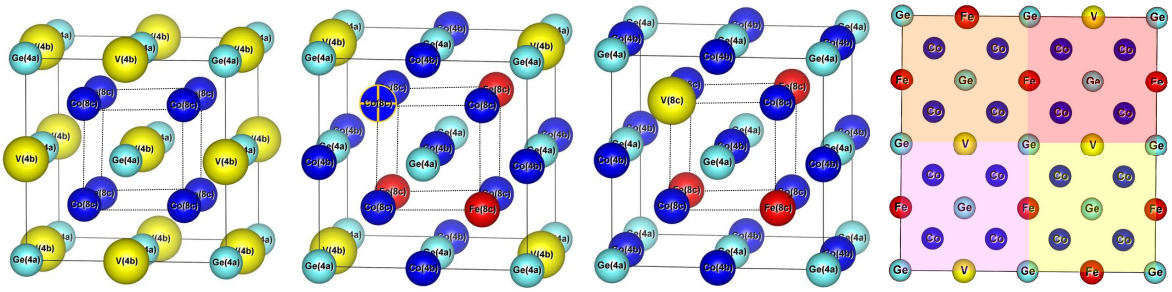

(a) (b) (c) (d)

Figure A.16: Crystal structure in unit cells of a Heusler alloys (a) Co_2VGe, (b) II configuration, (c) III configuration mentioned in main manuscript, and (d) a $2 \times 2 \times 2$ supercell involving 128 atoms/cell considered for $x = 0.375$ alloy in DFT calculation.

$x = 0.25$ and $x = 0.375$ in the $Co_2Fe_{1-x}V_xGe$ series at 300 K. Both alloys show soft ferromagnetic behavior. The saturation magnetic moments at 300 K were extracted to be 4.80 $\mu_B/f.u.$ and 4.29 $\mu_B/f.u.$ for alloys $Co_2Fe_{0.75}V_{0.25}Ge$ and $Co_2Fe_{0.625}V_{0.375}Ge$ respectively.

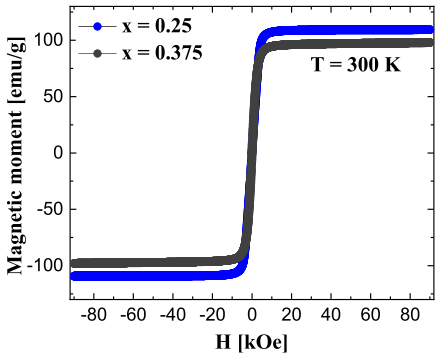

Figure A.17: The field-dependent magnetization at 300 K of $Co_2Fe_{1-x}V_xGe$ ($x = 0.25$ and 0.375).

A.3.3 Theoretical Results

Though higher V substitutions in CFG yielded multiphase behavior experimentally, we performed DFT calculation using GGA+U approach for them too to study the trend of electronic and magnetic structures in ordered form. We chose the most stable configurations (I) observed in $x = 0.25$ for calculations. Fig. A.18 shows the calculated spin resolved band structures and density of states (DOS) for $x = 0.50$, $x = 0.75$, and $x = 1$ respectively from top to bottom. All the systems appeared to be half-metallic with systematic shifting of Fermi level from conduction band edge in CFG to valence band edge in Co_2VG which is expected as we are replacing Fe atoms by bigger V atoms in each successive cases. The calculated magnetic moments are 4.5 μ_B, 3.75 μ_B, and 3 μ_B with corresponding energy gaps in minority spin channel 0.789 eV, 0.794 eV, and 0.890 eV for $x = 0.50$, $x = 0.75$, and $x = 1$ respectively. The atomic spin magnetic moments of theoretically predicted most stable configurations in $Co_2Fe_{1-x}V_xGe$ alloy series are given in Table A.7

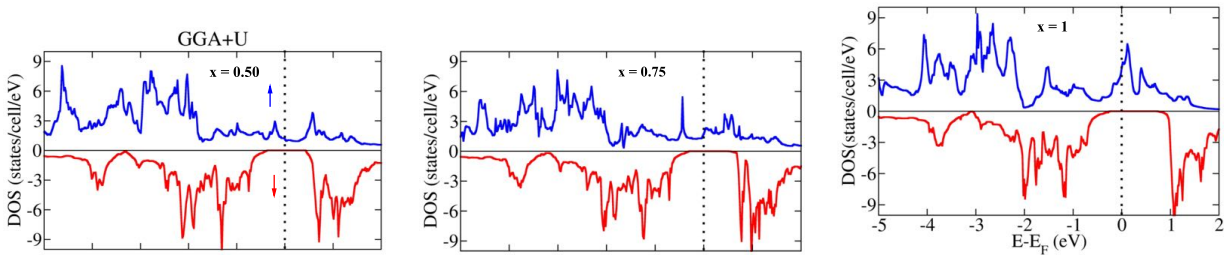

Figure A.18: Spin polarized DOS for $Co_2Fe_{1-x}V_xGe$ ($x = 0.50$, 0.75, and 1, from top to bottom) calculated using GGA+U. Number of states in each DOS plots are scaled with respect to one formula unit.

Table A.7: The calculated total (and normalized per formula unit indicated in the parenthesis) and atomic spin magnetic moments of the supercells for the $Co_2Fe_{1-x}V_xGe$ alloy series considering ordered $L2_1$ structure.

sites	Atoms ($x = 0$)	M (μ_B)	Atoms ($x = 0.25$)	M (μ_B)	Atoms ($x = 0.50$)	M (μ_B)	Atoms ($x = 0.75$)	M (μ_B)	Atoms ($x = 1$)	M (μ_B)
8c	Co	1.461	Co	1.365	Co	1.312	Co	1.251	Co	1.170
	Co	1.461	Co	1.365	Co	1.313	Co	1.251	Co	1.170
	Co	1.461	Co	1.365	Co	1.312	Co	1.251	Co	1.170
	Co	1.461	Co	1.365	Co	1.313	Co	1.252	Co	1.170
	Co	1.461	Co	1.365	Co	1.312	Co	1.251	Co	1.170
	Co	1.461	Co	1.365	Co	1.313	Co	1.252	Co	1.170
	Co	1.461	Co	1.365	Co	1.312	Co	1.251	Co	1.170
	Co	1.461	Co	1.365	Co	1.313	Co	1.251	Co	1.170
4b	Fe	3.102	Fe	3.102	Fe	3.122	Fe	3.146	V	0.681
	Fe	3.102	Fe	3.102	Fe	3.122	V	0.642	V	0.695
	Fe	3.102	Fe	3.102	V	0.701	V	0.643	V	0.686
	Fe	3.102	V	0.899	V	0.701	V	0.642	V	0.686
4a	Ge	-0.022	Ge	0.003	Ge	-0.045	Ge	-0.042	Ge	-0.023
	Ge	-0.022	Ge	-0.042	Ge	-0.011	Ge	-0.013	Ge	-0.021
	Ge	-0.022	Ge	-0.042	Ge	-0.045	Ge	-0.013	Ge	-0.024
	Ge	-0.022	Ge	-0.042	Ge	-0.011	Ge	-0.013	Ge	-0.024
Total		24.008 (6.002)		21.004 (5.251)		18.032 (4.508)		15.002 (3.751)		12.016 (3.004)

A.4 Supplementary Information: Effect of mixing the low-valence transition metal atoms Y = Co, Fe, Mn, Cr, V, Ti, or Sc on the properties of quaternary Heusler compounds $Co_{2-x}Y_xFeSi$ ($0 \leq x \leq 1$)

A.4.1 Experimental Results

A.4.1.1 Microstructural and Compositional analysis

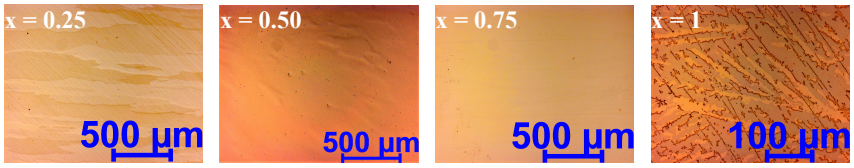

(a)

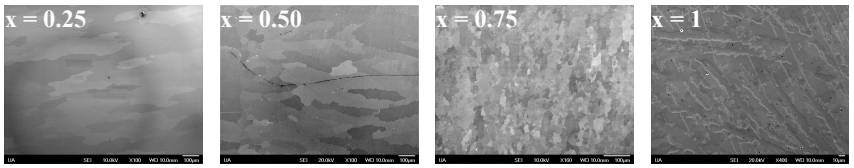

(b)

Figure A.19: (a) Optical and (b) SEM micrograph of $Co_{2-x}Ti_xFeSi$, $0.25 \leq x \leq 1$) annealed at 900°C for 7 days followed by slow cooling showing the granular microstructures.

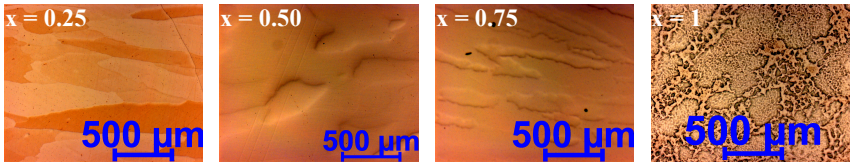

(a)

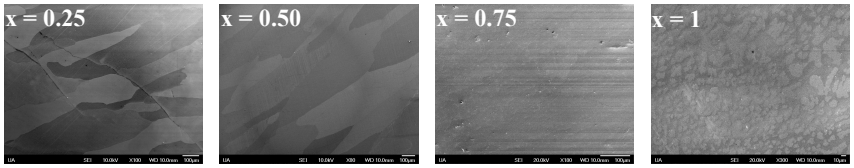

(b)

Figure A.20: (a) Optical and (b) SEM micrograph of $Co_{2-x}V_xFeSi$, $0.25 \leq x \leq 1$) annealed at 900°C for 7 days followed by slow cooling showing the granular microstructures.

Microstructures of all single phase specimens with $x = 0.50$ from $Co_{2-x}Y_xFeSi$ (Y = Co, Fe, Mn, Cr, V, or Ti) series are already presented in main manuscript. Here, Fig. A.19(a) and (b), Fig. A.20(a) and (b), Fig. A.21(a) and (b), and Fig. A.22(a) and (b) show the optical and electron micrographs for all the alloys in the series $Co_{2-x}Y_xFeSi$ (Y = Ti, V, Cr, and Mn, $0 \leq x \leq 1$). Fig. A.23 shows the optical and electron micrographs for $Co_{1.50}Sc_{0.50}FeSi$ alloy. From the micrographs, it is clear that Mn and Cr substitution for Co in Co_2FeSi result stable alloys for $0 \leq x \leq 1$, while V and

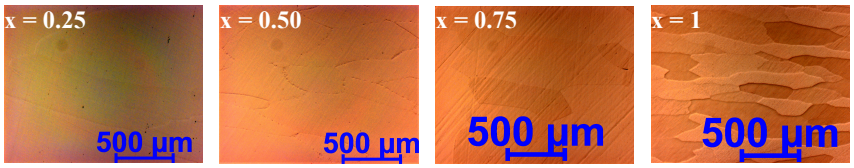

(a)

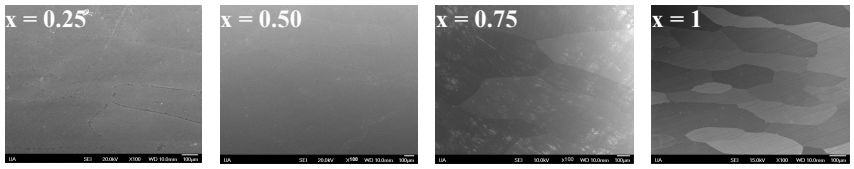

(b)

Figure A.21: (a) Optical and (b) SEM micrograph of $Co_{2-x}Cr_xFeSi$, $0.25 \leq x \leq 1$) annealed at 900°C for 7 days followed by slow cooling showing the granular microstructures.

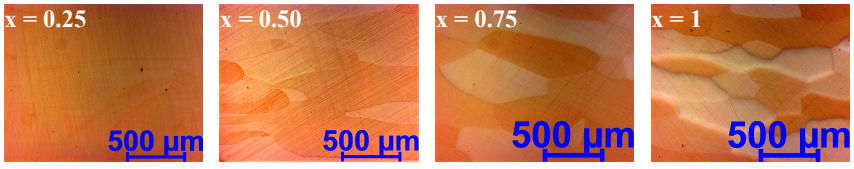

(a)

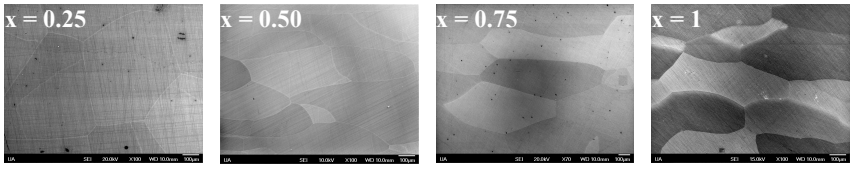

(b)

Figure A.22: (a) Optical and (b) SEM micrograph of $Co_{2-x}Mn_xFeSi$, $0.25 \leq x \leq 1$) annealed at 900°C for 7 days followed by slow cooling showing the granular microstructures.

Ti substitution result stable alloys for $0 \leq x \leq 0.75$ only. Equiatomic quaternary alloys CoFeVSi and CoFeTiSi are not stable. Also, Sc substitution also results multiphase behavior. There are three distinct phases represented by A, B, and C in the images. The composition of all the specimens within the series was analyzed using EDS and the average composition of all the specimens with $x = 0.50$ are presented in Table A.8.

A.4.1.1.1 Crystal structure

Fig. A.24(a-d) show the powder XRD spectra of the $Co_{2-x}Ti_xFeSi$, $Co_{2-x}V_xFeSi$, $Co_{2-x}Cr_xFeSi$, and $Co_{2-x}Mn_xFeSi$ ($0 \leq x \leq 1$) alloy series, respectively. The asterisks correspond to the secondary phase/unknown impurity phase in CoFeTiSi and CoFeVSi alloys consistent with microstructures observed in previous section. All the XRD peaks in single-phase alloys can be indexed as face centered cubic (*fcc*) structure. The Variation of atomic radius with atomic number of Y element in $Co_{2-x}Y_xFeSi$ is shown in Fig. A.25(d). Fig. A.25(a) and (b) display the crystal structures in unit cells of a Heusler alloy $Co_{1.50}Y_{0.50}FeSi$ as described in main manuscript. Fig. A.25(c) shows

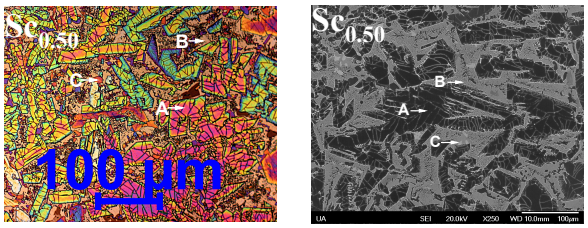

Figure A.23: Optical and SEM micrographs of $Co_{1.50}Sc_{0.50}FeSi$, heat treated at 900°C for 7 days followed by normal cooling in the furnace.

Table A.8: Average composition of $Co_{2-x}Y_xFeSi$ (Y = Co, Fe, Mn, Cr, V, Ti, or Sc, $x = 0.50$) alloy series as determined from EDS analysis (annealed at 900°C for 7 days followed by normal cooling in the furnace).

	Main phase	Secondary phase	Composition in grain boundary	Target
Co	$Co_{1.988}Fe_{1.004}Si_{1.008}$	-	$Co_{1.998}Fe_{1.007}Si_{0.995}$	Co_2FeSi
Fe	$Co_{1.503}Fe_{1.499}Si_{0.998}$	-	$Co_{1.498}Fe_{1.504}Si_{0.998}$	$Co_{1.500}Fe_{1.500}Si$
Mn	$Co_{1.507}Mn_{0.505}Fe_{0.995}Si_{0.993}$	-	$Co_{1.497}Mn_{0.495}Fe_{1.010}Si_{0.998}$	$Co_{1.500}Mn_{0.500}FeSi$
Cr	$Co_{1.498}Cr_{0.507}Fe_{0.997}Si_{0.998}$	-	$Co_{1.493}Cr_{0.497}Fe_{1.015}Si_{0.995}$	$Co_{1.500}Cr_{0.500}FeSi$
V	$Co_{1.496}V_{0.505}Fe_{0.996}Si_{1.003}$	-	$Co_{1.496}V_{0.505}Fe_{0.996}Si_{1.003}$	$Co_{1.500}V_{0.500}FeSi$
Ti	$Co_{1.499}Ti_{0.497}Fe_{0.994}Si_{1.010}$	-	$Co_{1.499}Ti_{0.497}Fe_{0.994}Si_{1.010}$	$Co_{1.500}Ti_{0.500}FeSi$
Sc†	$Co_{1.389}Sc_{0.700}Fe_{0.574}Si_{1.337}$ (A)	$Co_{0.962}Sc_{0.090}Fe_{1.737}Si_{1.211}$ (B) & $Co_{0.991}Sc_{0.020}Fe_{1.838}Si_{1.151}$ (C)	$Co_{0.962}Sc_{0.090}Fe_{1.737}Si_{1.211}$	$Co_{1.500}Sc_{0.500}FeSi$

† Multiphase specimen

the the crystal structures of equiatomic Heusler alloy CoFeYSi. Fig. A.26 shows the observed, calculated and difference profiles for the best fit configuration (I) after performing the Rietveld refinement for $Co_{2-x}Y_xFeSi$ (Y = Co, Fe, Mn, Cr, V, or Ti, $x = 0.50$) alloys. The goodness of fit parameters for all $x = 0.50$ alloys are given in main manuscript.

A.4.1.2 Magnetic Characterization

Fig. A.27 shows the isothermal magnetization curves for all single-phase alloys $Co_{1.50}Y_{0.50}FeSi$ (Y = Co, Fe, Mn, Cr, V, or Ti) measured at room temperature (300 K). All the single phase alloys are observed to be ferromagnets at room temperature as well with slightly small saturation magnetization values than those observed at 5 K. The extracted saturation magnetic moments at room temperature are given in Table A.9. Fig. A.28(a-d) show the magnetization curves measured at 5 K for all the alloys in the series $Co_{2-x}Y_xFeSi$ (Y = Ti, V, Cr, Mn, $0 \leq x \leq 1$). While Fig. A.28(e-h) show the temperature dependent specific magnetization of the investigated specimens $Co_{2-x}Y_xFeSi$ (Y = Ti, V, Cr, Mn, $0 \leq x \leq 1$), measured by means of a vibrating sample magnetometer in a constant magnetic field of 100 Oe. The corresponding saturation magnetic moments at 5 K and Curie temperatures are given in main manuscript.

A.4.2 Theoretical Results

Fig. A.29 shows the calculated spin resolved total density of states (TDOS) along with the partial density of states (PDOS) of constituent atoms per formula unit (f.u.) of $Co_{1.50}Y_{0.50}FeSi$ (Y = Co, Fe, Mn, Cr, V, Ti, or Sc) alloys using both GGA (left column) and GGA+U (right

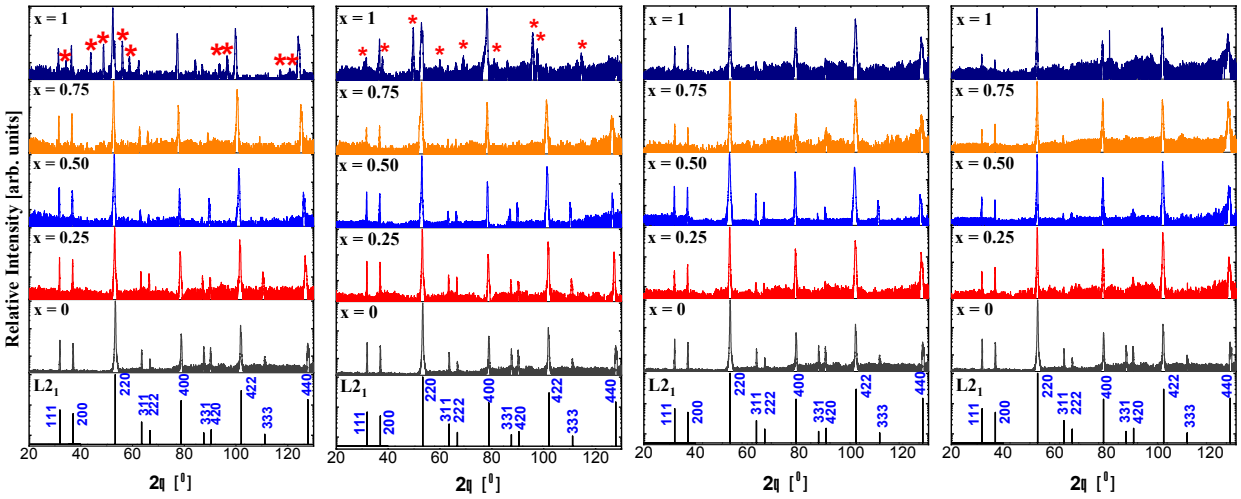

Figure A.24: Experimental XRD patterns of (a) $Co_{2-x}Ti_xFeSi$, (b) $Co_{2-x}V_xFeSi$, (c) $Co_{2-x}Cr_xFeSi$, and (d) $Co_{2-x}Mn_xFeSi$, ($0 \leq x \leq 1$) alloy series annealed at 900°C for 7 days investigated at room temperature, here, $*$ corresponds secondary phase/unknown impurity phase in the alloys. The first from the bottom in each is the simulated XRD pattern for ordered $L2_1$ structure of CFS. The relative Intensity (y-axis) is plotted in log scale so that all the peaks can be seen clearly.

column) methods. The atom resolved DOS (the d-orbital contribution from transition metal atoms and sp-orbital contribution from main group elements) are presented to elucidate the contribution to TDOS. There is a small contribution deep in energy to TDOS from sp-states of main group elements. The main contribution is from the 3 d-states of the transition metal atoms. In general from the atom resolved DOS, it is seen that Co, Fe, and Mn atoms majority-spin d-states are almost completely occupied while majority of the weight is above the Fermi level in early transition metal atoms V, Ti, and Sc. There is a peak in majority-spin d-states in the vicinity of Fermi level with large exchange splitting between the occupied majority-spin and unoccupied minority-spin states in the case of Cr atom. This feature makes Cr ideal for using it as an impurity in Heusler alloys to get larger band gaps with higher degree of spin-polarization at the Fermi level. These results are consistent with previous observations [154, 305, 306].

The contribution to DOS from type I, II, and III atoms are estimated due to the different magnetic environments in considered structures of substituted alloys as shown in Fig. A.27. From calculated atom resolved spin magnetic moments (see Table A.10 and Table A.11), it is clear that Fe(I) atoms, which share the same sublattice A with Y atoms, and Fe(II) atoms sharing the same sublattice B with Co have different nearest neighbor environment. Though all Co atoms occupy B sublattice, there are three different magnetic environments which are represented by Co(I), Co(II), and Co(III) in Fig. A.27. Likewise, in A sublattice, the nearest neighbor environment of Si(I) and Si(II) are different, but that of two substituted Y atoms is same. The contribution to spin-resolved DOS from same atom types with different nearest neighbor environment is different, which is depicted in PDOS plots in Fig. A.29. We can safely conclude that symmetry and the nearest-neighbors environment play a crucial role in the properties of the various atoms in half-metallic

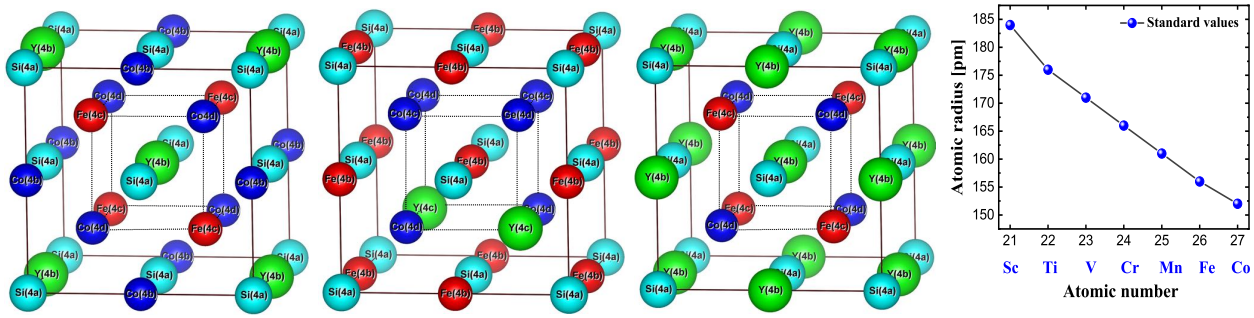

(a) (b) (c) (d)

Figure A.25: Crystal structure in unit cells of a Heusler alloy $Co_{1.50}Y_{0.50}FeSi$ (Y = Co, Fe, Mn, Cr, V, Ti, or Sc) (a) II configuration, (b) III configuration, and (c) CoFeYSi. The structures are shown in their ideal, unrelaxed forms. (d) Variation of atomic radius with atomic number of Y element in $Co_{2-x}Y_xFeSi$.

Table A.9: Saturation magnetic moments extracted at T = 300 K $Co_{1.50}Y_{0.50}FeSi$ (Y = Co, Fe, Mn, Cr, V, and Ti) alloy series. The numbers in parentheses are the uncertainty in the last digit, *e.g.*, $5.76(3) = 5.76 \pm 0.03$.

Y element	Expt. M_s (μ_B/f.u.)
Co	5.76(3)
Fe	5.42(5)
Mn	4.93(2)
Cr	4.33(5)
V	3.65(5)
Ti	3.21(4)

Heusler compounds. All Co atoms have almost similar DOS as their atom-resolved spin magnetic moments differ only by small amount. In the case of Fe atoms, the situation is more complex and their nearest-neighbors environment is completely different. As a result and as shown in Fig. A.29 their DOS is completely different. The Fe(I) atoms present a d-DOS which shares a lot of features with the one of the Y atoms. There is a very large exchange splitting between majority-spin occupied and minority-spin unoccupied d-states resulting to a very large minority spin gap and a very large Fe(I) spin magnetic moment, which is more than double the spin magnetic moment of the Fe(II) atoms. 3d atoms Co, Fe, Mn, and Cr in $Co_{1.50}Y_{0.50}FeSi$ series have parallel spin magnetic moments and are ferromagnetically coupled while V, Ti, and Sc are coupled anti-ferromagnetically.

The calculated atomic spin magnetic moments of $Co_{1.50}Y_{0.50}FeSi$ (Y = Co, Fe, Mn, Cr, V, Ti, or Sc) alloys are given in Table A.10.

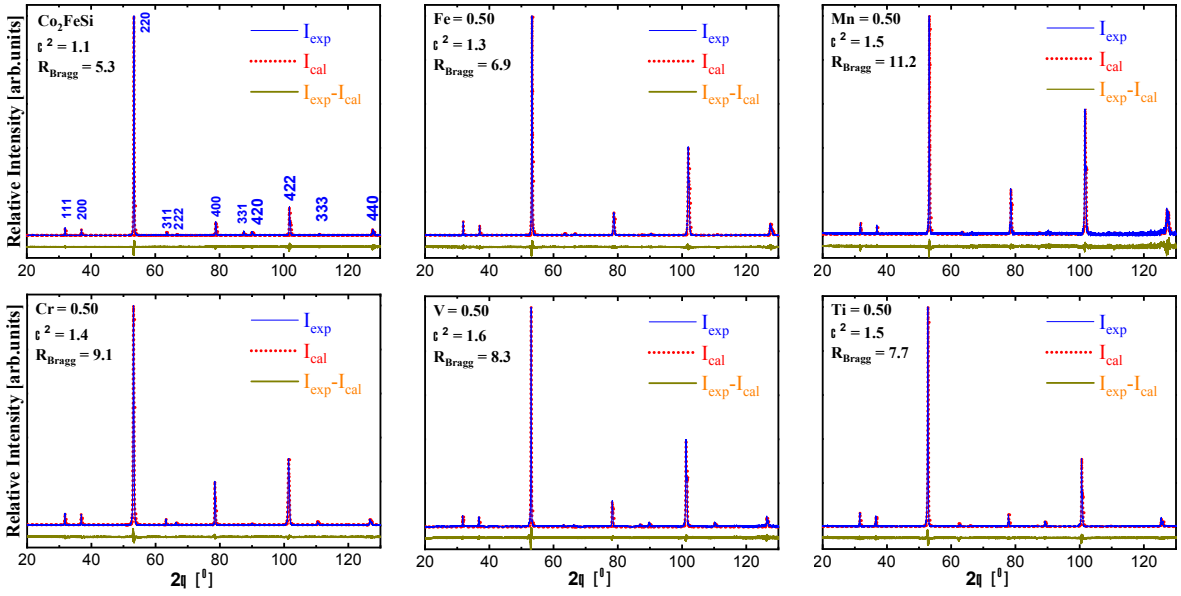

Figure A.26: Rietveld refinement performed on $Co_{1.50}Y_{0.50}FeSi$ (Y = Co, Fe, Mn, Cr, V, or Ti) alloys annealed at 900°C for 7 days followed by slow cooling considering first atomic configuration given in Table 4.13.

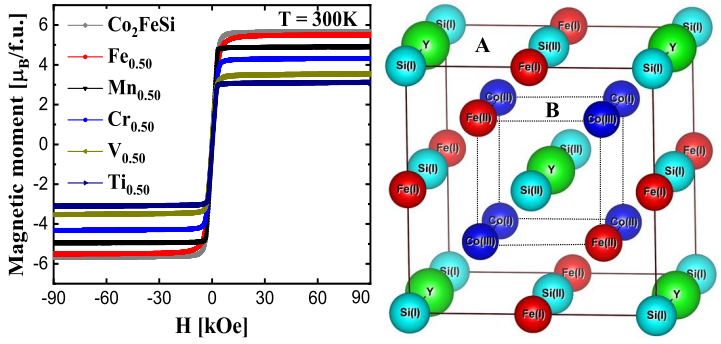

(a) (b)

Figure A.27: (a) Isothermal M-H curves measured at room temperature for $Co_{2-x}Y_xFeSi$ (Y = Co, Fe, Mn, Cr, V, or Ti, $x = 0.50$). The behavior is similar to that observed in low temperature case. (b) Crystal structure showing the different magnetic environments in unit cell of $Co_{1.50}Y_{0.50}FeSi$ (Y = Fe, Mn, Cr, V, Ti, or Sc) assuming I configuration in Table 4.15.

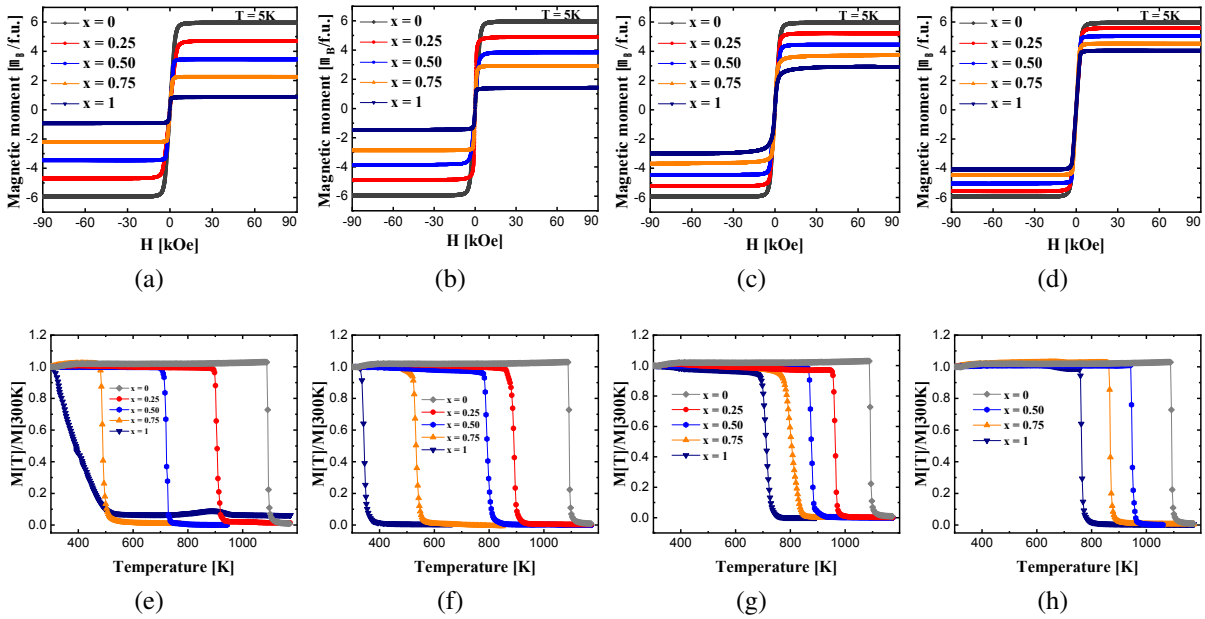

Figure A.28: Isothermal magnetization curves of (a) $Co_{2-x}Ti_xFeSi$, (b) $Co_{2-x}V_xFeSi$, (c) $Co_{2-x}Cr_xFeSi$, and (d) $Co_{2-x}Mn_xFeSi$ alloy series measured at 5 K. Temperature dependence of magnetization at 100 Oe for (e) $Co_{2-x}Ti_xFeSi$, (f) $Co_{2-x}V_xFeSi$, (g) $Co_{2-x}Cr_xFeSi$, and (h) $Co_{2-x}Mn_xFeSi$ alloys.

Table A.10: GGA+U: The calculated total (and normalized per formula unit indicated in the parenthesis) and atomic spin-magnetic moments of the 16 atoms supercell of $Co_{1.50}Y_{0.50}FeSi$ (Y = Co, Fe, Mn, Cr, V, Ti, or Sc) alloys using GGA+U approach.

Sites	Co_2FeSi (atoms)	M (μ_B)	Y=Fe (atoms)	M (μ_B)	Y=Mn (atoms)	M (μ_B)	Y=Cr (atoms)	M (μ_B)	Y=V (atoms)	M (μ_B)	Y=Ti (μ_B)	M (atoms)	Y=Ti (μ_B)	M
4d	Co	1.439	Co	1.195	Co	0.960	Co	0.984	Co	1.202	Co	1.024	Co	0.836
	Co	1.439	Co	1.143	Co	0.946	Co	0.997	Co	1.168	Co	1.036	Co	0.844
	Co	1.439	Co	1.143	Co	0.946	Co	0.997	Co	1.168	Co	1.036	Co	0.844
	Co	1.439	Co	1.195	Co	0.960	Co	0.984	Co	1.202	Co	1.024	Co	0.836
4c	Co	1.439	Co	1.198	Co	0.983	Co	1.007	Co	1.191	Co	1.076	Co	0.918
	Co	1.439	Co	1.198	Co	0.983	Co	1.007	Co	1.191	Co	1.076	Co	0.918
	Co	1.439	Fe	1.800	Fe	1.252	Fe	1.132	Fe	1.671	Fe	1.452	Fe	1.072
	Co	1.439	Fe	1.800	Fe	1.252	Fe	1.132	Fe	1.671	Fe	1.452	Fe	1.072
4b	Fe	3.117	Fe	2.883	Fe	2.834	Fe	2.888	Fe	3.001	Fe	2.967	Fe	2.844
	Fe	3.117	Fe	2.883	Fe	2.834	Fe	2.888	Fe	3.001	Fe	2.967	Fe	2.844
	Fe	3.117	Fe	2.883	Mn	3.152	Cr	2.098	V	-0.147	Ti	-0.530	Sc	-0.440
	Fe	3.117	Fe	2.883	Mn	3.152	Cr	2.098	V	-0.147	Ti	-0.530	Sc	-0.440
4a	Si	0.006	Si	-0.042	Si	-0.071	Si	-0.066	Si	-0.024	Si	-0.019	Si	-0.023
	Si	0.006	Si	-0.042	Si	-0.046	Si	-0.035	Si	0.005	Si	-0.010	Si	-0.037
	Si	0.006	Si	-0.042	Si	-0.071	Si	-0.066	Si	-0.024	Si	-0.019	Si	-0.023
	Si	0.006	Si	-0.042	Si	-0.046	Si	-0.035	Si	0.005	Si	-0.010	Si	-0.037
Total		24.004 (6.001)		22.033 (5.508)		20.021 (5.005)		18.010 (4.503)		16.015 (4.004)		14.002 (3.501)		12.025 (3.006)

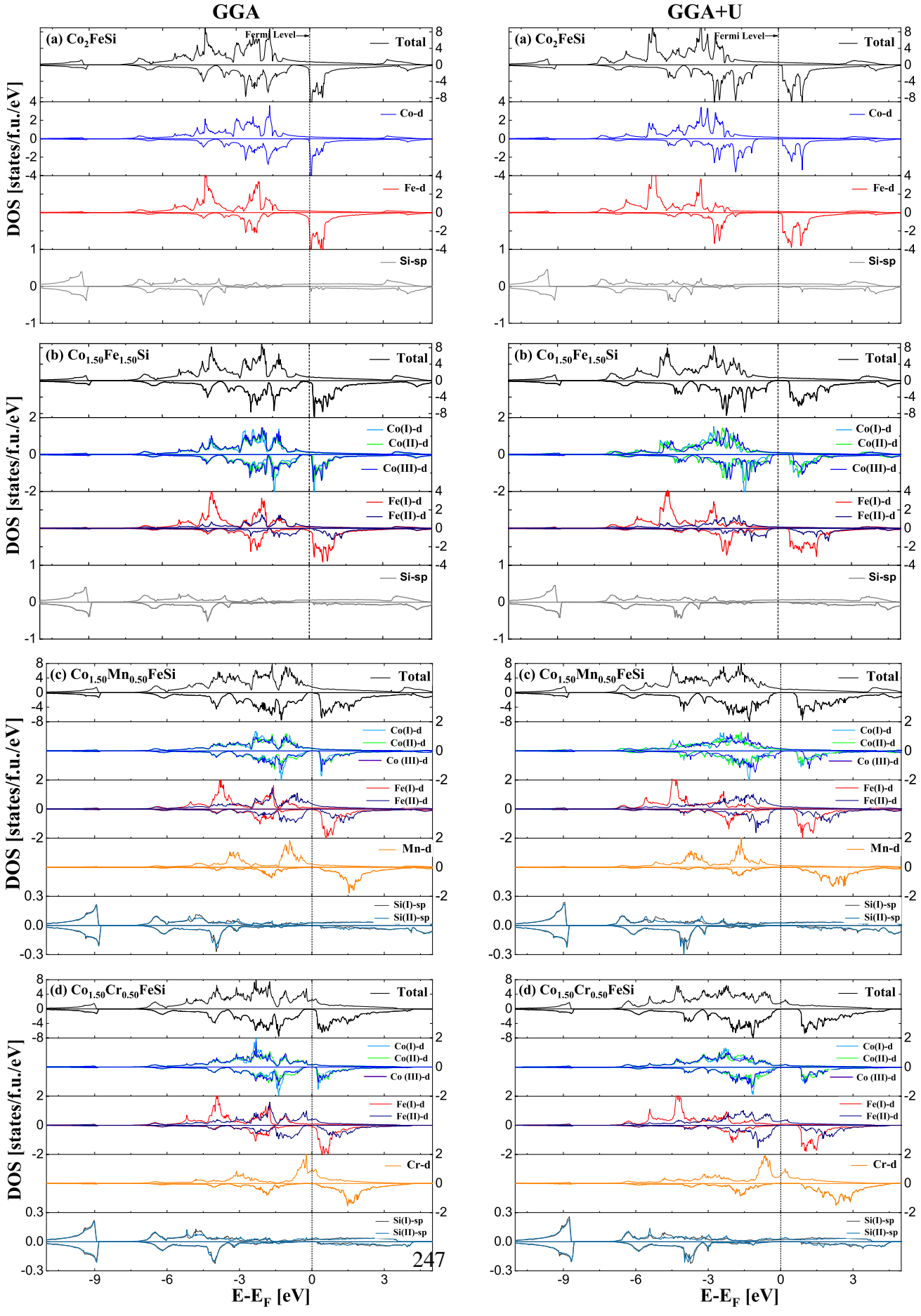
GGA
GGA+U
(a) Co2FeSi
(b) Co1.50Fe1.50Si
(c) Co1.50Mn0.50FeSi
(d) Co1.50Cr0.50FeSi
Fermi Level
Total
Co-d
Fe-d
Si-sp
Co(I)-d
Co(II)-d
Co(III)-d
Co (III)-d
Fe(I)-d
Fe(II)-d
Mn-d
Cr-d
Si(I)-sp
Si(II)-sp
DOS [states/f.u./eV]
E-EF [eV]

Continue...

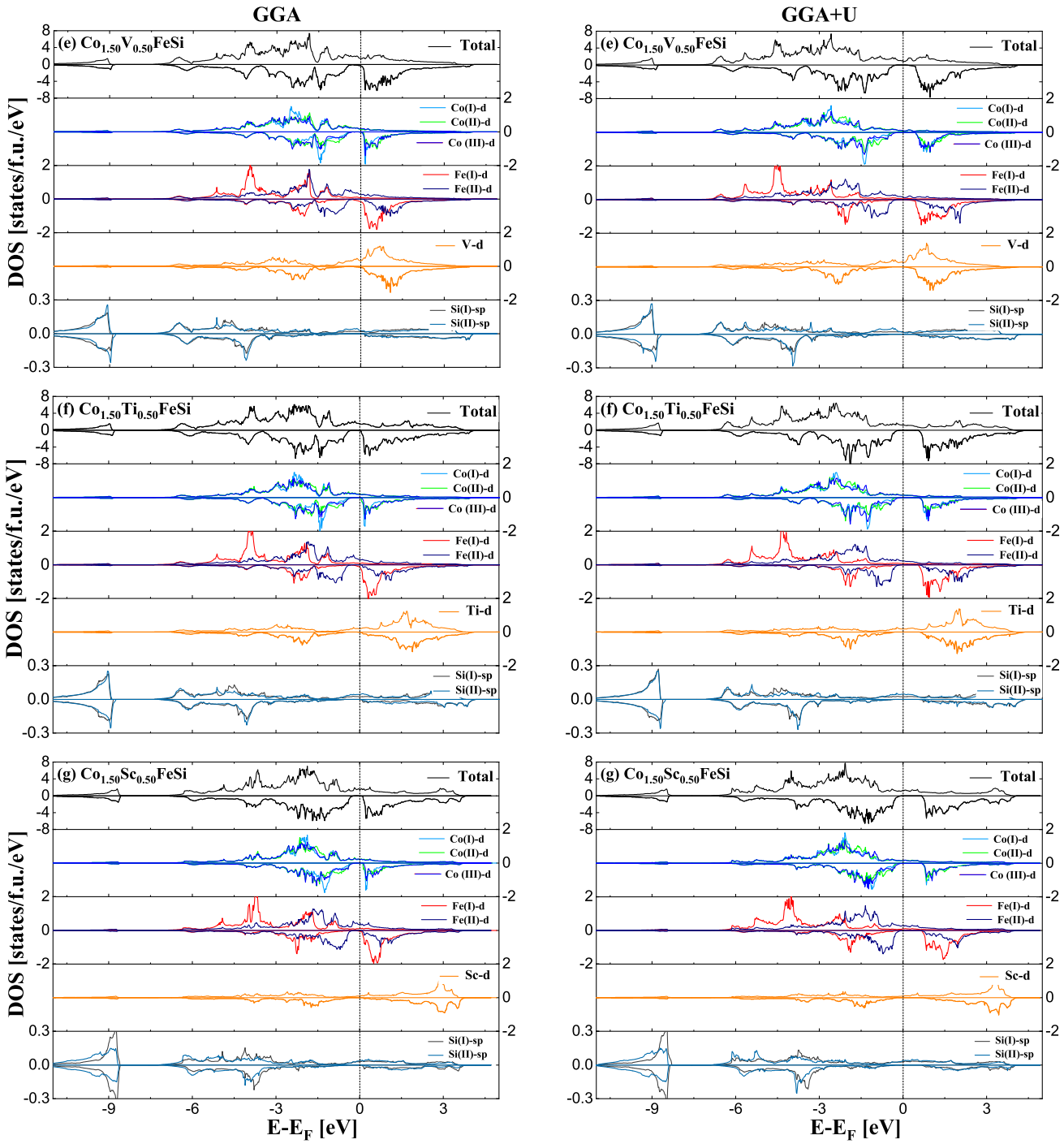

Figure A.29: Spin polarized total density of states (TDOS) along with the partial density of states (PDOS) of constituent atoms of $Co_{1.50}Y_{0.50}FeSi$ (Y = Co, Fe, Mn, Cr, V, Ti, or Sc) alloys using both GGA (left column) and GGA+U (right column) methods. Number of states in each plot is scaled with respect to one formula unit.

Table A.11: GGA: The calculated total (and normalized per formula unit indicated in the parenthesis) and atomic spin-magnetic moments of the 16 atoms supercell of $Co_{1.50}Y_{0.50}FeSi$ (Y = Co, Fe, Mn, Cr, V, Ti, or Sc) alloys using GGA approach.

Sites	Co_2FeSi (atoms)	M (μ_B)	Y=Fe (atoms)	M (μ_B)	Y=Mn (atoms)	M (μ_B)	Y=Cr (atoms)	M (μ_B)	Y=V (atoms)	M (μ_B)	Y=Ti (μ_B)	M (atoms)	Y=Ti (μ_B)	M
4d	Co	1.334	Co	1.231	Co	1.048	Co	1.075	Co	1.144	Co	1.001	Co	0.848
	Co	1.334	Co	1.164	Co	1.031	Co	1.054	Co	1.121	Co	0.998	Co	0.827
	Co	1.334	Co	1.164	Co	1.031	Co	1.054	Co	1.121	Co	0.998	Co	0.827
	Co	1.334	Co	1.231	Co	1.048	Co	1.075	Co	1.144	Co	1.001	Co	0.848
4c	Co	1.334	Co	1.203	Co	1.044	Co	1.052	Co	1.112	Co	1.015	Co	0.881
	Co	1.334	Co	1.203	Co	1.044	Co	1.052	Co	1.112	Co	1.015	Co	0.881
	Co	1.334	Fe	1.702	Fe	1.305	Fe	1.201	Fe	1.501	Fe	1.284	Fe	0.997
	Co	1.334	Fe	1.702	Fe	1.305	Fe	1.201	Fe	1.501	Fe	1.284	Fe	0.997
4b	Fe	2.794	Fe	2.740	Fe	2.745	Fe	2.767	Fe	2.927	Fe	2.189	Fe	2.724
	Fe	2.794	Fe	2.740	Fe	2.745	Fe	2.767	Fe	2.927	Fe	2.189	Fe	2.724
	Fe	2.794	Fe	2.740	Mn	2.897	Cr	1.877	V	-0.115	Ti	-0.214	Sc	-0.230
	Fe	2.794	Fe	2.740	Mn	2.897	Cr	1.877	V	-0.115	Ti	-0.241	Sc	-0.230
4a	Si	0.006	Si	-0.015	Si	-0.041	Si	-0.039	Si	-0.011	Si	-0.003	Si	-0.006
	Si	0.006	Si	-0.015	Si	-0.020	Si	-0.013	Si	0.014	Si	0.008	Si	-0.013
	Si	0.006	Si	-0.015	Si	-0.041	Si	-0.039	Si	-0.011	Si	-0.003	Si	-0.006
	Si	0.006	Si	-0.015	Si	-0.020	Si	-0.013	Si	0.014	Si	0.008	Si	-0.013
Total		21.870 (5.468)		21.500 (5.375)		20.015 (5.004)		17.948 (4.485)		15.385 (3.846)		13.814 (3.454)		12.056 (3.014)

A.5 Supplementary Information: Tuneable structure and magnetic properties in $Fe_{3-x}V_xGe$ alloys

A.5.1 Experimental details

A.5.1.0.1 Synthesis and Thermal treatments

We have synthesized polycrystalline $Fe_{3-x}V_xGe$ alloy series in bulk form, each with a mass of ~ 5 g, by repeated arc-melting of pure Fe (99.98%, Alfa Aesar), V (99.7%, Alfa Aesar), and Ge (99.999%, Alfa Aesar) under an ultrahigh purity Argon (99.999%) pressure of 10^{-4} mbar using an Edmund Buehler compact arc melter MAM-1. The mixture of constituent elements Fe, V and Ge in a ratios $3-x:x:1$ was melted at least 6 times, turning the specimen over before each melting cycle, in order to improve homogeneity of the samples. The as-cast cut pieces were examined repeatedly using scanning electron microscopy (SEM) and energy dispersive X-ray spectroscopy (EDS) analysis in a JEOL 7000 Field Emission Scanning Electron Microscope (FESEM) to confirm homogeneity and correct composition. After confirming the anticipated target composition, as-cast samples were sealed in quartz tubes under vacuum for thermal treatments. The samples were annealed in a furnace at different temperatures ranging from 650°C to 1000°C for different dwell times (5 days to 25 days), and at the end of each annealing cycle, the samples were cooled slowly in the furnace to get optimum crystallization and granular structures.

A.5.1.1 Metallography

A hot mounting technique was used to mount the annealed samples in conductive graphite powder prior to metallography to observe the surface morphology on a microscopic level. The graphite powder avoids charge accumulation by providing conductive path during SEM/EDS analysis. The metallography begins with grinding using silicon carbide abrasive discs (120 through 1200 grit size) followed by diamond suspension polishing. Colloidal silica suspension of grit size $0.02\,\mu m$ was used at last for the finest polishing. After obtaining a smooth and reflective surface, the samples were etched with Adler etchant (9 g of $CuNH_3Cl$, 45 g of hydrated $FeCl_2$, 150 mL of HCl and 75 mL of DI Water) [243]. The purpose of etching is that etchant attacks different phases present in the samples at different rates, and provides high quality surface contrast for microstructure characterization.

A.5.1.2 Characterization

A Bruker *D*8 Discover X-ray diffractometer equipped with a monochromatic Co-K_α ($\lambda = 0.179$ *nm*) radiation source was used to determine the crystal structure of samples prepared. The polished samples mounted in graphite powder were rotated around the ϕ-axis during the XRD measurement to minimize surface effects. The crystal structures determined from XRD were further confirmed using electron backscatter diffraction (EBSD) phase mapping analysis in a JEOL 7000 FESEM system. CaRIne crystallography 4.0 software [78] and in-house PYTHON code [79] including the dispersive corrections to the atomic scattering factors were used to evaluate the observed XRD patterns. Rietveld refinement was done using the CRYSTAL IMPACT MATCH! software based on the FULLPROF algorithm [80].

The low temperature magnetic and electrical transport characteristics were measured using Quantum Design Physical Property Measurement System (PPMS) Dynacool with both vibrating sample magnetometry (VSM) and electrical transport features, while the high temperature magnetization was measured using the Lakeshore VSM 7410. DSC measurements were carried out to confirm the diffusionless martensitic transformation (with a ramp rate 10°C/min during heating and cooling) in the temperature range up to 1200°C in a Setaram Labsys Evo. in Ar gas flux at the rate of 20 mL/min to prevent the possible oxidation of the samples. The temperature and the heat reaction were calibrated using high purity indium, aluminum, silver and nickel standards. The Vickers micro hardness of alloy series was measured on a Buehler model 1600-6100 hardness tester by using a square-based diamond-pyramid indenter.

A.5.2 Experimental Results

A.5.2.1 Microstructural and Compositional analysis

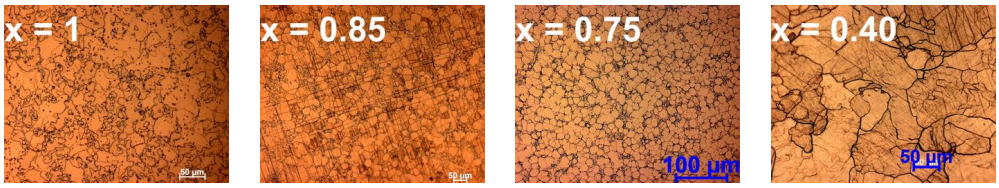

Figure A.30: Optical micrograph of $Fe_{3-x}V_xGe$ ($0 \leq x \leq 1$) heat treated at 950°C for 7 days showing the grain structures. The samples were etched for 25 seconds using the Adler etchant.

Starting from the fully stoichiometric Fe_2VGe, multi-phase microstructure was obtained in every heat treatment performed at 800, 900, 950, or 1000°C for different dwelling times; 3, 5, 7, or 14 days. While the major granular phase was identified to be $Fe_{2.15}V_{0.86}Ge_{0.99}$, the secondary phase was observed to be an Fe-deficient phase, whose composition was identified as $\sim Fe_{1.5}VGe$ using EDS (see Fig. A.30 for $x = 1$). This motivated us to directly prepare the major Fe-rich phase, the investigation of which again showed multi-phase behavior, with majority phase being rich in Fe *i.e.*, $Fe_{2.22}V_{0.78}Ge$ and a Fe-deficient secondary phase as compared to initial $Fe_{2.15}V_{0.85}Ge$ composition (see Fig. A.30 for $x = 0.85$). One fact evident from the investigation of those compositions is that increasing the amount of Fe by decreasing the V fraction in the parent Fe_2VGe alloy, the fraction of Fe tends to increase on the main phase, and at the same time the area covered by the secondary phase decreases, as shown in Fig. A.30 for $x = 0.75$ the area covered by secondary phase in $Fe_{2.25}V_{0.75}Ge$ is only about 5% of total area. This is suggestive that higher Fe content is needed in order to stabilize a single phase microstructure. Finally, after several iterations we were able to obtain stable single-phase granular microstructure for compositions with x = 0.625, 0.50, 0.40, 0.375, 0.25, 0.125, and 0, respectively, heat treated at 950°C for 7 days. Optical and SEM images of all single phase samples for same high temperature annealing condition *i.e.*, 7 days at 950°C are reported in the main text while those for multiphase samples are presented in Fig. A.30 and Fig. A.31, respectively. The average grain size is observed to decrease dramatically with increasing the V content as shown in Fig. A.33(A),

Fig. A.32 and Fig. A.33 respectively show the optical and SEM images of all samples annealed at low temperature (650°C for 25 days). For low temperature annealing of alloy with $x = 0.75$,

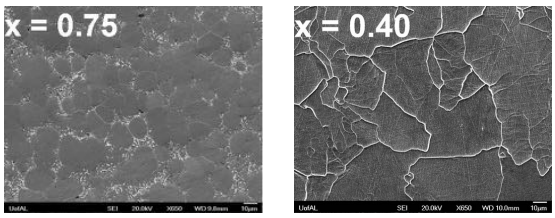

Figure A.31: SEM micrograph of $Fe_{3-x}V_xGe$ ($0 \leq x \leq 1$) heat treated at 950°C for 7 days showing the granular microstructure.

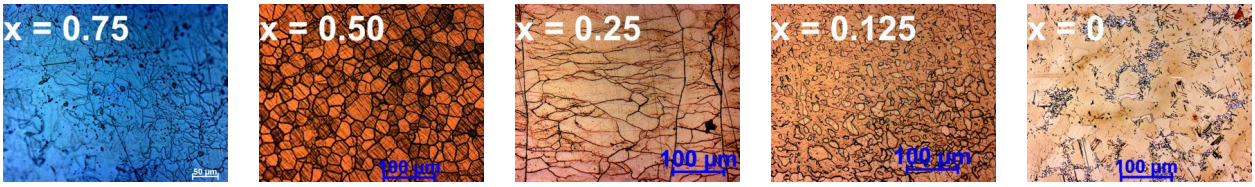

Figure A.32: Optical micrograph of $Fe_{3-x}V_xGe$ ($0 \leq x \leq 1$) heat treated at 650°C for 25 days showing the grain structures. The samples were etched for 25 seconds using the Adler etchant.

multi-phase microstructure was seen, as observed in higher temperature annealing, however for the intermediate compositions (x = 0.50, 0.25), single phase granular microstructures were observed. Multi-phase behavior was also observed in case of V substituted samples for $x = 0.125$. In the case of Fe_3Ge ($x = 0$), small amounts of secondary phases were observed (see Fig. A.32), in agreement with detailed studies on the parent Fe_3Ge compound [67, 239, 240]. The composition of all samples from the series as observed using EDS are tabulated in Table A.12

Table A.12: Composition of $Fe_{3-x}V_xGe$ ($0 \leq x \leq 1$) alloy series as determined from EDS analysis.

x	Crystal structure	Main phase	Secondary phase	Composition in grain boundary	Target composition
1	$L2_1^{\dagger *}$	$Fe_{2.15}V_{0.86}Ge_{0.99}$	$Fe_{1.71}V_{1.14}Ge_{1.15}$	$Fe_{2.05}V_{0.91}Ge_{1.04}$	Fe_2VGe
0.85	$L2_1^{\dagger *}$	$Fe_{2.22}V_{0.78}Ge$	$Fe_{1.69}V_{1.13}Ge_{1.18}$	$Fe_{2.11}V_{0.82}Ge_{1.07}$	$Fe_{2.15}V_{0.85}Ge$
0.75	$L2_1^{\dagger *}$	$Fe_{2.27}V_{0.75}Ge_{0.98}$	$Fe_{1.69}V_{1.16}Ge_{1.15}$	$Fe_{2.22}V_{0.76}Ge_{1.02}$	$Fe_{2.25}V_{0.75}Ge$
0.625	$L2_1^{\dagger}$	$Fe_{2.373}V_{0.626}Ge_{1.01}$	-	$Fe_{2.22}V_{0.76}Ge_{1.02}$	$Fe_{2.375}V_{0.625}Ge$
0.50	$L2_1^{\dagger}$	$Fe_{2.51}V_{0.50}Ge_{0.99}$	-	$Fe_{2.46}V_{0.51}Ge_{1.03}$	$Fe_{2.50}V_{0.50}Ge$
0.40	$L2_1^{\dagger}$	$Fe_{2.61}V_{0.39}Ge$	-	$Fe_{2.59}V_{0.40}Ge_{1.01}$	$Fe_{2.60}V_{0.40}Ge$
0.375	$L2_1^{\dagger}$	$Fe_{2.626}V_{0.374}Ge$	-	$Fe_{2.617}V_{0.363}Ge_{1.02}$	$Fe_{2.625}V_{0.375}Ge$
0.25	DO_{19}	$Fe_{2.75}V_{0.25}Ge$	-	$Fe_{2.73}V_{0.24}Ge_{1.03}$	$Fe_{2.75}V_{0.25}Ge$
0.25	$L2_1^{\ddagger}$	$Fe_{2.76}V_{0.25}Ge_{0.99}$	-	$Fe_{2.74}V_{0.25}Ge_{1.01}$	$Fe_{2.75}V_{0.25}Ge$
0.125	$DO_{19}^{\dagger}$	$Fe_{2.869}V_{0.128}Ge$	-	$Fe_{2.868}V_{0.122}Ge_{1.01}$	$Fe_{2.875}V_{0.125}Ge$
0	$DO_{19}^{\dagger}$	$Fe_{3.01}Ge_{0.99}$	-	$Fe_{2.98}Ge_{1.02}$	Fe_3Ge
0	$L1_2^{\ddagger} *$	$Fe_{3.03}Ge_{0.97}$	$Fe_{2.55}Ge_{1.45}$	-	Fe_3Ge

† annealed at 950°C for 7 days, ‡ annealed at 650°C for 25 days, * multi-phased samples

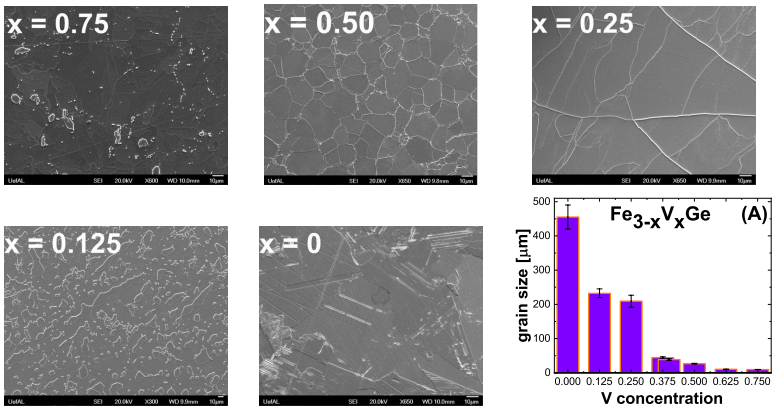

Figure A.33: SEM micrograph of $Fe_{3-x}V_xGe$ ($0 \leq x \leq 1$) heat treated at 650°C for 25 days showing the granular microstructure, and (A) variation of average grain size with V concentration for all single phase samples annealed at 950°C for 7 days.

A.5.3 Theoretical Results

In this theoretical supplementary information we provide the total and atomic magnetic moments (not normalized per formula unit) for each atom in the supercell for the stable studied alloys in Table A.13 and Table A.14. We also provide the calculated electronic band structures of each stable studied alloy in Fig. A.34.

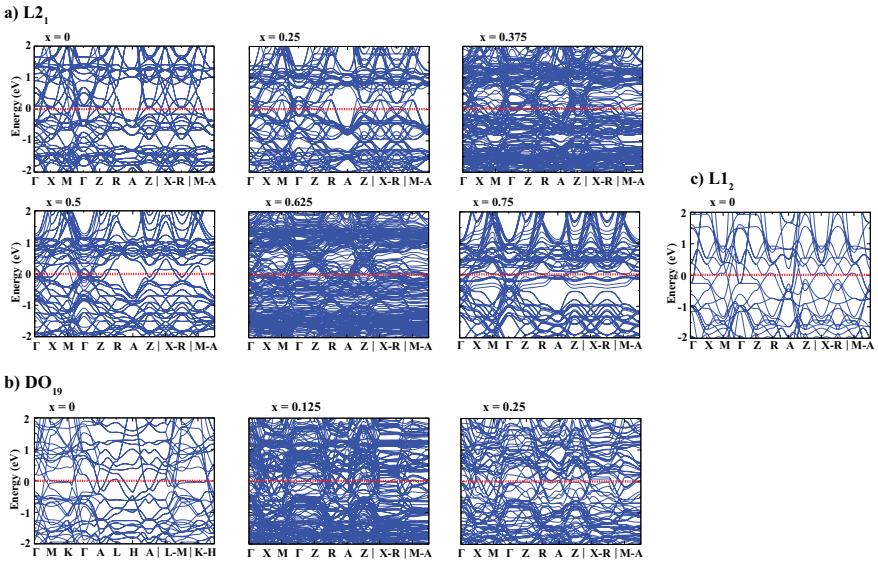

Figure A.34: The calculated electronic band structures for each alloy series. The red line indicates the Fermi level.

Table A.13: The total and atomic magnetic moments for the $L2_1$ alloy series.

Structure	**Concentration**
$L2_1$	**x = 0**
Atom	$M_s(\mu_B)$
Fe	1.433
Fe	1.432
Fe	1.433
Fe	1.432
Fe	1.432
Fe	1.432
Fe	1.432
Fe	1.433
Fe	2.585
Fe	2.584
Fe	2.584
Fe	2.584
Ge	-0.08
Ge	-0.08
Ge	-0.08
Ge	-0.08
Total	21.476

Structure	**Concentration**
$L2_1$	**x = 0.5**
Atom	$M_s(\mu_B)$
Fe	0.641
Fe	0.641
Fe	0.642
Fe	0.639
Fe	0.641
Fe	0.641
Fe	0.639
Fe	0.642
Fe	2.765
Fe	2.765
Ge	-0.026
Ge	-0.038
Ge	-0.026
Ge	-0.038
V	-0.379
V	-0.379
Total	9.77

Structure	**Concentration**
$L2_1$	**x = 0.25**
Atom	$M_s(\mu_B)$
Fe	0.996
Fe	0.998
Fe	0.996
Fe	0.998
Fe	0.998
Fe	0.996
Fe	0.998
Fe	0.996
Fe	2.678
Fe	2.678
Fe	2.678
Ge	-0.049
Ge	-0.068
Ge	-0.049
Ge	-0.049
V	-0.59
Total	15.205

Structure	**Concentration**
$L2_1$	**x = 0.625**
Atom	$M_s(\mu_B)$
Fe	1.321
Fe	1.82
Fe	1.88
Fe	1.313
Fe	2.29
Fe	2.335
Fe	2.298
Fe	1.497
Fe	1.668
Fe	1.713
Fe	1.355
Fe	1.675
Fe	1.488
Fe	1.364
Fe	1.808
Fe	2.408
Fe	2.576
Fe	2.439
Fe	2.559
Ge	-0.031
Ge	0.006
Ge	0.005
Ge	-0.029
Ge	-0.029
Ge	-0.077
Ge	-0.071
Ge	-0.032
V	-0.957
V	-0.217
V	-0.908
V	-0.507
V	-0.4
Total	32.56

Structure	**Concentration**
$L2_1$	**x = 0.375**
Atom	$M_s(\mu_B)$
Fe	1.228
Fe	1.143
Fe	1.658
Fe	1.228
Fe	1.657
Fe	1.142
Fe	2.423
Fe	2.634
Fe	2.408
Fe	0.941
Fe	1.653
Fe	1.632
Fe	1.031
Fe	1.653
Fe	0.941
Fe	1.031
Fe	1.632
Fe	2.4
Fe	2.591
Fe	2.393
Fe	2.601
Ge	-0.054
Ge	-0.025
Ge	-0.021
Ge	-0.054
Ge	-0.03
Ge	-0.075
Ge	-0.065
Ge	-0.031
V	-0.879
V	-0.879
V	-0.627
Total	33.28

Structure	**Concentration**
$L2_1$	**x = 0.75**
Atom	$M_s(\mu_B)$
Fe	0.567
Fe	0.572
Fe	0.571
Fe	0.568
Fe	0.573
Fe	0.566
Fe	0.569
Fe	0.57
Fe	2.81
Ge	-0.019
Ge	-0.027
Ge	-0.027
Ge	-0.027
V	-0.251
V	-0.251
V	-0.251
Total	6.513

Table A.14: The total and atomic magnetic moments for the DO_{19} and $L1_2$ alloy series.

Structure	**Concentration**
DO_{19}	**x = 0**
Atom	$M_s(\mu_B)$
Fe	2.216
Fe	2.215
Fe	2.215
Fe	2.216
Fe	2.216
Fe	2.215
Ge	-0.134
Ge	-0.134
Total	13.025

Structure	**Concentration**
$L1_2$	**x = 0**
Atom	$M_s(\mu_B)$
Fe	2.176
Fe	2.176
Fe	2.176
Ge	-0.149
Total	6.379

Structure	**Concentration**
DO_{19}	**x = 0.125**
Atom	$M_s(\mu_B)$
Fe	2.266
Fe	2.243
Fe	2.009
Fe	2.138
Fe	2.013
Fe	2.207
Fe	2.194
Fe	2.199
Fe	2.202
Fe	2.209
Fe	2.213
Fe	2.205
Fe	2.22
Fe	2.217
Fe	2.195
Fe	2.215
Fe	2.216
Fe	2.228
Fe	2.297
Fe	1.966
Fe	2.205
Fe	2.069
Fe	2.235
Ge	-0.086
Ge	-0.102
Ge	-0.139
Ge	-0.136
Ge	-0.137
Ge	-0.136
Ge	-0.132
Ge	-0.102
V	-0.726
Total	48.465

Structure	**Concentration**
DO_{19}	**x = 0.25**
Atom	$M_s(\mu_B)$
Fe	2.226
Fe	2.025
Fe	1.974
Fe	2.174
Fe	2.296
Fe	2.109
Fe	2.267
Fe	2.226
Fe	2.065
Fe	2.299
Fe	2.278
Ge	-0.091
Ge	-0.068
Ge	-0.127
Ge	-0.125
V	-0.688
Total	22.84

A.6 Supplementary Information: Influence of Cr-substitution on the structural, magnetic, electron transport, and mechanical properties of $Fe_{3-x}Cr_xGe$ Heusler alloys

A.6.1 Experimental details

A.6.1.1 Synthesis and Thermal treatments

The series of polycrystalline $Fe_{3-x}Cr_xGe$ ($0 \leq x \leq 1$) ingots were prepared by arc-melting the mixture of constituent elements Fe, Cr and Ge in a ratios $3-x : x : 1$ in an ultrahigh purity Argon atmosphere (99.999%) with pressure of 10^{-4} mbar using an Edmund Buehler compact arc melter MAM-1. The purity of the raw materials was 99.9% or higher. As an oxygen getter, Ti was melted inside the vacuum chamber separately before melting the compound to avoid oxygen contamination. All the ingots were melted at least six times, turning the specimen over before each melting cycle, for homogenization. The as-cast cut pieces were examined repeatedly using scanning electron microscopy (SEM) and energy dispersive X-ray spectroscopy (EDS) analysis in a JEOL 7000 Field Emission Scanning Electron Microscope (FESEM) to confirm homogeneity and correct composition. After confirming the anticipated target composition, as-cast samples were sealed in quartz tubes under the protection of argon atmosphere for thermal treatments. The samples were annealed in a furnace at different temperatures ranging from 650°C to 1000°C for different dwell times (5 days to 25 days), and at the end of each annealing cycle, the samples were cooled slowly in the furnace to get optimum crystallization and granular structures.

A.6.1.2 Metallography

We adopted metallography to observe the surface morphology on a microscopic level. A hot mounting technique was used to mount the annealed samples in conductive graphite powder prior to metallography. The graphite powder avoids charge accumulation by providing conductive path during SEM/EDS analysis. The metallography begins with grinding using silicon carbide abrasive discs (120 through 1200 grit size) followed by diamond suspension polishing. Colloidal silica suspension of grit size $0.02\,\mu m$ was used at last for the finest polishing. After obtaining a smooth and reflective surface, the samples were etched with Adler etchant (9 grams of $CuNH_3Cl$, 45 grams of hydrated $FeCl_2$, 150 mL of HCl and 75 mL of DI Water) [243]. The purpose of etching is that etchant attacks different phases present in the samples at different rates, and provides high quality surface contrast for microstructure characterization.

A.6.1.3 Characterization

A Bruker D8 Discover X-ray diffractometer equipped with a monochromatic Co-K_α(λ = 0.179 nm) radiation source was used at room temperature to determine the crystal structure of samples prepared. The polished samples mounted in graphite powder were rotated around the ϕ-axis during the XRD measurement to minimize surface effects. The crystal structures determined from XRD were further confirmed using electron backscatter diffraction (EBSD) phase mapping analysis in a JEOL 7000 FESEM system. CaRIne crystallography 4.0 software [78] and in-house PYTHON code [79] including the dispersive corrections to the atomic scattering factors were used to evaluate the observed XRD patterns. XRD analysis (Rietveld refinement) was done using the

CRYSTAL IMPACT MATCH! software based on the FULLPROF algorithm [80] that uses the least-square refinement between experimental and calculated intensities. The low temperature magnetic and electrical transport characteristics were measured using Quantum Design Physical Properties Measurements System (PPMS) with both vibrating sample magnetometry (VSM) and electrical transport features in a temperature range 5 K to 400 K, while the high temperature magnetization was measured using the Lakeshore VSM 7407 equipped with an oven. DC electrical resistivity measurements were carried out using van der Pauw method [179]. Al wire bonding was used to make the contacts. The Vickers micro hardness of alloy series was measured on a Buehler model 1600-6100 hardness tester by using a square-based diamond-pyramid indenter.

A.6.2 Experimental Results

A.6.2.0.1 Microstructural and Compositional analysis

Starting from the full stoichiometric Fe_2CrGe, multi-phase microstructure was obtained in every heat treatments performed at 650, 800, 900, or 1000°C for different dwelling times; 3, 5, 7, 15 or 25 days. However, it is difficult to obtain a pure phase in the stoichiometric Fe_2CrGe, where the major phase is identified to be hexagonal $Fe_{2.15}Cr_{0.85}Ge$, and a substantial Fe-deficient cubic secondary phase $Fe_{1.5}CrGe$ is always present as confirmed by EDS and XRD (discussed in XRD section of main manuscript). Thus, we adopted isostructural alloying to accomplish a pure hexagonal $D0_{19}$ structure (Mg_3Cd type, $P6_3/mmc$, space group no. 194 [64, 65]) in a series of alloys that contain Fe-Cr-Ge. So, we directly prepare the major Fe-rich phase, the investigation of which again showed multi-phase behavior, with majority phase being rich in Fe and a Fe-deficient secondary phase as compared to initial $Fe_{2.15}Cr_{0.85}Ge$ composition. One fact evident from the investigation of those compositions is that increasing the amount of Fe by decreasing the Cr fraction in the parent Fe_2CrGe alloy, the fraction of Fe tends to increase on the main phase, while the area covered by the secondary phase decreases (see Fig. A.35 for $x = 1$ and $x = 0.80$). This is suggestive that higher Fe content is needed in order to stabilize a single phase microstructure. Finally, after several iterations we were able to obtain stable single-phase microstructure for compositions with $x = 0.70$, 0.50, 0.25, and 0 heat treated at 1000°C for 15 days (discussed in main manuscript). Relatively large grains are observed. The average grain size is observed to decrease with the addition of Cr content. The effect of Cr substitution on the microstructure is substantial.

In addition to high temperature annealing, we also attempted to investigate low temperature annealing of our Cr-substituted structures to check if a stable $L1_2$ phase exists, similar to Fe_3Ge which is known to crystallize in $L1_2$ structure at temperatures below ∼700°C [21, 163, 238, 239]. But, multi-phase microstructure was seen for all compositions. Even in the case of Fe_3Ge ($x = 0$), small amounts of secondary phases were observed, in agreement to previous report by Kanematsu *et al.* [240]. Hence, our observations after complete analysis suggested that the high temperature $D0_{19}$ phase is, in fact, easily stabilized at room temperature and the formation of low temperature $L1_2$ phase is very slow process and takes longer time to form, in agreement with detailed studies on the parent Fe_3Ge compound [239]. The nominal composition of all including multiphase samples is presented in Table A.15.

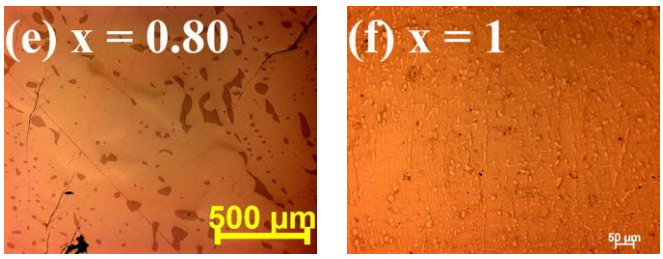

Figure A.35: Optical micrograph of x = 0.80 and x = 1 in $Fe_{3-x}Cr_xGe$ series, heat treated at 1000°C for 15 days showing multiphase structures. The samples were etched for 1 minutes seconds using the Adler etchant.

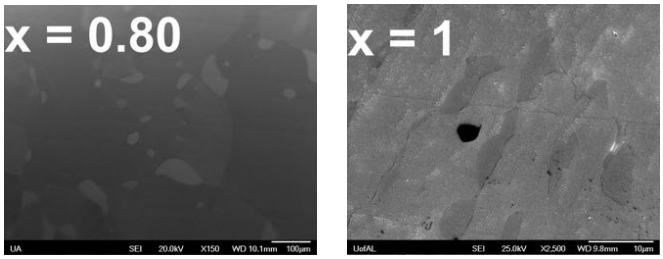

Figure A.36: SEM micrograph of x = 0.80 and x = 1 in $Fe_{3-x}Cr_xGe$ series, heat treated at 1000°C for 15 days showing multiphase structures.

A.6.2.1 Crystal structure and atomic order analysis

As discussed in main manuscript, the texturing effect (unknown degree) is more pronounced in sample $x = 0.25$ giving more intense $22\bar{4}0$ peak instead of $20\bar{2}1$. Although, all the peak positions are matched to the calculated patterns, the variation of peak intensities from expected ones made Rietveld refinement difficult to converse lower fitting parameters. The single digit reduced χ^2 values for $x = 0$ and $x = 0.70$ indicate relatively good fitting. The goodness of fit parameters are summarized in Table A.16.

A.6.2.2 Magnetic Characterization

Fig. A.38(a) shows the first-order derivative of magnetization as a function of temperature for $x = 0.25$ showing two possible magnetic transitions. The magnetic transition at 546 K corresponds to the ferro-paramagnetic transition but the origin of the transition at 436 K is not clear. One possible reason could be order-disorder phase transition introduced by the substitution of Cr on parent Fe_3Ge. Although the possibility of secondary phase formation due to vacuum annealing cannot be completely ruled out, the composition measured using EDS was within $\sim 5\%$ instrumental uncertainty range and XRD is not always sufficient to confirm the phase purity if the impurity phase content is less than 5% of the overall volume [105, 163, 168, 169]. The temperature dependence of magnetization at low temperatures (5-400 K) is also presented in Fig. A.38(b) for $x = 0.25$ and $x = 0.70$.

Table A.15: Composition of $Fe_{3-x}Cr_xGe$ ($0 \leq x \leq 1$) alloy series as determined from EDS analysis, all annealed at 1000°C for 15 days.

x	Main phase	Secondary phase	Target composition
1*	$Fe_{2.16}Cr_{0.86}Ge_{0.98}$	$Fe_{1.70}Cr_{1.15}Ge_{1.15}$	Fe_2CrGe
0.85*	$Fe_{2.20}Cr_{0.79}Ge_{1.01}$	$Fe_{1.70}Cr_{1.14}Ge_{1.16}$	$Fe_{2.15}Cr_{0.85}Ge$
0.80*	$Fe_{2.26}Cr_{0.73}Ge_{1.01}$	$Fe_{1.68}Cr_{1.13}Ge_{1.19}$	$Fe_{2.20}Cr_{0.80}Ge$
0.70	$Fe_{2.31}Cr_{0.70}Ge_{0.99}$	-	$Fe_{2.25}Cr_{0.75}Ge$
0.50	$Fe_{2.51}Cr_{0.50}Ge_{0.99}$	-	$Fe_{2.50}Cr_{0.50}Ge$
0.25	$Fe_{2.74}Cr_{0.25}Ge_{1.01}$	-	$Fe_{2.75}Cr_{0.25}Ge$
0	$Fe_{3.01}Ge_{0.99}$	-	Fe_3Ge

* multi-phased samples

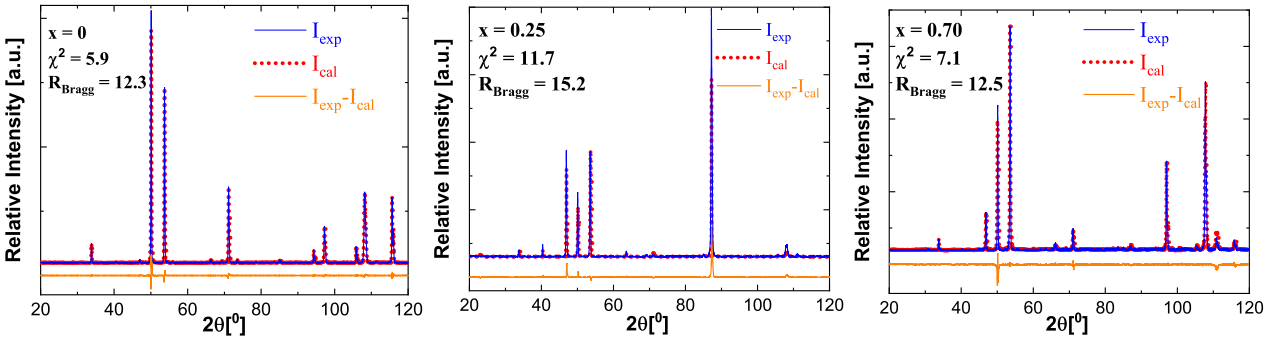

(a) (b) (c)

Figure A.37: The Rietveld refinement of XRD pattern for (a) $x = 0$, (b) $x = 0.25$, and (c) $x = 0.70$.

A.6.2.3 Electrical resistivity

The measured temperature dependence of resistivity is observed to obey the following Matthiessen's rule [99];

$$\rho(T) = \rho_0 + \rho_{e-ph}(T) + \rho_{e-m}(T) = \rho_0 + \alpha T + \beta T^2 \tag{A.1}$$

where ρ_0 is the temperature independent residual resistivity due to lattice imperfections, impurities *etc.*, ρ_{e-ph} and ρ_{e-m} are temperature dependent terms due to the scattering by phonons (T dependence) and magnons (T^2 dependence) respectively. As reported in the literatures [174, 219, 250], a parallel shunting resistivity is also introduced to the total resistivity to include the contribution from grain boundaries, assuming weak variation of highly disordered grain boundaries with temperature, which leads to the following expression for the resistivity;

$$1/\rho_{tot}(T) = 1/\rho_i(T) + 1/\rho_{shunt} \tag{A.2}$$

Fig. A.39 shows the plot of a nonlinear least-squares fit to this model, with fitting parameters summarized in Table A.17. With these fitting parameters, the electron-magnon contribution looks dominant above approximately 150 K. The T^2 term arising due to the electron-magnon interaction implies the presence of minority states at the Fermi level. One can also extract the intrinsic resistivity ρ_i from Equation A.2 as $\rho_i = \rho_{shunt}\rho_{tot}/(\rho_{shunt} - \rho_{tot})$. The inset in each plots of Fig. A.39 shows variation of the extracted ρ_i versus T^2 along with a linear fit, also indicating the dominant

Table A.16: The goodness of fit parameters extracted from the Rietveld refinement for $x = 0, 0.25, 0.50, and\ 0.70$.

x	reduced χ^2	R-factor
0	5.9	12.3
0.25	11.7	15.2
0.50	4.8	12.2
0.70	7.1	12.5

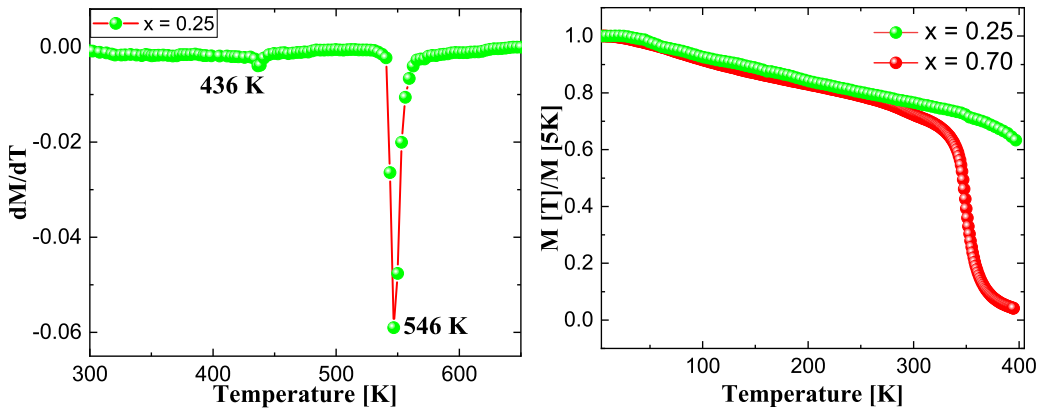

(a) (b)

Figure A.38: (a) The first-order derivative of magnetization as a function of temperature for $x = 0.25$ showing two magnetic transitions. (b) The temperature (low) dependence of magnetization M(T) for $x = 0.25$ and $x = 0.70$.

contribution from the electron-magnon scattering to the resistivity at higher temperatures.

Table A.17: Fitted parameters of resistivity data of $Fe_{3-x}Cr_xGe$ with x = 0.25, 0.50 and 0.70.

x	$\rho_0(\mu\Omega$-cm)	α ($\mu\Omega$-cm/K) times 10^{-2}	β ($\mu\Omega$-cm/K^2)$\times 10^{-3}$	$\rho_{shunt}(\mu\Omega$-cm)	Reduced chi-square $\times 10^{-12}$
0.25	39.79 ± 0.45	5.68 ± 1.40	7.72 ± 0.10	199.56 ± 0.40	2.47
0.50	71.27 ± 0.80	18.60 ± 2.56	10.68 ± 0.20	217.05 ± 0.49	1.05
0.70	105.15 ± 0.25	67.95 ± 2.01	15.30 ± 0.25	259.18 ± 0.45	1.35

A.6.3 Theoretical Results

In this theoretical supplementary information we provide the total (and normalized per formula unit) and atomic magnetic moments for each atom in the supercell and the corresponding symmetry for the stable studied alloys in Table A.18. In addition we supply the symmetry of each corresponding supercell. Note that although these $D0_{19}$ alloys are hexagonal, the supercells that contain the fewest amount of atoms (for the SQS structure creation) are rectangular to preserve specific alloying concentrations.

To investigate the mechanical properties of Fe_3Ge and $Fe_{3-x}Cr_xGe$ alloys, we calculated their

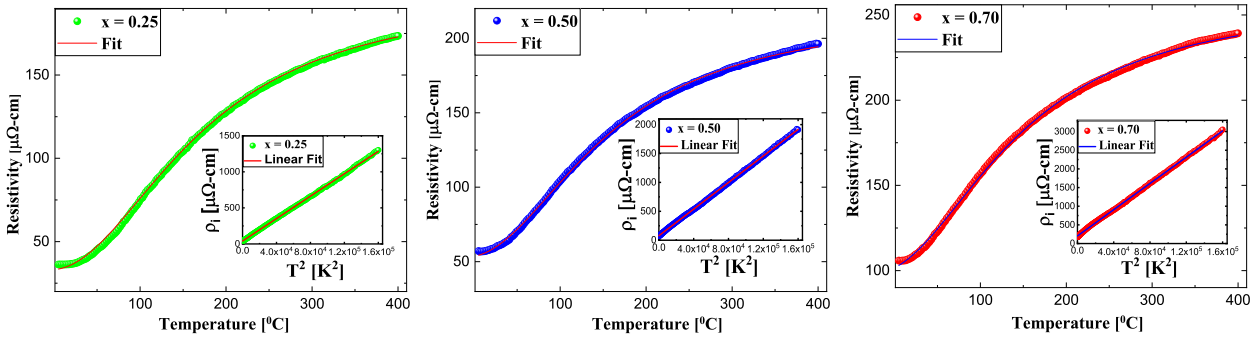

(a) (b) (c)

Figure A.39: The measured and fitted temperature dependence of resistivity for (a) $x = 0.25$, (b) $x = 0.50$, and (c) $x = 0.70$.

Table A.18: The total (and normalized per formula unit indicated in the parenthesis) and atomic magnetic moments of the supercells for the $Fe_{3-x}Cr_xGe$ alloy series. Structure type and corresponding space group are also indicated.

Atoms ($x=0$) $L1_2$ ($Pm\bar{3}m$)	M_s (μ_B)	Atoms ($x=0$) $D0_{19}$ ($P6_3/mmc$)	M_s (μ_B)	Atoms ($x=0.25$) $D0_{19}$ ($P6/m$)	M_s (μ_B)	Atoms ($x=0.50$) $D0_{19}$ ($P6/m$)	M_s (μ_B)	Atoms ($x=0.75$) $D0_{19}$ ($P6/m$)	M_s (μ_B)
Fe	2.196	Fe	2.21	Cr	0.397	Cr	0.695	Cr	0.189
Fe	2.196	Fe	2.21	Fe	2.232	Cr	0.011	Cr	0.189
Fe	2.196	Fe	2.21	Fe	2.020	Fe	2.234	Cr	0.179
Ge	-0.14	Fe	2.21	Fe	2.020	Fe	1.996	Fe	2.282
		Fe	2.21	Fe	2.232	Fe	2.227	Fe	2.282
		Fe	2.21	Fe	2.268	Fe	2.200	Fe	2.282
		Ge	-0.15	Fe	2.120	Fe	2.126	Fe	1.983
		Ge	-0.15	Fe	2.254	Fe	2.246	Fe	2.312
				Fe	0.564	Fe	2.255	Fe	2.312
				Fe	0.53	Fe	2.054	Fe	1.983
				Fe	0.555	Fe	2.245	Fe	2.254
				Fe	0.562	Fe	2.148	Fe	2.016
				Ge	-0.027	Ge	-0.081	Ge	-0.082
				Ge	-0.025	Ge	-0.056	Ge	-0.053
				Ge	-0.033	Ge	-0.112	Ge	-0.088
				Ge	-0.032	Ge	-0.110	Ge	-0.128
Total	6.448	Total	21.476(6.480)	Total	23.873(5.979)	Total	21.924(5.520)	Total	19.634(4.978)

elastic constants using density functional perturbation theory as implemented in VASP. Additionally, from these elastic constants we computed the mechanical properties of the considered alloys such as shear modulus (G), bulk modulus (K), Young's modulus (E) and Poisson's ratio (ν) using the open-source online application ELATE [307]. For these calculations, Voigt relations were used which calculate the upper limits of G, K, and E [308]. The calculated shear modulus (G_V), bulk modulus (K_V), and Young's modulus (E_V), K_V/G_V and $k = G_V/K_V$ (Pugh's ratios (ν) of Fe_3Ge and $Fe_{3-x}Cr_xGe$ alloys in $L1_2$ and $D0_{19}$ structures within GGA are given in Table A.19.

To obtain Vickers hardness we used following equations which are derived by Chen *et al.* [294] and then modified by Tian *et al.* [295];

$$H_{VC} = 2(k^2 G_V)^{0.585} - 3, \tag{A.3}$$

$$H_{VT} = 0.92 k^{1.137} G^{0.708}. \tag{A.4}$$

The calculated mechanical properties suggest that Fe_3Ge and $Fe_{3-x}Cr_xGe$ alloys in $L1_2$ and $D0_{19}$ phases are rather hard materials opposite to our experimental results. Pugh's ratio ($k = G_V/K_V$) is related to the ductility or brittleness of materials and also emphasize the relationship between the

Table A.19: The calculated mechanical properties for Fe_3Ge and $Fe_{3-x}Cr_xGe$ alloys (for $x = 0$, 0.25, 0.50, and 0.75) in $L1_2$ and $D0_{19}$ structures; Shear modulus (G_V), bulk modulus (K_V), Young's modulus (E_V), Pugh's ratio ($k = G_V/K_V$), Vickers hardness H_{VC} and H_{VT}, and Poisson's ratios (ν).

x	structure	G_V (GPa)	K_V (GPa)	E_V (GPa)	$k = G_V/K_V$	H_{VC} (GPa)	H_{VT} (GPa)	ν
0	$L1_2$	90.8	205.2	237.4	0.44	7.70	8.80	0.307
0	$D0_{19}$	76.7	184.3	202.1	0.42	6.18	7.41	0.317
0.25	$D0_{19}$	65.2	151.1	170.9	0.43	5.58	6.78	0.311
0.50	$D0_{19}$	66.7	167.0	176.6	0.40	4.99	6.35	0.324
0.75	$D0_{19}$	74.2	183.9	196.2	0.40	5.50	6.85	0.322

plastic and elastic properties of pure polycrystalline metals. For example, ductile materials have low k values while brittle materials have high ones. Our calculated Pugh's ratios ($k = G_V/K_V$) and K_V/G_V values indicate that these structures are ductile materials. In addition, as is known from the literature, if Poisson's ratio of a material ranges from 0.25 to 0.42 and if the K_V/G_V ratio ranges from 1.7 to 5.6, this material has metallic properties [309]. Our obtained results for Poisson's ratios and K_V/G_V values of Fe_3Ge and $Fe_{3-x}Cr_xGe$ alloys in $L1_2$ and $D0_{19}$ phases indicate that the bonding character of these materials are metallic. Theoretically estimated Vickers hardness values indicate that the material with the highest hardness is $L1_2$ Fe_3Ge.

As mentioned in the literature, if we compare both Vickers hardness equations, both of them can obtain values that agree with experimental results when the hardness of the material is larger than 5 GPa [295]. Otherwise, they can predict overestimated hardness values for low hardness values [295]. We note that the H_{VT} approximation overestimates Vickers hardness values of the materials according to our experimental results while the H_{VC} approximation gives closer results to experiment. However, both H_{VC} and H_{VT} for the $L1_2$ and $D0_{19}$ Fe_3Ge are almost two times larger than the experimentally obtained results. This can be attributed to the low hardness values for these structures. We can see that for larger experimental values of hardness (larger than 5 GPa) such as for $x = 0.50$ and 0.75, the calculated values for Vickers hardness are much closer to experiment and follow the same increasing trend.

A.7 Structural order-disorder and magnetism in quaternary Heusler compounds $Co_{2-x}Y_xFeAl$ (Y = Ti, V, Cr, Mn, Fe, and Co, $x = 0.50$)

A.7.1 Experimental Results

Here, the optical micrographs, experimental XRD patterns, variation of lattice parameter with atomic number of Y element, isothermal magnetization curves, variation magnetic moment with valence electron concentartion and the variation of mechanical hardness values with Y elements in Heusler alloys $Co_{2-x}Y_xFeAl$ (Y = Ti, V, Cr, Mn, Fe, and Co, $x = 0.50$ are presented.

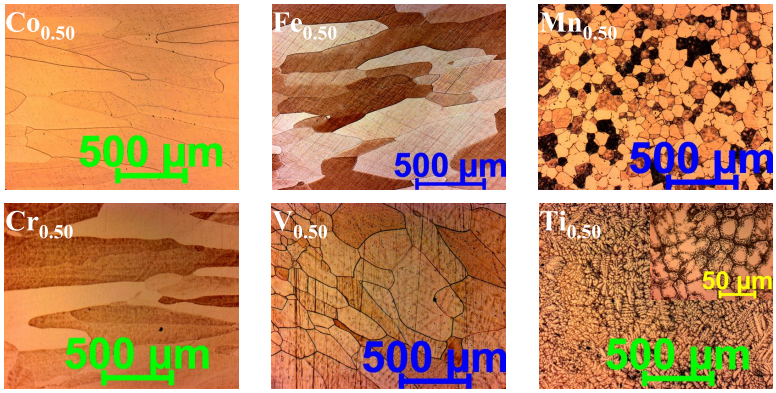

Figure A.40: Optical micrographs of $Co_{2-x}Y_xFeAl$ (Y = Ti, V, Cr, Mn, Fe, or Co, $x = 0.50$ Heusler series, heat treated at 850°C for 7 days followed by normal cooling in the furnace.

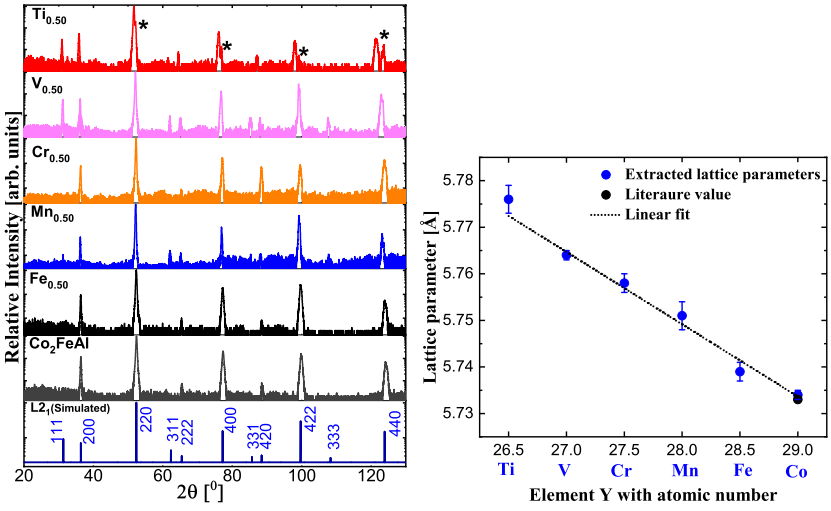

(a) (b)

Figure A.41: (a) Experimental XRD patterns of $Co_{2-x}Y_xFeAl$ (Y = Ti, V, Cr, Mn, Fe, or Co, $x = 0.50$) alloy series annealed at 850°C for 7 days investigated at room temperature. (b) Variation of lattice parameter with Y element showing linear behavior.

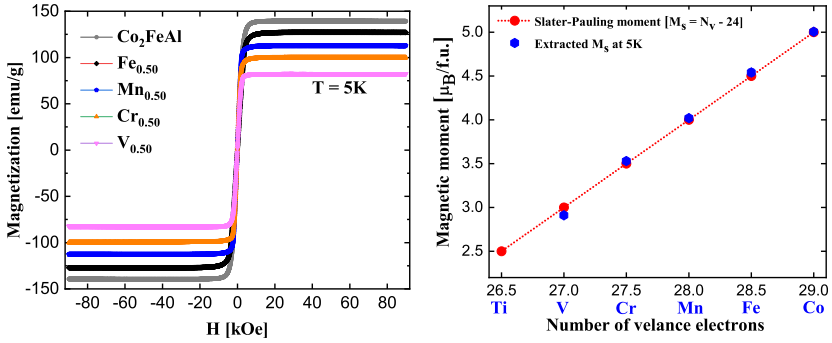

(a) (b)

Figure A.42: (a) The field-dependent magnetization at 5 K of $Co_{2-x}Y_xFeAl$ (Y = Ti, V, Cr, Mn, Fe, or Co, $x = 0.50$). (b) The saturation magnetic moment versus number of valence electrons in the alloy series, both experimental and expected from Slater Pauling rule for half metals.

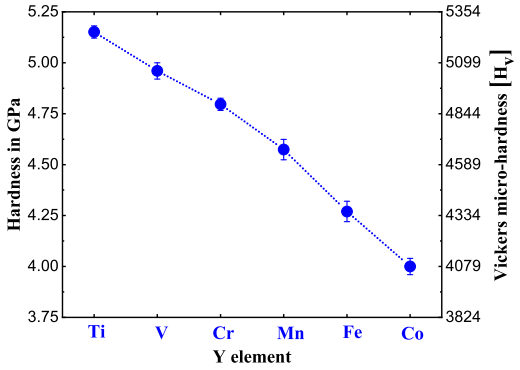

Figure A.43: Vickers hardness versus Y atom in $Co_{2-x}Y_xFeAl$ (Y = Ti, V, Cr, Mn, Fe, or Co, $x = 0.50$), all annealed at 850°C for 7 days.